Neutron Scattering Study of Magnetism in Insulating and Superconducting Lamellar Copper Oxides

by

Martin Greven

Vordiplom, Heidelberg University, Germany
(August 1988)

Submitted to the Department of Physics
in partial fulfillment of the requirements for the degree of

Doctor of Philosophy

at the

MASSACHUSETTS INSTITUTE OF TECHNOLOGY

June 1995

Author .....
Department of Physics
May 19, 1995

Certified by .....
Robert J. Birgeneau
Dean of Science and Cecil and Ida Green Professor of Physics
Thesis Supervisor

Accepted by .....
George F. Koster
Chairman, Departmental Committee on Graduate Students

Neutron Scattering Study of Magnetism in Insulating and Superconducting Lamellar Copper Oxides

by

Martin Greven

Submitted to the Department of Physics
on May 19, 1995, in partial fulfillment of the
requirements for the degree of
Doctor of Philosophy

Abstract

The static structure factor $S(q_{2D})$ of the spin-S two-dimensional (2D) square-lattice quantum Heisenberg antiferromagnet (2DSLQHA) is studied by means of neutron scattering experiment (for $S = 1/2$ and $S = 1$), Monte Carlo simulation ($S = 1/2$), and high-temperature series expansion ($1/2 \leq S \leq 5/2$). Neutron scattering measurements of the magnetic correlation length $\xi(T)$ in the $S = 1/2$ 2DSLQHA systems $Sr_2CuO_2Cl_2$ and La_2CuO_4 agree quantitatively with Monte Carlo and series expansion over a wide temperature range. The combined experimental and numerical data for $\xi(T)$, which cover the length scale from ~ 1 to 200 lattice constants, are predicted accurately with no adjustable parameters by renormalized classical (RC) theory for the quantum non-linear sigma model (QNLσM). For the $S = 1$ systems K_2NiF_4 and La_2NiO_4, $\xi(T)$ is in quantitative agreement with series expansion. However, RC theory for the QNLσM describes the experimental data only if the spin stiffness is reduced by $\sim 20\%$ from the theoretically predicted value. Series expansion for $S > 1$ exhibits an even larger discrepancy with theory. Several scaling scenarios are considered in order to account for the basic trends with S of $\xi(T)$. Experimentally it is found that $S(0) \sim \xi^2(T)$ for both $S = 1/2$ and $S = 1$, in disagreement with Monte Carlo, series expansion, and RC theory for the QNLσM, which all give $S(0) \sim T^2\xi^2(T)$.

The momentum-dependent single-particle excitation spectrum of the highest energy band in insulating $Sr_2CuO_2Cl_2$ is studied by means of photoemission spectroscopy. Calculations based on the t-J and one-band Hubbard models accurately predict the band width and the location of the valence band maximum, but do not correctly describe the overall band shape. A comparison with data previously reported for metallic samples leads to new suggestions for the phenomenology of doping.

Neutron scattering experiments of the temperature dependence of the low-energy incommensurate magnetic peak intensity in superconducting $La_{1.85}Sr_{0.15}CuO_4$ ($T_c = 37.3K$) reveal a pronounced maximum near T_c. A superconducting magnetic gap is observed at low temperatures, consistent with predictions based on a

$d_{x^2-y^2}$ superconducting order parameter. The inelastic magnetic scattering in non-superconducting $La_{1.83}Tb_{0.05}Sr_{0.12}CuO_4$ is incommensurate, and the dynamical susceptibility resembles that of lightly Sr-doped La_2CuO_4.

Thesis Supervisor: Robert J. Birgeneau
Title: Dean of Science and Cecil and Ida Green Professor of Physics

Acknowledgments

First and foremost, I would like to express my sincere gratitude to my thesis advisor Bob Birgeneau for his superb guidance and support. Bob has provided a truly outstanding learning and working environment, and his unparalleled drive for excellence and love for physics have been, and shall always be, a great inspiration to me.

It has been a distinct honor as well as a great pleasure to learn from and work with Gen Shirane. I have also benefited tremendously from the guidance of Marc Kastner and Uwe-Jens Wiese.

I would like to thank Yasuo Endoh, Kazu Yamada, Masa Matsuda, and Kenji Nakajima for many excellent collaborations as well as for their generosity during my stay in Japan.

Many thanks to Bernhard Keimer and Tom Thurston for their help and advice during the early stages of my graduate education, and to Arlete Cassanho and Bernhard for teaching me how to grow crystals.

I wish to thank Barry Wells, Sasha Sokol, Z.-X. Shen, John Perkins, and John Graybeal for sharing their insights with me and for our fruitful collaborations.

I would like to thank the members of the neutron scattering group at Brookhaven National Laboratory. In particular, I thank Ben Sternlieb, whose hospitality and great sense of humor were always appreciated. Also, I thank Peter Gehring, Marie Grahn, Kazu Hirota, Emilio Lorenzo, Steve Shapiro, and John Tranquada for their help and support, and for many enjoyable conversations.

I am very grateful to the former and present members of Bob Birgeneau's research group for their help and encouragement over the years, and for countless science and non-science conversations: Michael Young, Barry Wells, Yongmei Shao, Monte Ramstad, Bill Nuttall, Do Young Noh, Alan Mak, Young Lee, Bernhard Keimer, Young-June Kim, John Hill, Joan Harris, Qiang Feng, Kevin Fahey, Fang-Cheng Chou, and Kenny Blum have all made life at MIT and Brookhaven much more colorful. I have also enjoyed and benefited from my interactions with the members of Marc Kastner's group, as well as with many other people in Building 13.

I wish to thank Peggy Berkovitz for always patiently helping me to get through the maze of MIT's bureaucracy. Many thanks to Debra Harring for her help with our manuscripts. Peggy's and Debra's cheerfulness has often done wonders in moments of stress.

For the roles they played in my early science education, I would like to thank my high-school teacher Volker Kern as well as Dirk Dubbers, who let me work in his research group the summer before I took up my studies in Heidelberg.

I am very grateful to all my friends, especially to Ruth and Oren Bergman, Marie-Theres Gawlik, Hong Jiao, Kavita Khanna, Sabina Nawaz, Jens Niewöhner, Karim Safaee, Heather and Jared Tausig, and Michael Wolf, for their friendship and encouragement.

I am extremely grateful to Karen Ching-Yee Seto for her love and support, and for so many wonderful times.

Finally, I thank my family from the bottom of my heart for all their love and their support of my endeavors.

Contents

List of Figures

List of Tables

Chapter 1

Introduction

The collective properties of quantum systems are among the most interesting topics in condensed matter physics today. In particular, the discovery in 1986 by J.G. Bednorz and K.A. Müller of superconductivity in lamellar copper oxides has provided for much fertile ground to study quantum many-body phenomena. One of the fundamental features of these compounds is the presence of strong electron-electron Coulomb interactions. However, the electronic structure in highly correlated electron systems, one of the most difficult problems in physics, is still largely unsolved.

In many regards the simplest lamellar copper oxide is $La_{2-x}Sr_xCuO_4$. Neutron scattering experiments have established that stoichiometric La_2CuO_4 is the first spin-1/2 (S = 1/2) two-dimensional (2D) square-lattice quantum Heisenberg antiferromagnet (2DSLQHA) found in nature. Although the physics of quantum Heisenberg antiferromagnets has been the subject of research ever since the advent of quantum and statistical mechanics, a quantitative finite-temperature theory for 2DSLQHA has only recently emerged. The main part of this thesis is devoted to the experimental and computational study of these 2D magnets and the results obtained are compared with the theoretical predictions. A historical background to the physics of quantum Heisenberg antiferromagnets will be given in Chapter 4.

The complexity of the many-body phenomena observed increases dramatically as the doping level x is increased from zero. For $0.05 < x < 0.25$, $La_{2-x}Sr_xCuO_4$ is a high-temperature superconductor with many unusual metallic properties in its

normal state. It is well known, again from neutron scattering experiments, that 2D magnetic fluctuations are still very prominent in the superconducting doping range. Indeed, the presence of antiferromagnetic correlations plays an important role in many theoretical models that attempt to describe the electronic properties of the lamellar copper oxides. In the last Chapter of this thesis neutron scattering results of the magnetism in $La_{1.85}Sr_{0.15}CuO_4$ are presented and contrasted with those for the non-superconducting material $La_{1.83}Tb_{0.05}Sr_{0.12}CuO_4$. As an introduction to the physics of the lamellar copper oxides, a brief historical background is given in the next Section.

1.1 Brief history of superconductivity

The phenomenon of superconductivity has been known to exist ever since the discovery in 1911 by H. Kamerlingh Onnes [10] that mercury undergoes a phase transition at the critical temperature $T_c = 4.2K$ from a state with normal d.c. electrical resistivity to a superconducting state with *zero resistivity.* A second defining property of the superconducting phase of a material is the *"Meissner effect".* In 1933, Meissner and Ochsenfeld [11] discovered that a bulk superconductor is also a *perfect diamagnet*, i.e. a (small) external magnetic field is expelled from the main body of the material and will penetrate the surface only over a distance λ_0, the *London penetration depth.* Another characteristic feature of conventional superconductors is the *isotope effect*: The critical temperature varies with isotopic mass as $T_c \sim M^{-\alpha_0}$, with $\alpha_0 \sim 0.5$, indicating that lattice vibrations (phonons) play an essential role in bringing about superconductivity. Furthermore, in the superconducting state, an *isotropic energy gap* $E_g \simeq 3.5kT_c$ separates superconducting electrons below from normal electrons above the gap. Consequently, many thermodynamic quantities exhibit an exponentially activated behavior at low temperatures.

It was not until the late 1950's that a satisfactory microscopic description of these phenomena was given. Through the seminal theoretical work by J. Bardeen, L.N. Cooper, and J.R. Schrieffer [12] (BCS), it is now known that superconductivity in

metals like mercury, aluminium, and tin, is due to the pairing of electrons mediated by the electrons' interations with the crystal lattice. The BCS pairing theory can be thought of in terms of a two-fluid picture [13, 14, 15, 16, 17]. In a superconductor, at zero temperature, all the electrons are condensed into a macroscopic "superfluid". The superfluid consists of pairs of electrons bound together through lattice polarization forces. Electon-electron and pair-pair correlations lead to the energy gap in the excitation spectum from which many of the superconductor's properties can be derived. As the temperature is raised from zero, an increasing number of electron-pairs (also known as *Cooper pairs*) are broken apart and form a "normal fluid", interpenetrating the superfluid. The superfluid (and thus the superconducting properties) eventually disappears as the temperature reaches a material-specific critical temperature T_c.

Superconductors can be either of type I or of type II. A type I specimen exhibits perfect diamagnetism up to a critical magnetic field at which superconductivity disappears abruptly, and the field penetrates completely. A type II superconductor, on the other hand, is characterized by a *Meissner phase* for fields below a critical field H_{c1}, and a *mixed (or Shubnikov) phase* for $H_{c1} < H < H_{c2}$. In the mixed phase, the field is only partially excluded and the superconductor is threaded by flux lines. As the magnetic field is increased beyond H_{c1}, the density of flux lines increases until their non-superconducting cores overlap at the upper critical field H_{c2}, and superconductivity disappears. The magnetic flux enclosed by a vortex is quantized. The value of the flux quantum in conventional superconductors is $\Phi_0 = hc/(-2e)$, which implies that the carriers are pairs of charge $-2e$. While H_{c1} is primarily determined by λ_0, H_{c2} is determined by the *coherence length* ξ_0, which is the second fundamental length scale in the system. Heuristically, ξ_0 is the average size of the Cooper pairs. Most pure metals are of type I, with $\lambda_0 < \xi_0$. Type II superconductors (e.g., alloys) are characterized by a short electronic mean free path in the normal state (i.e., a high electrical resistivity) which corresponds to the situation when $\lambda_0 > \xi_0$.

One of the main objectives of superconductivity reasearch since Kamerlingh Onnes' discovery has been to find new materials with higher transition temperatures. How-

ever, for more than half a century progress was rather slow. In 1930, it was discovered that Nb has a T_c of $9.5K$, the highest transition temperature among all the elemental superconductors. During the next several decades, various Nb compounds were found to superconduct at somewhat higher temperatures. In 1973, the $20K$ mark was eventually broken with $T_c = 23.2K$ in Nb_3Ge [18]. However, this field of research had basically stagnated due to the lack of innovative ideas.

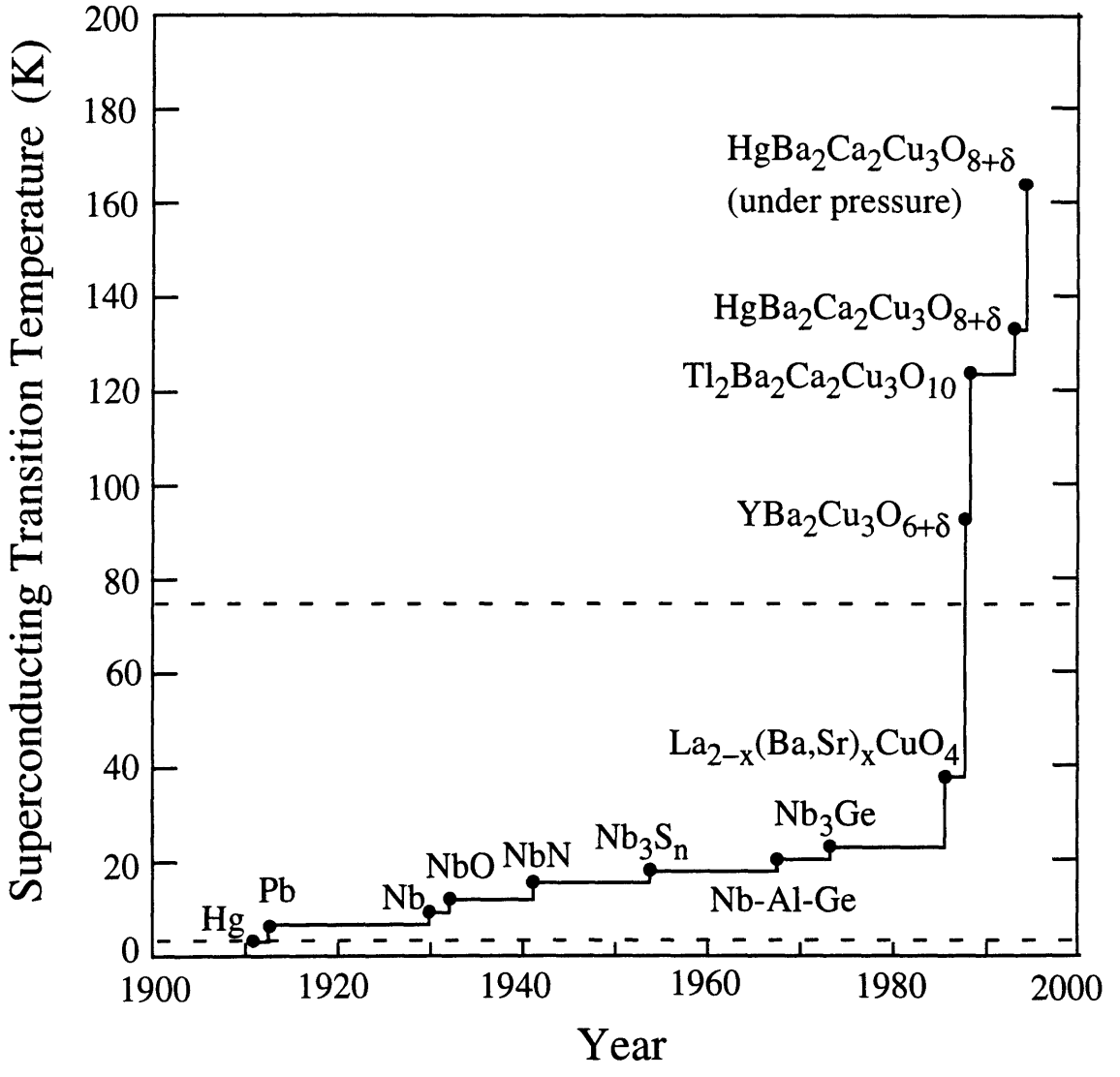

Figure 1-1: Superconducting transition temperatures of various materials plotted versus year of discovery. The two dashed lines indicate the boiling temperatures at ambient pressure of helium ($4.2K$) and nitrogen ($77K$).

Then, in 1986, came the spectacular breakthrough by J.G. Bednorz and K.A. Müller [19] who found evidence of superconductivity near $30K$ in the lamellar copper oxide system La-Ba-Cu-O. Their result was quickly confirmed in other laboratories around the world. To most researchers in the field, this discovery came as a complete surprise since related compounds were known to be poor conductors. By the end of 1986, a race for the discovery of related materials with even higher T_c's was under way. The high-T_c family $La_{2-x}M_xCuO_4$, with M = Ba, Sr, or Ca, was found to have a maximum T_c of $40K$ for M = Sr. Very soon it was discovered, that the application of pressure in $La_{2-x}Sr_xCuO_4$ drives the transition temperature to almost $60K$. It was then realized by Wu and collaborators [20], that the application of external pressure could be mimicked by "chemical pressure", the substitution of atoms by smaller isovalent ones. Attempting to replace La with Y, they discovered that the compound $YBa_2Cu_3O_{6+\delta}$ has a T_c of $\gtrsim 90K$ for $\delta \simeq 1$ [20]. For the first time a material with a critical temperature above the liquid nitrogen boiling point of $77K$ had been found. Since it is much cheaper to liquefy nitrogen rather than helium, the standard coolant up to that point, many technological applications became now feasible: "Eight years after transition temperatures first exceeded that of liquid nitrogen, high-T_c superconductors are being used in magnetometer sensors, prototype filters for cellular-phone base stations and magnetic resonance applications. Further progress in thin-film technology and electronics could lead to applications such as nondestructive testing, medical and geophysical sensors, communications, and multichip modules" (G. B. Lubkin, in Physics Today, March 1995). Eventually, Thallium-based [21, 22] and Mercury-based [23, 24] lamellar copper oxides with respective T_c's of 123K and 133K were discovered. When put under hydrostatic pressure, a Mercury compound was even found to superconduct at 164K. The evolution of these discoveries is summarized in Fig. 1-1.

Since superconductivity in the lamellar copper oxides takes place at unusually high temperatures, this new class of materials is also known as high-temperature superconductors. These superconductors are all of type II, and their material parameters (e.g., T_c, λ_0, ξ_0, etc.) lie in a new range, leading to interesting novel physical properties

such as the melting of the vortex lattice and the creation of new vortex-liquid phases [25]. The flux quantum is $hc/2e$, which implies that the carriers are pairs of charge $+2e$ and renders the lamellar copper oxides hole superconductors (there are a few exceptions, e.g. $Nd_{2-x}Ce_xCuO_4$ is an electron superconductor). Many normal state properties of these systems are very unconventional and not yet understood. The BCS pairing theory, in conjunction with the mechanism of phonon-mediated pairing, has worked remarkably well for ordinary superconducting metals. However, there appears to be a broad consensus among researchers in this field that this conventional pairing mechanism alone cannot account for the many unusual electronic properties of the lamellar copper oxides. While the BCS pairing theory combined with a novel pairing mechanism might still describe the physics of these materials, several fundamentally different theoretical models have been suggested.

1.2 Crystal and magnetic structures

The crystal structures and chemistry of the lamellar copper oxides are rather complicated. However, all of these materials have one fundamental ingredient in common: Two-dimensional (2D) sheets of CuO_2. These sheets are separated by layers of other atoms. It is widely believed that the superconductivity is primarily due to processes occuring in the CuO_2 sheets. The role of the intervening layers is to stabilize the lamellar structure and to provide charge-carriers to the CuO_2 sheets.

Because of its relatively simple structure, $La_{2-x}Sr_xCuO_4$ is the archetype lamellar copper oxide. The crystal structure of stoichiometric La_2CuO_4 is shown in Fig. 1-2(a). In this material, the CuO_2 sheets are separated by LaO bi-layers. Many other lamellar copper oxides exist, some of which have multiple CuO_2 sheets, separated by intervening layers. There is a general tendency for materials with several nearby CuO_2 layers to have a higher transition temperature, but also to be structurally more complicated. For example, $Tl_2Ca_{n-1}Ba_2Cu_nO_{4+2n}$ has single ($n = 1$), double ($n = 2$), and triple ($n = 3$) layers of CuO_2 with $T_c = 85, 105$, and $125K$, respectively. However, the essential physics must already be contained in the struc-

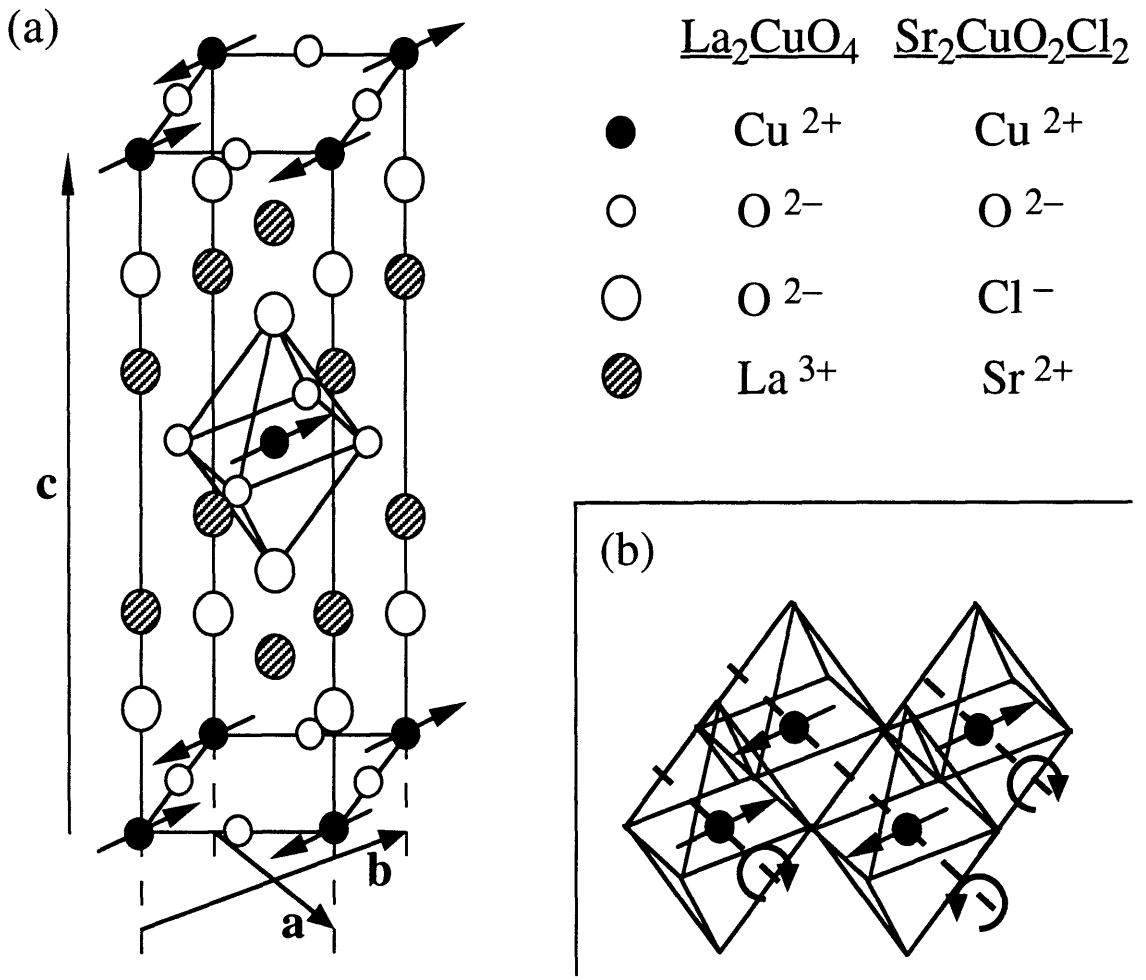

Figure 1-2: (a) Crystal and magnetic structures of La_2CuO_4 and $Sr_2CuO_2Cl_2$. The definition of the lattice parameters pertains to the orthorhombic space group Bmca. (b) Staggered tilting of the CuO_6 octahedra about the $\hat{a}$-direction in the orthorhombic phase of La_2CuO_4.

turally simpler single-layer compounds.

La_2CuO_4 is an antiferromagnetic insulator: Atomic La, Cu, and O have the respective electronic configurations [Xe]5d6s^2, [Ar]3d^{10}4s, and 1s^{2}2s^{2}2p^4. In the stoichiometric material, La^{3+} ions have the stable electronic configuration of Xe, and O^{2-} ions have a filled 2p^6 orbital. For overall charge neutrality, the Cu^{2+} ion has the configuration [Ar]3d^9 and therefore possesses a single 3d hole. In La_2CuO_4, the Cu^{2+}

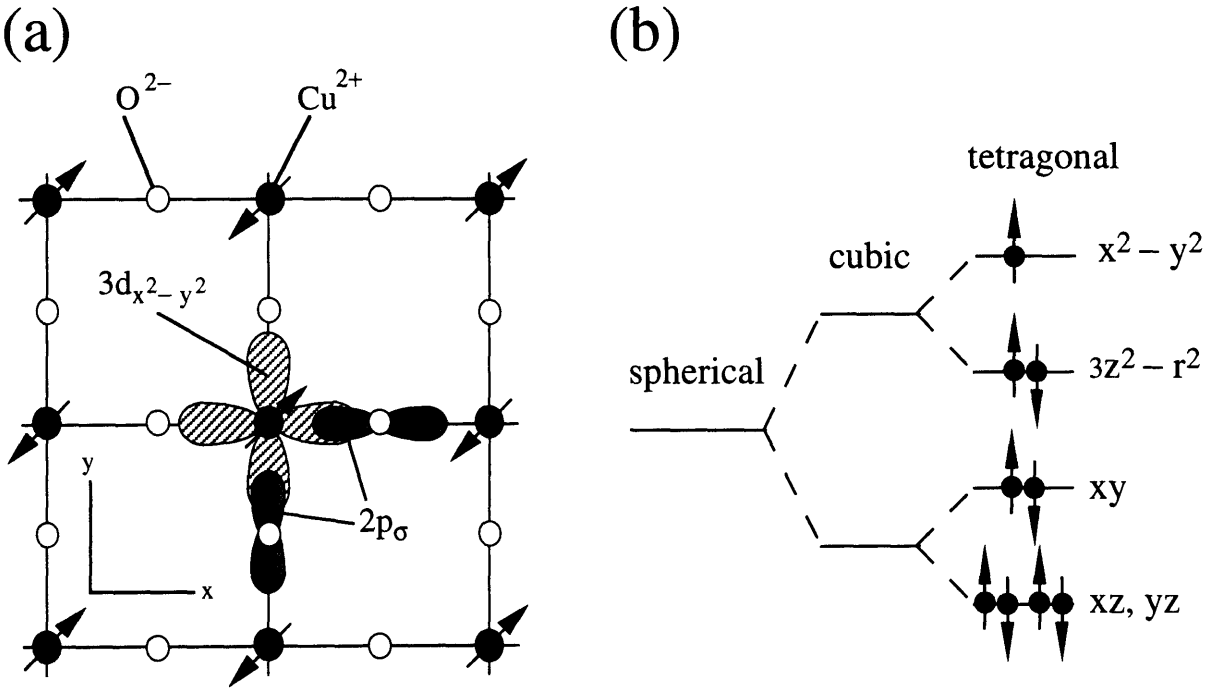

Figure 1-3: (a) CuO_2 sheet and (b) crystal field levels of Cu^{2+}.

sites are in an octahedral environment, surrounded by six oxygen ions. The resultant crystalline field lifts the five-fold d-degeneracy, so that holes exist in isolated $3d_{x^2-y^2}$ orbitals, as shown in Fig. 1-3(b). Since the apical oxygens are further away than those in the planes, the $3d_{x^2-y^2}$ state has a higher energy than the $3d_{3z^2-r^2}$ state. Experimentally, one observes localized copper S = 1/2 moments with an unusually strong antiferromagnetic superexchange interaction mediated by the in-plane oxygen ions [26].

Interestingly, one-electron band structure calculations wrongly predict La_2CuO_4

to be a non-magnetic metal [27, 28], since there is an odd number of electrons in the d-band. While band theory has been very successful at describing electronic properties in semiconductors and simple metals, it has been known to fail for materials that contain partially occupied localized orbitals. In band theory, also referred to as one-electron theory, electrons are described by delocalized wave functions, and the correlations between them (due to their mutual Coulomb repulsion) are treated only in a mean-field manner. In La_2CuO_4, the energy cost for two holes to be on the same Cu site far outweighs the kinetic energy that would be gained from the required hole motion. The 3d holes therefore remain at their respective Cu sites, and the material is an antiferromagnetic insulator. The prevalence of strong Coulomb interactions even in the metallic phase of the lamellar copper oxides poses a major challenge for the construction of a successful theoretical model.

In $La_{2-x}Sr_xCuO_4$, some of the tri-valent La^{3+} ions are replaced by bi-valent Sr^{2+} ions. For the system to maintain overall charge neutrality electrons have to be removed from some of the CuO_6 octahedra. It is well established that the corresponding holes primarily go onto the in-plane oxygen sites, converting O^{-2} ions to O^{-1} ions [29, 30, 31, 32, 33]. For reasons not yet understood, as the density of charge carriers in the CuO_2 sheets is increased, the lamellar copper oxides evolve from antiferromagnetic insulators, to superconducting metals, and eventually, to non-superconducting metals. It should be noted that substitutionally doping La_2CuO_4 with Sr introduces disorder into the system. However, the presence of disorder does not appear to be essential to the electronic properties in the lamellar copper oxides [34]. For example, the $YBa_2Cu_3O_{6+\delta}$ has its highest T_c of $\sim 90K$ in the stoichiometric limit $\delta \simeq 1$. The phase diagram of the compound $La_{2-x}Sr_xCuO_4$, as well as some of its physical properties as a function of the hole doping level x will be addressed in the next Section. In the remainder of this Section, the structures and spin Hamiltonians of the four antiferromagnetic insulators studied in this thesis (La_2CuO_4, $Sr_2CuO_2Cl_2$, K_2NiF_4, and La_2NiO_4) will be discussed.

At high temperatures, the crystal structure of La_2CuO_4 is body-centered tetragonal (space group I4/mmm). The material undergoes a structural transition at

$T_{ST} \simeq 530K$ into an orthorhombic phase (space groups Bmab or Cmca; unless noted otherwise, the notation pertaining to the space group Bmab will be used throughout this thesis *even for the description of the tetragonal phases.* In the Bmab notation, the $\hat{a}$- and $\hat{b}$-directions are in the basal plane, as indicated in Fig. 1-2(a).), in which the CuO_6 octahedra rotate by a few degrees in a staggered fashion, as illustrated in Fig. 1-2(b). To a first approximation it is appropriate to neglect corrections to the 2D Heisenberg Hamiltonian due to the local orthorhombicity and the 3D structure since these terms are several orders of magnitude smaller than the primary energy scale set by the Heisenberg superexchange J. At low temperatures, these corrections are nevertheless important as is evidenced by the fact that the zero-temperature transition of the underlying two-dimensional square-lattice Heisenberg antiferromagnet (2DSLQHA) is shifted to $T_N = 325K$ in La_2CuO_4.

For $S = 1/2$ single-layer copper oxides, the general form of the nearest-neighbor (NN) spin Hamiltonian is

$$\begin{aligned} H &= J \sum_{\langle ij \rangle} \mathbf{S}_i \cdot \mathbf{S}_j \\ &+ J \sum_{\langle ij \rangle} [\alpha_{DM}(S_i^c S_j^b - S_j^c S_i^b) - \alpha_{XY} S_i^c S_j^c] + J \sum_{\langle ij_\perp \rangle} \alpha_{j_\perp} \mathbf{S}_i \cdot \mathbf{S}_{j_\perp}, \end{aligned} \tag{1.1}$$

where $\langle ij \rangle$ and $\langle ij_\perp \rangle$ label in-plane and inter-plane NN, respectively. The Heisenberg superexchange J between planar NN copper spins sets the primary energy scale for spin excitations. High-energy neutron scattering experiments of the spin-wave dispersion [35] imply that $J = 135(6)\, meV$ in La_2CuO_4, in good agreement with a theoretical analysis [36] of two-magnon Raman spectra [1, 37] for this material. Spin-orbit coupling and direct exchange result in an exchange anisotropy of XY symmetry [38, 39]. In the orthorhombic phase of La_2CuO_4, the XY degeneracy is lifted by an antisymmetric (Dzyaloshinski-Moriya) exchange term due to spin-orbit interactions [40, 41, 42, 43, 44, 45, 46]. This term, which vanishes in the tetragonal phase of La_2CuO_4, is present only in crystal structures with low enough symmetry. In the Néel phase, it leads to the spin structure shown in Fig. 1-2(a) with ordered moments in the $\hat{b} - \hat{c}$-plane [26], canted by a small angle away from the $\hat{b}$-direction. As a re-

	La_2CuO_4	$Sr_2CuO_2Cl_2$	K_2NiF_4	La_2NiO_4
S	1/2	1/2	1	1
$T_N\,(K)$	325	256.5	97.23	327.5
$J\,(meV)$	135	125	8.9	28.4
α_{DM}	7.5×10^{-3}	-	-	-
α_{XY}	1.5×10^{-4}	1.4×10^{-4}	-	-
α_I	-	-	0.021	0.020
$\alpha_\perp$	5×10^{-5}	$\sim 10^{-8}$	$\sim 10^{-8}$	$\sim 10^{-4}$

Table 1.1: Néel temperature, superexchange energy, and corrections to the 2D Heisenberg Hamiltonian for the $S = 1/2$ and $S = 1$ materials studied.

sult of this canting, each CuO_2 sheet has a non-zero ferromagnetic moment [47]. The isotropic interplanar NN exchange is nearly frustrated in the orthorhombic phase, and the effective interlayer coupling $\alpha_\perp = 5 \times 10^{-5}$ has been obtained for La_2CuO_4 from an analysis of magnetoresistive anomalies at spin reorientation transitions [47, 48]. Both the symmetric and antisymmetric exhange energies manifest themselves as small gaps in the low-temperature spin-wave excitation spectrum and can be measured by neutron scattering [49]. All the correction terms are given in Table 1.1.

The second $S = 1/2$ system that has been studied is $Sr_2CuO_2Cl_2$. Instead of the $La^{3+}O^{2-}$ bi-layers of La_2CuO_4, this material has $Sr^{2+}Cl^-$ bi-layers separating the CuO_2 sheets, as indicated in Fig. 1-2(a). For several reasons, $Sr_2CuO_2Cl_2$ is the most ideal $S = 1/2$ NN 2DSLQHA known to-date. First, $Sr_2CuO_2Cl_2$ is difficult to dope chemically with either electrons or holes, so that the possibility that extrinsic carriers affect the magnetism of the CuO_2 sheets is minimal. Second, the material is isostructural to the high-temperature phase of La_2CuO_4 (space group I4/mmm), and it remains tetragonal down to very low temperatures. The antisymmetric exchange term, which is the dominant anisotropy in the orthorhombic phase of La_2CuO_4, is therefore absent. Moreover, the isotropic exchange between NN CuO_2 sheets is fully frustrated, i.e. the mean field exerted by one CuO_2 layer on an adjacent layer vanishes for tetragonal symmetry. Finally, the distance between neighboring CuO_2 sheets is very large for $Sr_2CuO_2Cl_2$ ($\sim$ 20% larger than that of La_2CuO_4), a property which further reduces the interplanar coupling $\alpha_\perp$.

However, $\alpha_\perp$ cannot be zero as evidenced by a finite-temperature transition at $T_N = 256.5K$ into a 3D Néel state. It has recently been demonstrated [38] that, once the bond-dependent anisotropic parts of the interplanar exchange tensor are taken into account, the frustration due to the isotropic interplanar exchange is lifted. There are two additional contributions to $\alpha_\perp$ which are similar in magnitude. One is the magnetic dipole interaction between planes, which has been estimated to be $\sim 2\times10^{-8}$ in $Sr_2CuO_2Cl_2$ [26]. The second additional contribution to $\alpha_\perp$ stems from the consideration of spin-wave quantum zero-point energy [50]. The authors of Ref. [38] have demonstrated that there also exists a corresponding in-plane quantum zero-point energy, which in the absence of interplanar coupling would lead to a staggered magnetization in the $\hat{a}$ direction. For $Sr_2CuO_2Cl_2$, the subtle competition between all these energies is believed to give the same spin structure as that of La_2CuO_4, albeit without the canting of moments [38].

From the two-magnon Raman measurments by Tokura et al. [1], shown in Fig. 1-4, it is possible to deduce the antiferromagnetic superexchange J. The peak position of the Raman spectra (in B_{1g} symmetry) scales linearly with J [36]. Since for La_2CuO_4, $J \simeq 135\ meV$ is known from neutron scattering experiments [35], the relative peak positions of the Raman spectra imply that $J = 125(6)\ meV$ for $Sr_2CuO_2Cl_2$. This value is consistent with theoretical estimates for the peak position in the Raman spectra [36]. The neutron scattering measurements of the out-of-plane spin-wave gap in $Sr_2CuO_2Cl_2$, discussed in Chapter 4, give $\alpha_{XY} = 1.4(1)\times10^{-4}$ which agrees with the value in La_2CuO_4 to within the experimental error.

The materials K_2NiF_4 and La_2NiO_4 are isomorphous to the two $S = 1/2$ systems discussed so far, with NiF_2 and NiO_2 sheets instead of CuO_2 sheets. In both systems, Ni exists as Ni^{2+}, which has the electronic configuration $[Ar]3d^8$. Experimentally, one observes ordered moments in the Néel phase which correspond to a $S = 1$ spin state. This implies that the two 3d holes are in separate $d_{x^2-y^2}$ and $d_{3z^2-r^2}$ orbitals. For materials with $S > 1/2$, the full spin Hamiltonian contains an on-site anisotropy term which can be adequately represented by a staggered field: $\sum_i g_i\mu_B H_i^A S_i^c$. This term is the dominant perturbation in the $S = 1$ materials K_2NiF_4 and La_2NiO_4. Neutron

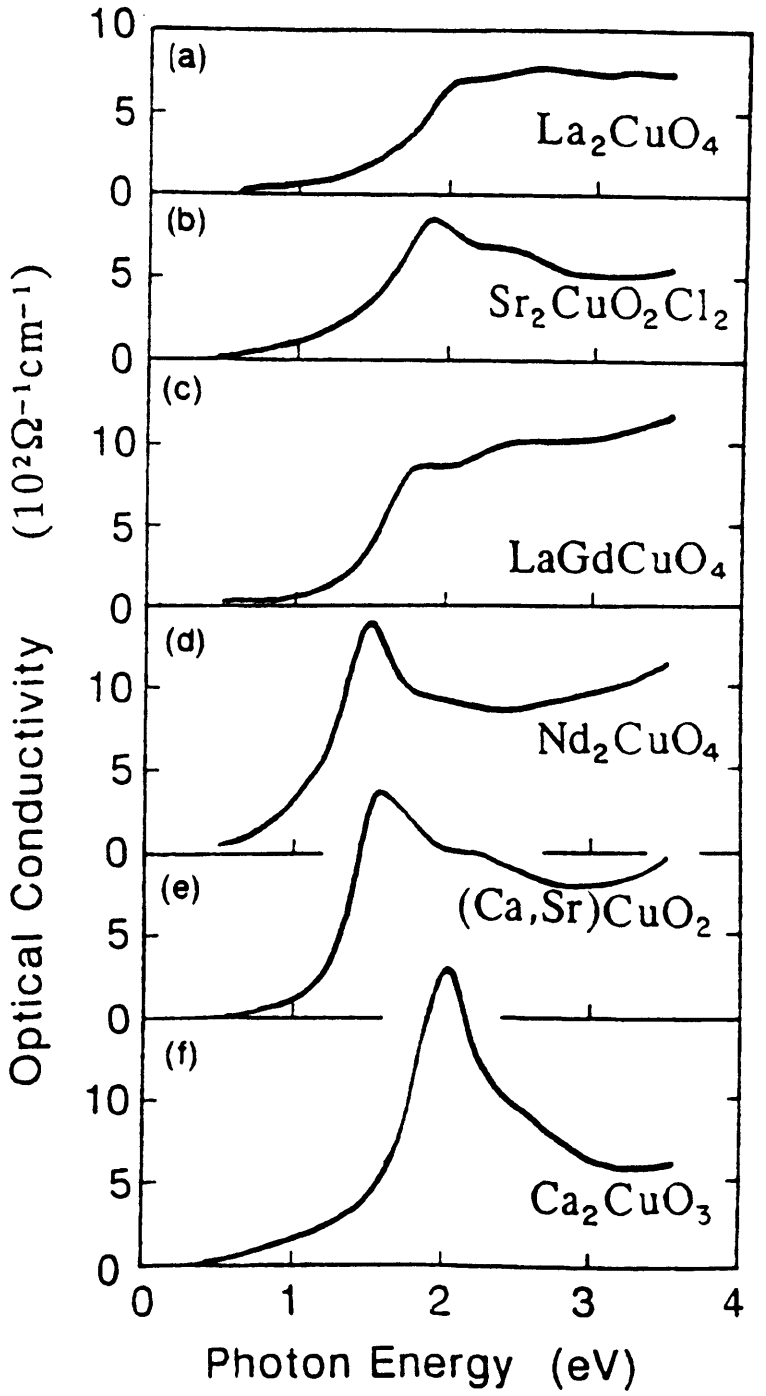

Figure 1-4: Raman spectra, at $T = 300K$, for B_{1g} two-magnon excitations in several single CuO_2 layer compounds (from Tokura et al. [1])

scattering measurements in K_2NiF_4 [51, 52, 53] yield a NN exchange $J = 8.9\ meV$, and a reduced anisotropy

$$\alpha_I = \frac{g\mu_B H_i^A}{\sum_{j=NN} JS_j} = 2.1 \times 10^{-3}. \tag{1.2}$$

For La_2NiO_4, $J = 28.7(7)\ meV$ and $\alpha \simeq 2.0(1) \times 10^{-3}$ [54].

At high enough temperatures, in the 2D correlated paramagnetic state, the Heisenberg term in Eq. (1.1) dominates the physics. The anisotropies and interplanar couplings become important only at temperatures close to T_N. In the tetragonal systems $Sr_2CuO_2Cl_2$ and K_2NiF_4, one observes a crossover from 2D Heisenberg to 2D XY and 2D Ising physics, respectively. The transitions to long-rang order in these two systems are essentially 2D in character, and the 3D ordering follows parasitically. Both La_2CuO_4 and La_2NiO_4 are orthorhombic at their respective Néel temperatures, and the resultant 3D interactions increase T_N from the underlying 2D value. The nature of the transition in La_2CuO_4 is furthermore complicated by the presence of the antisymmetric term in the spin Hamiltonian.

1.3 Phase diagram and electronic properties of $La_{2-x}Sr_xCuO_4$

For several reasons, $La_{2-x}Sr_xCuO_4$ is the system best suited for systematic experimental studies as a function of hole doping x. This material has a comparatively simple structure, as discussed in the previous Section. Furthermore, it is possible to grow the sizable crystals needed for neutron scattering studies. Another advantage is that $La_{2-x}Sr_xCuO_4$ can be doped even beyond the hole concentration at which superconductivity occurs. The basic features of the phase diagram of $La_{2-x}Sr_xCuO_4$, shown in Fig. 1-5, are shared by all the lamellar copper oxides.

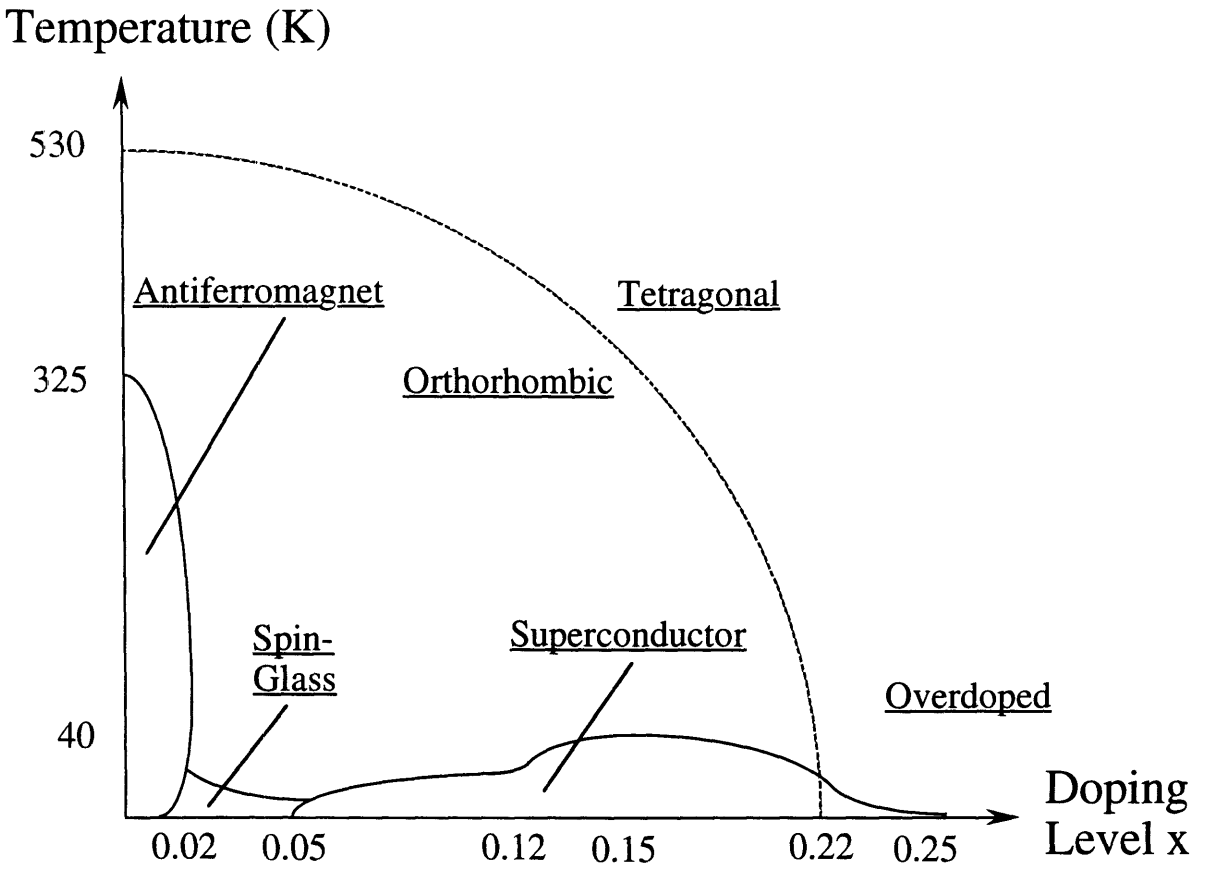

Figure 1-5: Phase diagram of $La_{2-x}Sr_xCuO_4$.

1.3.1 Phase diagram and magnetic properties

Stoichiometric La_2CuO_4 is an antiferromagnetic insulator with 3D Néel order below $T_N = 325K$. The 2D magnetic fluctuations above T_N are known to be rather well described by theoretical predictions [55, 56, 57] for the $S = 1/2$ 2D NN SLQHA [2, 58]. Figure 1-6 shows the inverse magnetic correlation length as obtained in the

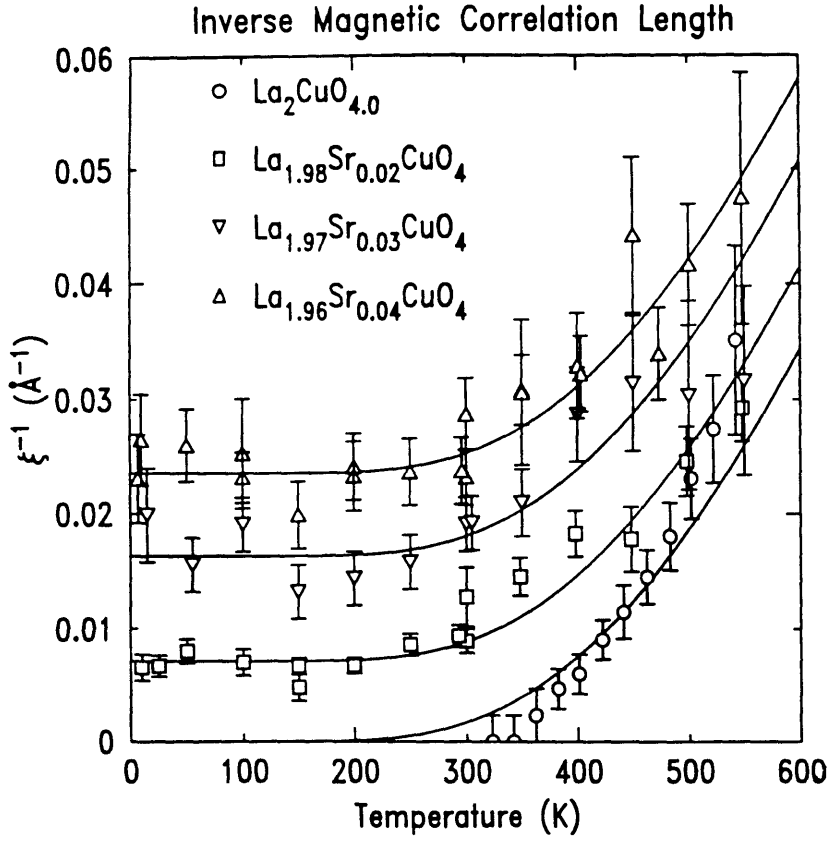

Figure 1-6: Inverse magnetic correlation length of four $La_{2-x}Sr_xCuO_4$ samples (from Keimer et al. [2]). The solid lines were calculated from $\xi^{-1}(x,T) = \xi^{-1}(x,0) + \xi^{-1}(0,T)$, as discussed in the text.

neutron scattering experiments by Keimer et al. [2]. The data for La_2CuO_4 are found to agree well with the theoretical prediction by Hasenfratz and Niedermayer [57] (indicated by the lowest line).

For $0 \leq x \lesssim 0.02$, $La_{2-x}Sr_xCuO_4$ exhibits 3D Néel order at $T = 0$, but the Néel temperature decreases very rapidly upon doping [59, 60, 61]. Transport measurements imply that the doped holes are localized below $\sim 100K$ [62]. Below $T_f \simeq (815K)x$

($T_f \simeq 16K$ at $x = 0.02$), a new spin-glass-like state, superimposed onto the long-range antiferromagnetic background of the Cu^{2+} spins, has been observed [63]. This low-temperature state is thought to be due to the freezing of the effective transverse (out-of-plane) spin degrees of freedom associated with the (localized) doped holes [63, 64, 65, 66].

For $0.02 \lesssim x \lesssim 0.05$, the 2D spin fluctuations are still commensurate with the ordering wavevector of the undoped system, and the correlation length is finite at $T = 0$ [2]. The neutron scattering data in Fig. 1-6 for the three Sr-doped samples are well described by the heuristic form

$$\xi^{-1}(x,T) = \xi^{-1}(x,0) + \xi^{-1}(0,T). \tag{1.3}$$

Here, $\xi(0,T)$ is the theoretical prediction for the Heisenberg model [57], and $\xi(x,0) = 150, 65,$ and $42\mathring{A}$ for the $x = 0.02, 0.03,$ and 0.04 samples, respectively. For 2D correlation lengths longer than $\sim 150\mathring{A}$ the residual anisotropic and interplanar spin interactions precipitate a transition to 3D long-range Néel order, while for shorter lengths only short-range order occurs down to $10K$. Already for $x \simeq 0.02$ and $T > 100K$ the transport is metallic, with a conductance per carrier approximately the same as that found in the normal state of the highest T_c superconductors [2, 59]. However, the holes are still localized at low temperatures for $0.02 \lesssim x \lesssim 0.05$. There is strong experimental evidence for a rather conventional spin-glass phase at low temperatures [2, 67, 68, 69], which had been predicted to exist in this doping regime [70, 71]. Unlike for $x < 0.02$, the transition temperature has been found to vary inversely with hole concentration: $T_g \sim 1/x$ [63].

In the doping range $0.05 \lesssim x \lesssim 0.25$, $La_{2-x}Sr_xCuO_4$ is metallic, and at low temperatures superconducting. The "optimal" doping level is reached for $x = 0.15$, in the sense that the superconducting transition temperature is the highest with $T_c \simeq 40K$. The regimes of the phase diagram with $x < 0.15$ and $x > 0.15$ are often referred to as "underdoped" and "overdoped", respectively. Neutron scattering experiments have revealed that the spin fluctuations are incommensurate in this doping regime and per-

sist up to at least $x = 0.15$ [8, 9, 72, 73, 74, 75]. The superconducting phase boundary exhibits a small plateau for $x \simeq 0.12$. Interestingly, in $La_{1.88}Ba_{0.12}CuO_4$ superconductivity is completely suppressed and, unlike in the Sr-doped case, the Ba-doped system furthermore undergoes a second structural transition at low temperatures from orthorhombic to tetragonal (space group P42/ncm) [76, 77]. Near $x = 0.12$, the isotope effect is anomalously large for both the Ba- and Sr-doped systems ($\alpha_0 \sim 0.8$) [78]. However, away from this doping level it is rather small ($\alpha_0 < 0.1$ for $x > 0.14$). Quite generally, it is found for the lamellar copper oxides that the isotope effect is very small in the vicinity of the optimal doping level.

For $x \gtrsim 0.25$, $La_{2-x}Sr_xCuO_4$ no longer exhibits superconductivity [79]. It has been claimed that the disappearance of superconductivity near $x \sim 0.25$ is closely related to the presence of the structural phase boundary [79]. However, more recent work on $La_{2-x-y}Pr_ySr_xCuO_4$ suggests that this is not the case [80]. Co-doping $La_{2-x}Sr_xCuO_4$ with Pr was found to shift the structural phase boundary to larger x, while superconductivity still vanished for $x \simeq 0.25$. The disappearance of superconductivity is therefore likely to be a consequence of electronic overdoping and the related modification of electronic states.

The close proximity of the superconducting phase to an antiferromagnetic phase is one of the most distinctive characteristics of the lamellar copper oxides. As stated above, significant 2D magnetic fluctuations persist deep into the superconducting doping regime. In fact, in several theoretical models the pairing is assumed to be mediated by antiferromagnetic fluctuations. The substitution of about 2% of the $S = 1/2$ Cu^{2+} moments by non-magnetic Zn^{2+} ions is known to destroy superconductivity [81]. This behavior is just the opposite of that in ordinary (non-magnetic) superconductors like Al, where superconductivity is destroyed by tiny amounts of magnetic impurities. However, even the substitution with small amounts of magnetic Ni^{2+} ions is known to be detrimental to the superconductivity in the lamellar copper oxides [82]. Quite apparently, the lattice of Cu^{2+} $S = 1/2$ moments constitutes a fundamental ingredient of this new class of materials. It is therefore often thought of as the "vacuum" in which superconductivity occurs upon addition of a sufficient amount

of charge carriers. Nevertheless, even in the highly anisotropic lamellar copper oxides superconductivity is, in the end, a 3D phenomenon.

1.3.2 Normal state transport properties

Many electronic properties in the normal state of the lamellar copper oxides are very unusual and differ markedly from the Fermi-liquid behavior exhibited by ordinary metals. Perhaps the most widely discussed normal state anomaly is the linear temperature dependence of the in-plane resistivity observed near the optimal doping level in all of the hole-doped materials [83]. For $La_{2-x}Sr_xCuO_4$, the in-plane resistivity ρ_{ab} has been measured over a wide doping and temperature range by Takagi et al. [3], as shown in Fig. 1-7. The resistivity is linear near $x \simeq 0.15$ over the entire temperature range $T_c < T \leq 1000K$, and it extrapolates approximately to zero at $T = 0K$. This behavior is very remarkable, since for a Fermi-liquid metal the low-temperature resistivity would be dominated by electron-electron scattering processes, which give $\rho \sim T^2$. It should be noted, that in an ordinary metal the high-temperature resis-

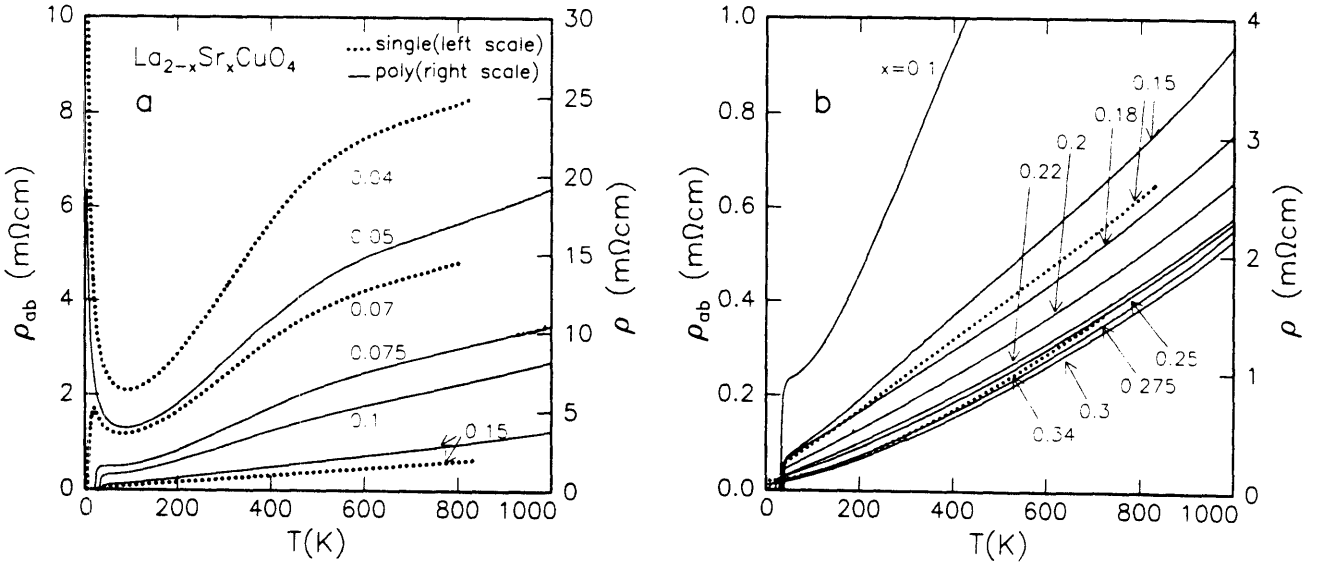

Figure 1-7: Temperature dependence of the resistivity in $La_{2-x}Sr_xCuO_4$ for (a) $0.04 \leq x \leq 0.15$ and (b) $0.1 \leq x \leq 0.34$. Dotted lines mark the in-plane resistivity ρ_{ab} of single-crystal films with (001) orientation. Solid lines mark the resistivity (ρ) of polycrystalline materials (from Takagi et al. [3]).

tivity is dominated by electron-phonon scattering processes and is also linear in T. However, the slope of the $T-$linear resistivity is strikingly similar in many optimally doped high-temperature superconductors, and thus exhibits no clear dependence on T_c [83]. Since both phonon spectra and degrees of crystal imperfections vary greatly in these compounds, a common scattering mechanism other than phonons and defects is likely to dominate $\rho_{ab}(T)$.

Even in the non-superconducting overdoped regime the measurements by Takagi et al. [3] give $\rho_{ab} \sim T^{1.5}$ (for $x \geq 0.30$), still different from that of a conventional Fermi-liquid. For $x \lesssim 0.10$ the resistivity exhibits a decreasing slope at high temperatures, which might indicate that the mean free path of the holes has become comparable to the lattice constant. An analysis based on Boltzman transport theory yields estimates for the Fermi momentum k_F which are consistent with a small Fermi surface containing $\sim x$ holes [3].

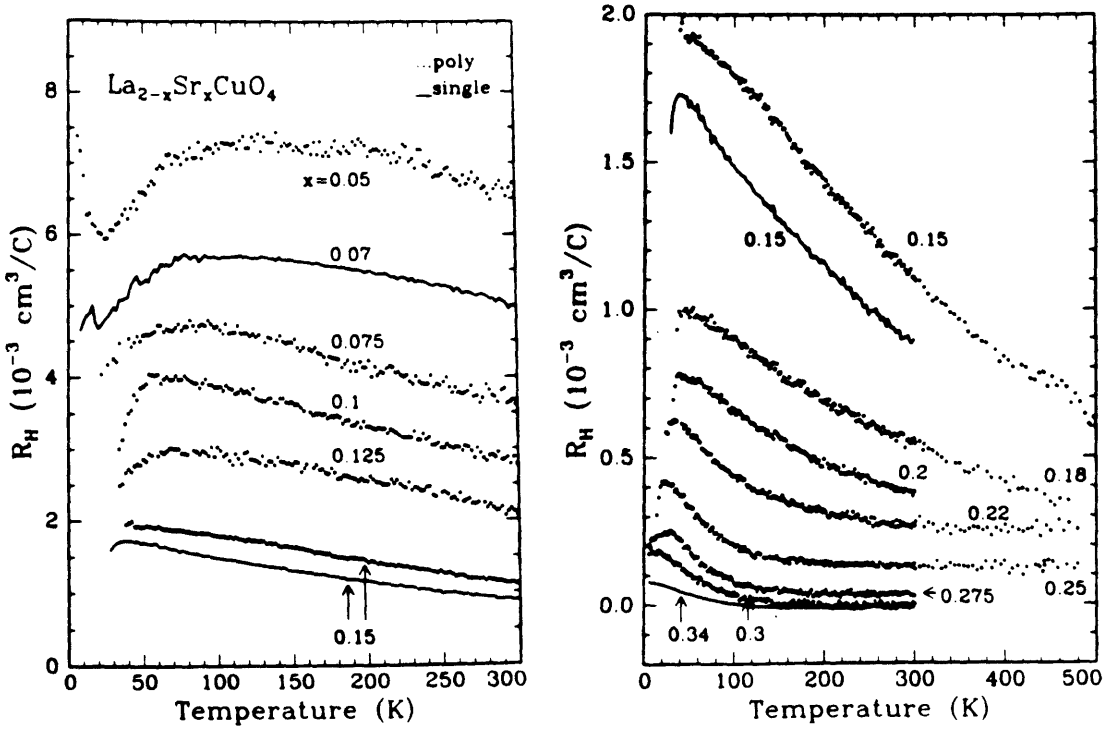

Figure 1-8: Temperature dependence of the Hall coefficient for $La_{2-x}Sr_xCuO_4$ in the composition range $0.05 \leq x \leq 0.34$. Solid lines denote single-crystal data with field $\mathbf{H}||\mathbf{c}$, and dots denote polycristalline data (from Hwang et al. [4]).

Another striking normal state feature is the strong and extended temperature dependence observed for the Hall coefficient R_H near the optimal doping level. In conventional models of a metal this quantity is approximately constant. Hwang et al. [4] have measured $R_H(T)$ for $La_{2-x}Sr_xCuO_4$ over a wide doping range. As can be seen from Fig. 1-8, $R_H(T)$ is large and positive at low doping and decreases quickly with increasing Sr content, consistent with an increasing hole concentration as well as with the rapid drop observed for ρ_{ab}. The strong temperature dependence of R_H persists at temperatures above any phonon-related temperature. Interestingly, the most dramatic temperature dependence of R_H is observed near the optimal composition ($x = 0.15$), for which the resistivity is strictly linear in T, and the isotope effect is small.

As a result of the predominantly 2D nature of the lamellar copper oxides, large anisotropies are observed for many physical quantities. As an example, the resistivity anisotropy will be briefely discussed. At low temperatures, for $x \lesssim 0.15$, the slope of the out-of-plane resistivity ρ_c is negative, whereas that of ρ_{ab} is positive [84]. This fact suggests that the conduction mechanism is different in the two directions and that the material can be regarded as a 2D metal over some extended temperature range above T_c. For $x = 0.30$, ρ_c is metallic with the same temperature dependence as ρ_{ab} ($\sim T^{1.5}$), while the anisotropy is still ~ 100 [84]. The constant ratio ρ_c/ρ_{ab} suggests that the same conduction mechanism is at work in all directions. Overall, the resistivity exhibits a crossover from 2D to 3D metallic behavior with increasing temperature and/or doping level.

In conventional superconductors, like Hg and Al, BCS-theory, in conjunction with the model of phonon-mediated pairing, has worked remarkably well. However, the unusual properties of the lamellar copper oxides discussed in this Section seem to rule out the possibility that the relevant energy scale is set by phonons. For the latter materials strong electron-electron correlations are known to exist. It is a widely held view that the high transition temperatures and pairing energy scales in the copper oxides result from the interacting electronic degrees of freedom.

There is one last issue that deserves special attention: Electron-doped compounds

exhibit much more conventional normal state properties than their hole-doped counterparts. For example, the temperature dependence of the in-plane resistivity is found to be quadratic for optimally doped $Nd_{2-x}Ce_xCuO_4$ [85, 86], consistent with electron-electron scattering in a Fermi liquid. One of the key differences between hole- and electron-doped materials is that in the former the carriers predominantly reside on the oxygen ions and consequently frustrate the antiferromagnetic order, while in the latter the carriers prefer to reside on the copper ions and therefore dilute the magnetic system [87]. The lack of universality between electron- and hole-doped materials is a missing ingredient in most theoretical models for the lamellar copper oxides.

1.4 Theoretical Models

It is generally believed that an understanding of the peculiar normal state is a prerequisite for the elucidation of the mechanism behind the superconductivity in the lamellar copper oxides. The presence of strong 2D magnetic fluctuations, the linear resistivity down to very low temperatures, the extended temperature dependence of the Hall coefficient, and the rather weak isotope effect are all properties which suggest that the BCS model of phonon-mediated pairing is inappropriate for these materials. Since the Fermi liquid paradigm underlies the conventional BCS theory of superconductivity, major conceptual advances are required in order to arrive at a satisfactory understanding of the phase diagram illustrated in Fig. 1-5.

Nevertheless, it is still possible that BCS pairing theory combined with a mechanism other than phonon-mediated pairing might capture the essential physics. In BCS theory, an effective attractive interaction between fermions causes them to form overlapping bosonic pairs which make up the macroscopic condensate. The source of the attractive interaction is not crucial for this theory, which has also been successful at describing the superfluid state of ^{3}He as well as neutron star matter. In superfluid ^{3}He, for example, the attractive interaction is provided by the exchange of magnetic excitations of the surrounding atomic sea. For the lamellar copper oxides, various pairing interactions have been considered [88, 89]. Among these models, those based

on antiferromagnetic spin fluctuations have received the widest attention. Other theories are more exotic and are based on the notion that it will be necessary to go well beyond a Landau Fermi liquid approach [34, 88, 89, 90, 91, 92].

What makes a theoretical and numerical description of the lamellar copper oxides so extremely difficult is the fact that their electronic structure at small and intermediate hole doping levels is neither in the itinerant or localized limit. At very high doping levels, beyond the region of the phase diagram in which superconductivity occurs, the electronic properties of these materials appear to approach those of a conventional Landau Fermi liquid. In this regime one might therefore expect a one-electron band theoretical (itinerant) description to be appropriate. However, conventional band theory treats correlations between electrons only in a mean-field manner, and therefore cannot capture the stong correlation effects known to exist at intermediate and small doping. At zero doping, the electrons are localized. In this limit, the lamellar copper oxides are antiferromagnetic insulators for which the low-energy physics is correctly captured by the $S = 1/2$ Heisenberg Hamiltonian.

By far most electronic theories start from the well-defined localized limit of the phase diagram, and are generally based on several simplifying assumptions. First, the model Hamiltonians are strictly two-dimensional as it is believed that the essential physics of the lamellar copper oxides is that of the CuO_2 sheets. Second, only one orbital per Cu site is considered: the orbital of $d_{x^2-y^2}$ symmetry (see Fig. 1-3(b)). A third assumption that is normally made is that the Coulomb repulsion at intermediate and large distances is screened by the non-zero density of doped carriers.

Based on the above assumtions, the most general Hamiltonian considered is the three-band (Hubbard) Hamiltonian given by [33, 89, 93, 94, 95]

$$\begin{aligned} H &= -t_{pd}\sum_{\langle ij\rangle} p_j^\dagger(d_i + H.c.) - t_{pp}\sum_{\langle jj'\rangle} p_j^\dagger(p_{j'} + H.c.) \\ &\quad + U_d\sum_i n_{i\uparrow}^d n_{i\downarrow}^d + U_p\sum_j n_{j\uparrow}^p n_{j\downarrow}^p + U_{dp}\sum_{\langle ij\rangle} n_i^d n_j^p \\ &\quad + \epsilon_d\sum_i n_i^d + \epsilon_p\sum_j n_j^p, \end{aligned} \tag{1.4}$$

where $p_j^\dagger$ and $d_i^\dagger$ (p_j and d_i) are hole creation (destruction) operators at the oxygen and copper sites, respectively. Undoped La_2CuO_4 is a charge-transfer insulator with a gap between the highest occupied (oxygen) state and the lowest unoccupied (copper) state. The three bands of the model are the two oxygen bands $2p_x$ and $2p_y$ (normally both referred to as $2p_\sigma$) and the copper $3d_{x^2-y^2}$ band. This is shown schematically in Fig. 1-9(a). Due to the relatively large Coulomb repulsion U_d on the Cu sites, the Cu-band is split into the upper (UHB) and lower (LHB) Hubbard bands. The terms U_p and U_{dp} in the Hamiltonian describe the Coulomb repulsion for holes at the same oxygen orbital and for holes on neighboring copper and oxygen sites, respectively. The on-site energies ϵ_d and ϵ_p represent the difference between occupied orbitals of Cu and O. The kinetic energy terms t_{pd} and t_{pp} describe the oxygen-copper and oxygen-oxygen hopping of the holes on the lattice. At half-filling (i.e., with one hole per unit cell) and in the strong coupling (i.e., large U_d) limit, the above Hamiltonian correctly reduces to the $S = 1/2$ NN 2DSLQHA model [95, 96]. The terms in the Hamiltonian can be estimated from band structure calculations to be $\Delta = \epsilon_p - \epsilon_d \simeq 3.6eV$, $t_{pd} \simeq 1.3eV$, $t_{pp} \simeq 0.65eV$, $U_d \simeq 10.5eV$, $U_p \simeq 4eV$, and $U_{pd} \simeq 1.2eV$ [89, 97]. Since $U_d > \Delta$, an additional hole will preferably occupy the oxygen orbitals, as required from experiment [29, 30, 31].

The three-band Hubbard model is still very hard to work with, despite the various simplifying assumptions that it is based on. Consequently, simpler one-band models have been considered by many theorists: the $t-J$ model and the one-band Hubbard model. The $t-J$ model [98] is defined by the Hamiltonian

$$\begin{aligned} H &= -t \sum_{\langle ij \rangle \sigma} \left[c_{i\sigma}^\dagger \left(1 - n_{i-\sigma}\right) \left(1 - n_{j-\sigma}\right) c_{j\sigma} + H.c. \right] \\ & \quad J \sum_{\langle ij \rangle} \left[\mathbf{S_i} \cdot \mathbf{S_j} - \frac{1}{4} n_i n_j \right], \end{aligned} \tag{1.5}$$

where J is the antiferromagnetic coupling between spins on NN sites i and j on a square lattice. In this effective model, the oxygen ions are no longer present, and double occupancy of sites in not allowed. A site can either be occupied with an

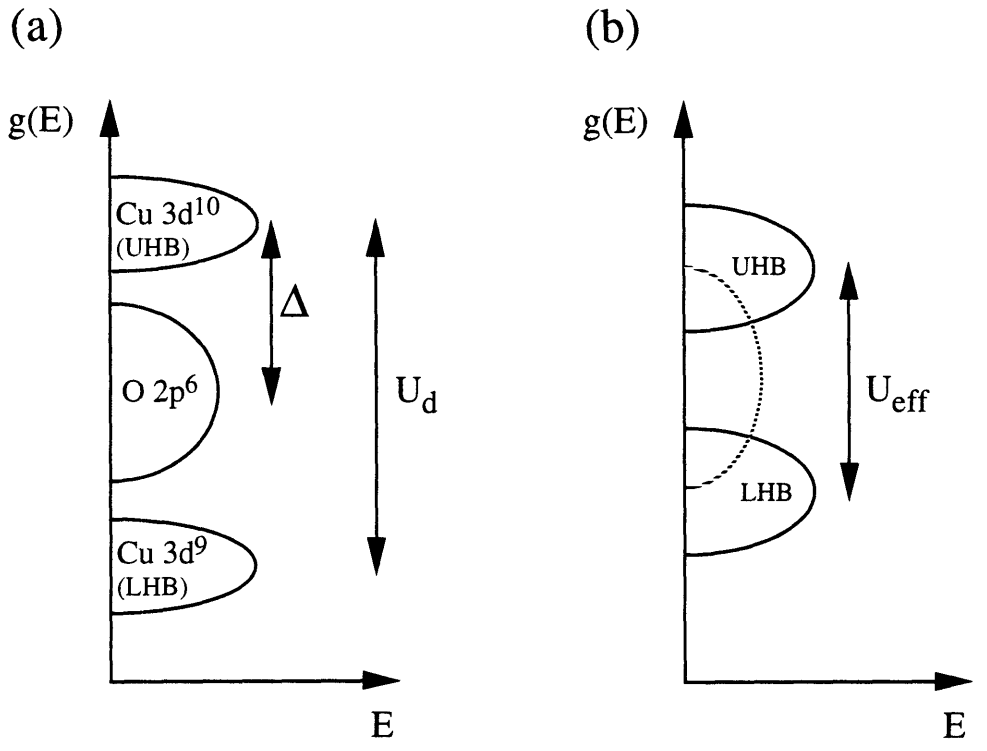

Figure 1-9: Schematic density of states of the CuO_2 planes: (a) Three-band Hubbard model. U_d is the Coulomb repulsion at the Cu^{2+} sites. The charge-transfer gap Δ is the energy difference between copper and oxygen orbitals. (b) One-band Hubbard model. The charge-transfer gap is mimicked by an effective Hubbard gap U_{eff}. For strong on-site repulsion ($U_{eff} >> t$) the electrons are localized. In the weak coupling limit ($t >> U_{eff}$), indicated by the dashed line, the model describes a band of extended states.

electron (of spin "up" or "down") or unoccupied (i.e., occupied with a hole). Note, that the $t-J$ model does not contain a Coulomb term, and is therefore only strictly defined for one hole which moves in the antiferromagnetic background via the hopping term t. It has been suggested that it is possible to reduce the low-energy spectrum of the more realistic three-band Hubbard model to the much simpler $t-J$ model [99], but this issue is still controversial [89]. Regardless of this open question, the $t-J$ model is heavily studied by theorists since it is believed to contain many of the essential features of the doped CuO_2 planes.

The other effective model is the one-band Hubbard model, originally introduced in 1963 by J. Hubbard [100] in an attempt to understand the crossover from localized to extended states. It is defined by the Hamiltonian

$$H = -t \sum_{\langle ij \rangle \sigma} (c^{\dagger}_{i\sigma} c_{j\sigma} + c^{\dagger}_{j\sigma} c_{i\sigma}) + U_{eff} \sum_{i} (n_{i\uparrow} - 1/2)(n_{i\downarrow} - 1/2), \qquad (1.6)$$

where the operator $c^{\dagger}_{i\sigma}$ ($c_{i\sigma}$) creates (destroys) an electron at site i. This model is used in an attempt to mimick the presence of the charge-transfer gap Δ of the material through an effective Coulomb repulsion U_{eff}, as indicated in Fig. 1-9(b). The oxygen band of the three-band model is absorbed into the UHB and LHB of that model, to form the UHB and LHB of the one-band model. In the weak coupling limit, $t >> U_{eff}$, the UHB and LHB merge into one band of extended states, shown by the dashed line in Fig. 1-9(b). In the strong coupling limit, $U_{eff} >> t$, the electrons are completely localized. The lamellar copper oxides lie in between these two limits.

1.5 Outline

The format of his thesis is as follows: In the next Chapter, the nuclear and magnetic neutron scattering cross-sections will be discussed, and an overview of the neutron scattering technique will be given. Chapter 3 addresses the growth and characterization of single crystals. In Chapter 4, the neutron scattering investigation of the $S = 1/2$ 2DSLQHA materials $Sr_2CuO_2Cl_2$ and La_2CuO_4 is presented. Chapter 5 con-

tains a complementary quantum Monte Carlo study of the 2D $S = 1/2$ NN SLQHA. In the first part of Chapter 6, previous results for the $S = 1$ 2DSLQHA system K_2NiF_4 are re-analysed. Moreover, new results for the $S = 1$ material La_2NiO_4 are presented. The second part of Chapter 6, contains a comparison of experimental ($S = 1/2$ and 1), Monte Carlo ($S = 1/2$), and high-temperature series expansion ($1/2 \leq S \leq 5/2$) results. The crossover from quantum ($S = 1/2$) to classical (large S) physics is discussed. Chapter 7 describes a photoemission study of the insulator $Sr_2CuO_2Cl_2$. The results are compared with existing data for metallic lamellar copper oxides, as well as with theoretical predictions for one-band models. In Chapter 8, a neutron scattering experiment of the low-energy fluctuations in the high-temperature superconductor $La_{1.85}Sr_{0.15}CuO_4$ is presented. The results for the superconductor are compared with those for non-superconducting $La_{1.83}Tb_{0.05}Sr_{0.12}CuO_4$.

Chapter 2

Neutron Scattering

2.1 Introduction

Since their discovery by J. Chadwick in 1932 [101, 102], neutrons have played an increasingly important role as a tool to study a wide variety of phenomena in condensed matter [103]. Neutrons are uncharged particles [101, 102, 104] of spin $S = 1/2$ [105, 106] with a magnetic moment $\vec{\mu}_n = \gamma \mu_N \vec{\sigma_n}$, where $\gamma = -1.913$ [107, 108] and $\mu_N = e/(2m_p)$ is the nuclear magneton. Since they carry no charge, neutrons can penetrate deeply into matter and interact through either nuclear forces or with unpaired electrons of magnetic ions. This property, together with the rather long neutron liftetime (half-life $\sim 10^3 s$ [109]; β-decay: $n \rightarrow p + e^- + \bar{\nu}_e$), makes the scattering of neutrons an ideal tool to study bulk structural and magnetic phenomena.

As a consequence of the relatively large neutron mass, the de Broglie wavelength of thermal neutrons is of the order of interatomic distances (~ 1 $\mathring{A}$) in both solids and liquids. Thus, interference effects occur in a neutron diffraction experiment which yield information on nuclear and magnetic structures of the scattering system. Moreover, the energy of thermal neutrons is of the order of many interesting excitations in condensed matter (e.g. phonons, magnetic excitations, crystalline field excitations), a property which allows for the characterization of these excitations by means of inelastic neutron scattering.

One generally distinguishes between cold ($0.1 - 10\, meV$), thermal ($10 - 100\, meV$),

hot ($100 - 500\,meV$), and epithermal ($> 500\,meV$) neutrons [110]. For the various neutron scattering experiments in this thesis, neutrons with initial energies in the range $E_i = 4 - 115\,meV$ were utilized. In the scattering process, the neutron changes from a state characterized by an initial momentum $\vec{k}_i$ to a state with final momentum $\vec{k}_f$. The wavevector change and the concomitant change in neutron energy are respectively given by

$$\vec{Q} = \vec{k}_i - \vec{k}_f, \tag{2.1}$$

$$\omega = E_i - E_f = \frac{1}{2m}(\vec{k}_i^2 - \vec{k}_f^2). \tag{2.2}$$

(Note, that throughout this thesis units in which $\hbar = k_B = 1$ will be used.) From Eqs. (2.1) and (2.2) it is clear that energy and momentum transfers can in general not be varied independently. However, as we will see later on, this kinematic constraint for inelastic scattering processes can be be fully overcome in systems that are one- and two-dimensionally correlated.

In a neutron scattering experiment, one normally measures the *partial differential cross − section* $d^2\sigma/d\Omega dE_f$, defined as the number of neutrons scattered per second into a solid angle $d\Omega$ with final energy between E_f and $E_f + dE_f$, normalized by the incident neutron flux. Without the energy discrimination, one measures the *differential cross − section*

$$\frac{d\sigma}{d\Omega} = \int \left(\frac{d^2\sigma}{d\Omega dE_f}\right) dE_f. \tag{2.3}$$

The integration of the differential cross-section over all solid angles yields the *total scattering cross − section*,

$$\sigma_s = \int \left(\frac{d\sigma}{d\Omega}\right) d\Omega, \tag{2.4}$$

the total number of neutrons scattered per second, normalized by the incident flux.

The most general expression of the partial differential scattering cross-section for a specific transition of a scattering system from a quantum state λ_i, with energy E_{λ_i},

to a state λ_f, with energy E_{λ_f}, is given by

$$\frac{d^2\sigma}{d\Omega dE_f} = \frac{k_i}{k_f}\left(\frac{m_n}{2\pi}\right)^2 |\langle \vec{k}_f \sigma_n^f \lambda_f | V | \vec{k}_i \sigma_n^i \lambda_i \rangle|^2 \, \delta(E_{\lambda_i} - E_{\lambda_f} + \omega). \tag{2.5}$$

Here, $m_n = 1.675 \times 10^{-24} g$ is the neutron mass and V is the interaction potential (either nuclear or magnetic) between the neutron and the scattering system. Note, that the consideration of the initial and final neutron spin states, σ_n^i and σ_n^f, is only necessary for magnetic scattering.

2.2 Nuclear Scattering

Since the range of nuclear forces ($\sim 1 fm$) is much smaller than the de Broglie wavelength of thermal neutrons (~ 1 $\mathring{A}$), the scattering, when analyzed in terms of partial waves, is entirely due to s-waves ($l = 0$) and therefore isotropic. The strength of a scattering process involving a *single* nucleus can then be characterized by a complex parameter b, called the *scattering length*. The imaginary part of b represents neutron absorption, mostly radiative capture for thermal neutrons, and is small for most nuclei. The total cross-section is given by the sum of the cross-sections for scattering and for absorption:

$$\sigma = \sigma_s + \sigma_a = 4\pi |b|^2 + \frac{4\pi}{k_i} Im(b). \tag{2.6}$$

A table of the nuclear cross-sections of various nuclei pertinant to this thesis is given in Appendix A. For the majority of nuclei $Im(b)$ is small, so that

$$\sigma \simeq \sigma_s = 4\pi |b|^2. \tag{2.7}$$

In the discussion below we will take b to be real.

The scattering lengths generally differ for different isotopes, and they furthermore depend on the relative orientation of neutron spin and nuclear spin (unless the nuclear spin is zero). As a result, one is led to distinguish between coherent and incoherent parts of the cross-section. In its most general form, the nuclear partial differential

cross-section of a *monatomic* condensed matter system can be written as

$$\frac{d^2\sigma}{d\Omega dE_f} = \frac{1}{4\pi}\frac{k_f}{k_i}N(\sigma_c\, S(\vec{Q},\omega) + \sigma_{inc}\, S_{inc}(\vec{Q},\omega)), \tag{2.8}$$

where

$$\sigma_c = 4\pi(\bar{b})^2, \tag{2.9}$$

and

$$\sigma_{inc} = 4\pi(\bar{b^2} - (\bar{b})^2), \tag{2.10}$$

are the coherent and incoherent parts of the total scattering cross-section of the nucleus, respectively.

The *dynamic structure factor* (also called *scattering function* or *dynamic correlation function*)

$$S(\vec{Q},\omega) = \frac{1}{2\pi N}\sum_{j\,j'}\int_{-\infty}^{\infty}\langle e^{i\vec{Q}\vec{R}_j(0)}e^{i\vec{Q}\vec{R}_{j'}(t)}\rangle e^{-i\omega t}dt \tag{2.11}$$

is the space-time Fourier transform of the *time-dependent pair-correlation function*

$$G(\vec{r},t) = \frac{1}{N}\sum_{j\,j'}\int\langle\delta(\vec{r}' - \vec{R}_{j'}(0))\delta(\vec{r}' + \vec{r} - \vec{R}_j(t))\rangle d\vec{r}' \tag{2.12}$$

The Heisenberg operator $\vec{R}_j(t)$ denotes the position of the j^{th} atom and the angular brackets denote the thermal average at a temperature T. The *incoherent scattering function*, $S_{inc}(\vec{Q},\omega)$, is the Fourier transform of the *self time-dependent pair-correlation function*

$$G_{inc}(\vec{r},t) = \frac{1}{N}\sum_{j}\int\langle\delta(\vec{r}' - \vec{R}_j(0))\delta(\vec{r}' + \vec{r} - \vec{R}_j(t))\rangle d\vec{r}'. \tag{2.13}$$

The formulation of the cross-section in terms of correlation functions is originally due to Van Hove [111, 112], and can also be applied to the case of magnetic neutron scattering as well as to the scattering of x-rays. Both the coherent and the incoherent cross-sections are factorized into a part that depends on the interaction between the neutrons and the scattering system, σ_c and σ_{inc}, and a part that is solely a property of

the scattering system, $S(\vec{Q},\omega)$ and $S_{inc}(\vec{Q},\omega)$. The relevance of this formalism is two-fold. First, it gives a clear picture of the physical significance of the terms that occur in the cross-section. It is only the coherent part of the cross-section Eq. (2.8) that gives interference effects. Since the scattering system has different scattering lengths for different nuclei, the coherent scattering can be viewed as the scattering that the same system would exhibit if all the scattering lengths were fixed at their mean value $\bar{b}$. The incoherent part of the cross section, which depends on the correlations between positions of the same nucleus at different times, arises from the random distribution of deviations of the various scattering lengths from $\bar{b}$.

The second point is a rather fundamental one. In experimental physics, one is generally interested in the investigation of the spectrum of spontaneous fluctuations of a system. Since neutrons interact only weakly with matter, the sample response is appropriately described by first-order perturbation theory. The response and the spontaneous fluctuation spectrum are therefore the same, that is, in a neutron scattering experiment one measures the truly undistorted properties of the scattering system. This property, which will be discussed in more detail later on, allows for a straightforward comparison of experimental results with theoretical predictions for a particular scattering system.

The scattering of x-rays can also be treated in first order perturbation theory. However, this technique can only yield information about the *static pair-correlation function* $G(\vec{r},0)$, since photons propagate too fast for temporal interference effects to occur. Thermal Neutrons, on the other hand, have a rather small velocity of order $v \sim 10^3\, m/s$. The time for a neutron to traverse the typical distance $a \sim 1\ \mathring{A}$ between two neighboring particles in the scattering system is $\sim a/v \sim 10^{-13}\, s$, which is of the order of the characteristic relaxation time for most condensed matter systems. The scattering of thermal neutrons can therefore provide information about both the *spatial and temporal* parts of the correlation function $G(\vec{r},t)$. This property, and the fact that neutron scattering is a structural and magnetic bulk probe, makes this technique a very powerful tool to study condensed matter phenomena.

A limitation of this experimental technique is the relatively low flux provided by

even the best neutron sources ($\sim 10^6 - 10^7$ neutrons/cm^2/s at the sample position). This disadvantage has in part been overcome by the optimization of the spectrometer instrumentation. However, large single crystals are still needed for inelastic measurements. Most of the neutron scattering experiments presented in this thesis became feasable only because of the successful gowth of lage single crystals.

2.2.1 Dynamic structure factor and susceptibility

The dynamic structure factor $S(\vec{Q},\omega)$, which is the quantity obtained in neutron scattering experiments, is the spectrum of spontaneous *microscopic* fluctuations. In this Section, we will discuss the intimate relationship between $S(\vec{Q},\omega)$ and the quantity $Im\chi(\vec{Q},\omega)$ which describes the dissipation in response to small *macroscopic* disturbances. The relationships given in this Section apply to both nuclear and magnetic scattering.

The linear response to an external field $\vec{H}(\vec{r},t)$ of a property of a system described by an operator $\vec{O}(\vec{r},t)$ is characterized by a *response function*, the susceptibility $\chi^{\alpha\beta}(\vec{r},t)$, defined by

$$\langle O^{\beta}(\vec{r},t)\rangle = \langle O^{\beta}(\vec{r},t)\rangle_{H=0} + \int_{-\infty}^{t}\int H^{\alpha}(\vec{r}',t')\chi^{\alpha\beta}(\vec{r}-\vec{r}',t-t')d\vec{r}'dt'. \qquad (2.14)$$

In our case, the external field is provided by the neutrons.

To facilitate comparison with scattering experiments, it is convenient to work with the corresponding momentum- and energy-dependent susceptibility $\chi^{\alpha\beta}(\vec{Q},\omega)$. The susceptibility is a complex function and is the quantity predicted by theoretical models for a system. Its real part gives the in-phase response of the system, while its imaginary part gives the out-of-phase response which governs energy dissipation. Both are connected via the *Kramers-Kronig* relation

$$Re\chi^{\alpha\beta}(\vec{Q},\omega) = \frac{1}{\pi}\int \frac{Im\chi^{\alpha\beta}(\vec{Q},\omega')}{(\omega'-\omega)}d\omega' \qquad (2.15)$$

The *fluctuation dissipation* theorem relates the dissipative part of $\chi^{\alpha\beta}(\vec{Q},\omega)$ di-

rectly to the dynamic structure factor $S^{\alpha\beta}(\vec{Q},\omega)$:

$$S^{\alpha\beta}(\vec{Q},\omega) = \frac{1}{\pi}(n(\omega)+1)Im\chi^{\alpha\beta}(\vec{Q},\omega), \tag{2.16}$$

where

$$n(\omega) = \frac{1}{e^{\omega/T}-1} \tag{2.17}$$

is the Bose factor. The dynamic correlation function $S^{\alpha\beta}(\vec{Q},\omega)$, which is the quantity that is obtained directly in a neutron scattering experiment, therefore solely depends on the dynamics of the scatterer.

An important property of the dynamic correlation function, which is independent of the dynamics and structure of the scattering system, warrants special attention: $S^{\alpha\beta}(\vec{Q},\omega)$ satisfies the *detailed balance* condition,

$$S^{\alpha\beta}(\vec{Q},\omega) = exp(\omega/T)S^{\alpha\beta}(-\vec{Q},-\omega), \tag{2.18}$$

which relates the energy loss and energy gain cross-sections. This is a very useful property as it allows to discern intrinsic inelastic scattering, which has to satisfy the detailed balance condition, from spurious scattering processes.

The *static susceptibility* $\chi^{\alpha\beta}(\vec{Q})$ is simply given by

$$\chi^{\alpha\beta}(\vec{Q}) = \chi^{\alpha\beta}(\vec{Q},\omega=0). \tag{2.19}$$

It can be seen from Eq. (2.15), that as a consequence of the divergence of the static susceptibility at a continuous phase transition with incipient wavevector $\vec{\tau}$, the spectral weight of $Im\chi(\vec{\tau},\omega)$ shifts to smaller ω. This effect, which was first discussed by Van Hove [111], is called the *critical slowing down.*

Since $\chi^{\alpha\beta}(\vec{Q})$ attains its maximum value for $\vec{Q}=\vec{\tau}$, one can expand $(\chi^{\alpha\beta}(\vec{Q}))^{-1}$ about its minimum. Defining a deviation wavevector $\vec{q} \equiv \vec{Q}-\vec{\tau}$, one has for an isotropic system (e.g. the Heisenberg model):

$$\chi^{-1}(\vec{Q}) \equiv \chi^{-1}(q) = \chi^{-1}(0)\left[1+(\xi_0 q)^2+(\xi_1 q)^4+...\right]. \tag{2.20}$$

The expansion coefficients ξ_i ($i = 0, 1, etc.$) are proportional to the *correlation length* ξ: $\xi_0 = \xi, \xi_1 = c_1\xi, etc.$. Since $1 >> c_1 >> etc.$, it is generally only the correlation length that is obtained experimentally. (However, in the Monte Carlo simulation of the $S = 1/2$ 2DSLQHA discussed in Chapter 5, both ξ and ξ_1 were observed.) Since $\chi(\vec{Q})$ diverges only for $\vec{Q} = \vec{\tau}$ as the critical temperature is approached, ξ diverges as well.

For $T >> \omega$, the *static structure factor*,

$$S^{\alpha\beta}(\vec{Q}) = \int_{-\infty}^{\infty} S^{\alpha\beta}(\vec{Q}, \omega) d\omega, \tag{2.21}$$

is closely related to the static susceptibility $\chi^{\alpha\beta}(\vec{Q})$:

$$T\chi^{\alpha\beta}(\vec{Q}) = \int_{-\infty}^{\infty} \frac{1 - e^{-\omega/T}}{\omega/T} S(\vec{Q}, \omega) \tag{2.22}$$

$$\simeq S^{\alpha\beta}(\vec{Q}) \ (\omega << T). \tag{2.23}$$

This relationship, follows from Eqs. (2.15) and (2.16), is rather important, and the magnetic neutron scattering experiments described in Chapters 4 and 6 rely on it. Note, that while all x-ray scattering experiments measure energy-integrated scattering (and thus yield information only about the static pair correlation function $G(\vec{r}, 0)$), a special scattering geometry has to be used in a neutron scattering experiment. This will be discussed in more detail in Chapter 2.4.2.

The nuclear cross-sections for a single crystal with d atoms per unit cell will now be discussed. It will first be assumed that the interatomic forces are *harmonic*. Eventually, we will see that it is necessary to include the effects of *anharmonic* forces in order to fully describe a real system. When the position coordinates $\vec{R}(t)$ are expanded in powers of atomic displacements, the nuclear cross-section can be written as the sum of elastic, one-phonon, and multiphonon parts. Both coherent and incoherent multiphonon scattering are nearly $\vec{Q}$-independent and therefore simply add to the background scattering. Incoherent elastic scattering is also nearly anisotropic. However, very meaningful information can be extracted form elastic and one-phonon

coherent scattering, and in some special cases also from one-phonon incoherent scattering.

2.2.2 Nuclear Bragg scattering

Coherent elastic scattering, or *Bragg scattering*, is determined by the *average* atomic positions in a crystal. In the correlation function language introduced earlier, it is the $t \rightarrow \infty$ contribution of $G(\vec{r}, t)$ to the cross-section, and can be written as

$$\left(\frac{d^2\sigma}{d\Omega dE_f}\right)_{Bragg} = N\frac{(2\pi)^3}{v_0}|F(\vec{Q})|^2 \sum_{\vec{\tau}} \delta(\vec{Q} - \vec{\tau})\ \delta(\omega), \tag{2.24}$$

where N is the number of unit cells of volume v_0, $\vec{\tau}$ is a vector of the reciprocal lattice, and

$$F(\vec{Q}) = \sum_d \bar{b}_d e^{i\vec{Q}\vec{d}} e^{-W_d} \tag{2.25}$$

is the *elastic structure factor*. The sum is over the d atoms in a unit cell. The *Debye-Waller factor* e^{-W_d} ($e^{-W_d} < 1$) is a measure of the atoms' fluctuations about its equilibrium position. For an idealized rigid lattice, i.e. in the absence of thermal and quantum fluctuations, this factor would be unity. At low temperatures, W_d is indeed very small. Since $W_d = W_d(\vec{Q}) \sim |\vec{Q}|^2$, the intensity of Bragg peaks decreases not only with increasing temperature, but also with increasing Q. Most experiments, however, are carried out at temperatures low enough so that the Debye–Waller factor can be neglected.

The structure of a crystal is determined by the systems' Bragg reflections, which according to Eq. (2.24) occur for the discrete momentum transfers $\vec{Q} = \vec{\tau}$. Any 3D crystal structure belongs to one of 230 space groups. It was discussed in Chapter 1 that $La_{2-x}Sr_xCuO_4$ undergoes a continuous structural phase transition with decreasing temperature from a tetragonal phase (space group Immm; also called HTT phase) to an orthorhombic phase (space group Bmab; also called LTO1 phase) of lower symmetry. For a continuous structural phase transition, the atomic displacements associated with the distortion in the low-symmetry phase can be described by

normal mode coordinates [113]. The simplest case of such a transition involves only one normal mode. This is the case for $La_{2-x}Sr_xCuO_4$, where the atomic displacements primarily correspond to the long-range staggered tilting, with tilt amplitude N_0, of the CuO_6 octahedra about the $\hat{a}$-axis. In the HTT phase, the $\hat{a}$- and $\hat{b}$-directions are equivalent, so that at the structural phase transition two equivalent types of domains form. This effect is called *twinning*. The transition is described by a two-component order parameter and lies in the 3D XY with cubic anisotropy universality class. The order parameter may be represented by the tilt amplitude N_0 and the phase θ, which corresponds to the degree of rotation of the octahedra tilt direction away from the $\hat{a}$-axis. For the transition in $La_{2-x}Sr_xCuO_4$ one has $\theta = 0$. Since neutron scattering is a bulk probe, both sets of twin domains are measured simultaneously. The superposed (H,0,L) and (0,K,L) reciprocal lattice zones of the orthorhombic phase of $La_{2-x}Sr_xCuO_4$ are shown in Fig. 2-1.

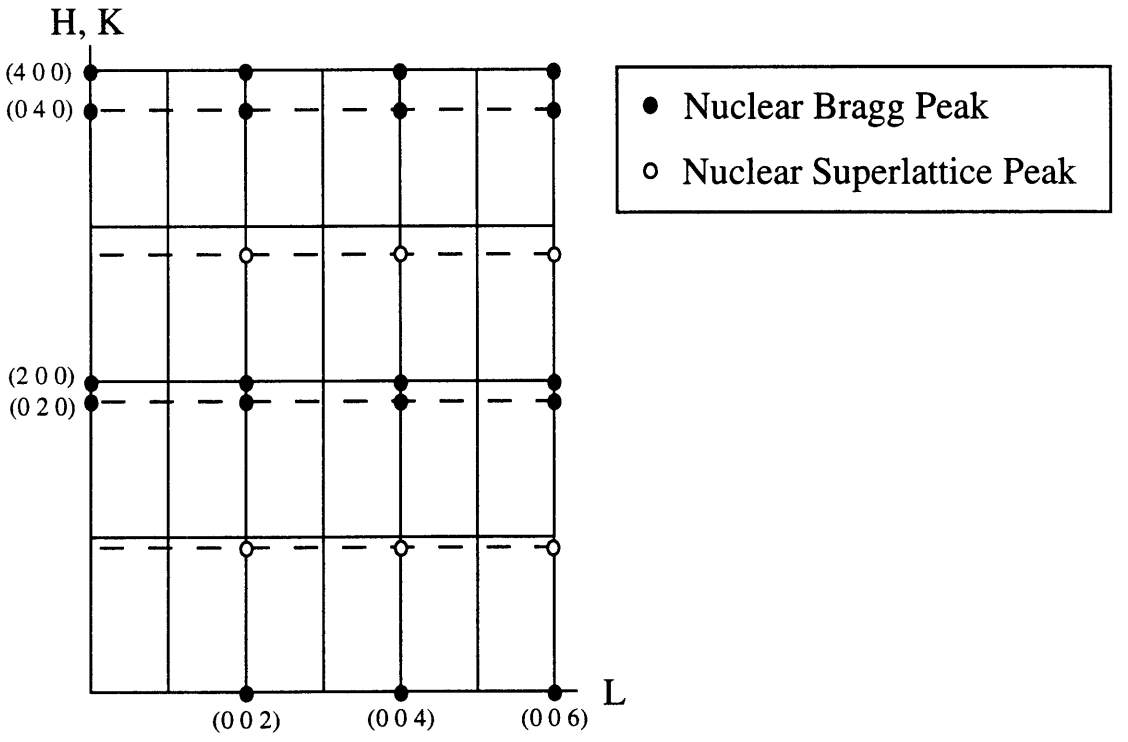

Figure 2-1: Nuclear reciprocal lattice of orthorhombic $La_{2-x}Sr_xCuO_4$.

The temperature dependence of the order parameter can be measured in a rather

straightforward fashion. As a result of the lower symmetry structure, new Bragg reflections become allowed in the LTO1 phase. These *superlattice peaks* are indicated by open circles in Fig. 2-1. It can be shown that the elastic structure factor for these reflections is simply proportional to the square of the tilt amplitude. The order parameter exponent β can thus be obtained directly from the temperature dependence of the superlattice peak intensity I_{SL}:

$$I_{SL} \sim |F(\vec{\tau}_{SL})|^2 \sim N_0^2 \sim (T_{ST} - T)^{2\beta}. \tag{2.26}$$

In Fig. 2-2 the temperature dependence of the (0 1 2) superlattice peak is shown for both La_2CuO_4 and $La_{1.85}Sr_{0.15}CuO_4$, and the solid lines correspond to $\beta = 0.25(3)$ and $\beta = 0.35(3)$, respectively. The data for La_2CuO_4 are not accurate enough to yield a meaningful exponent. However, the order parameter measurement for the sample with $x = 0.15$ is rather accurate, and the value of $\beta = 0.35$ is that expected for the 3D XY model. Note, that for systems with a multi-component order parameter, the sizes of the different components can be determined from the relative intensities of the new superlattice Bragg reflections $\vec{\tau}_{SL}$.

2.2.3 Coherent one-phonon scattering

Inelastic scattering ($|\omega| > 0$) arises because of systematic correlations between atomic positions at different times. The coherent one-phonon scattering cross-section can be written as

$$\left(\frac{d^2\sigma}{d\Omega dE_f}\right)_{c\ 1ph} = \frac{k_f}{k_i} \sum_{\alpha} |F_\alpha(\vec{Q})|^2 S^{\alpha\alpha}(\vec{Q},\omega), \tag{2.27}$$

where

$$S^{\alpha\alpha}(\vec{Q},\omega) = \frac{1}{2\pi} \int_{-\infty}^{\infty} \langle N^\alpha(-\vec{Q},0) N^\alpha(\vec{Q},t)\rangle e^{i\omega t} dt. \tag{2.28}$$

The normal mode coordinate of the α^{th} phonon branch ($\alpha = x, y, z$) is denoted as N^α, and the *inelastic structure factor*, $F_\alpha(\vec{Q})$, is given by

$$F_\alpha(\vec{Q}) = \sum_d \frac{\bar{b}}{\sqrt{m_d}} (\vec{Q}\hat{e}_{d\alpha})\, e^{i\vec{Q}\vec{r}_d}\, e^{-W_d}, \tag{2.29}$$

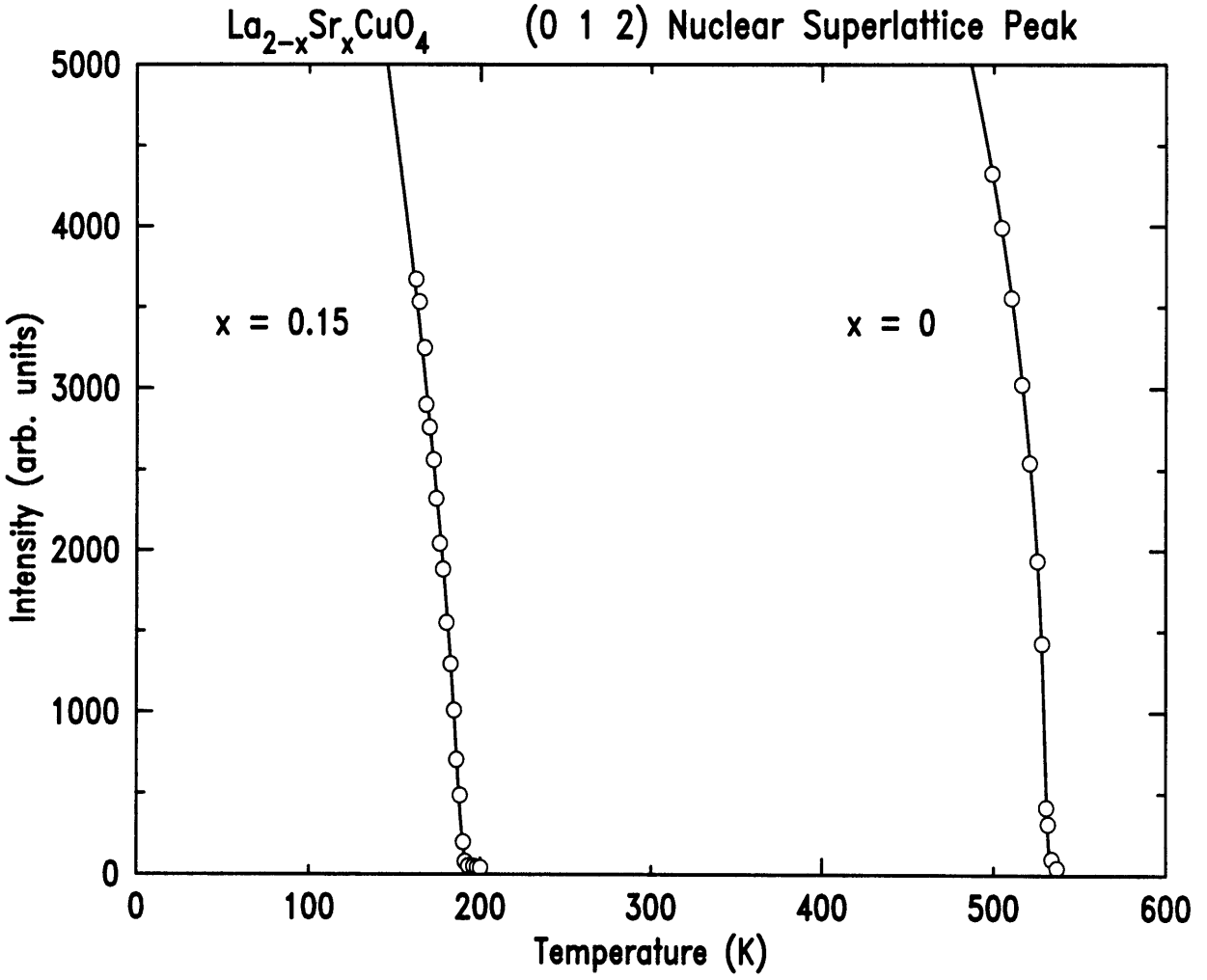

Figure 2-2: Temperature dependence of the (0 1 2) nuclear superlattice peak in $La_{2-x}Sr_xCuO_4$ for $x = 0$ and $x = 0.15$.

where m_d is the mass of the d^{th} atom and $\hat{e}_{d\alpha}$ is the polarization vector of the d^{th} atom for the α^{th} phonon branch. The $\vec{Q}$-dependence of $F_\alpha(\vec{Q})$ implies that the scattering intensity is approximately proportional to Q^2.

For harmonic one-phonon processes, the imaginary part of the dynamic susceptibility is given by

$$Im\chi^{\alpha\alpha}(\vec{Q},\omega) = \frac{\pi}{2\,\omega_{ph}^{\alpha}(\vec{Q})}\left[\delta(\omega-\omega_{ph}^{\alpha}(\vec{Q})) - \delta(\omega+\omega_{ph}^{\alpha}(\vec{Q}))\right], \tag{2.30}$$

and according to Eq. (2.15),

$$Re\chi^{\alpha\beta}(\vec{Q},\omega) = \left[\omega_{ph}^{\alpha}(\vec{Q})^2 - \omega^2\right]^{-1}. \tag{2.31}$$

In many cases, a continuous structural phase transition can be viewed as an instability of the crystal against a particular normal mode. The normal mode frequency goes to zero at the transition, and the mode freezes in below T_{ST}, which results in the long-range distortion of the lower symmetry phase. This is known as the *soft mode* concept [114, 115], and it has been applied successfully to the transition in $La_{2-x}Sr_xCuO_4$ [116, 117]. As the temperature is lowered toward the structural transition, the static normal mode susceptibility $\chi_0(\vec{\tau}_{SL})$ of a system diverges as $(T-T_{ST})^{-\gamma}$, so that

$$\chi_0^{-1}(\vec{\tau}_{SL}) \sim (T-T_{ST})^{\gamma} \sim \omega_{ph}^2(\vec{\tau}_{ST}) \longrightarrow 0. \tag{2.32}$$

While classical theory predicts $\gamma = 1$ for the susceptibility exponent, the experimentally observed values are often larger [113].

The result of Eq. (2.32) appears to contradict the underlying assumption of harmonic interatomic forces. In such a theory the normal mode frequencies $\omega_{ph}^2(\vec{\tau}_{ST})$ do not interact, and are therefore independent of temperature. Real systems have anharmonic force components, as is evidenced by their thermal expansion. Soft mode frequencies are thus to be viewed as effective (or renormalized) frequencies. To account for anharmonicity effects, one can introduce a phenomenological damping constant Γ

in the expression of the classical dynamic susceptibility:

$$\chi^{\alpha\alpha}(\vec{Q},\omega)^{-1} = \omega_{ph}^{\alpha}(\vec{Q})^2 - \omega^2 - i\omega\Gamma. \tag{2.33}$$

For comparison with neutron scattering experiments, one needs the dynamic structure factor, which according to Eq. (2.16) is then given by

$$S^{\alpha\alpha}(\vec{Q},\omega) = \frac{1}{\pi}\frac{\omega}{1-e^{-\omega/T}}\frac{\Gamma}{(\omega_{ph}^{\alpha}(\vec{Q})^2-\omega^2)^2+(\omega\Gamma)^2}\,. \tag{2.34}$$

The delta functions in the harmonic one-phonon cross-section are thus replaced by a Lorentzian of non-zero width Γ.

2.2.4 Incoherent nuclear scattering

For the sake of completenes the incoherent elastic and one-phonon cross-sections will be briefly discussed. In the experiments described in this thesis, incoherent nuclear scattering was simply part of the measured background scattering. Incoherent elastic scattering is given by

$$\left(\frac{d^2\sigma}{d\Omega dE_f}\right)_{inc\ el} = N\sum_d \frac{\sigma_{inc,d}}{4\pi}\, e^{-W_d}\,\delta(\omega). \tag{2.35}$$

It depends on the scattering direction only through $W = W(\vec{Q})$, and therefore becomes isotropic at low temperatures.

The incoherent one-phonon cross-section is again largely $\vec{Q}$-independent, but it is proportional to the phonon density of states. For materials with predominantly nuclear incoherent scattering (e.g., Vanadium: $\sigma_{inc} = 500\,barns >> \sigma_c = 2\,barns$), the phonon density of states can thus be measured.

2.3 Magnetic Scattering

Magnetic neutron scattering occurs due to the coupling of the magnetic dipole moment of the neutron with the magnetic field from the orbital motion and the spin of

unpaired electrons in an ion. For magnetic ions belonging to the iron group of the periodic table (e.g., Cu^{2+}, Ni^{2+}, e.t.c.), the orbital angular momentum in a crystal is quenched by crystalline electric fields. For the purpose of this thesis, it is then sufficient to only consider magnetic scattering due to the spin of a single type of magnetic ion. This is described by Eq. (2.5) with a magnetic interaction potential

$$V_{spin} \sim \vec{\mu}_n \vec{\mu}_e \sim (\gamma \frac{e}{2m_p})(g \frac{e}{2m_e}). \tag{2.36}$$

The magnetic cross-section to unpolarized neutrons of a system of N nearly localized spins is given by [112, 118, 119]

$$\frac{d^2\sigma}{d\Omega dE_f} = A(\vec{k}_i, \vec{k}_f) \sum_{\alpha\beta} (\delta_{\alpha\beta} - \hat{Q}_\alpha \hat{Q}_\beta) S^{\alpha\beta}(\vec{Q}, \omega), \tag{2.37}$$

where the factor

$$A(\vec{k}_i, \vec{k}_f) = (\gamma r_0)^2 \frac{k_i}{k_f} N \left[\frac{g}{2} f(\vec{Q})\, e^{-W(\vec{Q})}\right]^2 \tag{2.38}$$

determines the order of magnitude of the magnetic cross-section. The magnetic form factor, $f(\vec{Q})$, is the Fourier transform of the normalized density of unpaired electrons in a single magnetic ion, and $r_0 = e^2/(m_e c^2)$ is the classical radius of the electron. As in the case of nuclear scattering, the dynamic structure factor is the essential part of the cross-section. For magnetic scattering, $S^{\alpha\beta}(\vec{Q}, \omega)$ is given by

$$S^{\alpha\beta}(\vec{Q}, \omega) = \frac{1}{2\pi} \sum_{\vec{l}} \int_{-\infty}^{\infty} \langle S^\alpha(0,0) S^\beta(\vec{r}, t) \rangle e^{i(\vec{l}\vec{r} - \omega t)} dt, \tag{2.39}$$

the *Fourier transform of the unequal-time spin-pair correlation function.* The indices α and β indicate the three cartesian components of $\vec{Q}$, and the sum is over the lattice positions $\vec{l}$ of the magnetic ions. The geometric factor that multiplies $S^{\alpha\beta}(\vec{Q}, \omega)$ results from the summation over initial neutron polarization states for an unpolarized neutron beam. Its $\vec{Q}$-dependence can be employed to determine the spin directions of a scattering system.

2.3.1 Magnetic Bragg scattering

In analogy to nuclear Bragg scattering, the scattering from a system with long-range magnetic order is the coherent elastic part of Eq. (2.39), given by the $t \rightarrow \infty$ limit of $\langle S^{\alpha}(0,0)S^{\beta}(\vec{l},t)\rangle$. It can be written as

$$\left(\frac{d^2\sigma}{d\Omega dE_f}\right)_{Bragg} = A(\vec{k}_i,\vec{k}_f)\sum_{\alpha\beta}(\delta_{\alpha\beta}-\hat{Q}_{\alpha}\hat{Q}_{\beta})\sum_{\vec{l}}\langle S^{\alpha}(0,0)\rangle\langle S^{\beta}(0,\vec{l})\rangle\, e^{i\vec{Q}\vec{l}}\,\delta(\omega). \quad (2.40)$$

For elastic magnetic scattering from a system with collinear magnetic moments in the direction $\hat{e}_m$ (ferro- or antiferromagnets), the above expression can be simplified and combined with the nuclear Bragg cross-section:

$$\left(\frac{d^2\sigma}{d\Omega dE_f}\right)_{Bragg} = N\frac{(2\pi)^3}{v_0}\left(|F_m(\vec{Q})|^2+|F_n(\vec{Q})|^2\right)\sum_{\vec{\tau}}\delta(\vec{Q}-\vec{\tau})\,\delta(\omega), \quad (2.41)$$

where $F_n(\vec{Q})$ is the elastic structure factor for nuclear scattering, Eq. (2.24), and

$$F_m(\vec{Q}) = \sum_{\vec{d}_m} p(\vec{Q})e^{i\vec{Q}\vec{d}_m} \quad (2.42)$$

its magnetic counterpart. The magnetic scattering length, $p(\vec{Q}_m)$, is defined as

$$p(\vec{Q}_m) = (\gamma r_0)f(\vec{Q})\,|\sin(\Phi)|\,(\hat{e}_m\vec{S}_m)\,e^{-W}, \quad (2.43)$$

where Φ is the angle subtended by $\vec{Q}$ and $\hat{e}_m$. Note, that the magnetic cross-section depends on the square of the spin of the ion under investigation. Note also, that the sign of $p(\vec{Q}_m)$ depends on the relative orientation of a particular spin $\vec{S}_m$ with respect to $\hat{e}_m$. As a consequence, the magnetic and nuclear unit cells of an antiferromagnet are not identical. It is due to this fortunate fact, that many interesting magnetic phenomena in antiferromagnets can be investigated in a straightforward fashion. The study of magnetism in ferromagnets, for which magnetic and nuclear scattering are fully commensurate, is often only possible with polarized neutrons. The full reciprocal lattice, nuclear and magnetic, of La_2CuO_4 is shown in Fig. 2-3(a). It has already

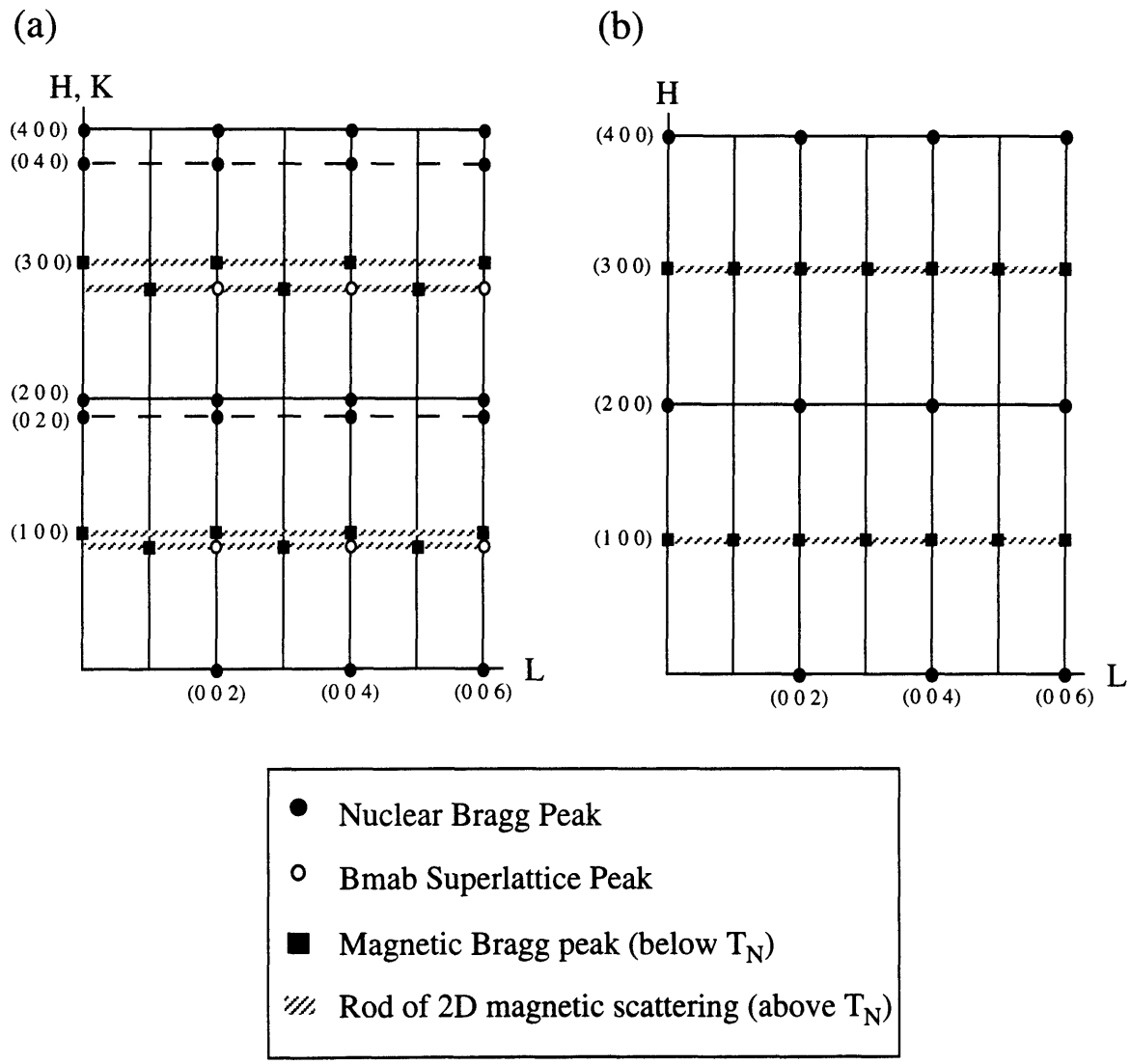

Figure 2-3: Nuclear and magnetic reciprocal lattice of (a) orthorhombic La_2CuO_4 and (b) tetragonal $Sr_2CuO_2Cl_2$.

been discussed earlier, that two equally populated twin domains are formed at the structural transition. As a result, (H 0 L) and (0 K L) reflections are superposed, and since $b > a$ in the orthorhombic phase, the respective Bragg peaks can be distinguished. The observed Bragg intensity pattern of La_2CuO_4 corresponds to the spin structure shown in Fig. 1-2. In particular, the absence of a magnetic peak at the (0 1 0) position implies that the spins lie along the [0 1 0] direction ($\Phi = 0$).

As a second example, the reciprocal lattice of $Sr_2CuO_2Cl_2$ is shown in Fig. 2-3(b). Since the structure of this material is tetragonal, there exists only one type of nuclear domain. The observed magnetic Bragg scattering pattern implies that the spin direction is in the CuO_2 sheets. However, since $Sr_2CuO_2Cl_2$ is tetragonal it is not possible to determine the spin direction within the sheets, as all in-plane spin orientations would yield the same pattern.

In analogy to nuclear Bragg scattering, the measured magnetic Bragg intensity is proportional to the square of the order parameter, the staggered magnetization M_s in this case:

$$I_m \sim |F_m(\vec{Q})|^2 \sim M_s^2 \sim (T_N - T)^{2\beta}. \tag{2.44}$$

In Fig. (2-4), the temperature dependence of the (1 0 0) magnetic Bragg peak of $Sr_2CuO_2Cl_2$ is shown. The solid and dashed lines correspond to $\beta = 0.22$ and $\beta = 0.25$, respectively. The implications of these values will be discussed in Chapter 4.

2.3.2 Coherent inelastic magnetic scattering

Coherent inelastic magnetic scattering is given by [119]

$$\left(\frac{d^2\sigma}{d\Omega dE_f}\right)_{c\,inel} = A(\vec{k}_i, \vec{k}_f) \sum_{\alpha\beta} (\delta_{\alpha\beta} - \hat{Q}_\alpha \hat{Q}_\beta)[S^{\alpha\beta}(\vec{Q},\omega) - S^{\alpha\beta}_{Bragg}(\vec{Q},\omega)]. \tag{2.45}$$

If the total z-component of spin is a constant of motion (as for a Heisenberg system), the off-diagonal terms of $S^{\alpha\beta}(\vec{Q},\omega)$ vanish, and the fluctuation-dissipation theorem

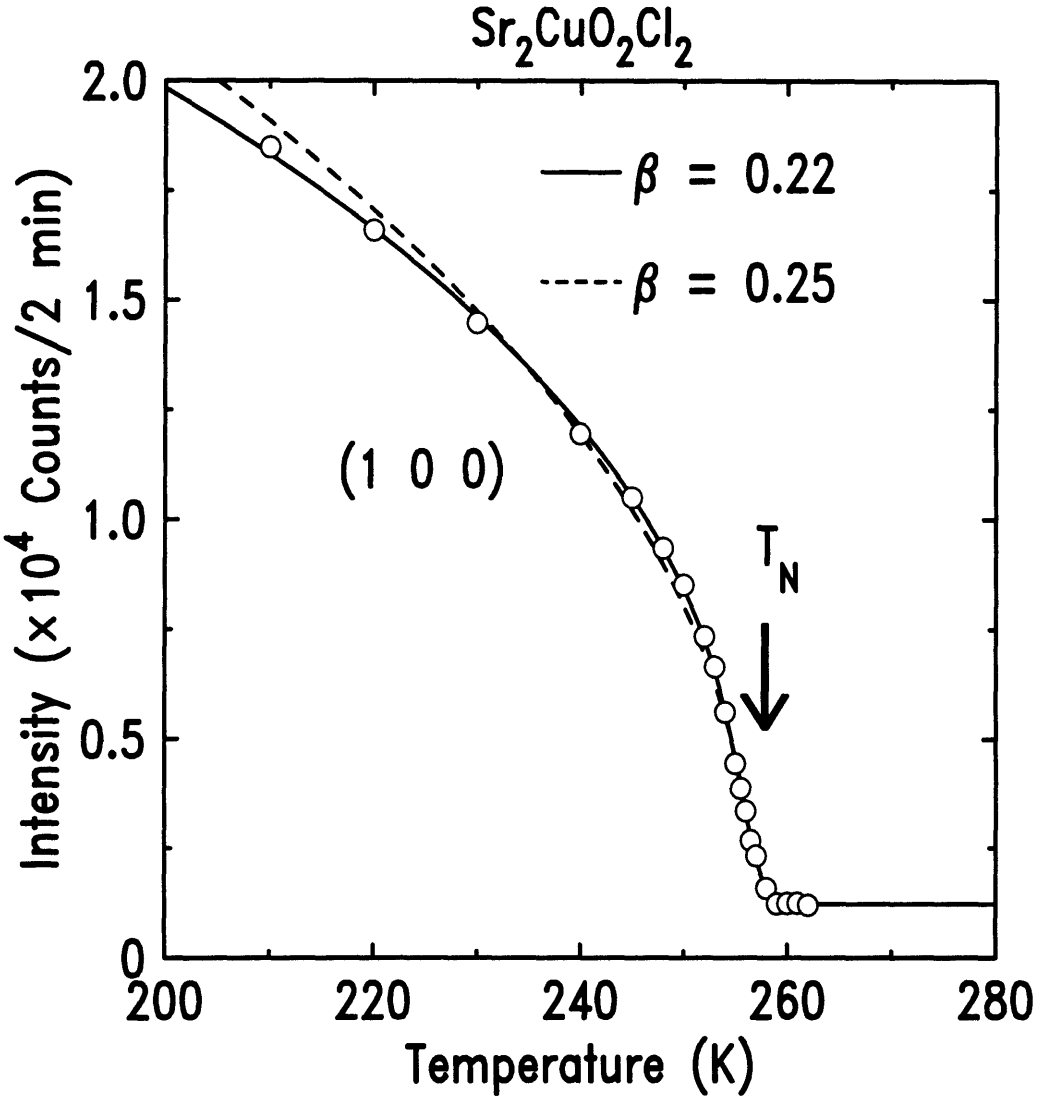

Figure 2-4: Temperature dependence of the (1 0 0) magnetic Bragg peak in $Sr_2CuO_2Cl_2$. The Néel temperature is $T_N = 256.5(1.5)K$.

takes on the simple form [118]

$$S^{\alpha\alpha}(\vec{Q},\omega) - S^{\alpha\alpha}_{Bragg}(\vec{Q},\omega) = \frac{1}{\pi g^2 \mu_B^2}(n(\omega)+1) Im\chi^{\alpha\alpha}(\vec{Q},\omega), \tag{2.46}$$

Note, that $S^{\alpha\alpha}_{Bragg}(\vec{Q},\omega)$ vanishes above T_N. The cross-section Eq. (2.44) can be cast into the useful form

$$(\frac{d^2\sigma}{d\Omega dE_f})_{cel} = A(\vec{k}_i,\vec{k}_f)\left[\frac{1}{2}(1+\cos^2(\phi))S^{||}(\vec{Q},\omega) + \sin^2(\phi)S^{\perp}(\vec{Q},\omega)\right], \tag{2.47}$$

where ϕ is the angle subtended by $\vec{Q}$ and the [0 0 1] direction.

For harmonic one-magnon excitations in the antiferromagnetically ordered (Néel) phase of a system, the in-plane component $S^{||}(\vec{Q},\omega)$ is given by

$$S^{||}(\vec{Q},\omega) = \delta(\vec{Q}-\vec{q}-\vec{\tau}_m)\left[\delta(\omega-\omega_{||})\frac{1+n(\omega_{||})}{\omega_{||}} + \delta(\omega+\omega_{||})\frac{n(\omega_{||})}{\omega_{||}}\right]. \tag{2.48}$$

A similar relation holds for the out-of-plane component $S^{\perp}(\vec{Q},\omega)$. To account for a finite magnon lifetime Γ^{-1}, the delta functions in Eq. (2.48) have to be replaced by Lorentzians of width Γ. This is in complete analogy to the one-phonon cross-section discussed in Chapter 2.2.3.

In the Néel phase of the $S = 1/2$ materials studied in this thesis, the dispersion relations for the out-of-plane and in-plane polarized spin waves near the 3D zone center are respectively given by

$$\omega_{\perp}(q_{2D}) = 4Z_c JS[2\alpha_{XY} + \frac{1}{2}(aq_{2D})^2]^{1/2}, \tag{2.49}$$

$$\omega_{||}(q_{2D}) = 4Z_c JS[\alpha^2_{DM} + \frac{1}{2}(aq_{2D})^2]^{1/2}. \tag{2.50}$$

The measurement of α_{XY} in $Sr_2CuO_2Cl_2$ is described in Chapter 4.

2.3.3 Incoherent magnetic scattering

Incoherent magnetic scattering is given by the *self time-dependent correlation function* $\langle S^{\alpha}(0,0)S^{\beta}(0,t)\rangle$ in Eq. (2.38). In a Heisenberg paramagnet the incoherent magnetic scattering is elastic, since the spin operator commutes with the Hamiltonian and is therfore time-independent.

Inelastic incoherent magnetic scattering may arise from transitions between the discrete levels crystal field levels of single ions in noninteracting or weakly coupled systems. As an example, the lowest-lying crystal field excitation within the ground state multiplet of the Nd^{3+} ions in $La_{1.35}Nd_{0.49}Sr_{0.16}CuO_4$ is shown in Fig. 2-5. The

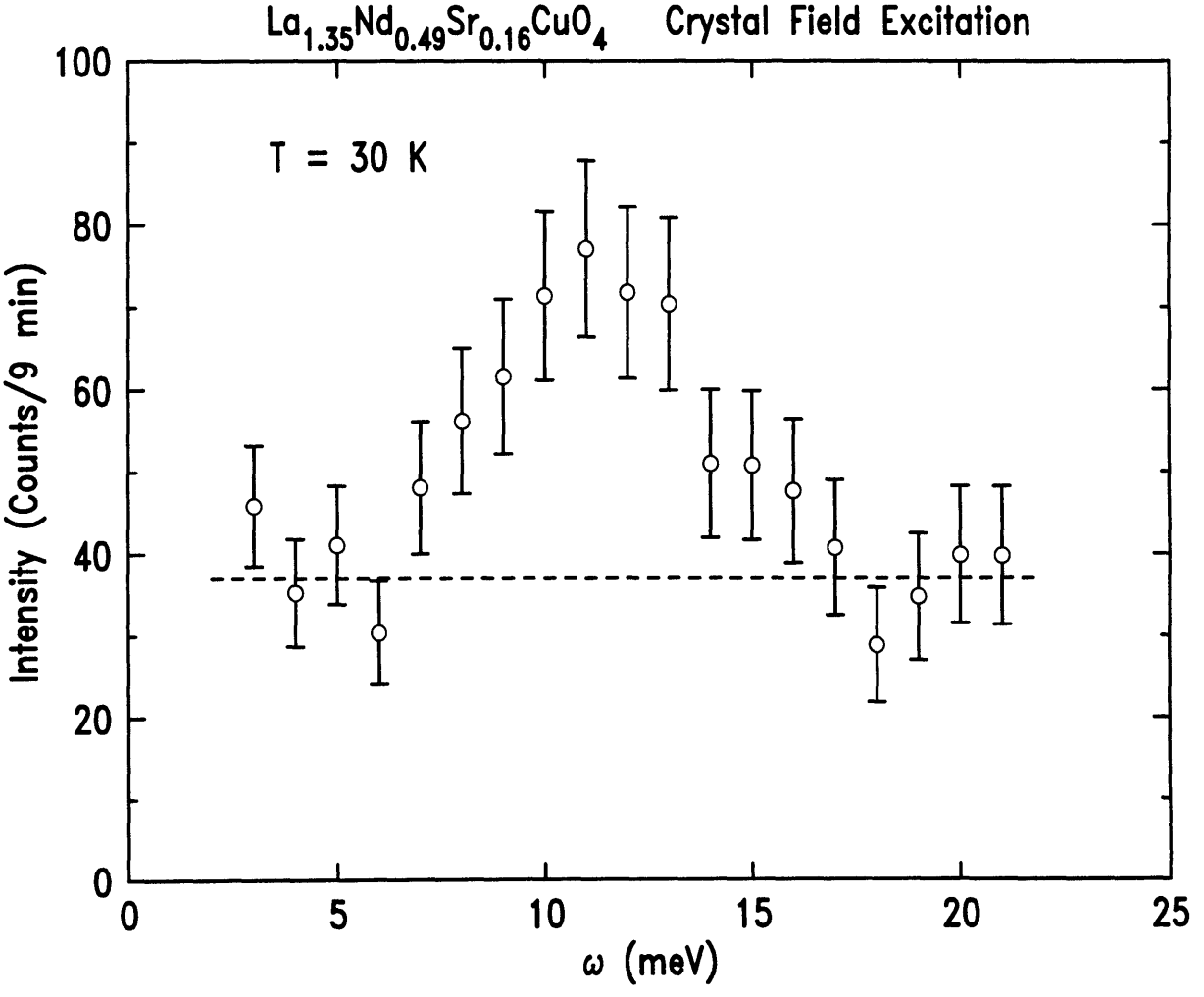

Figure 2-5: Crystal field excitation in $La_{1.35}Nd_{0.49}Sr_{0.16}CuO_4$.

energy of the excitation, $\omega \sim 11meV$, is about $5meV$ smaller than the corresponding excitation in stoichiometric Nd_2CuO_4 [120].

2.4 Neutron spectrometers and resolution

2.4.1 The three-axis spectrometer

After the nuclear fission process in a research reactor, neutrons are thermalized by a moderator, e.g. heavy water. The resulting velocity distribution of the neutrons is Maxwellian, with a maximum that depends on the temperature of the moderator, usually $\sim 300K - 350K$ for thermal neutrons. In the three-axis neutron spectrometer

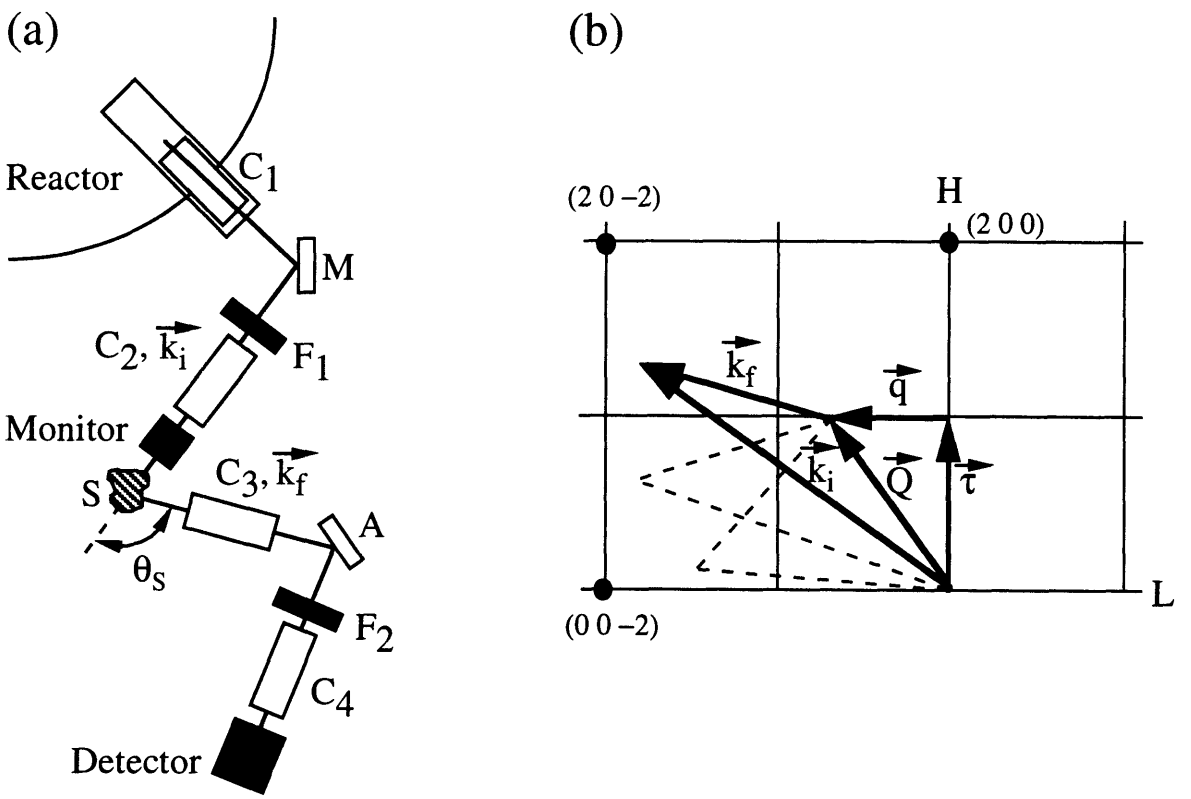

Figure 2-6: (a) Three-axis spectrometer. (b) Scattering diagram for a constant-$\vec{Q}$ scan in the E_f-fixed mode.

configuration shown in Fig. 2-6(a), neutrons have to scatter three times before they reach the detector. The initial and final neutron energies, E_i and E_f, are selected by

the monochromator (M) and analyzer (A) crystals by virtue of the condition

$$\lambda_{i(f)} = 2d_{M(A)}\, sin(\theta_{M(A)}) \tag{2.51}$$

for Bragg scattering. In all the neutron scattering experiments presented in this thesis, the (0 0 2) reflection of pyrolytic graphite was used to monochromatize and analyze the neutron beam energy. Pyrolytic graphite is oriented graphite with a highly preferred orientation of the (0 0 L)-planes, while all the other (H K L)-planes are aligned randomly [121, 122]. Due to this randomness, unwanted effects (e.g. double Bragg scattering) are greatly reduced compared to those in single crystals, and the reflectivity is increased significantly. At the (0 0 2) reflection, the reflectivity of pyrolytic graphite is $\sim 60 - 70\%$, depending on the exact neutron energy used.

Along their paths from the reactor core to the detector, the neutrons are collimated by four collimators ($C_1 - C_4$). While the horizontal collimations can be varied to be either 10', 20', 40', or 80', the vertical collimations are held fixed. Apart from relatively small divergencies of the neutron beam due to the finite vertical collimations, the neutron paths are confined to a scattering plane defined by $\vec{k}_i$ and $\vec{k}_f$. The momentum transfers $\vec{Q}$ are thus also confined to this scattering plane, so that without remounting of the sample crystal only a 2D slice of its 3D reciprocal lattice is accessible. However, for most of the experiments in this thesis this has not been a constraint since 2D correlated systems were studied.

Higher order Bragg scattering due to neutrons with wavelengths $\lambda/n\,(n = 2, 3, ...)$ from the monochromator and analyzer crystals is minimized by inserting appropriate filters (labelled F_1 and F_2 in Fig. 2-6(a)) into the neutron beam [22, 122]. Pyrolytic graphite, with the $\hat{c}$-axis along the beam direction, also functions as a very efficient filter. It has narrow energy windows of very low neutron absorption at $E \sim 13.7, 14.7, 30.5$, and $41meV$, and higher order neutrons with energies $E_n = n^2E$ are largely absorbed. For experiments that employ low-energy neutrons, that is $E \lesssim 5meV$, polycrystalline Be is an effective filter, since higher order neutrons are Bragg scattered out of the beam in Debye-Scherrer cones [123].

Neutrons are detected indirectly through nuclear reactions in which charged particles are created. At Brookhaven National Laboratory (BNL), ^{3}He detectors based on the reaction n $+^3$He $\rightarrow$ p $+^3$H are used (the neutron absorption cross-section for this process is rather large: $\sigma_a(^3\mathrm{He}) = 5333\, barns$). The protons are then detected due to their ionizing properties. Note, that such a detector serves simply as a neutron counter and can not be employed to determine E_f. The final neutron energy is determined through the Bragg scattering condition for the analyzer crystal.

In an inelastic scattering experiment either E_i is held fixed and the second filter is taken out, or E_f is held fixed and the first filter is taken out. The measured signal in the detector is normalized by the monitor count rate, which is proportional to the incident neutron flux. The monitors used at BNL are fission counters which operate with very small amounts of highly enriched Uranium. This type of monitor is very efficient as it minimizes the loss due to neutron absorption. If the spectrometer is run in the E_f-fixed mode, it is necessary to correct the measured intensity for the higher order neutron contamination that is picked up by the monitor. This correction factor is also known as "*Cowley correction*" [124].

With a three-axis spectrometer, it is possible to carry out either constant-ω or constant-$\vec{Q}$ scans. In Fig. 2-6(b) a constant-$\vec{Q}$ scan, with E_f held fixed, is shown schematically. A typical constant-ω scan of the 2D magnetic excitations in a $\sim 2cm^3$ crystal of $La_{2-x}Sr_xCuO_4$ takes about 5 hours. While this allows for a reasonably broad mapping of the $\vec{Q}$- and ω-dependence of the dynamic structure factor $S(\vec{Q},\omega)$, it is not feasable to determine the static structure factor via the relation Eq. (2-21) in this fashion. Nevertheless, it is possible to obtain $S(\vec{Q})$ approximately, and in some cases even exactly, by employing a two-axis spectrometer.

2.4.2 The two-axis spectrometer

The triple-axis spectrometer can be modified to be operated in a two-axis mode. One simply removes the analyzer and the fourth collimator, as shown in Fig. 2-7(a). In the two-axis configuration, the final neutron energy discrimination is removed while the incident neutron energy is held fixed. At a fixed scattering angle θ, neutrons with

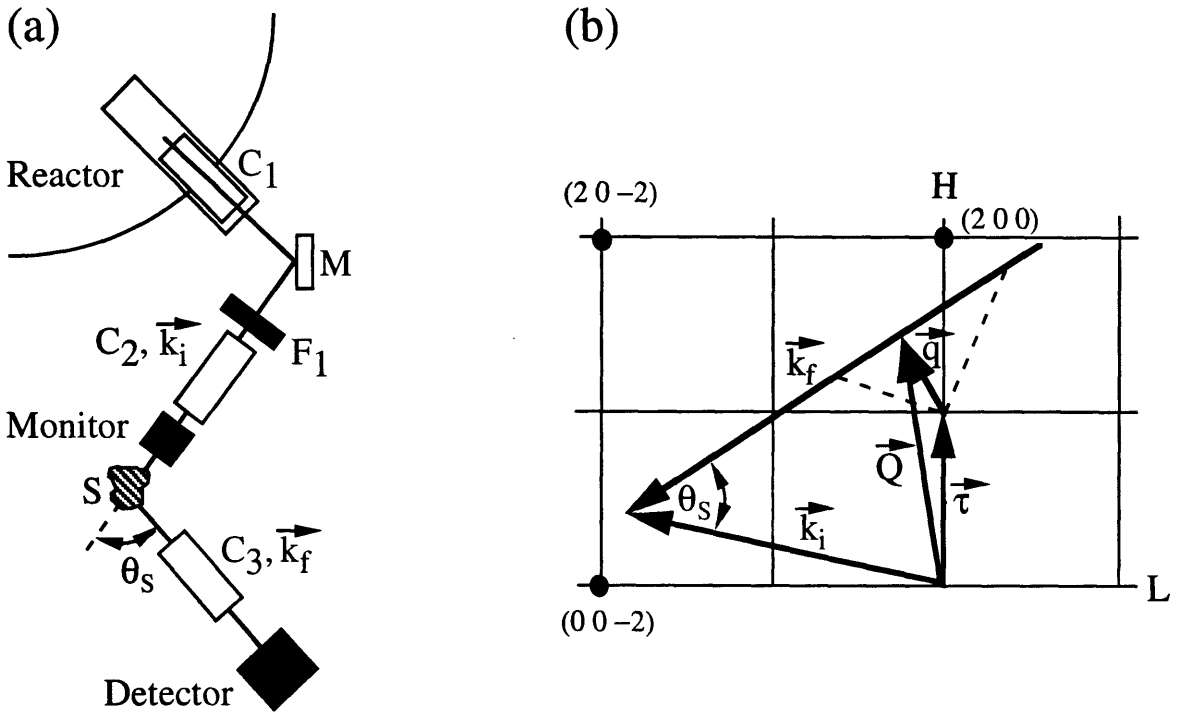

Figure 2-7: (a) Two-axis spectrometer and (b) scattering diagram.

different final energies E_f, corresponding to scattering processes with different energy transfers ω, are collected in the detector. However, it can be seen from Fig. 2-7(b) that the energy integration

$$\int_{-\infty}^{E_i} S(\vec{Q},\omega)d\omega \tag{2.52}$$

is in general not carried out at a fixed momentum transfer $\vec{q}$. Note, that $\vec{q}$ is defined as the deviation wavevector $\vec{q} = \vec{Q} - \vec{\tau}$, where $\vec{\tau}$ is a vector of the reciprocal lattice. The measured intensity at a fixed scattering angle θ represents a cut of the cross-section in $\vec{Q} - \omega$ space along the path

$$\vec{Q}(\omega) = 2[k_i^2 - m_n\omega - k_i\sqrt{k_i^2 - 2m_n\omega}\,\cos\theta]\hat{Q}(\omega) \tag{2.53}$$

In order to obtain the differential cross-section, the energy integration has to be carried out at a constant $\vec{Q}$. From the above equation, it can be seen that this can

be achieved approximately when

$$\frac{2m_n|\omega|}{Q^2} << 1. \tag{2.54}$$

For non-zero ω this relation becomes exact only in the limit $E_i \rightarrow \infty$.

However, for a 3D correlated system very close to its critical temperature, the dynamic spectrum is shifted to very low energies near the critical wavevector. This critical slowing down was discussed in Chapter 2.2.1, and is related to the fact that the static susceptibility at the critical wavevector diverges as the critical temperature is approached. In this case, both the conditions Eq. (2.54) and $\omega << T$ hold, and one measures the static susceptibility to a good approximation. This is called the *quasielastic approximation*, since it is required that $|\omega|$ is very small [125, 126, 127]. When the quasielastic condition is satisfied, the neutrons traverse a correlated volume in a time that is much shorter than the typical fluctuation time $\sim \omega_{max}^{-1}$ of the scattering system. One therefore obtains a *"snapshot picture"*. In the correlation function language, this situation corresponds to the $t \rightarrow 0$ limit of $G(\vec{r}, t)$.

In scattering experiments on 1D and 2D correlated systems, it is possible to arrange the scattering geometry of the *constant angle* setup to be a *constant-$\vec{q}$* setup [52]. In particular, the Heisenberg systems studied in this thesis are 2D correlated above their respective Néel temperatures, and the dynamic structure factor is therefore independent of the momentum transfer $Q_\perp$ perpendicular to the CuO_2 sheets. As shown in Fig. (2-8), one can take advantage of this fact by arranging the scattering geometry such that $\vec{k}_f$ is parallel to the 2D scattering rod for each point of the scan. The momentum transfer $\vec{q}_{2D}$ is then independent of the value of k_f.

The magnetic form factor is nearly independent of $Q_\perp$ in the relevant Q-range [128, 129]. Furthermore, the condition $\omega << T$ holds to a good approximation for the Heisenberg systems in the temperature range studied. If one then chooses E_i large enough so that $\omega << E_i$, it is possible to measure the static susceptibility very

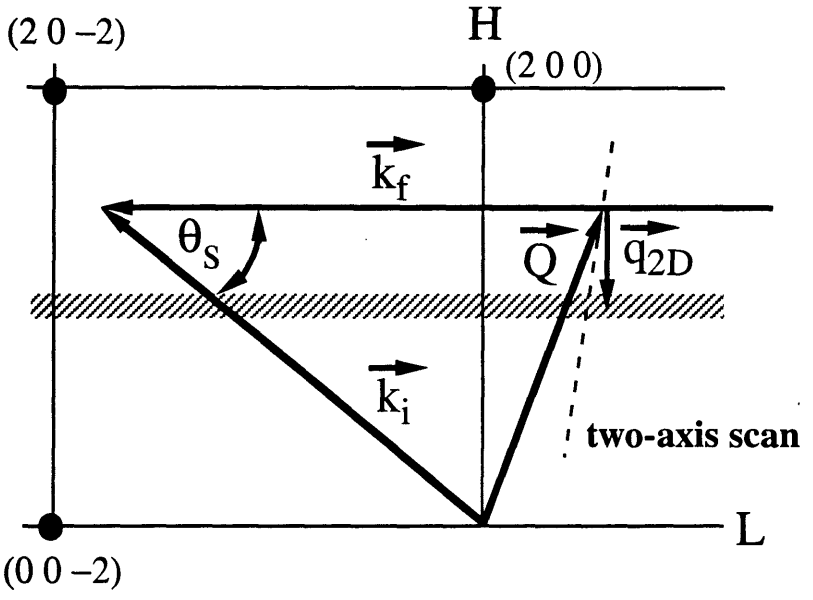

Figure 2-8: Two-axis scan for a 2D correlated system.

well. The two-axis intensity is then given by (see Eq. 2-47):

$$I_{2D}(q_{2D}) \simeq \int_{-\infty}^{E_i} \left[\frac{1}{2}\left(1+cos^2(\phi)\right) S^{||}(q_{2D},\omega) + sin^2(\phi) S^{\perp}(q_{2D},\omega)\right] d\omega \qquad (2.55)$$

At temperatures well above T_N, the spin system is isotropic, so that $S^{||}(q_{2D},\omega) = S^{\perp}(q_{2D},\omega) \equiv S(q_{2D},\omega)$, and

$$I_{2D}(q_{2D}) \sim \int_{-\infty}^{E_i} S(q_{2D},\omega)\, d\omega \sim S(q_{2D}) \simeq T\chi(q_{2D}). \qquad (2.56)$$

2.4.3 Spectrometer resolution

Due to the non-zero angular spread in the collimations as well as the non-zero mosaic spread in the monochromator and analyzer, the incident and final neutron wavevectors $\vec{k}_i$ and $\vec{k}_f$ are not perfectly well defined. Neutrons will in general deviate by some amout $\Delta\vec{k}_i$ and $\Delta\vec{k}_f$ from their most probable path. The resolution function of a spectrometer is the probability of detection of neutrons as a function of $\Delta\vec{k}_i$ and $\Delta\vec{k}_f$

when the instrument has been set to measure a scattering process with wavevectors $\vec{k}_i$ and $\vec{k}_f$. However, the six cartesian coordinates ($\vec{k}_i$,$\vec{k}_f$) are not independent of each other. The energy and momentum relations Eqs. (2.1) and (2.2) allow the problem to be formulated in terms of only four coordinates: $(\Delta\vec{Q}, \Delta\omega)$. The measured intensity for a triple-axis spectrometer is then given by the four-dimensional (4D) integral [130, 131]

$$I(\vec{Q},\omega) = \int R(\Delta\vec{Q},\Delta\omega) \left[\frac{d^2\sigma}{d\Omega dE_f}(\vec{Q}-\Delta\vec{Q},\omega-\Delta\omega)\right] d\Delta\vec{Q}d\Delta\omega, \qquad (2.57)$$

where $R(\Delta\vec{Q},\Delta\omega)$ is the resolution function which depends on $\vec{Q}, E_i, E_f$, the horizontal and vertical collimations, and the mosaic spreads.

Neutron scattering data are analyzed with the aid of a computer program which calculates the resolution function and carries out the convolution with an appropriate cross-section. The resolution function can be visualized as a 4D resolution ellipsoid, defined as the volume enclosed by the surface on which $R(\Delta\vec{Q},\Delta\omega) = R(0,0)/2$. When the ellipsoid is "scanned" through an intrinsic sample process with coordinates $(\vec{Q},\omega)$, the measured signal increases above its background level. This is illustrated schematically in Fig. 2-9 for both constant-$\vec{Q}$ and constant-ω scans.

Although the resolution ellipsoid is a 4D object, the vertical $\vec{Q}$-resolution (i.e., the resolution perpendicular to the scattering plane) is completely decoupled from the remaining three dimensions of the resolution function. In order to increase the signal, the vertical collimations are kept very coarse. As a result, the vertical resolution (which then only depends on E_i and E_f) is generally so large that the intrinsic scattering in this direction is automatically integrated over. It is then instructive to consider the projections of the remaining three dimensions of the resolution ellipsoid onto the scattering plane and the energy axis. This is demonstrated in Fig. 2-10 for a typical constant-ω scan in the H-direction accross the rod of 2D magnetic scattering. In Figs. 2-10(a)-(d) the projections of the resolution ellipsoid onto the scattering plane are shown for different values of L. The shaded ovals indicate the slice at $\omega = 0$ of the resolution ellipsoid. The parameters were chosen for an energy

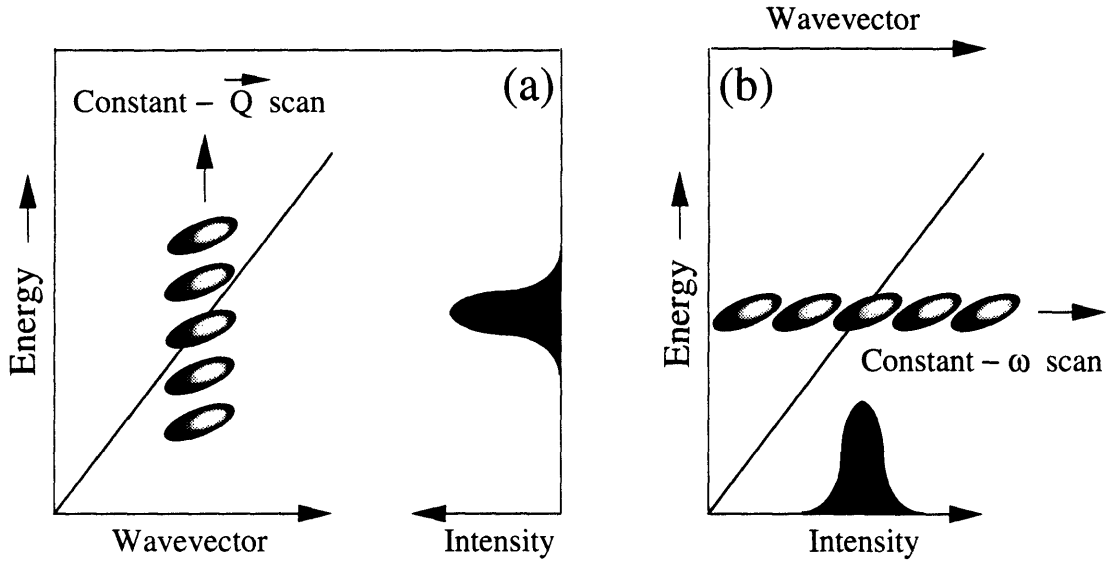

Figure 2-9: (a) Constant-$\vec{Q}$ and (b) constant-ω scans.

transfer $\omega = 3meV$, a fixed incident energy $E_i = 14.7meV$, and horizontal collimations $40' - 80' - S - 80' - 80'$. The degree of alignment of the resolution ellipsoid with the (1 0 L)-rod depends on the value of L. In order to optimize the signal-to-background-ratio of an inelastic scan, one generally attempts to find a spectrometer configuration that corresponds to a maximum alignment of the resolution ellipsoid with the intrinsic signal. Since the cross-section is independent of L, the highest signal-to-background-ratio for a scan in the H-direction at $\omega = 3meV$ is achieved for L = −0.55: The resolution ellipsoid is *"focussed"* for L = −0.55. In this case, the resolution in the H-direction (i.e., the direction of the scan) is $\sim 0.03\,a^* \sim 0.035\mathring{A}^{-1}$, while the much coarser vertical resolution is $\sim 0.13\mathring{A}^{-1}$.

Figure 2-10(e) shows the projection (of width $\sim 1.3meV$) of the resolution ellipsoid onto the energy axis for L = −0.55, as seen from the reciprocal origin. Similarly, Fig. 2-10(f) shows the same projection perpendicular to $\vec{Q}$. Note, that the energy projection is much larger than the width of the slice obtained from a Bragg peak (which is a delta function in both $\vec{Q}$ and ω).

For two-axis measurements the resolution function takes on a somewhat simpler

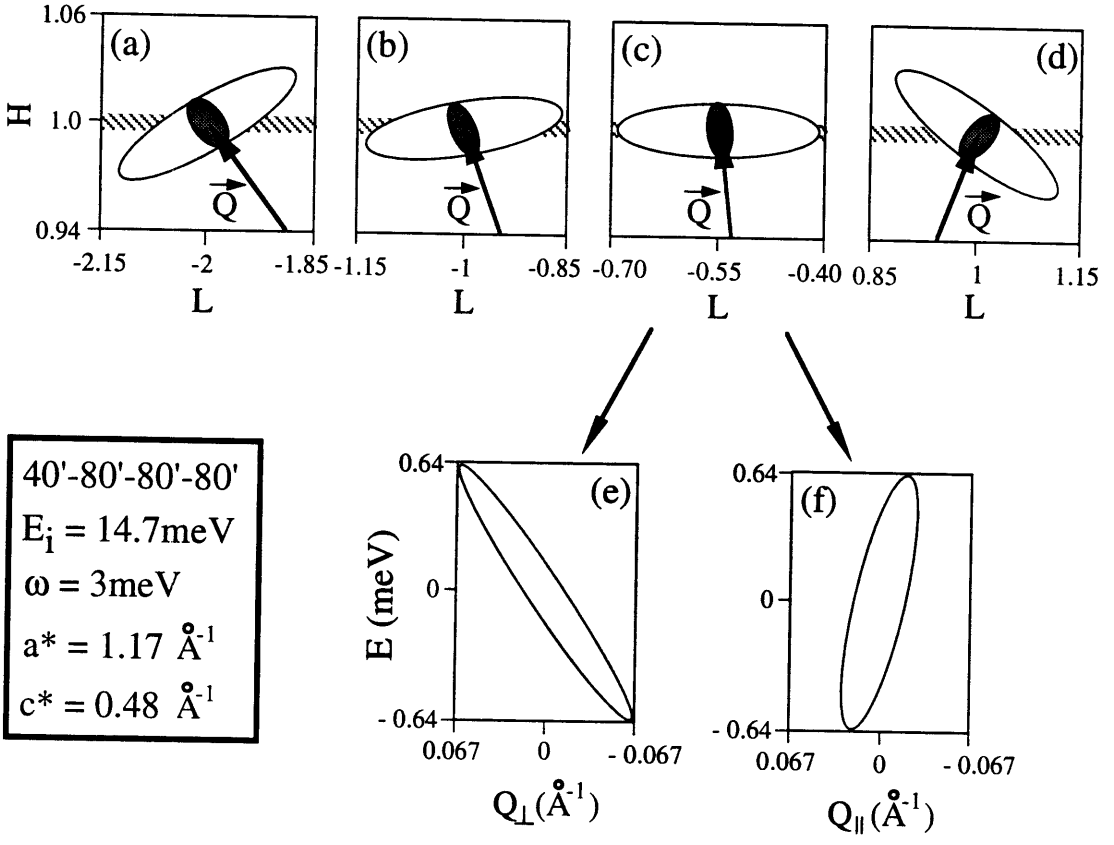

Figure 2-10: Focusing condition for a typical inelastic magnetic scan.

form [132], since it is independent of ω. The deconvolution program uses a Gaussian functional from for the vertical resolution. While this is a good approximation for low values of E_i, above $E_i \sim 30meV$ the vertical resolution has a trapezoidal shape. The analysis of the two-axis data for large values of E_i was therefore carried out with an analytical deconvolution of the vertical component of the resolution function using the measured vertical resolution.

2.4.4 Polarized Neutrons

If a polarized incident neutron beam is used, the Bragg cross-section Eq. (2.40) aquires an additional term. For neutrons polarized to degree ϵ in the direction $\hat{\lambda}$, this term can be written as

$$2\epsilon\hat{\lambda}\hat{P}F_n(\vec{Q})F_m(\vec{Q}), \tag{2.58}$$

where $\hat{P} = \hat{e}_m - (\hat{Q}\hat{e}_m)\hat{Q}$ so that $|\vec{P}| = \sin(\Phi)$. In fact, the term Eq. (2.58) is the key to polarizing a beam of neutrons. Suppose that an unpolarized neutron beam, devided equally into "up" and "down" polarized neutrons (i.e. $\hat{\lambda}\hat{e}_m = \pm 1$), is incident onto a simple Bravais ferromagnet under the condition $\vec{Q}\hat{e}_m = 0$. The cross-section for "up" and "down" polarized neutrons then is $(\bar{b}+p)^2$ and $(\bar{b}-p)^2$, respectively. In a Heusler monochromator, a reflection for which $\bar{b} = p$ is used such that only "up" neutrons are reflected.

It is possible to determine if a crystal is a bulk superconductor through a neutron depolarization measurement. For such an experiment the three-axis spectrometer is operated with a Heusler analyzer and monochromator. The "up"-polarized neutrons are guided by vertical magnetic fields in order to maintain their polarization. Accross the sample, a vertical (VF) or horizontal field (HF, perpendicular to the neutron beam) can be applied. The setup is calibrated at high temperatures (above T_c), such that the intensity of a Bragg peak is the same for both the VF and HF modes of operation. To test for bulk superconductivity, the sample is then VF-cooled to $\sim 5K$, and the intensity of a Bragg peak is measured. If the sample becomes superconducting, it will set up a flux lattice which will depolarize the neutrons to some degree. Once the

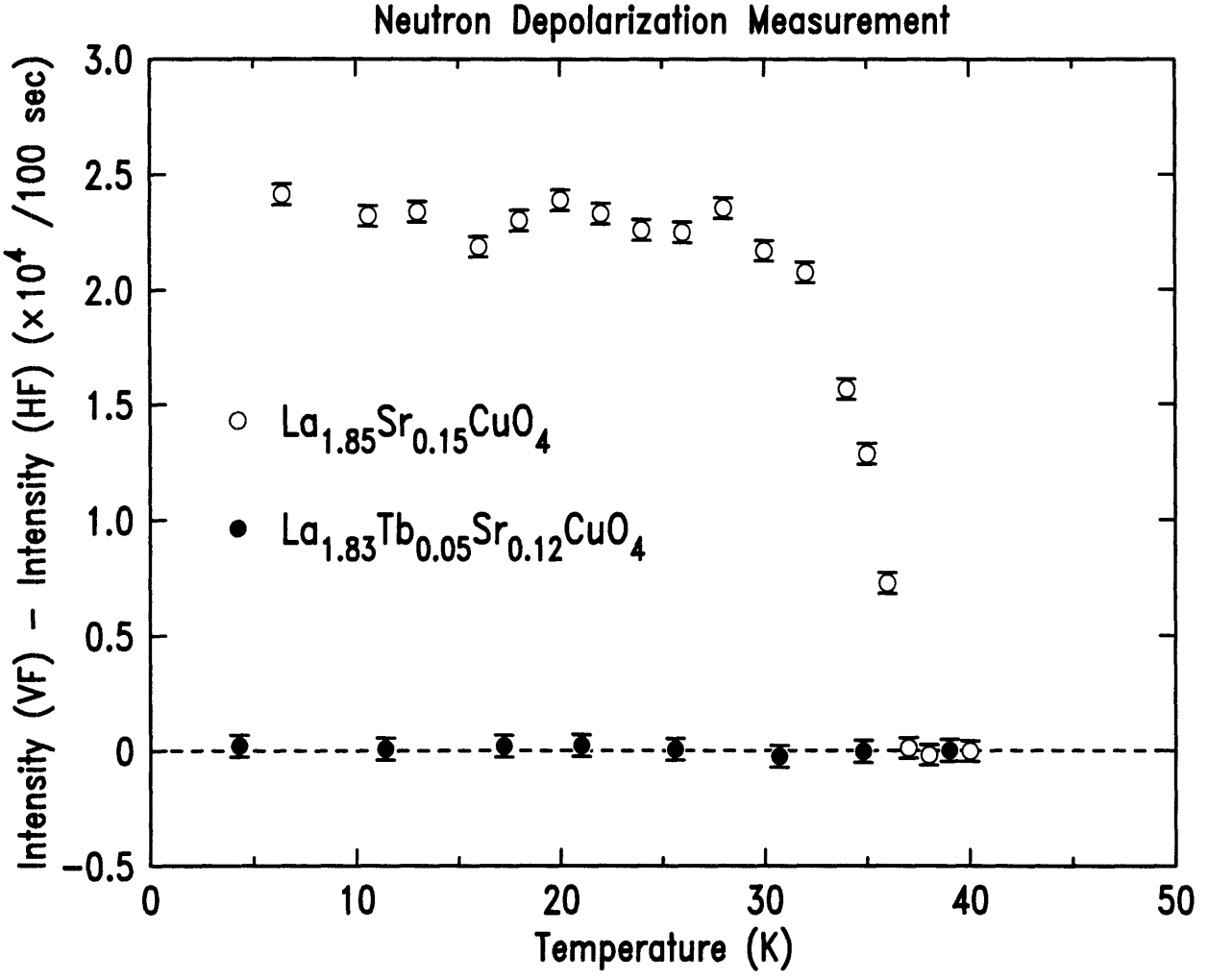

Figure 2-11: Neutron depolarization measurement.

VF is turned off and the HF is applied, the flux lattice will be disturbed and neutrons passing through the sample will be depolarized to a different degree. As a result, the measured Bragg intensities differ. In Fig. 2-11, the difference between the VF- and HF-intensities of the (0 0 6) nuclear peak is shown for both $La_{1.85}Sr_{0.15}CuO_4$ and $La_{1.83}Tb_{0.05}Sr_{0.12}CuO_4$. While the former sample shows a very nice depolarization effect (and is therfore a bulk superconductor), the latter sample does not superconduct at $\sim 4K$. The result for the Tb-doped sample has important consequences for the interpretation of the inelastic magnetic spectra presented in Chapter 8.

Chapter 3

Crystal Growth and Characterization

Bednorz and Müller's discovery of high-temperature superconductivity in the lamellar copper oxides initiated a tremendous amout of research activity, both experimental and theoretical. On the experimental side, the main objectives have been the search for new materials (with possibly higher T_c's and H_c's), and the subsequent determination of their physical properties. Initially, many irreproducible and unreliable results were reported because of the poor quality of the crystals that were used. Since high-temperature superconductors have very short coherence lengths, crystals homogeneous on very small length scales are required. Eventually, the synthesis procedures for several copper oxide families were optimized and experimental results have, in general, become reproducible.

The first major challenge in the synthesis of a newly discovered material generally is to isolate the individual phases from a multiply polycristalline material, and to identify the phases that are responsible for the superconductivity. For example, Bednorz and Müller's original discovery was made for a synthesized mixture of a perovskite, and two lamellar phases $La_{2-x}Ba_xCuO_4$ and $La_{1+y}Ba_{2-y}Cu_3O_7$ with $x \sim 0.15$ and $y \sim 0.5$, respectively. While the observed superconductivity was due to the first lamellar phase, it is known by now that the second lamellar phase also superconducts, with a maximum transition temperature above $90K$ for $y \simeq 0$.

Once a single lamellar phase has been successfully isolated, a subsequent challenge is the growth of high-quality single crystals. The availability of bulk single crystals is crucial for several reasons. First, anisotropies of physical properties can only be measured on single (ideally untwinned) crystals. Second, the comparison of measurements on single crystals with those on polycrystalline materials allows to gain insight into the role of defects, intergrain, and twin boundaries. Secondly, anisotropies of physical properties can only be measured on single (ideally untwinned) crystals. The lamellar copper oxides are highly anisotropic, a feature which lies at the core of many of their unusual properties. Finally, large single crystals with volumes $\gtrsim 1\,cm^3$ are required for inelastic neutron scattering measurements.

$La_{2-x}(Ba,Sr)_xCuO_4$ has the simplest structure among the many copper oxide families, since it is made up out of single CuO_2 sheets. All attempts to grow sizable single crystals of the Ba-doped compound with $x > 0.06$ have failed so far. Fortunately, this has not been the case for the Sr-doped compound, which can be grown over a wide doping range. The growth of large single crystals of $La_{2-x}Sr_xCuO_4$ was pioneered by Picone et al. [133] (MIT, USA) and Hidaka et al. [134] (NTT, Japan).

3.1 Growth of $Sr_2CuO_2Cl_2$ and rare-earth co-doped $La_{2-x}Sr_xCuO_4$

As part of this thesis work, a series of single crystals of $La_{2-x-y}RE_ySr_xCuO_4$ (RE = Nd or Tb) were grown for use in neutron scattering experiments. The inelastic magnetic neutron scattering measurements in the largest crystal of this series are presented in Chapter 8. Furthermore, high-purity single crystals of $Sr_2CuO_2Cl_2$ were grown for photoemission [135, 136] and optical absorption [137, 138] studies. The photoemission work is discussed in Chapter 7.

A schematic diagram of the furnace that was used is shown in Fig. 3-1. A $150ml$ Pt crucible is surrounded by an alumina cup placed upside down, in order to obtain very low thermal gradients. The seed rod, made of alumina, passes through a small hole in the cup. The seed is attached to the seed rod with a Pt wire. Since it is

not possible to look into the melt, the contact between the crystal and the melt was determined by measuring the resistance between a Pt wire attached to the seed and a Pt wire welded to the crucible.

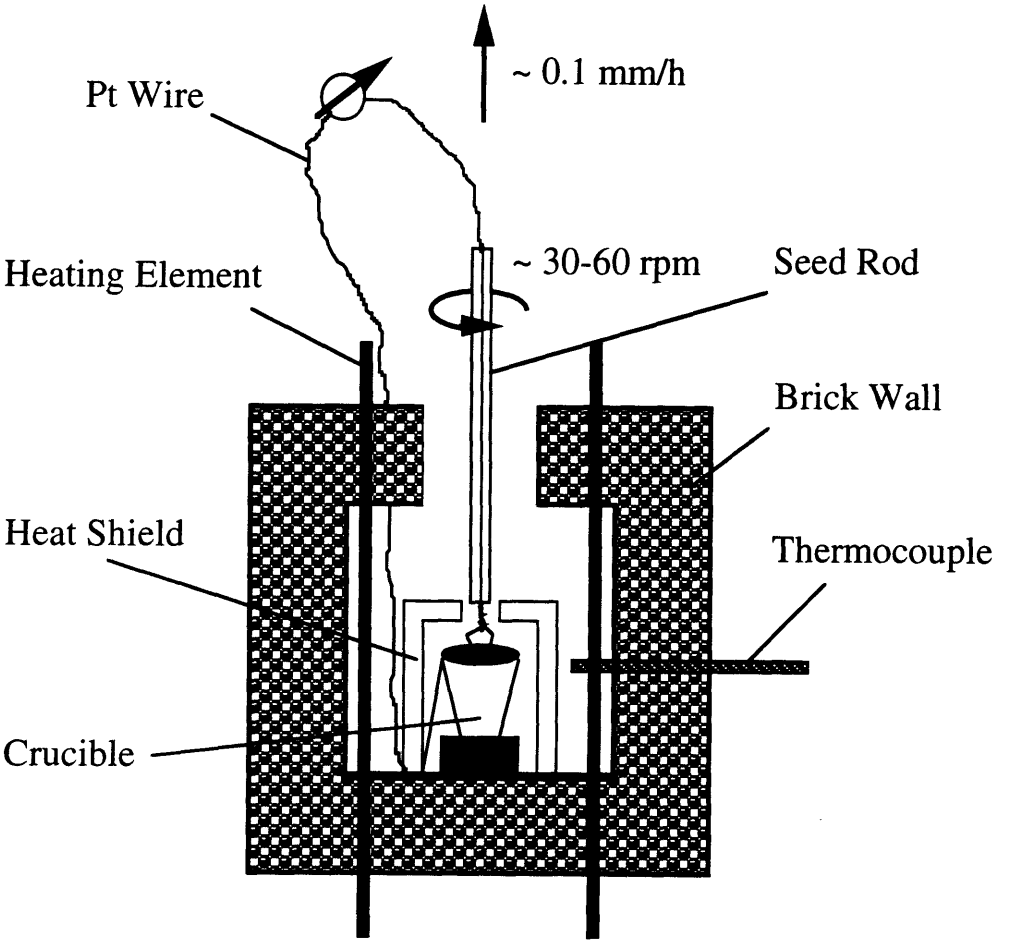

Figure 3-1: Schematic diagram of the furnace used for the growth of $Sr_2CuO_2Cl_2$ and rare-earth co-doped $La_{2-x}Sr_xCuO_4$.

The $La_{2-x-y}RE_ySr_xCuO_4$ crystals were grown by the top-seeded solution growth technique in an excess of CuO. As starting materials powders of La_2O_3 (99.99%), CuO (99.99%), $SrCO_3$ (99.99%), and either Nd_2O_3 (99.99%) or Tb_4O_7 (99.99%), were used. After the crucible was filled with $\sim 350g$ of material, of which $85 - 88\,mol\%$ was CuO (flux), the temperature was raised at a rate of $\sim 100°/h$. Once the material was melted (typically at $\sim 1250°C$), the temperature was lowered again at a rate of $\sim 10°C/h$, while a Pt wire attached to the seed rod was dipped into the melt to

check for crystallization. As soon as crystallization was found to occur on the Pt wire, the wire was removed. Instead, a seed crystal was attached to the seed rod and brought in contact with the melt surface. The seed was then pulled out at a rate of $\sim 0.1mm/h$, and rotated at $\sim 30 - 50rpm$, while the temperature of the furnace was lowered by $\sim 0.25 - 1°C/h$. With this setup, $La_{2-x-y}RE_ySr_xCuO_4$ crystals up to $\sim 2\,cm^3$ could be grown in the [0 0 1]-diretion.

Important precautions have to be taken for successful growth. If sufficient cooling is not provided to the seed, the melt tends to creep up over the seed and the Pt wire holding it, resulting in a polycrystalline mass. The seed rod cannot, however, be so cold that spontaneous nucleation occurs on the melt surface. To ensure that the seed is cooled it has to be in good contact with the seed rod. The seed should also be free of flux, to keep its shape during seeding and not lose contact with the seed rod.

Previously, it had been found that the segregation coefficient for Sr in $La_{2-x}Sr_xCuO_4$ varied from $K_{Sr} \sim 1$ for low doping, to $K_{Sr} \sim 0.5$ for $x \sim 0.2$, and to $K_{Sr} \sim 0.3$ for $x \sim 0.3$ [139]. For higher Sr concentrations, no good quality crystals could be grown with the top-seeded solution growth technique, and a maximum of $x \sim 0.10$ with $T_c \sim 15K$ was obtained. Polycrystalline and float-zone grown crystals with $x = 0.10$, however, have $T_c \sim 30K$. It is known [140], that Pt contamination depresses T_c. Electron probe microanalysis (EPMA) carried out on $La_{2-x}Sr_xCuO_4$ crystals grown from a Pt crucible, indicate an increasingly large Pt contamination for larger x. While for $x \sim 0$ generally no Pt is detectable within the resolution of the EPMA ($\sim 0.01\,at\%$), a contamination of $\sim 0.1at\%$, or $\sim Pt_{0.01}$, for $x \sim 0.08 - 0.10$ is typical [139].

It was found that rare earth co-doping of $La_{2-x}Sr_xCuO_4$ not only facilitates the growth of large single crystals, but also alows for the incorporation of higher levels of Sr. The results are summarized in Table 3.1. The highest Sr content was achieved in run number 1868, which resulted in a single crystal ($1\,cm^3$ in volume) with composition $La_{1.35}Nd_{0.49}Sr_{0.16}CuO_4$, as determined by EPMA. However, along with the higher Sr levels the Pt contamination was also found to increase. The largest crystal grown had a volume of $2cm^3$ and the composition $La_{1.83}Tb_{0.05}Sr_{0.12}CuO_4$.

	Melt Composition			Segregation Coefficient		Crystal Composition		
Run #	CuO (mol%)	Nd	Sr	K_{Nd}	K_{Sr}	Nd	Sr	Pt
1839	85	0.40	-	0.63	-	0.25	-	0.0015
1862	85	0.40	0.10	0.73	0.60	0.29	0.06	0.0015
1869	87	0.49	0.24	0.69	0.43	0.34	0.10	0.0050
1855	88	0.50	0.30	0.78	0.37	0.39	0.11	0.0085
1860	87	0.51	0.31	0.78	0.39	0.40	0.12	0.0105
1868	88	0.56	0.46	0.88	0.35	0.49	0.16	0.0175
Run #	CuO (mol%)	Tb	Sr	K_{Tb}	K_{Sr}	Tb	Sr	Pt
1880	88	0.20	0.42	0.25	0.30	0.050	0.125	0.0150

Table 3.1: Melt composition, segregation coefficients, and crystal composition for Nd and Tb co-doped $La_{2-x}Sr_xCuO_4$.

Single crystals of $Sr_2CuO_2Cl_2$ were grown following the same synthesis procedure as used by Miller et al. [141]. Very high purity powders of $SrCl_2$ (99.999%), $SrCO_3$ (99.999%), and CuO (99.999%), were used. Stoichiometric amounts of predried $SrCl_2$ and prereacted $SrCuO_2$ were mixed, and then heated to $1140°C$. After cooling at an initially slow rate of $1°C/h$, $Sr_2CuO_2Cl_2$ crystals with typical dimensions $10 \times 10 \times 1mm^3$ were removed form the solidified melt. No traces of Pt contamination could be detected by EPMA, presumably because of the relatively low growth temperature and the rather small (stoichiometric) amount of CuO in the melt.

3.2 Characterization

The first step after the successful growth of a crystal is generally an electron probe microanalysis (EPMA). EPMA is a non-destructive technique in which an electron beam is focussed onto the sample, and output signals which provide information about the sample composition (e.g., backscattered electrons and characteristic x-rays) are tapped and analyzed. The electron beam is typically focussed onto ten different spots in order to obtain information about the homogeneity of a sample. Since EPMA is a surface sensitive technique information from complementary probes (e.g., neutron scattering and SQUID magnetometry) is required in order to arrive at a complete

characterization of a crystal.

Elastic neutron scattering may be used in various ways as a tool to determine the composition and overall homogeneity of a bulk single crystal. For example, the temperature and sharpness of the structural transition in $La_{2-x}Sr_xCuO_4$ give information about the hole doping level and homogeneity, respectively. As-grown crystals generally contain small excess amounts of oxygen, i.e. their stoichiometry is actually $La_{2-x}Sr_xCuO_{4+\delta}$ with $\delta \gtrsim 0$. Excess oxygen, just as Sr-doping, introduces hole carriers into the CuO sheets. In fact, it is known that polycrystalline La_2CuO_4 can be turned into a superconductor with $T_c \sim 40K$ if oxygenated under high pressure. (For sizable single crystals this can be achieved by means of electrolysis.) The orthorhombic superlattice peak intensity is shown in Fig. 2-2 for two samples with transition temperatures $T_{ST} = 530K$ and $T_{ST} = 188K$. From studies on polycrystalline samples it is known that a transition temperature of $T_{ST} = 530K$ corresponds to the undoped limit $x = \delta = 0$. Similarly, the transition temperature of the second sample implies that the hole doping level p is $p = 0.15$. Since δ is relatively small, this means that $x \sim 0.15$ for the second sample, consistent with EPMA measurements.

It can also be seen from Fig. 2-2 that the smearing of the transition temperature T_{ST} is only a few degrees. The solid lines are the results of fits to a power-law form with a Gaussian spread of transition temperaturs. For both samples the Gaussian width is very small: $\sigma \simeq 1.5K$. Since T_{ST} decreases by about $20K$ for a change $\Delta p = 0.01$ in the hole content, both samples are uniform on a scale 10^{-3}.

In Fig. 3-2 the superlattice peak intensity for the Sr-doped sample (labelled "Sendai", since it was grown at Tohoku University, Sendai, Japan) is compared with that of a second crystal with similar hole content (from Koshu, Japan). The Gaussian spread in transition temperatures is almost an order of magnitude larger for the Koshu crystal. Also shown in the inset of Fig. 3-2 are susceptibility data for a piece of a Sendai sample as obtained with a SQUID magnetometer. The onset of superconductivity is very high, $T_c = 37.3K$, and the transition is very sharp, with a width of $\Delta T_c \sim 2K$. These values of T_c and ΔT_c are unusual for a voluminous single crystal (the Sendai crystals are $\sim 1.5\,cm^3$ in volume), and had previously only been

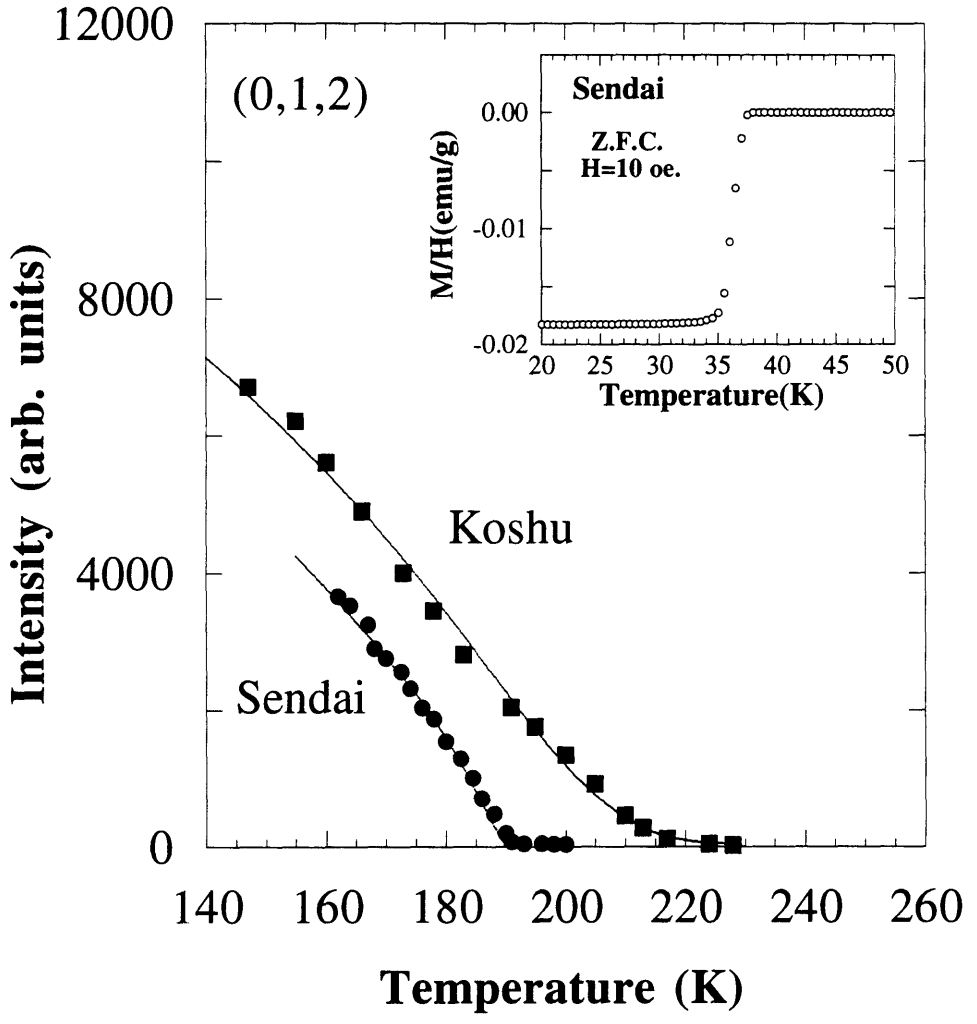

Figure 3-2: (0 1 2) nuclear superlattice peak intensity in the critical regime for two $La_{2-x}Sr_xCuO_4$ crystals. Inset: Meissner effect for the superconducting sample studied in this thesis.

achieved for polycrystalline samples.

The neutron depolarization measurement for the Sendai sample Fig. 2-11 is fully consistent with the SQUID data of Fig. 3-2. While SQUID magnetometry can only be carried out for a small piece cut from the main crystal, a neutron depolarization measurement gives information about the bulk of the actual sample studied. In summary, the high value of T_c, the sharpness of both the structural and superconducting transitions, and the consistency between SQUID magnetometry and neutron depolarization measurements, are all indicators of the unusually high quality of the "Sendai" crystals used for the measurements described in Chapter 8.

Finally, it should be noted that the value and the smearing of T_N in lightly doped lamellar copper oxides can also be used as a measure of sample stoichiometry and homogeneity. Since $Sr_2CuO_2Cl_2$ does not exhibit a stuctural transition into an orthorhombic phase, the temperature dependence of the (1 0 0) magnetic Bragg peak (shown in Fig. 2-4) was used to verify the sample quality. $Sr_2CuO_2Cl_2$ is known to grow stoichiometrically with a Néel temperature of $\sim 255K$. The fits of the order parameter data in Fig. 2-4 allowed for a Gaussian spread in Néel temperatures, and resulted in $T_N = 256.5K$ with a spread of $1.5K$. While this value of T_N is consistent with that found in previous studies, the sharpness of the transition indicates that the sample is quite homogeneous.

Chapter 4

The 2D Square-Lattice Heisenberg Antiferromagnet: S = 1/2

4.1 History

The physics of quantum Heisenberg antiferromagnets (QHA) has been the subject of research ever since the advent of modern quantum and statistical mechanics. In 1931, Bethe [142] found the ground-state eigenfunction for the one-dimensional (1D) $S = 1/2$ QHA, and demonstrated that no long-range order exists in this system even at $T = 0$. Seven years later, Hulthén [143] calculated the ground-state energy of the latter model, and in 1962, des Cloizeaux and Pearson [144] were able to derive the locus of the first excited states at $T = 0$. Excellent agreement was found with des Cloizeaux and Pearson' s result in neutron scattering experiments on a material whose spin Hamiltonian is well described by the $S = 1/2$ 1DQHA model [145]. Because it is one-dimensional, this model is a quantum many-body problem simple enough to allow the exact calculation of several of its zero-temperature properties [146, 147, 148, 149]. Nevertheless, the development of a finite-temperature theory has so far been unsuccessful. However, the focus in this and the following two Chapters will be on the two-dimensional (2D) problem, for which there has recently been a great deal of progress both experimentally and theoretically.

In 1952, extending earlier work by Holstein and Primakoff [150] on ferromagnets,

Anderson [151] and Kubo [152] developed spin-wave theory to describe the ground-state of antiferromagnets with large spin. Spin-wave theory is based on the two assumptions that there exists long-range order at $T = 0$ and that the amplitude of quantum fluctuations about the classical Néel state is small. Since this theory is, in effect, an expansion in powers of $1/(zS)$, where z is the coordination number, its validity crucially depends on the dimensionality and the spin of the system under consideration. It was argued [151], that although the staggered magnetization may be reduced, a Néel ground-state is stable against quantum fluctuations in 2D even in the extreme quantum limit $S = 1/2$. In the mid 1960' s, Hohenberg [153] and Mermin and Wagner [154] proved that in dimensions $d \leq 2$ thermal fluctuations prohibit the existence of long-range order at non-zero temperature in systems with a continuous order parameter. However, the nature of the ground-state of the 2DQHA remained unclear. Indeed, a significant amount of theoretical effort was devoted to the idea that in 2D the extreme quantum nature of $S = 1/2$ moments might induce large enough quantum fluctuations to disorder the system even at $T = 0$. The original and most important contributions along these lines came again from Anderson, who proposed a *quantum disordered* ground-state in 1973 [155, 98]. Since at that time no $S = 1/2$ 2DQHA was known to exist in nature, it was not possible to resolve this issue experimentally. For many years, the tetragonal $S = 1$ system K_2NiF_4 was considered the best example of a nearest-neighbor (NN) 2D square-lattice QHA (2DSLHA) [156]. This material was consequently studied very thoroughly and an extensive series of neutron scattering measurements of the static structure factor were performed [51, 52, 53] and analyzed within the theoretical framework existing at that time.

It was recently proved that for $S \geq 1$ the NN 2DQHA model has an ordered ground-state on both a square lattice [157, 158] and a hexagonal lattice [159]. Despite the lack of an exact result for the case of $S = 1/2$, there now exists compelling evidence that the model has long-range order at $T = 0$ [160]. The important progress in this longstanding problem has only been achieved during the last eight years in a synergistic interplay between experiment and theory. Specifically, a nearly com-

plete description of the static and dynamic low-temperature properties has recently emerged.

In 1986, as discussed in Chapter 1, a novel type of superconductivity was discovered [19] in the system $La_{2-x}(Ba,Sr)_xCuO_{4+\delta}$. Neutron scattering experiments quickly established that La_2CuO_4, the parent compound of these original copper-oxide superconductors, was the first known experimental realization of an $S = 1/2$ 2DSLQHA [161, 162]. Stimulated by these experiments, Chakravarty, Halperin, and Nelson (CHN) [55, 56] developed a quantitative theory that predicts the temperature dependence of both the correlation length, ξ, and the static structure factor peak intensity, $S(0)$, of the 2DSLQHA for general spin S. Tyč, Halperin, and Chakravarty (THN) [163] then extended the theory to predict the form of the dynamic structure factor. Eventually, an exact expression for the low-temperature correlation length of the 2D quantum non-linear sigma model (QNLσM) was calculated by Hasenfratz and Niedermayer (HN) [57]. These predictions were verified with reasonable precision in a more elaborate set of experiments in the $S = 1/2$ system La_2CuO_4 [58, 2], although there were some persistent discrepancies comparable in size to the error bars. CHN's theory was also found to describe reasonably well the correlation length ξ and peak intensity $S(0)$ in the $S = 1$ system K_2NiF_4 above the crossover temperature to 2D Ising critical behavior [164].

$Sr_2CuO_2Cl_2$ is a much more ideal $S = 1/2$ 2DSLQHA than La_2CuO_4. This is primarily because $Sr_2CuO_2Cl_2$ remains tetragonal down to low temperatures and has a larger interplanar spacing. The additional terms that must be added to the 2D Heisenberg Hamiltonion in order to describe the 3D magnetism are thus significantly less important in $Sr_2CuO_2Cl_2$ than in La_2CuO_4. Furthermore, $Sr_2CuO_2Cl_2$ is difficult to dope chemically with either electrons or holes. The possibility that extrinsic carriers affect the magnetism of the CuO_2 sheets is therefore minimal. The data for the static structure factor of $Sr_2CuO_2Cl_2$ presented in Chapter 4.3.1 allow the most stringent test of theory to-date [165, 166, 167]. The experimental result for ξ is in excellent agreement with theory as well as with Monte Carlo simulations [168, 169] and series expansion results [170]. On the other hand, the result for $S(0)$ clearly

differs from existing theoretical predictions.

4.2 Theory

4.2.1 Zero-Temperature Spin-Wave Theory

Spin-wave theory (SWT) is known to be valid in three dimensions at low temperatures. Based on the assumption of an ordered ground state, SWT became a starting point for several theories that attempt to describe the finite-temperature properties of 2D QHAF. Several useful $T = 0$ SWT results will be reviewed here. In Chapter 4.2.2, the theoretical progress that has been made for $T > 0$ will be discussed.

Consider the Heisenberg Hamiltonian with spins S on a square lattice and NN interactions only [160]:

$$H = J \sum_{\langle i,j \rangle} \vec{S}_i \vec{S}_j. \tag{4.1}$$

The Holstein-Primakoff transformation [150] consists of replacing the spin operators by boson operators, and thus transforming from a problem of interacting spins to an equivalent and somewhat simpler problem of interacting bosons. For the sublattice i, with $\hat{n}_i = a_i^\dagger a_i$, one has:

$$S_i^+ = (2S)^{\frac{1}{2}} f_S(\hat{n}_i) a_i, \quad S_i^- = (2S)^{\frac{1}{2}} a_i^\dagger f_S(\hat{n}_i), \quad S_i^z = S - \hat{n}_i, \tag{4.2}$$

$$f_S(\hat{n}_i) = \left(1 - \frac{\hat{n}_i}{2S}\right)^{\frac{1}{2}} = 1 - \frac{\hat{n}_i}{4S} - \frac{\hat{n}_i^2}{32S^2} - \cdots. \tag{4.3}$$

A similar transformation applies for sublattice j. In the *non-interacting* or *linear* spin-wave approximation, only terms up to second order in the boson operators are retained, which corresponds to taking $f_S(\hat{n}_i) = 1$ in Eq. (4.3). The resulting quadratic Hamiltonian can then be diagonalized by a Fourier transformation and a successive canonical transformation, and the ground state energy is given by $E_{gs}^0 = -dNJS(S + \zeta)$. In 2D, for a square lattice and $S = 1/2$, one has $\zeta \simeq 0.158$ so that $E_{gs}^0 \simeq -0.658NJ$. One can normally account for simple boson interactions by retaining the term of $O(1/2S)$ in the expansion of $f_S(\hat{n}_i)$ [171]. The ground-state energy to this

order is given by $E_{gs}^1 = E_{gs}^0 - NJ\zeta^2/2$. For large enough S, the ground state energy converges, since the higher-order corrections are relatively small. But even in the extreme quantum limit of $S = 1/2$, where $E_{gs}^1 \simeq -0.671NJ$, there still could be convergence if the $\hat{n}_i$ in Eq. (4.3) are small, or, more accurately, if $\epsilon \equiv \frac{1}{N}\sum_{\vec{k}} \langle n_{\vec{k}} \rangle \ll 1$. In the case of a square lattice and S = 1/2, one obtains $\epsilon \simeq 0.197$. Since this is a fairly small value, linear SWT therefore predicts that the Néel state is at least a local minimum in configuration space.

In linear SWT, the spin-wave velocity c is given by

$$c = Z_c(S)\, c_0 = \left[1 + \frac{\zeta}{2S} + O\left(\frac{1}{2S}\right)^2\right] c_0\,, \tag{4.4}$$

where $c_0 = 2^{3/2} aJS$ is the bare spin-wave velocity in the non-interacting (classical) approximation. Similarly, the uniform magnetic susceptibility $\chi_\perp$ in the direction perpendicular to the staggered magnetization is given by

$$\chi_\perp = Z_{\chi_\perp}(S)\, \chi_{\perp,0} = \left[1 - \frac{\zeta + 2\epsilon}{2S} + O\left(\frac{1}{2S}\right)^2\right] \chi_{\perp,0}\,, \tag{4.5}$$

where $\chi_{\perp,0} = 1/(8J)$.

The spin-stiffness ρ_s, a measure of the energy required to twist the moment away from its staggered direction, is defined as

$$\rho_s \equiv c^2 \chi_\perp = JS^2 Z_\rho(S). \tag{4.6}$$

The renormalization factors $Z_c(S)$, $Z_\chi(S)$, and $Z_\rho(S) \equiv Z_c^2(S) Z_\chi(S)$, reflect the effect of quantum fluctuations in the Néel state. In the classical limit ($S \to \infty$), they all approach unity. Finally, linear SWT predicts that the ground-state expectation value of the staggered magnetization is reduced from its classical value $M_s = S$ to

$$M_s = S - \epsilon + O\left(\frac{1}{2S}\right)^2. \tag{4.7}$$

The ordered moment for the S = 1/2 2DSLQHA is therefore predicted to be

$gM_s \simeq 0.606\ \mu_B$ within linear SWT, in good agreement with experimental results for La_2CuO_4 [172].

More recently, SWT has been developed to higher order. Igarashi [173] and Hamer et al. [174] have obtained the $O(2S)^{-2}$ and $O(2S)^{-3}$ correction terms, respectively. The higher order corrections are indeed found to be rather small. In Table 4.1, the result by Hamer et al. [174] for both $Z_\rho(S)$ and $Z_c(S)$ is given for spin values $1/2 \leq S \leq 5/2$.

It is important to realize that the $T = 0$ SWT results can not serve as a proof for the existence of an ordered ground state in 2D since, after all, SWT is based on the assumption of the presence of antiferromagnetic long-range order. However, more elaborate theoretical and computational work is in qualitative agreement with $T = 0$ SWT. Hamer et al. [174] have also used series expansion techniques for the Heisenberg-Ising model for both $S = 1/2$ and $S = 1$ and obtained very good agreement with SWT. Another approach has been that by Wiese and Ying [175], who carried out a Monte Carlo study of the $S = 1/2$ 2DSLQHA. They employed the finite-size and finite-temperature relations by Hasenfratz and Niedermayer [57] for the quantum non-linear sigma model (QNLσM), and arrived at values for the $S = 1/2$ quantum renormalization factors consistent with those obtained from SWT and series expansion. For later reference, the quantum renormalization factors for the spin stiffness and spin-wave velocity as predicted by the latter two methods are also included in Table 4.1. Both $Z_\rho(S)$ and $Z_c(S)$ are required input parameters for the finite-temperature theories of the 2DSLQHA discussed in the next Section. For a quantitative comparison with neutron scattering experiments, it is furthermore necessary to know the superexchange J of the material studied.

Finally, for the analysis of the Monte Carlo results in Chapter 5 the $S = 1/2$ value for M_s will be needed. All three theoretical approaches give $M_s \simeq 0.307$, in very good agreement with linear SWT (Monte Carlo [175]: $M_s = 0.3074(4)$, analytic expansion around the Ising limit [176]: $M_s = 0.307(1)$, and SWT to order $O(2S)^{-2}$ [173]: $M_s = 0.3069$).

	Spin-Wave Theory		Series Expansion		Monte Carlo	
S	Z_ρ	Z_c	Z_ρ	Z_c	Z_ρ	Z_c
1/2	0.69864	1.17947	0.728(20)	1.170(8)	0.744(16)	1.188(7)
1	0.86900	1.08435	0.872(4)	1.0839(2)	-	-
3/2	0.91611	1.05504	-	-	-	-
2	0.93824	1.04083	-	-	-	-
5/2	0.95111	1.03245	-	-	-	-

Table 4.1: Theoretical predictions for the quantum renormalization of spin stiffness and spin-wave velocity. Note, that $Z_\rho = Z_c = 1$ in the classical limit.

4.2.2 Finite-Temperature Theories

As a result of the Hohenberg-Mermin-Wagner theorem, one has at least to modify SWT in order to study the finite-temperature properties of the 2D model. Microscopic approaches [177, 178, 179, 180] similar to SWT correctly predict the exponential temperature dependence of the magnetic correlation length:

$$\xi = \frac{a\,S\,c}{T} exp\left(\frac{2\pi\rho_S}{T}\right)\left[1 + O(T^2)\right]. \tag{4.8}$$

However, more accurate calculations discussed below reveal that the exponential prefactor is independent of temperature.

A different approach has been that by CHN [55, 56], who pursued a renormalization-group study of the QNLσM, an effective continuum field theory which correctly reproduces the low-energy, long-wavelength behavior of the 2DSLQHA. To one-loop order their result for the correlation length agrees with Eq. (4.8) [55]. However, an improved two-loop order calculation gave [56]

$$\xi = 0.24(7)\,\frac{c}{2\pi\rho_s}\,exp\left(\frac{2\pi\rho_s}{T}\right)\left[1 + O\left(\frac{T}{2\pi\rho_s}\right)\right]. \tag{4.9}$$

Since the pioneering work of CHN and THC provides a comprehensive theory of the low-temperature *static and dynamic* behavior of the 2D SLQHA, it is appropriate to review the main features of their theory. CHN argue that the nearest neighbor (NN)

quantum Heisenberg Hamiltonian Eq. (4.1) can be described by a quantum non-linear sigma model (QNLσM). At low temperatures, the latter is the simplest continuum model with the same symmetry, spin-wave spectrum, and spin-wave interactions as the Heisenberg antiferromagnet. The effective Euclidean action of the d-dimensional QNLσM is given by

$$S_{eff} = \frac{\rho_s^0}{2c_0\Lambda^{d-1}} \int^{c_0\Lambda/T} du \int d^d y \left(|\nabla_y \hat{\Omega}|^2 + |\frac{\partial \hat{\Omega}}{\partial u}|^2 \right), \tag{4.10}$$

where $\hat{\Omega}$ is a three-component unit vector field. The two parameters of this model are the spin-stiffness constant ρ_s^0 and the spin-wave velocity c_0, both defined on the microscopic scale Λ^{-1}. The above action is formally equivalent to a (d+1)-dimensional *classical* NLσM with reduced space and time dimensions $y = \Lambda x$ and $u = \Lambda c_0 \tau$, respectively. The additional imaginary time dimension u, which reflects the effect of quantum fluctuations, has a thickness inversely proportional to the temperature T.

In the classical limit ($S \to \infty$), the microscopic parameters ρ_s^0 and c_0 were related by Haldane [148, 149] to the parameters of the Heisenberg model: $\rho_s^0 = JS^2a^{2-d}$ and $c_0 = 2d^{1/2}JSa$, where a is the NN separation. A theoretical model is required to relate these parameters to their macroscopic counterparts ρ_s and c. The latter are the zero-temperature long-wavelength properties of the system, renormalized by quantum fluctuations. This issue has been discussed in Chapter 4.2.1, and the quantum renormalization factors predicted by several methods are given in Table 4-1.

At $T = 0$, the QNLσM is described by the dimensionless coupling constant

$$g_0 = \frac{c_0\Lambda^{d-1}}{\rho_s^0} \sim \frac{1}{S}, \tag{4.11}$$

which plays the role of $1/zS$ in SWT. In 2D, CHN's one-loop renormalization group analysis of the equilibrium properties of the QNLσM yields an interesting phase diagram with a nontrivial fixed point $g_c = 4\pi$ at $T = 0$. As shown in Fig. 4-1, one can identify three distinct regimes in parameter space. Defining $\bar{g} = g/g_c$ and $\bar{t} = T/2\pi\rho_s$, a *quantum disordered* (QD) region exists for $\bar{g} > 1 + \bar{t}^{\,1/\nu_3}$. The exponent

$\nu_3 = \nu_{d+1}$ obtained from the one-loop analysis is $\nu_3 = 1$ but should, more accurately, be the same as that of the 3D Heisenberg model, namely $\nu_3 = 0.70$. It is only in this

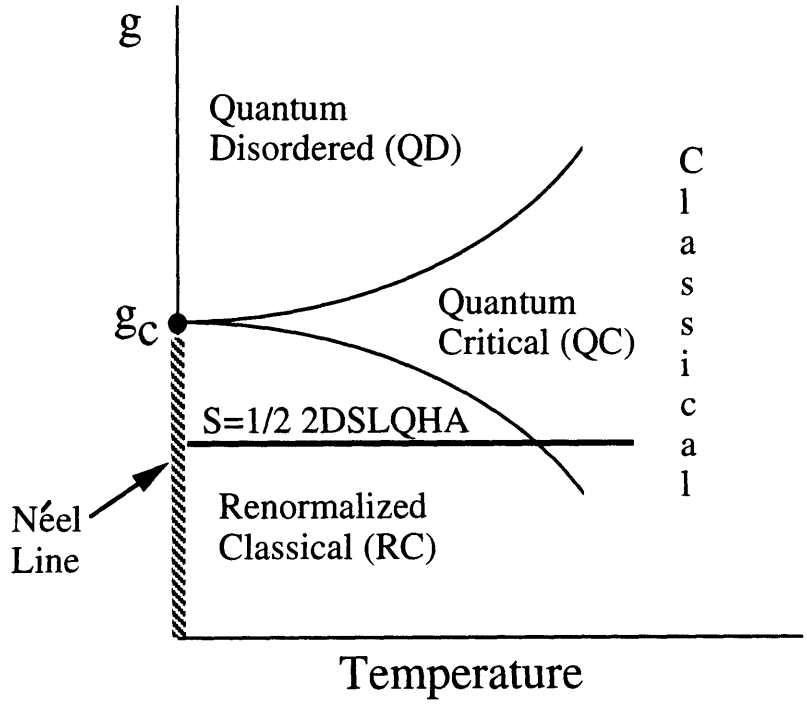

Figure 4-1: Phase diagram of the quantum non-linear sigma model (QNLσM).

regime that there is a gap (with energy $c/\xi(0) \sim (\bar{g}-1)^{\nu_3}$) in the excitation spectrum and that the correlation length remains finite at $T = 0$. In the *quantum critical* (QC) region, $1 + \bar{t}^{\,1/\nu_3} > \bar{g} > 1 - \bar{t}^{\,1/\nu_3}$, the correlation length is given by

$$\xi = C_{QC} \frac{c}{T - T_\rho}. \tag{4.12}$$

The universal constant C_{QC} was determined by CHN to be 1.1 to one-loop order. More accurate Monte Carlo renormalization group calculations yield $C_{QC} = 0.8$ [181, 182, 183]. At the quantum critical point ($g = g_c$ and $T = 0$), where $\rho_s = 0$, one has $T_\rho = 0$, and generally $T_\rho \geq 0$ [184, 185].

CHN predict that even in the extreme quantum limit of $S = 1/2$, the NN 2DSLQHA should lie in the *renormalized classical* (RC) region, $\bar{g} < 1 - \bar{t}^{\,1/\nu_3}$, of the phase diagram. *In this regime the 2DQNLσM maps directly onto the correspond-*

ing 2D classical model, for which it is possible to carry out a two-loop calculation. Their result for the correlation length is given by Eq. (4.9). The numerical prefactor is determined to within 30% accuracy by comparison with existing computer simulations [186].

Further comparison with results for the classical model as well as a scaling ansatz yield, in addition, expressions for the static and dynamic structure factors for the staggered magnetization. At low temperatures, the dynamic scaling hypothesis [187] is believed to be valid. Upon defining the scaling variables $k = q_{2D}\xi$ and $\nu = \omega/\omega_0$, the dynamic structure factor can be written as

$$S(q_{2D},\omega) = \frac{1}{\omega_0} S(q_{2D})\phi(k,\nu), \tag{4.13}$$

where $\phi(k,\nu)$ contains the dynamics and is discussed by THC [163]. The characteristic frequency

$$\omega_0 = \frac{c}{\xi}\left(\frac{T}{2\pi\rho_s}\right)^{\frac{1}{2}} \tag{4.14}$$

is a crossover frequency at which $q_{2D} \simeq \xi^{-1}$. For $q_{2D} < \xi^{-1}$ the excitations are overdamped and for $q_{2D} > \xi^{-1}$ they are weakly damped propagating spin-waves. The static structure factor can be expressed as

$$S(q_{2D}) = S(0)f(q_{2D}\xi) \tag{4.15}$$

with the scaling function

$$f(x) = \frac{1 + \frac{1}{2}B_f ln(1+x^2)}{1+x^2}, \tag{4.16}$$

where $B_f = 1$ to one-loop order. Higher order corrections lower this value, and the Monte Carlo simulations of THC and Makivić and Jarrell [188] yield $B_f = 0.1$ and $B_f = 0.23$, respectively. CHN's renormalization group analysis also predicts the temperature dependence of the $q_{2D} = 0$ instantaneous spin-spin correlation function

to be

$$S(0) = 2\pi Z_3 M_s^2 \left(\frac{T}{2\pi\rho_s}\right)^2 \sim T^2\xi^2, \tag{4.17}$$

where Z_3 is a universal number. As discussed in detail in Chapter 5, there exist several differing theoretical and numerical predictions for the value of Z_3.

In a more recent analytical calculation for the QNLσM, Hasenfratz and Niedermayer (HN) [57] obtained an exact low-temperature expression for the correlation length:

$$\xi/a = \frac{e}{8}\frac{c/a}{2\pi\rho_s} exp\left(\frac{2\pi\rho_s}{T}\right)\left[1 - \frac{1}{2}\left(\frac{T}{2\pi\rho_s}\right) + O\left(\frac{T}{2\pi\rho_s}\right)^2\right]. \tag{4.18}$$

In order to be able to compare the prediction of Eq. (4.18) for the 2DQNLσM with experiments, it is necessary to know ρ_s and c in terms of J. Recent theory and Monte Carlo simulations [173, 188, 175] have determined these relationships rather well. For $S = 1/2$, one has $Z_c = 1.18(1)$ and $2\pi\rho_s = 1.15(2)J$ (see Table 4-1). Substitution of these values into Eq. (4.18) then yields

$$\xi/a = 0.493\, exp\left(\frac{1.15\,J}{T}\right)\left[1 - 0.43\left(\frac{T}{J}\right) + O\left(\frac{T}{J}\right)^2\right]. \tag{4.19}$$

Similarly, the expression for ξ in the QC regime, Eq. (4.12), becomes

$$\xi/a = 1.34\frac{J}{T}\left[1 - \frac{T_\rho}{J}\frac{J}{T}\right]^{-1}. \tag{4.20}$$

4.3 Experiments

4.3.1 $Sr_2CuO_2Cl_2$ (paramagnetic phase)

In this Section energy-integrating two-axis measurements of the static structure factor in $Sr_2CuO_2Cl_2$ will be presented. The scattering geometry as well as the cross-section were discussed in Chapter 2. In order to optimize the momentum resolution, the tightest collimation configuration accessible, $10' - 10' - S - 10'$, was chosen for scans with $E_i = 5, 14.7$, and 30.5 meV. For scans with $E_i = 41$ meV, the first collimator was changed to $20'$ in order to increase the signal. A temperature and momentum inde-

pendent background was observed, largely due to Cl nuclear incoherent scattering (see also Appendix A.) The main concern in an energy-integrating neutron measurement is that E_i must be large enough for the experiment to integrate properly over the relevant dynamic fluctuations. Within CHN' s theory, the characteristic frequency ω_0 of the spin system scales inversely with ξ (Eq. (4.14)). Consequently, progressively larger neutron energies were used at higher temperatures. This procedure allowed to explicitly verify that $\xi = \kappa^{-1}$ was measured correctly. Figs. 4-2 and 4-3 show representative two-axis scans at various temperatures for $E_i = 14.7$ meV and $E_i = 41$ meV, respectively. According to CHN the static structure factor should be a modified Lorentzian, Eqs. (4.15)-(4.16). However, the logarithmic correction term only enters in the large-q_{2D} tails where the signal-to-background ratio is poor. Accordingly, the data analysis was carried out with the simpler Lorentzian form

$$S(q_{2D}) = \frac{S(0)}{(1 + \xi^2 q_{2D}^2)}, \tag{4.21}$$

which corresponds to $B_f = 0$ in Eq. (4-16), convoluted with the experimental resolution function. Clearly, the 2D Lorentzian form describes the measured profiles of Figs. 4-2 and 4-3 quite well. The result of the analysis for the inverse magnetic correlation length κ is shown in Fig. 4-4. As explained in Chapter 2, various necessary approximations are made in an energy-integrating neutron scattering experiment. In order to check for consistency, the neutron cross section was numerically integrated using the dynamic structure factor of THC [163], Eq. (4.13). The result of this simulation is indicated by the dashed lines in Figs. 4-2 and 4-3. The only noticeable difference between theory and experiment arises from a gradual cutoff in the energy integration which occurs above $\sim$ 400 K and $\sim$ 470 K for $E_i = 14.7$ meV and 41 meV, respectively. However, since it is only the large-q_{2D} part of the spectrum that is cut off, the effect on the width κ and especially on the peak intensity $S(0)$ is small. This is unambiguously demonstrated by the fact that the overlapping values of κ in Fig. 4-4, which are obtained using different values of the incoming neuton energy E_i, agree with each other to well within the combined experimental errors.

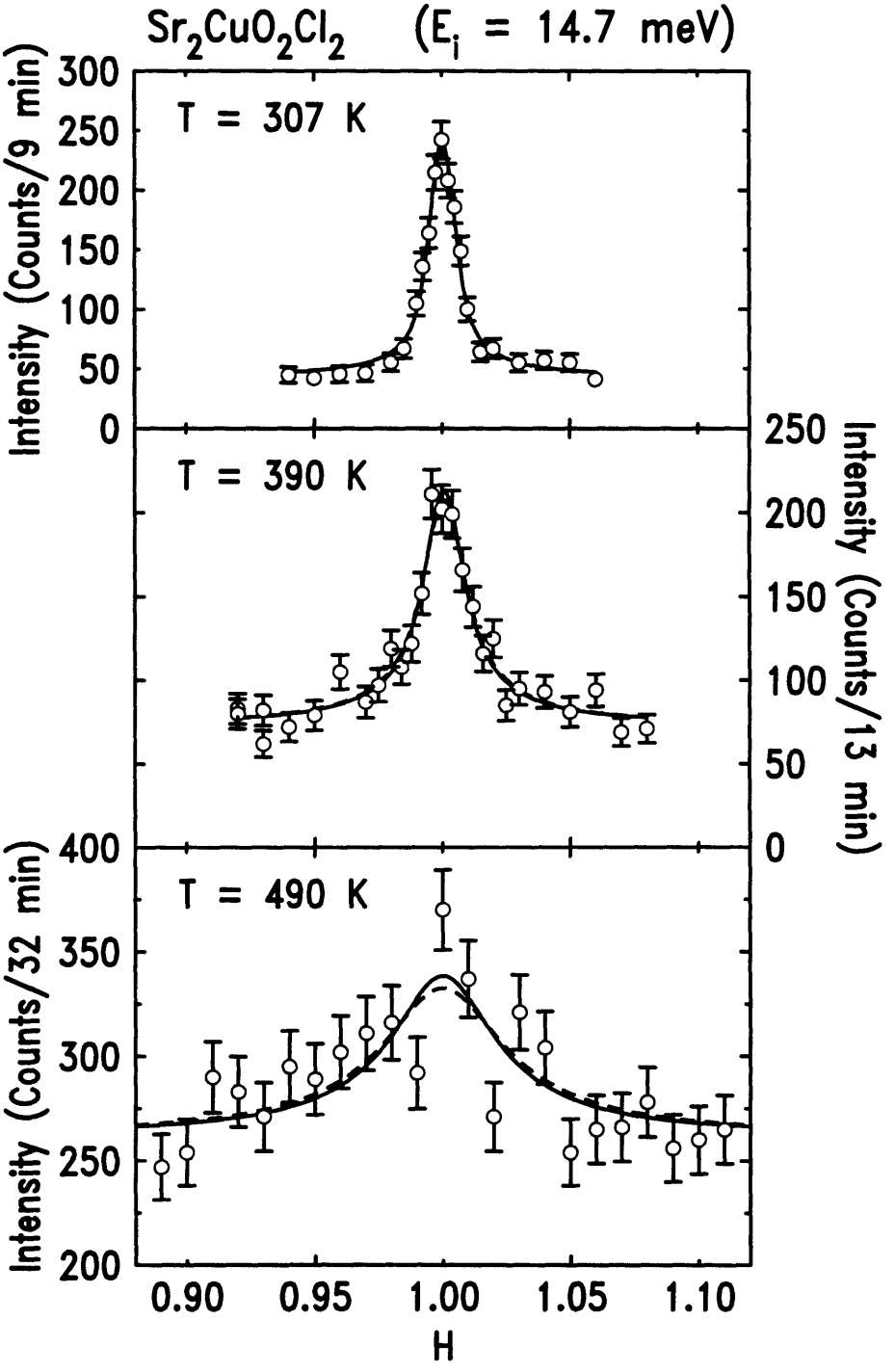

Figure 4-2: Representative energy-integrating two-axis scans for $E_i = 14.7meV$ with collimations $10' - 10' - S - 10'$. The solid line is the result of a fit to a 2D Lorentzian scattering function convoluted with the resolution function of the spectrometer, whereas the dashed line for $490K$ is the result of a simulation of the neutron scattering cross-section, as discussed in the text.

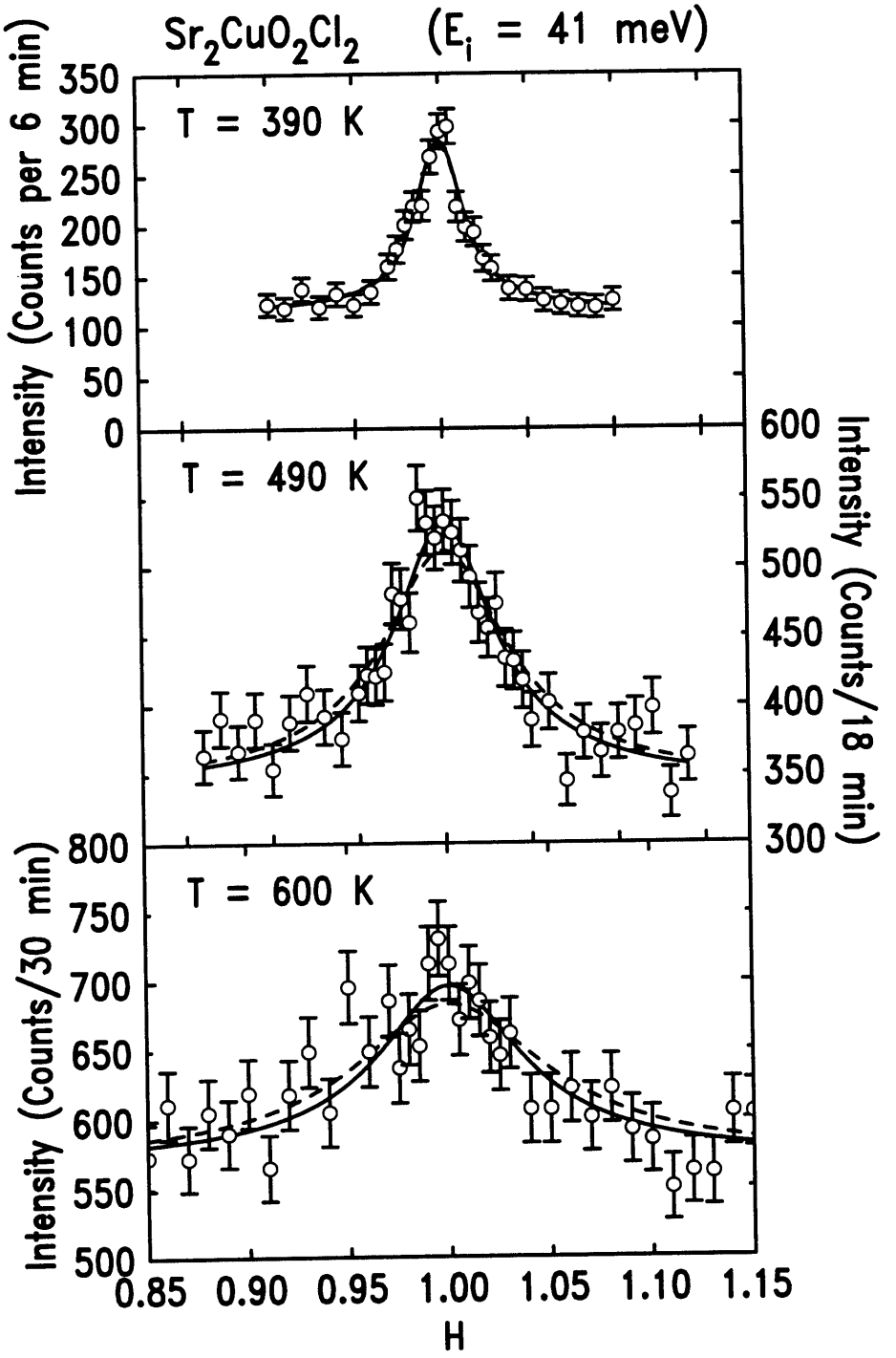

Figure 4-3: Representative energy-integrating two-axis scans for $E_i = 41meV$ and with collimations $20' - 10' - S - 10'$. The solid line is the result of a fit to a 2D Lorentzian scattering function convoluted with the resolution function of the spectrometer, whereas the dashed lines for $490K$ and $600K$ are the result of a simulation of the neutron scattering cross-section, as discussed in the text.

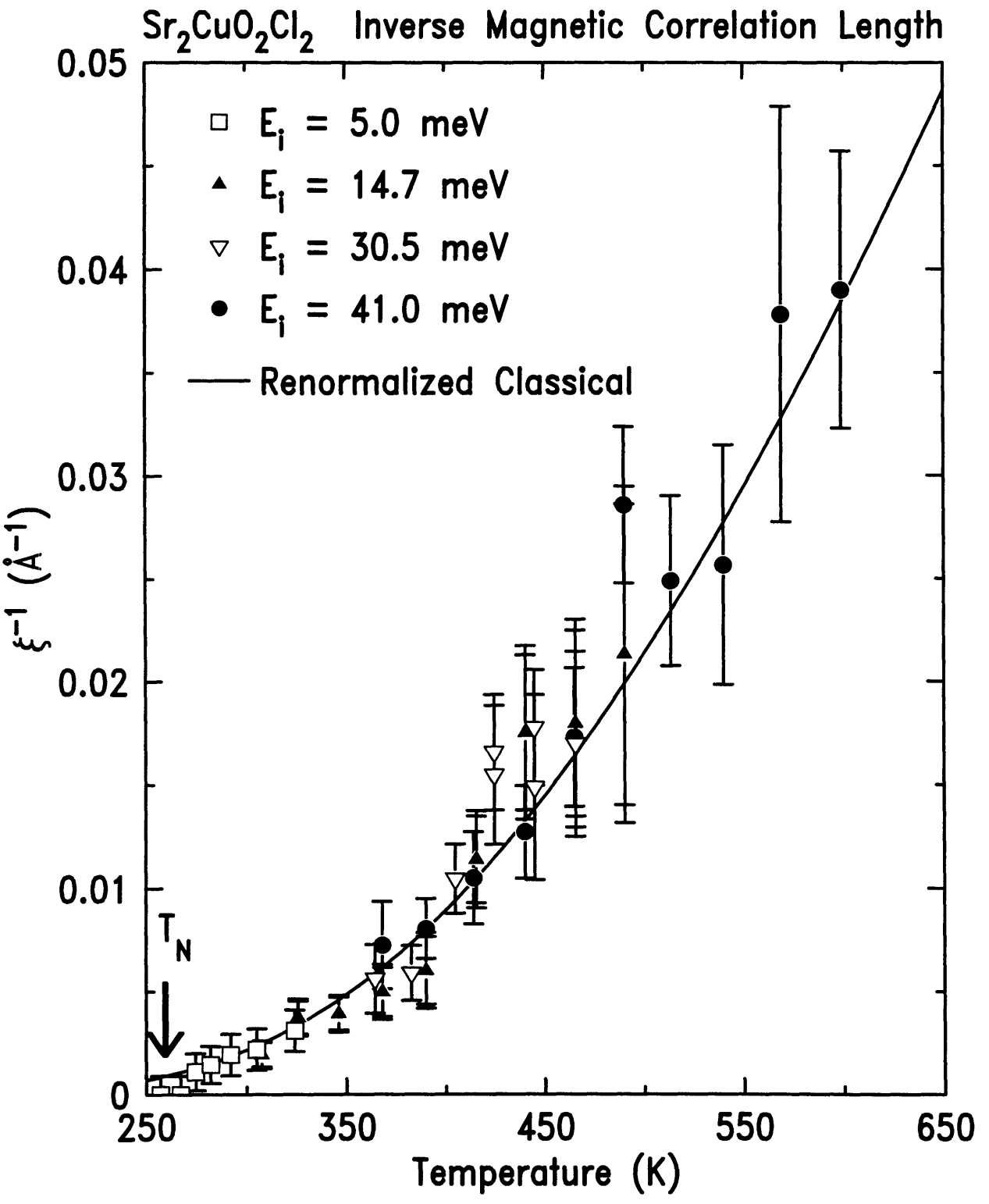

Figure 4-4: Inverse magnetic correlation length of $Sr_2CuO_2Cl_2$. The solid line is Eq. (4.19) with $J = 125meV$.

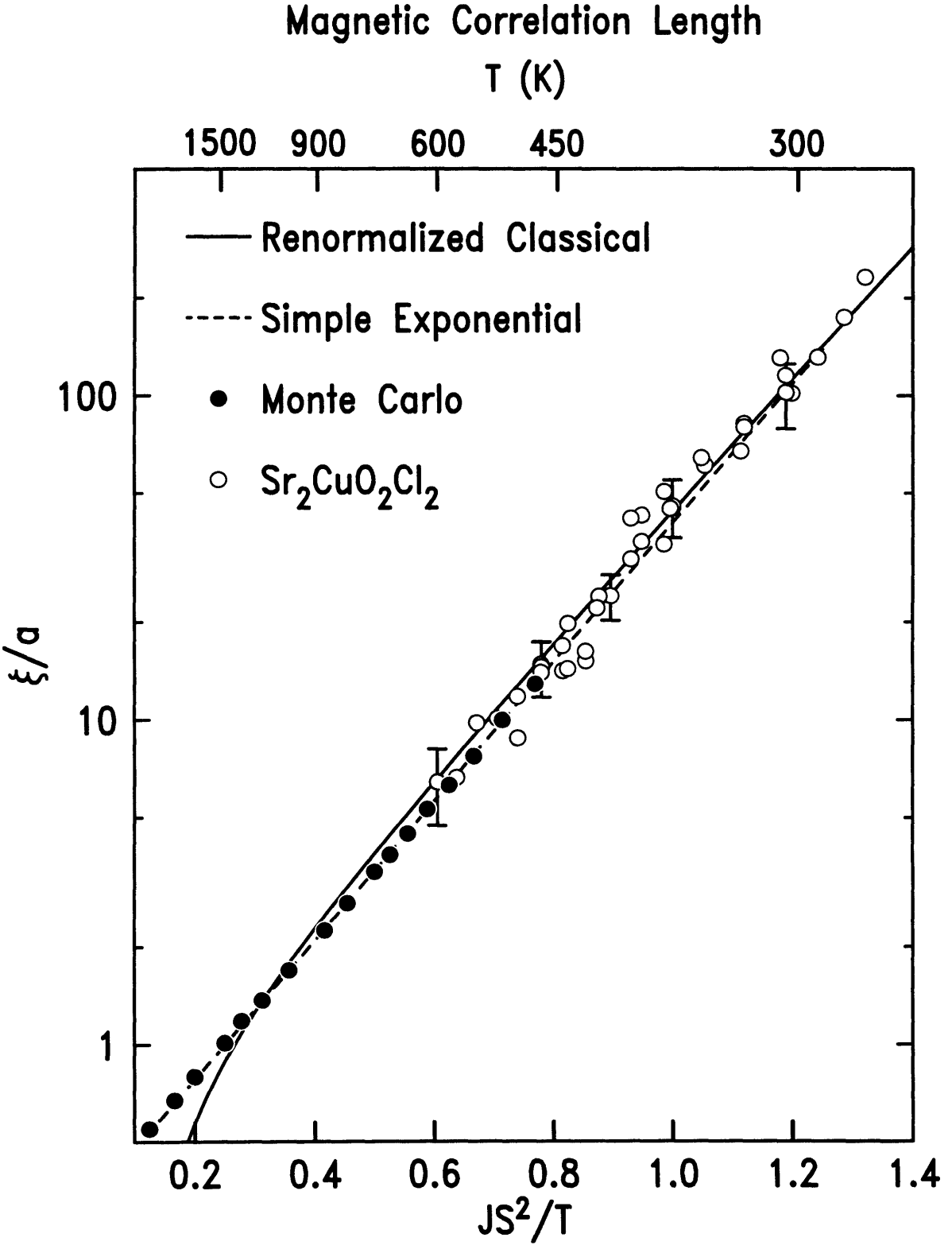

Figure 4-5: The logarithm of the reduced magnetic correlation length ξ/a versus J/S^2T. The open circles are data for $Sr_2CuO_2Cl_2$ plotted with $J = 125meV$ and the filled circles are the result of the Monte Carlo computer simulation described in detail in Chapter 5. The solid line is the RC prediction for the QNLσM.

The data for $Sr_2CuO_2Cl_2$ may be compared without any adjustable parameters with the renormalized classical theory of CHN and HN for the QNLσM. The solid line in Fig. 4-4 corresponds to Eq. (4.19) with the measured value $J = 125$ meV for $Sr_2CuO_2Cl_2$ [1]. Clearly Eq. (4.19) describes the experimental values for $\kappa = \xi^{-1}$ extremely well.

It is also germane to compare the data with the results of the Monte Carlo simulations discussed in Chapter 5. As is evident from Fig. 4-5, there is excellent agreement between the $Sr_2CuO_2Cl_2$ and Monte Carlo results in the region of overlap. Since J for $Sr_2CuO_2Cl_2$ is known, this comparison has no free parameters.

It should be noted, that Monte Carlo simulations for the NN $S = 1/2$ 2DSLQHA on large clusters were first carried out by Ding and Makivić [168, 169]. Their data for ξ agree with those presented in Chapter 5. Moreover, Sokol, Glenister, and Singh [170] have employed series expansion techniques to calculate ξ for the $t-J$ model. At half-filling, which corresponds to the $S = 1/2$ 2DSLQHA, their calculations extend up to correlation lengths of 17 lattice constants and are found to be in quantitative agreement with the Monte Carlo results.

Given the excellent agreement in absolute units in the intermediate temperature region, it is legitimate to view the Monte Carlo result as an extension of the $Sr_2CuO_2Cl_2$ data to higher temperatures. The combined $Sr_2CuO_2Cl_2$-Monte Carlo data in Fig. 4-5, which cover the inverse temperature range $0.2 \leq JS^2/T \leq 1.3$, or equivalently the length scale from ~ 1 to 200 lattice constants, are accurately predicted by renormalized classical theory for the QNLσM. Since Eq. (4.18) is actually the result for the 2DQNLσM rather than the 2DSLQHA, this proves that the isomorphism between the two models is valid down to very short length scales. Of course, at elevated temperatures higher order terms in (T/J) should become important. With appropriately chosen small terms of order $O(T/J)^2$ and $O(T/J)^3$ in Eq. (4.19), the agreement up to $T \sim J$ can be made essentially perfect. An analytical calculation of these terms would clearly be very desirable.

It was recently predicted that the $S = 1/2$ 2DSLQHA may exhibit a crossover from renormalized classical to quantum critical behavior at temperatures as low as

$T \sim 2\rho_S = 0.36J$ [170, 184, 189, 190, 191]. For the correlation length this would imply a crossover from exponential (Eq. (4.19)) to inverse temperature (Eq. (4.20)) behavior. This presumed crossover was claimed to have been observed by Imai et al. [192] in NMR and NQR measurements in La_2CuO_4.

The Monte Carlo data in Fig. 4-4 are described heuristically with the simple exponential

$$\xi/a = 0.290(5)\, exp\left(\frac{1.235(6)\, J}{T}\right), \tag{4.22}$$

which is very close to $\xi/a = 0.276(6)\, e^{1.250(13)J/T}$ as found by Ding and Makivić [168, 169]. The exponential Eq. (4.22), indicated by the dashed line in Fig. 4-4, obviously describes the combined $Sr_2CuO_2Cl_2$-Monte Carlo data very well. Since there is no evidence for a change in the slope of $ln\xi$ vs JS^2/T over the entire range of $0.2 \leq JS^2/T \leq 1.3$, one is led to conclude that there is no evidence for a crossover from renormalized classical to quantum critical behavior in the correlation length data [165]. Of course, if one plots κ vs T above $\sim$ 500 K in a narrow enough temperature range, κ may appear to vary linearly with T. However, the slope C_{QC} (Eq. (4.11)) so-obtained is a factor of $\sim$ 2 larger than the universal quantum critical value of 0.8 [183, 184, 189].

It is quite well established [193] that, analogous to its classical counterpart, the 2D quantum XY model goes through a finite-temperature phase transition of Kosterlitz-Thouless type [194]. Since $\alpha_{XY} >> \alpha_\perp$ for $Sr_2CuO_2Cl_2$, a crossover from 2D Heisenberg to 2D XY behavior is expected which should manifest itself in the characteristic behavior $\xi_{KT} \sim \exp[B/(T - T_{KT})^{1/2}]$ (B is a constant of order J) over an extended temperature range above the vortex unbinding transition. Because of the finite interlayer coupling, the Kosterlitz-Thouless transition will be preempted by a 3D XY transition [195]. At temperatures well above T_N, where $S^{\|}(q_{2D}) \simeq S^{\perp}(q_{2D})$, the correlation length ξ of the 2D Heisenberg model is the only length scale of the system and one can safely fit to the single 2D Lorentzian form of Eq. (4.21). Close to T_N, however, there are two length scales. The in-plane correlation length ξ_{KT} diverges at a finite temperature whereas the out-of-plane correlation length $\xi_\perp$ saturates at a

constant finite value. From Eq. (2.49) and the measured $\alpha_{XY} = 1.4\times10^{-4}$ (see Chapter 2.3.2) one can estimate that this ought to occur for $(\kappa_\perp a)^{-1} = \xi_\perp/a \simeq 85$. As was pointed out in Chapter 2, an energy-integrating neutron scattering experiment measures a superposition of the in-plane and out-of-plane instantaneous correlation functions with about equal weight. For $E_i = 5$ meV, for example, the measured intensity is $I(q_{2D}) \simeq 0.4S^{\parallel}(q_{2D}) + 0.6S^{\perp}(q_{2D})$. Accordingly, one should be able to observe the crossover behavior at temperatures close enough to T_N, where the fits to a single Lorentzian would be dominated by the more strongly diverging length ξ_{KT}. However, as is evident from Fig. 4-4, the data do not indicate a deviation from 2D Heisenberg behavior down to $T \simeq T_N + 18$ K, or equivalently up to $\xi/a = 200$ lattice constants. It has not been possible to extract an intrinsic width κ at temperatures closer to T_N since even for $E_i = 5$ meV the scans were limited by the experimental resolution. In a recent study of the ^{35}Cl nuclear-spin-lattice relaxation rate in $Sr_2CuO_2Cl_2$ [196], the crossover from 2D Heisenberg behavior to a power-law behavior of ξ was observed only below $T_N + 17$ K.

Up to this point, the discussion has focussed on the correlation length which could be compared with the exact result by HN, Eq. (4.18). CHN [55, 56] predict the temperature dependence of the static structure factor peak intensity at low temperatures to be $S(0) \sim T^2\xi^2$ (Eq. (4.17)). The same form was obtained by Kopietz [197] using the Schwinger boson formalism. Figure 4-5 shows the experimental results for $S(0)$, plotted as a function of JS^2/T. The data are for measurements with $E_i = 14.7$ meV and 41 meV, normalized in the region of overlap. These data cover a range of more than two orders of magnitude in $S(0)$ and about a factor of two in T. The dashed line corresponds to the CHN prediction $S(0) \sim T^2\xi^2$, whereas the solid line corresponds to the heuristic result $S(0) \sim \xi^2$. It is evident that the latter form describes the data much better than the former. This is illustrated in Fig. 4-6 in an alternative manner by plotting the Lorentzian amplitude $A = \kappa^2 S(0)$ of Eq. (4.21) versus temperature. Data obtained with 14.7 and 41 meV neutrons are shown, again normalized in the region of overlap. The Lorentzian amplitude is constant to within the errors, whereas the CHN form, $A \sim T^2$, increases by a factor of four over the temperature range of the

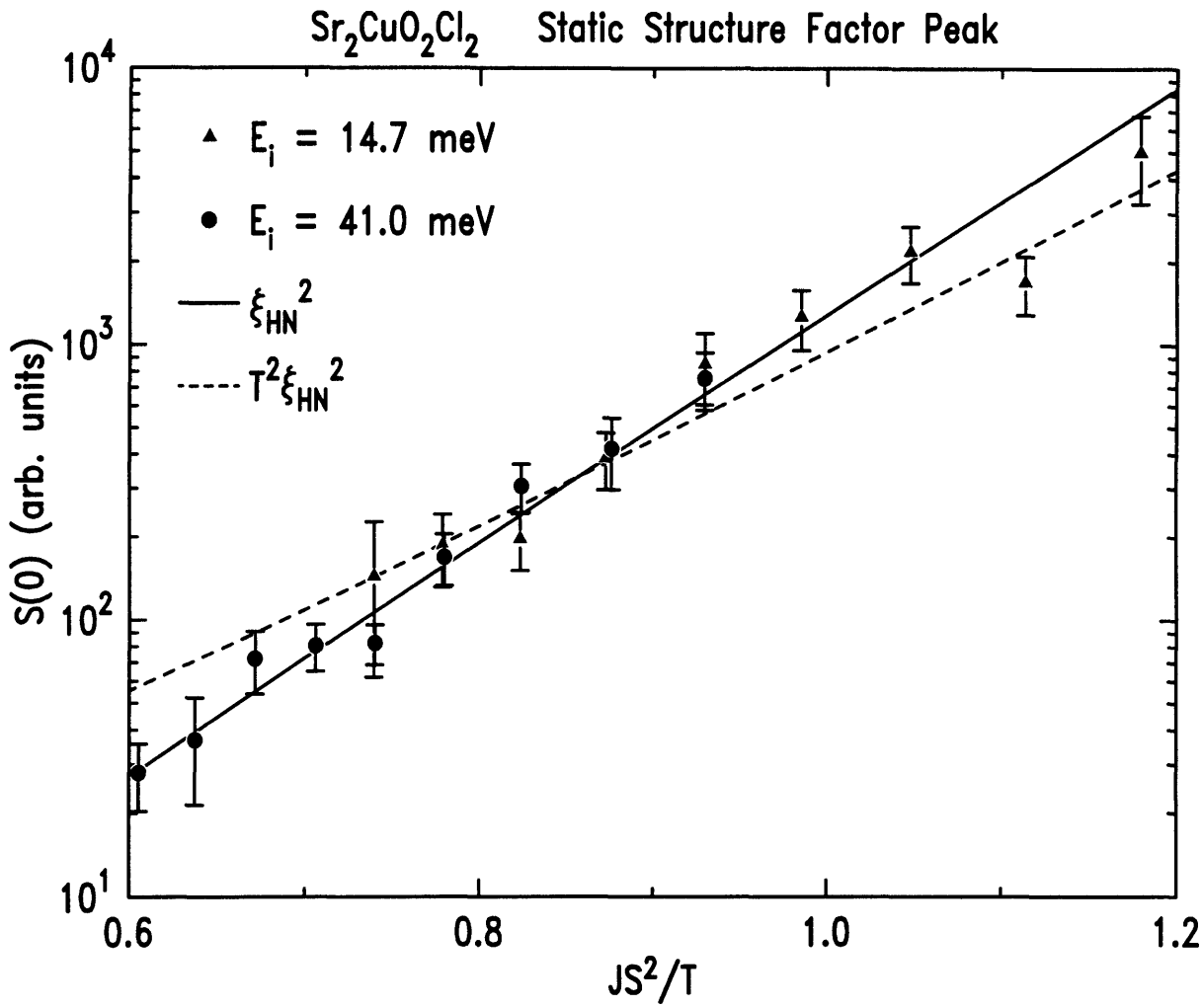

Figure 4-6: Peak intensities $S(0)$ of the 2D Lorentzian fits to the energy-integrating two-axis scans. The solid line refers to the square of the magnetic correlation length given by Eq. (4.19), whereas the dashed line corresponds to the theoretical prediction $S(0) \sim T^2\xi^2$, Eq. (4.17).

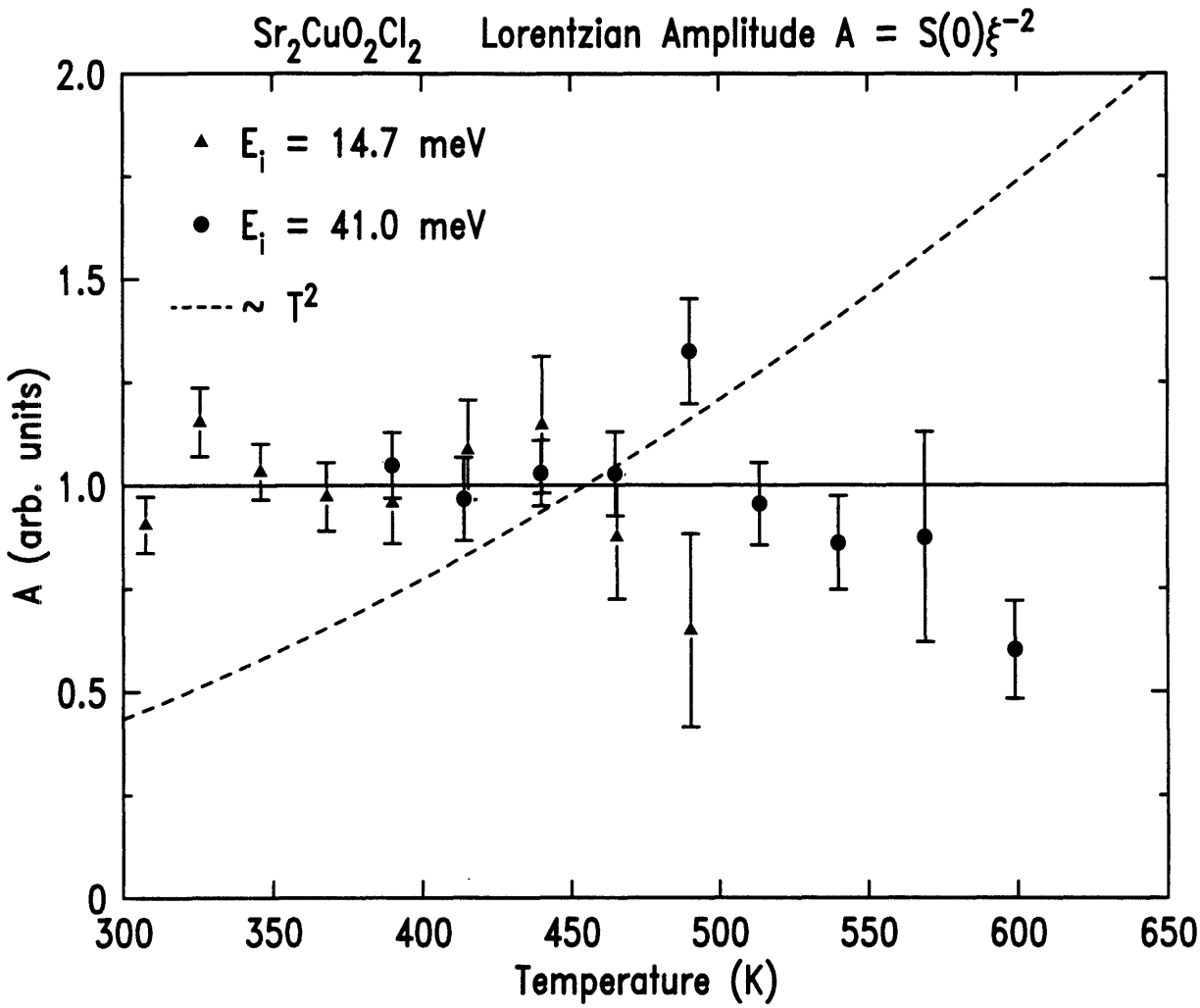

Figure 4-7: Lorentzian amplitude $A = \xi^{-2}S(0)$ for $E_i = 14.7$ and $41meV$, normalized in the region of overlap. The dashed line indicates the behavior $A \sim T^2$ predicted by theory.

measurements. Similar discrepancies are found for $La_{2-x}Sr_xCuO_4$ (Chapter 4.3.2) as well as for the $S = 1$ systems K_2NiF_4 and La_2NiO_4 (Chapter 6). The slight decrease of A at the highest temperatures for both $E_i = 14.7meV$ and $41meV$ can be ascribed to an incomplete integration over the dynamic spectrum at these temperatures.

All of these experiments correspond to the reduced temperature range $0.2 \lesssim T/2\pi\rho_S \lesssim 0.4$. The discrepancy with the CHN-prediction $S(0) \sim T^2\xi^2$ is quite robust. This might seem surprising given the excellent absolute agreement between experiment and theory for the correlation length. At low temperatures, the only relevant spin-wave interactions are at long wavelengths and are properly described by the QNLσM. It is quite possible that the temperature range of the experiment is above the dynamical scaling regime for which the dynamic correlation function is given by Eqs. (4.13)-(4.17). At higher temperatures, contributions from scattering processes involving short-wavelength spin-waves will become important and might alter the temperature dependencies of both $S(0)\xi^{-2}$ and $\omega_0\xi$ [188, 198].

The observed behavior of S(0) is of great importance in the interpretation of some derived quantities such as NMR relaxation rates [199, 192, 200]. Specifically, in recent theories [170, 201, 189] it is assumed that $\chi(0) \sim T\xi^2$ as opposed to the measured $\chi(0) \sim T^{-1}\xi^2$. Based on this erroneous assumption, important implications have been drawn from the measured T-dependences. At the minimum, the NMR experiment must be reconsidered in light of the neutron scattering results for S(0) presented here.

4.3.2 $Sr_2CuO_2Cl_2$ (Néel Ordered Phase)

The sublattice magnetization of $Sr_2CuO_2Cl_2$ has been measured previously in both neutron scattering [26] and muon-spin-rotation [202] experiments. In a fit to their data, the authors of Ref. [26] obtained $\beta = 0.30 \pm 0.02$ for the order parameter exponent. However, neither set of data appears to be precise enough to allow for a reliable determination of the order parameter critical behavior. The sublattice magnetization was therefore measured very carefully, with particular focus on the critical regime. In Fig. 4-8(b), the measured temperature dependence of the (1 0 0) Bragg peak intensity is shown. As mentioned in Chapter 2, this intensity is proportional

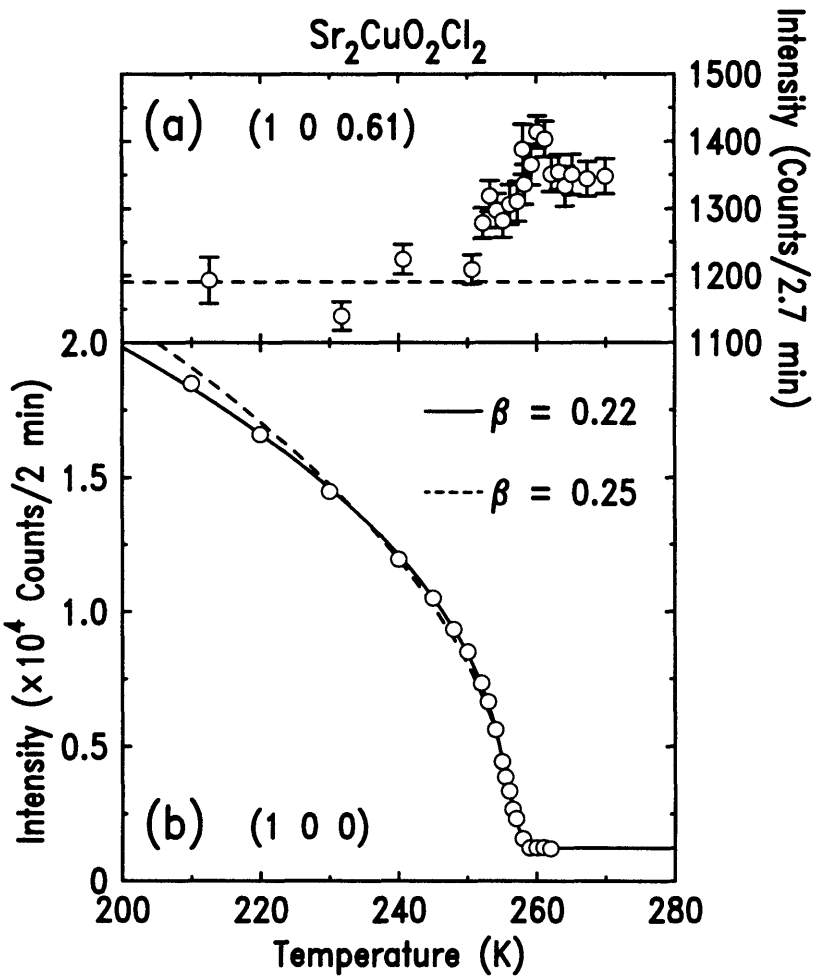

Figure 4-8: Temperature dependence in $Sr_2CuO_2Cl_2$ of (a) the magnetic rod intensity measured in the two-axis mode at (1 0 0.61), and (b) the magnetic order parameter squared in the critical regime. The solid and dashed lines are power laws with a Gaussian distribution of Néel temperatures.

to the square of the ordered moment at the Cu sites. For this measurement, a fixed incident neutron energy of 14.7 meV and collimations $40' - 40' - S - 40' - 80'$ were used. The data were fitted assuming a power law, $I \sim (1 - T/T_N)^{2\beta}$, with a Gaussian spread of Néel temperatures. This fit, shown as a solid line in Fig. 4-8(b), yields $\beta = 0.22 \pm 0.01$ and $T_N = (256.5 \pm 1.5)$ K for the order parameter exponent and the Néel temperature, respectively. The value so-obtained for the order parameter exponent is unusual albeit consistent with that found for other lamellar XY magnets. It might be understood in the context of recent work by Bramwell and Holdsworth [203, 204, 205], who suggest that $\beta = 3\pi^2/128 \simeq 0.23$ is a universal property of the finite-size 2D XY model. Since for $Sr_2CuO_2Cl_2$ the interlayer coupling is extraordinarily small, then concomitantly the 3D critical region should be extremely narrow. As a result, the effective transition temperature T_C, at which ξ_{KT} becomes of the order of $\sqrt{\alpha_\perp}$, is practically equal to T_N. The universal value $\beta \simeq 0.23$ is expected to hold over an extended, but non-universal, temperature regime for length scales less than that characterizing the 2D to 3D crossover region. On the other hand, the value $\beta = 0.22 \pm 0.01$ is rather close to the tricritical value of 0.25. Very recent work by Thio and Aharony [206] suggests that the transition to 3D Néel order in La_2CuO_4 is indeed very close to a tricritical point. For comparison, the fit was repeated with β fixed at 0.25. As can be seen from Fig. 4-8(b), the tricritical value for β describes the data almost as well as the fitted one.

Figure 4-8(a) shows the temperature dependence of the rod intensity, obtained in the two-axis configuration. The incident neutron energy was fixed at 14.7 meV and the collimations were $20' - 40' - S - 20'$. The rod intensity increases slightly as the temperature is lowered towards T_N. At T_N the 2D scattering intensity begins to decrease very rapidly, as the 2D dynamic scattering is converted into 3D Bragg scattering. This behavior is closely similar to that observed in K_2NiF_4 [53], where the 2D Ising nature of the transition leads to a rapid conversion of the nearly elastic rod intensity to the 3D Bragg peak. The transitions to long range order in these two systems are essentially 2D in character with the 3D ordering following parasitically.

In their studies of the system K_2NiF_4, Birgeneau et al. [52, 207, 208] found

empirically that the spin-wave gap energy scales linearly with the order parameter. In order to test if this simple relationship prevails in the case of $Sr_2CuO_2Cl_2$, and also to determine the magnitude of the XY-anisotropy α_{XY} in the spin Hamiltonian, measurements of the XY anisotropy gap were carried out at several temperatures. Energy scans were taken at the (1 0 -0.6)-position, where about 65% of the scattering intensity arises from out-of-plane excitations. At temperatures close to T_N, where the anisotropy gap is small, a spectrometer configuration with a relatively high energy resolution was required. Therefore, neutrons with $5meV$ incident energy were used

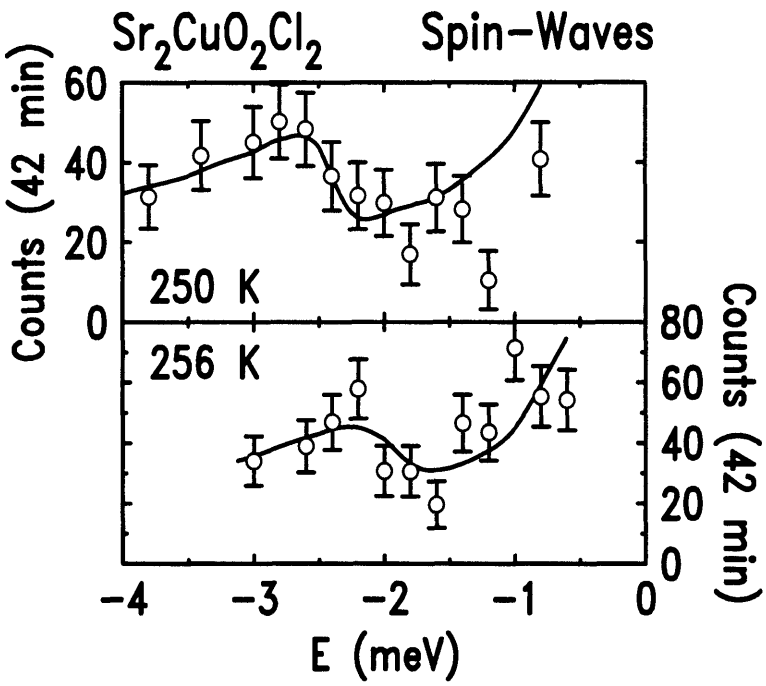

Figure 4-9: Background-subtracted spin-wave spectra for $Sr_2CuO_2Cl_2$ taken at (1 0 -0.6). The spectrometer was set for neutron energy gain, $E_i = 5meV$, and collimations $40' - 40' - S - 80' - 80'$. The solid lines are convolutions of the spin-wave cross-section with the experimental resolution function.

the spectrometer was set for neutron energy loss and the energy resolution was pro-

gressively relaxed at lower temperatures. Representative data with the background subtracted are shown in Fig. 4-10. In the temperature range $200 < T < 250K$, neutrons with $14.7meV$ incident energy and collimations $20' - 40' - S - 40' - 40'$ were used. At even lower temperatures, the final neutron energy was fixed at $14.7meV$ and the collimations were $20' - 40' - S - 20' - 40'$ and $40' - 40' - S - 40' - 40'$ above and below 100 K, respectively. For scans with fixed final neutron energy, the data were corrected for higher order contamination in the monitor. The values of the gap energy were extracted by comparing the measured spectra to convolutions of the cross section Eqs. (2.47)-(2.49) with the experimental resolution function. For excitations with a finite lifetime Γ^{-1}, the delta functions in the cross section have to be replaced by Lorentzians of width Γ. In the computation, this width was fixed at values well below the energy resolution of the spectrometer. The solid lines in Figs. 4-9 and 4-10 are the result of this analysis.

At low temperatures the spin gap is $5.0(3)meV$, which corresponds to an XY anisotropy value of $\alpha_{XY} = 1.4(1) \times 10^{-4}$. Fig. 4-11 displays both the spin-wave gap energy and the order parameter power-law with $\beta = 0.22$. As in the case of K_2NiF_4 [52, 207, 208], the agreement between the two is found to be very good. It is interesting to note that, within experimental error, α_{XY} has the same value for $Sr_2CuO_2Cl_2$ and La_2CuO_4 [49] as well as for the two-layer system $YBa_2Cu_2O_{6.1}$ [209]. This suggests that the XY anisotropy is determined primarily by interactions within the CuO_2 sheets. It has recently been pointed out [39], that this anisotropy may only be explained if both spin-orbit and Coulomb exchange interactions of NN spins in the CuO_2 plane are taken into account. The authors of Ref. [39] estimate that $\alpha_{XY} \simeq 1.5 \times 10^{-4}$, which is in very good agreement with the experimental value. Since the interlayer coupling varies by several orders of magnitude in these materials, the similarity of their ordering temperatures must be mainly attributed to the XY anisotropy [195, 210]. This idea has been explored quantitatively [60] in the framework of Schwinger-boson mean-field theory [177, 178].

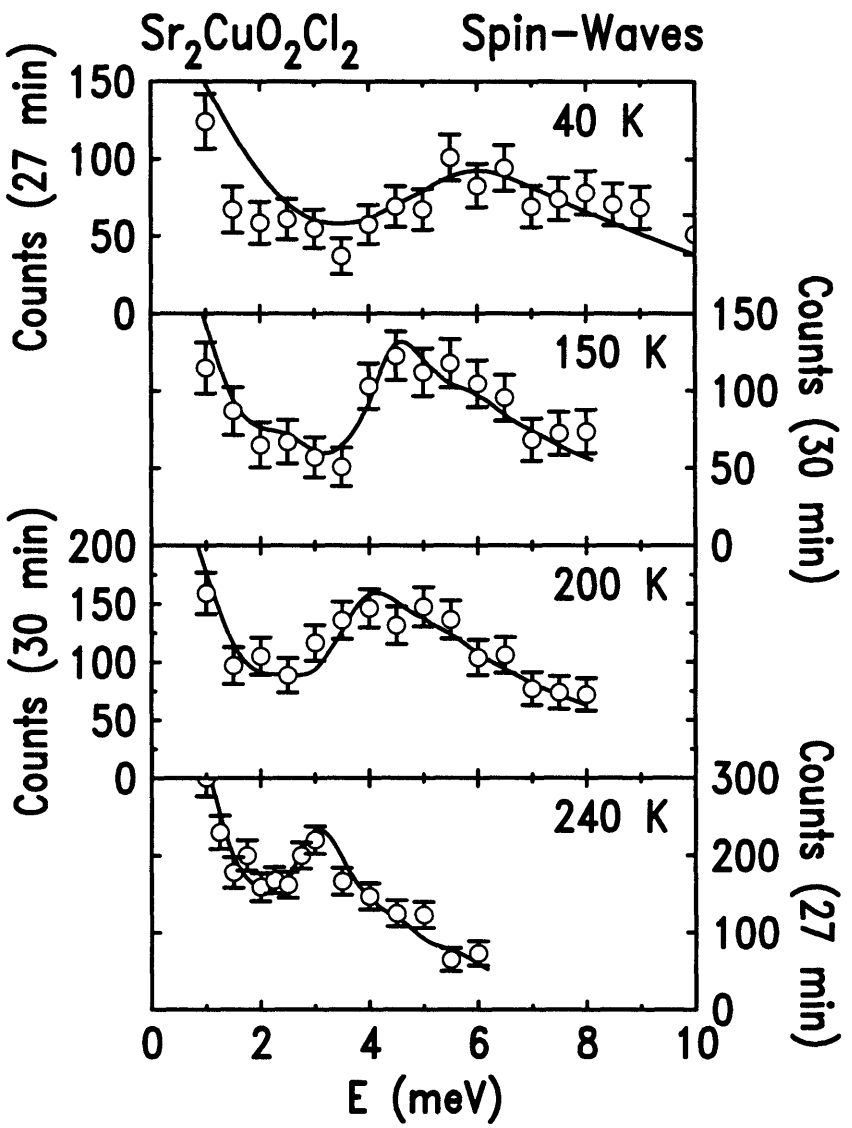

Figure 4-10: Background-subtracted spin-wave spectra for $Sr_2CuO_2Cl_2$ taken at (1 0 -0.6). The spectrometer resolution was progressively relaxed at lower temperatures. The solid lines are convolutions of the spin-wave cross-section with the experimental resolution function.

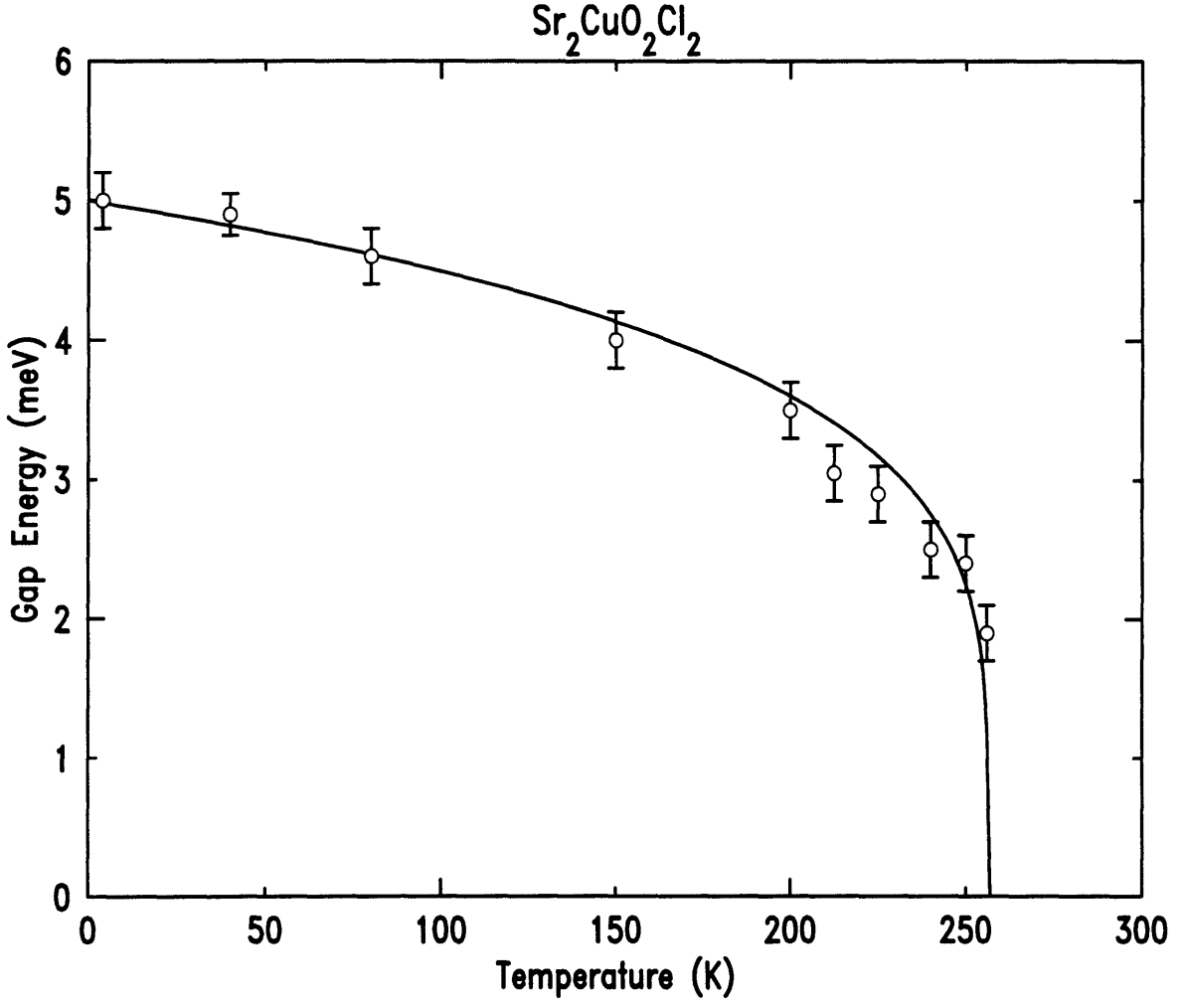

Figure 4-11: Spin-wave gap energy versus temperature for $Sr_2CuO_2Cl_2$. The solid line is a power-law with exponent $\beta = 0.22$, normalized to $5meV$ at $4.2K$.

4.3.3 La_2CuO_4 (paramagnetic phase)

In Chapter 4.3.1 it was shown that the spin-spin correlation length in $Sr_2CuO_2Cl_2$ agrees quantitatively with the results of quantum Monte Carlo simulations for the $S = 1/2$ 2DSLQHA over a wide range of temperatures. The combined $Sr_2CuO_2Cl_2$-Monte Carlo data, which cover the length scale from $\sim$ 1 to 200 lattice constants, are in turn accurately predicted without any adjustable parameters by the CHN-HN theory for the 2DQNLσM. Consequently, there is no evidence for a crossover from RC to QC behavior. This presumed crossover was claimed to have been observed in ^{63}Cu NMR and NQR measurements in La_2CuO_4 [192]. However, while the instantaneous spin-spin correlation length ξ can be obtained *directly* in a neutron scattering experiment, a theoretical model for the dynamic structure factor is required for the interpretation of NMR and NQR relaxation rates. This issue will be discussed now.

The relaxation of nuclear spins coupled to the antiferromagnetic order parameter (e.g., Cu nuclear spins in La_2CuO_4) is given by a *weighted* $\vec{q}$-average of the dynamic structure factor $S(\vec{q},\omega_r)$ at a *fixed* resonance frequency ω_r [211]. Since ω_r is very small ($\omega_r << T$), one has $S(\vec{q},\omega_r) \simeq T/\omega_r \, Im\chi(\vec{q},\omega_r)$. The *nuclear-spin-lattice relaxation rate* $1/T_1$ is given by

$$\frac{1}{T_1} = \frac{2T}{g^2\mu_B^2} \sum_{\vec{q}} A_{||}^2(\vec{q}) \, \frac{Im\chi(\vec{q},\omega_r)}{\omega_r}, \tag{4.23}$$

where $A_{||}(\vec{q})$ is the in-plane component of the form factor (due to the coupling of the nuclear moments to the electronic spin degrees of freedom). Since the resonance frequency ω_r is very small, the limit $\omega_r \rightarrow 0$ can be taken on the right hand side of Eq. (4.23). For the Cu site in the undoped lamellar copper oxides, $A_{||}(\vec{q})$ is peaked at $\vec{q} = 0$. If the fluctuations of the electronic spin system are in the critical region (i.e. if $q << T/c$, where c is the spin-wave velocity), the dominant contribution to $1/T_1$ arises from the $\vec{Q}$-region close to the incipient antiferromagnetic wavevector $\vec{\tau}_m = \vec{Q} - \vec{q}$. In this case, the $\vec{q}$–dependence of $A_{||}(\vec{q})$ can be neglected, and the

temperature dependence of $1/T_1$ is given by [199]

$$\frac{1}{T_1} \sim \frac{1}{\omega_0} \frac{S(0)}{\xi^2}. \tag{4.24}$$

With the scaling relations Eqs. (4.14) and (4.17) by CHN, one therefore expects

$$\frac{1}{T_1} \sim T^{3/2} \xi \tag{4.25}$$

in the RC regime of their theory.

The *Gaussian component of the spin echo decay rate* $1/T_{2G}$ is given by [212]

$$\left(\frac{1}{T_{2G}}\right)^2 = \sum_{\vec{q}} A_\perp^4(\vec{q}) \chi^2(\vec{q}) - \left[\sum_{\vec{q}} A_\perp^2(\vec{q}) \chi(\vec{q})\right]^2, \tag{4.26}$$

where $A_\perp(\vec{q})$ is the form factor in the direction perpendicular to the CuO_2 sheets. At low temperatures (i.e large ξ), the second term in Eq. (4.26) is negligible, and the form factor can again be taken at its $\vec{q} = 0$ value. One then obtains

$$\frac{1}{T_{2G}} \sim \left(\sum_{\vec{q}} \chi^2(\vec{q})\right)^{1/2} \sim \sqrt{S(0)}. \tag{4.27}$$

Deep in the RC regime, this becomes [56, 197]

$$\frac{1}{T_{2G}} \sim T \xi. \tag{4.28}$$

Imai et al. [192, 213] carried out a NQR study of $1/T_1$ and $1/T_{2G}$ in La_2CuO_4 for temperatures between $450K$ and $1000K$. They used the scaling form Eqs. (4.15)-(4.17) to deduce the magnetic correlation length ξ via Eq. (4.26), and argued that ξ exhibits a crossover from RC ($\sim exp(2\pi\rho_s/T)$) to QC behavior ($\sim 1/T$) above $\sim 600K$. This conclusion is in disagreement with the combined neutron scattering and Monte Carlo results presented in Fig. 4-5. While current theory predicts that $S(0) \sim T^2\xi^2$ [55, 56, 197] at low temperatures, the neutron data for $Sr_2CuO_2Cl_2$ were found to follow the simple empirical form $S(0) \sim \xi^2$ for $0.16 < T/(2\pi\rho_s) < 0.36$. This

discrepancy is peculiar, given the fact that for the correlation length experiment and theory were found to agree very well. However, it is possible that the true scaling behavior for $S(0)$ is indeed $S(0) \sim T^2\xi^2$, but is only observable at temperatures $T/(2\pi\rho_s) << 0.16$. Since the quantity $S(0)$ enters the expressions for the NMR and NQR relaxation rates in a fundamental way, it is clear that existing theory must at the minimum be extended to higher temperatures.

The static structure factor in La_2CuO_4 had previously been measured in neutron scattering experiments by Keimer et al. [2] for temperatures in the range $340K \leq T \leq 540K$. While the result for the magnetic correlation length, shown in Fig. 1-6, was in overall agreement with the analytic form Eq. (4.18) by HN, systematic discrepancies comparable in size with the error bars were found. Moreover, the Lorentzian amplitude was found to be best descibed by a linear temperature dependence, albeit with an uncertainty large enough to include both behaviors $A = constant$ and $A \sim T^2$ within the experimental error.

A new series of two-axis experiments in La_2CuO_4 was carried out with the intention of obtaining data with better statistics in the temperature range covered previously [2], and to extend the measurements to higher temperatures to allow for a direct comparison with the NMR results. In order to ensure that the energy integration was carried out correctly at high temperatures, neutrons with incoming energies up to $115meV$ were used. In Figs. 4-12 and 4-13 some representative energy-integrating scans for $E_i = 41meV$ and $E_i = 115meV$ are shown. The collimations were set to $20' - 10' - S - 10'$ in both cases, and for neutrons with $E_i = 41meV$ a pyrolytic graphite filter was used. For $E_i = 115meV$, the experiment was carried out without a filter in order to maximize the neutron flux. Higher order contamination from neutrons with energies above $\sim 400meV$ is not a concern as it results from the high-energy-tail of the thermal neutron spectrum peaked at $\sim 30meV$. The solid lines in Figs. 4-12 and 4-13 are the result of fits to the 2D Lorentzian form Eq. (4.21), convoluted with the resolution function of the spectrometer, and the result of the analysis for the inverse magnetic correlation length is shown in Fig. 4-14. Neutrons with $E_i = 14.7meV$ were used at low temperatures. With increasing temperature, the

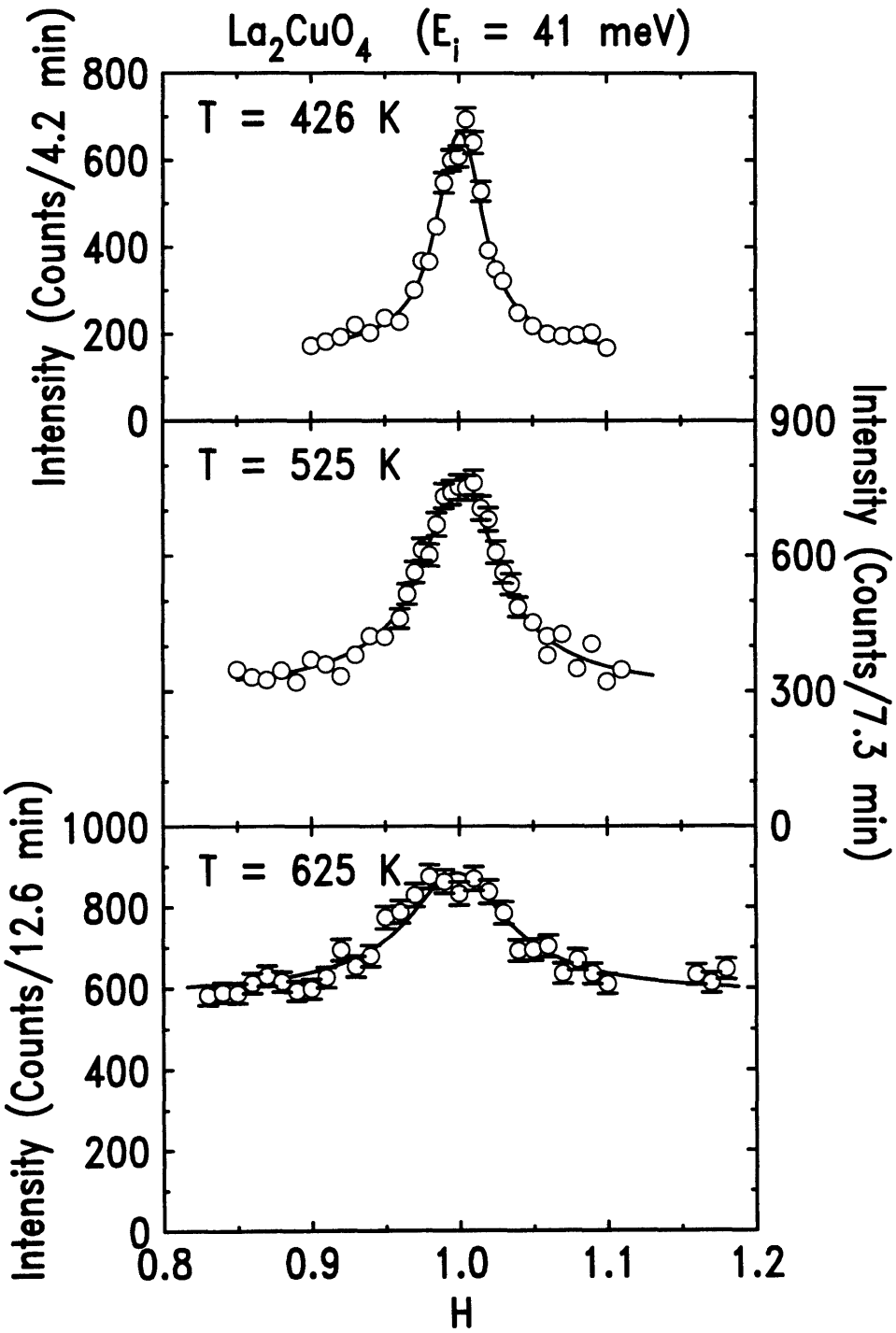

Figure 4-12: Representative energy-integrating two-axis scans in La_2CuO_4 with $E_i = 41meV$ and collimations $20' - 10' - S - 10'$. The solid lines are the result of fits to a 2D Lorentzian scattering function convoluted with the resolution function of the spectrometer.

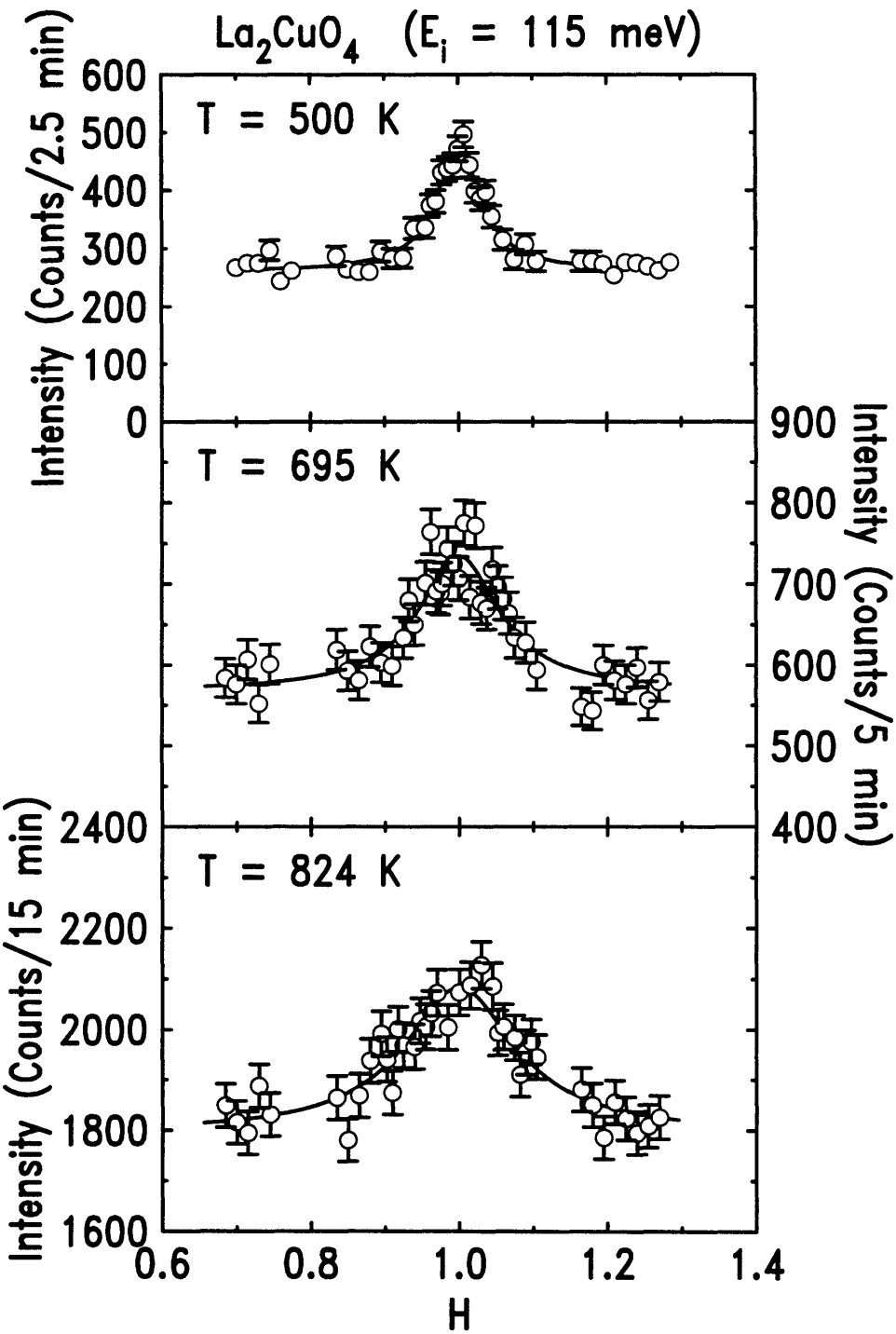

Figure 4-13: Representative energy-integrating two-axis scans in La_2CuO_4 with $E_i = 115meV$ and collimations $20' - 10' - S - 10'$. The solid lines are the result of a fits to a 2D Lorentzian scattering function convoluted with the resolution function of the spectrometer.

neutron energy was progressively raised to $41meV$, $90meV$, and $115meV$, to ensure that the energy integration of the two-axis experiment was carried out correctly. It is evident from Fig. 4-14 that data points in the regions of overlap agree well within the experimental error. Clearly, the RC form Eq. (4.19) describes the La_2CuO_4 data over the entire temperature range $340K \leq T \leq 820K$ very well. Since the superexchange constant is known to be $J = 135meV$ for La_2CuO_4, this comparison is free of adjustable parameters. However, the analytical result by HN is stictly valid only at temperatures for which $(T/2\pi\rho_s)^2 \sim (T/1800K)^2 << 1$. At temperatures above $\sim 600K$, it is therefore more appropriate to compare the neutron data with Monte Carlo results, which are more accurate at higher temperatures. The dashed line in Fig. 4-14 is the empirical exponential from Eq. (4.22). It can be seen that even at the highest temperature of the experiment the agreement with the simulation for the NN $S = 1/2$ SLQHA is excellent.

A subtle discrepancy between the highest temperature data points for $E_i = 41meV$ and the corresponding values obtained with higher-energy neutrons is discernible. Similarly, the data above $T = 700K$ for $E_i = 90meV$ lie slightly below those obtained with $115meV$- neutrons. It is possible that these small deviations indicate that part of the high-energy spectrum is missed at the very highest temperatures for $E_i = 41$ and $90meV$. The characteristic energy ω_0 in the dynamic scaling regime of CHN's theory (Eq. (4.14)) is given in Table 4-2 for several temperatures. Since the spin-wave velocity of La_2CuO_4 is known to be $c = 850meV\mathring{A}$ [35], one has

$$\omega_0^{CHN} \simeq \frac{850meV\mathring{A}}{\xi}\sqrt{\frac{T}{1800K}}. \tag{4.29}$$

The form for the characteristic energy as determined by CHN is believed to be valid only in the low-temperature ($T << 2\pi\rho_s$) and long-wavelength ($q_{2D} << T/c$) limit. At intermediate and high temperatures, Monte Carlo simulations are expected to be more reliable. Also given in Table 4-2 is therefore the result obtained by Makivić and Jarrell in a Monte Carlo study of the $S = 1/2$ NN 2DSLQHA [188]. Their work, which spans the temperature range $0.35J < T < 0.50J$ (which for La_2CuO_4 translates

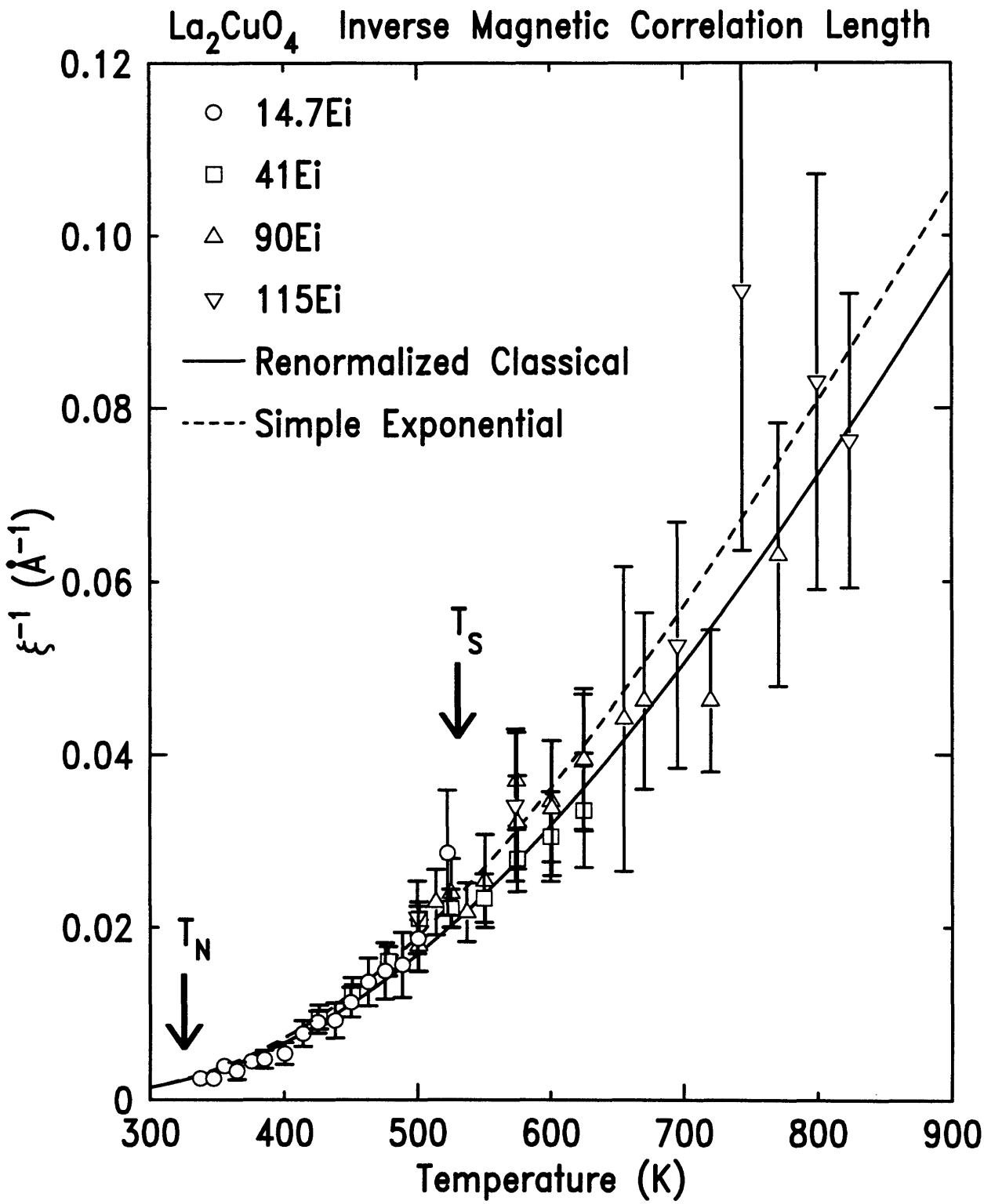

Figure 4-14: Inverse magnetic correlation length of La_2CuO_4. The solid line is Eq. (4.19) with $J = 135meV$ and the dashed line is Eq. (4.22). The Néel and structural transition temperatures are indicated by arrows.

T (K)	$\omega_0^{CHN}(meV)$	$\omega_0^{MJ}(meV)$
350	0.8	-
450	4.3	-
550	12.5	25
600	17	33
700	28	51
800	45	63

Table 4.2: Characteristic energy ω_0 at some selected temperatures for $J = 135meV$. The values ω_0^{CHN} are calculated from Eq. (4.29), determined by CHN [56], while the values ω_0^{MJ} are those obtained by Makivić and Jarrell [188].

into $500K \lesssim T \lesssim 800K$), is consistent with CHN's scaling form for the dynamic structure factor Eqs. (4.13)-(4.17). The scaling energy ω_0, however, was found to have a different temperature dependence: for $0.30 \leq T/J \leq 0.40$, they obtained $\omega_0 \xi = 1.81Ja$. The behavior $\omega_0 \xi = constant$ has also been found in Schwinger Boson Mean Field Theory [177, 178] and modified SWT [214, 215]. At higher temperatures, Makivić and Jarrell found that $\omega_0\xi$ decreases (similar to the *classical* Heisenberg model [216]), being $\omega_0\xi = 1.51Ja$ at $T = 0.50J$.

The values of ω_0 in Table 4.2, in conjunction with the observations made for the experimental data, imply that the energy integration is only carried out properly if $E_i > 2\omega_0$. This rule-of-thumb is fully consistent with the observations made for $Sr_2CuO_2Cl_2$ in the previous Section. Note, that in order for Table 4.2 to apply to $Sr_2CuO_2Cl_2$, the temperature values have to be scaled by a factor 125/135 (the ratio of the superexchange in the two $S = 1/2$ materials).

In Fig. 4-15, the logarithm of the correlation length is plotted versus JS^2/T. Now, the actual Monte-Carlo data are included, and for clarity only representative error bars are given. This Figure is the analog to Fig. 4-5 for $Sr_2CuO_2Cl_2$, and again no sign of a crossover to QC behavior is observed. The QC form Eq. (4-20) is explicitly included in Fig. 4-15. While the RC and simple exponential curves have no adjustable parameters, $T_\rho = 200K$ was chosen for the QC curve so as to obtain a fit in the middle of the claimed "quantum critical region". There is clearly no evidence

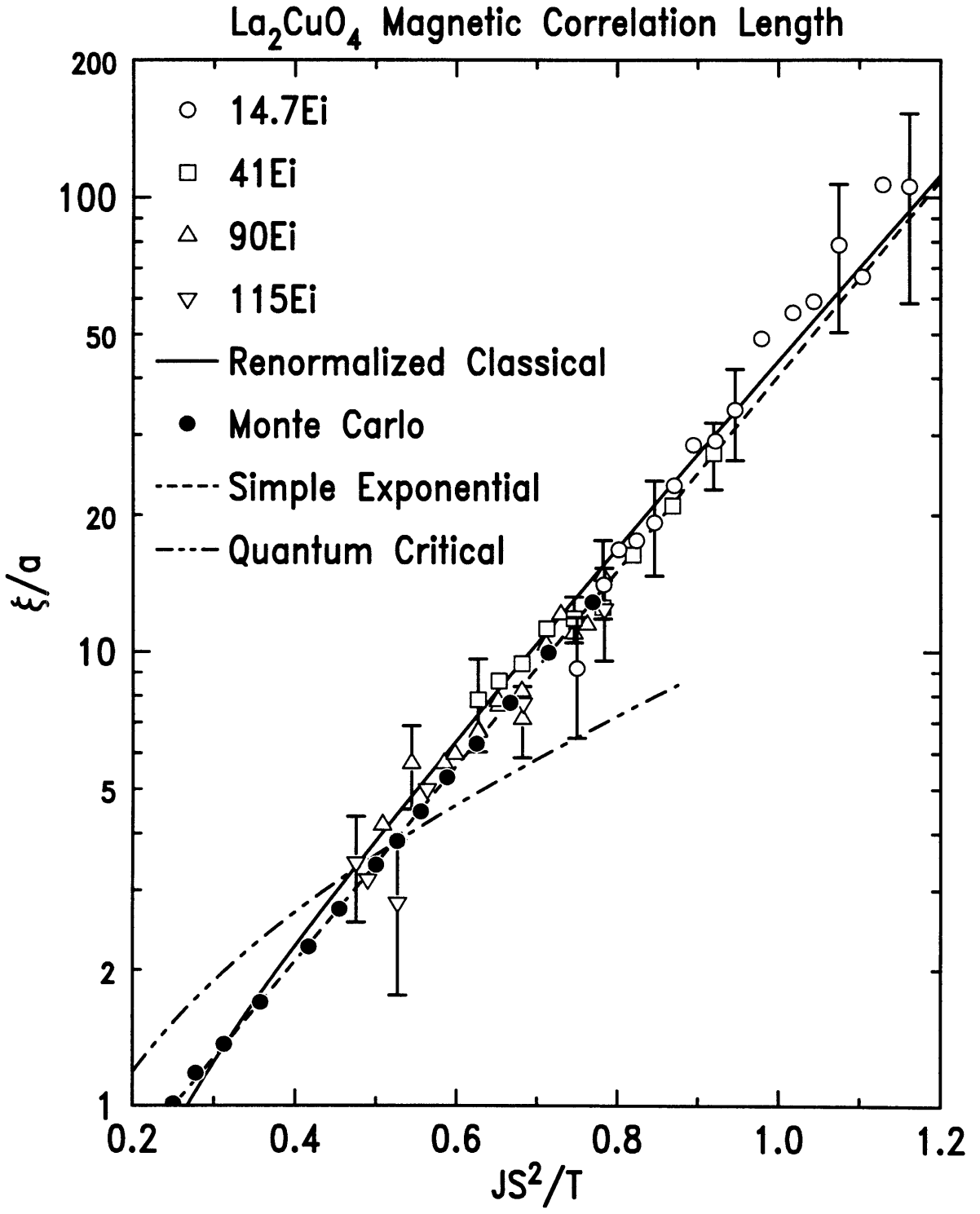

Figure 4-15: The logarithm of the reduced magnetic correlation length ξ/a versus J/S^2T. The open symbols are data for La_2CuO_4 plotted with $J = 135meV$, while the filled circles are the result of the Monte Carlo computer simulations described in Chapter 5. The various lines indicate the theoretical predictions of the 2DQNLσM for the renormalized classical (Eq. (4.19)) and quantum critical regimes (Eq. (4.20)), as well as the simple exponential form Eq. (4.22).

for a crossover from RC to QC behavior above $600K$ in La_2CuO_4.

The Lorentzian amplitude $A = \kappa^2 S(0)$ is shown in Fig. 4-16 for $E_i = 14.7$ and $41meV$. Since this amplitude can only be obtained in relative units in a neutron

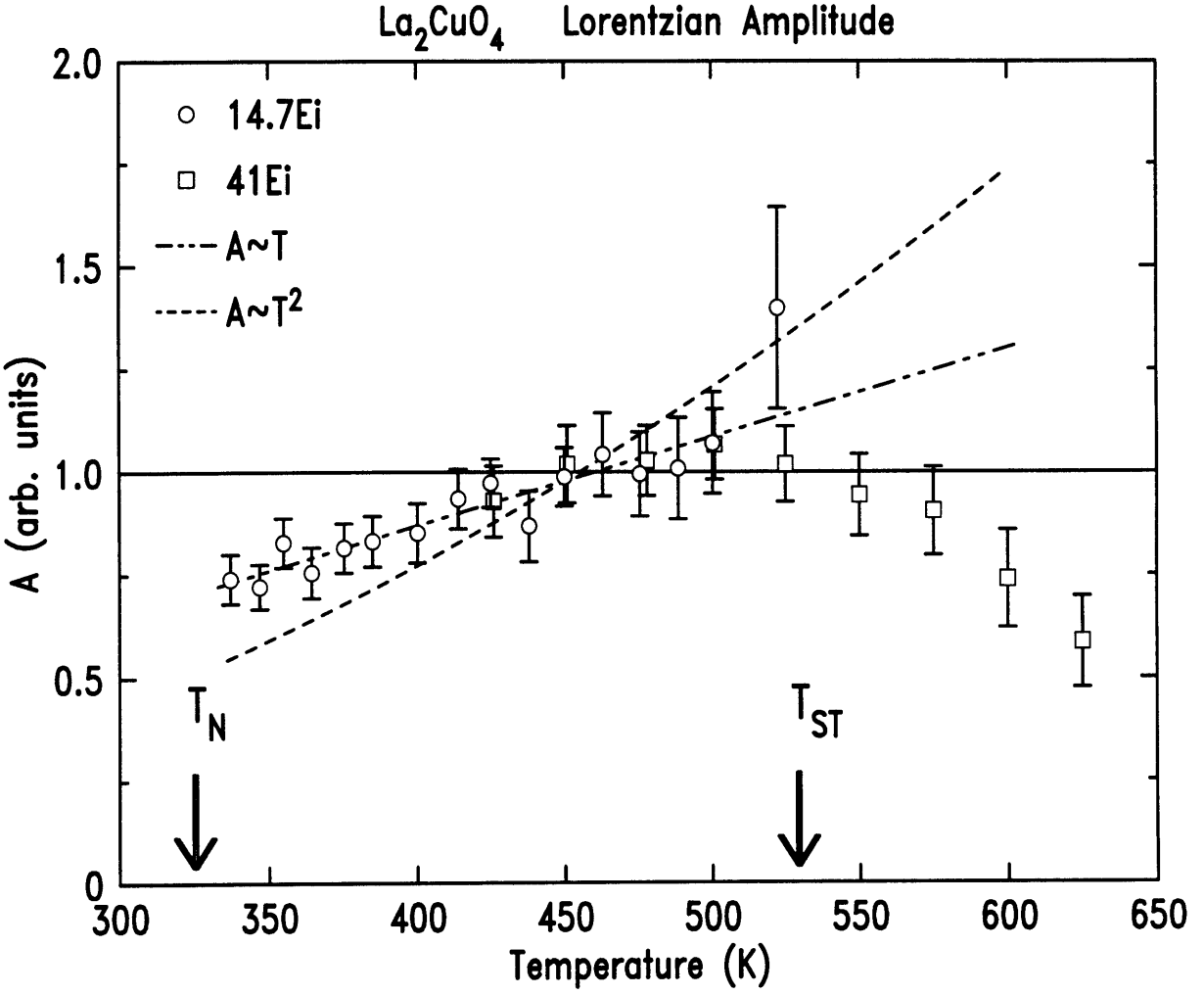

Figure 4-16: Lorentzian amplitude $A = \xi^{-2} S(0)$ for $E_i = 14.7$ and $41meV$, normalized for $T \leq 500K$.

scattering experiment, the data were cross-normalized for $T \leq 500K$. It is evident from this figure, that the form $A \sim T$ describes the data very well below the structural transition temperature $T_{ST} = 530K$. In particular, the $A \sim T^2$ behavior predicted by theory for low temperatures, as well as the behavior $A \sim$ *constant* observed for $Sr_2CuO_2Cl_2$ appear to be ruled out. As noted above, a linear temperature dependence of the Lorentzian amplitude had already been observed by Keimer et al [60] in the

range $340K \leq T \leq 540K$, albeit with much larger error bars. In Fig 4-17, A is shown for higher temperatures, as obtained with $90meV$ and $115meV$ neutrons. The

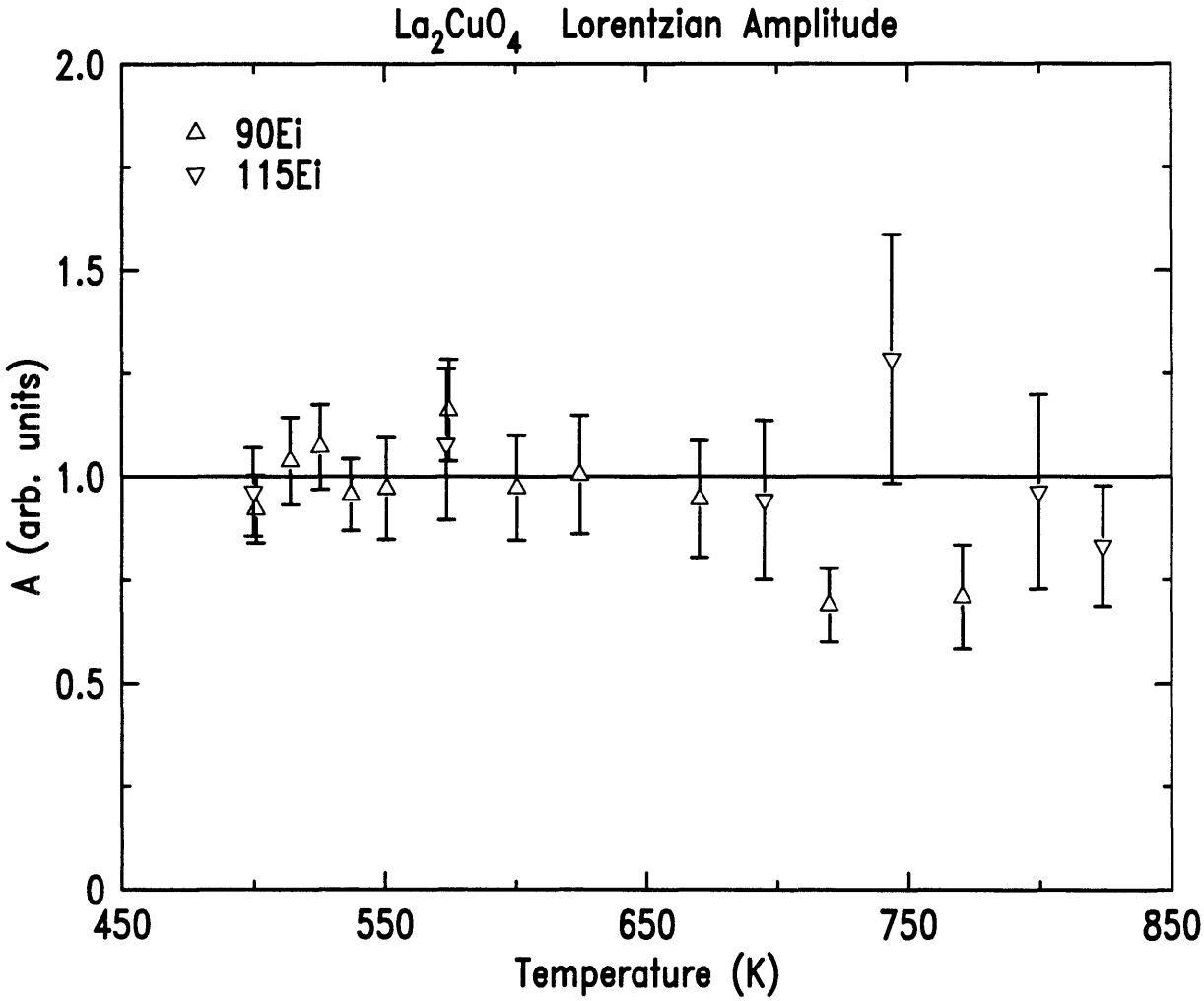

Figure 4-17: Lorentzian amplitude $A = \xi^{-2}S(0)$ for $E_i = 90$ and $115meV$, normalized for $T < 600K$.

two data sets were cross-normalized below $600K$. Above T_{ST} the $A = constant$ behavior observed in $Sr_2CuO_2Cl_2$ is regained. As discussed in Chapter 1, the spin Hamiltonian for La_2CuO_4 aquires an additional antisymmetric term below T_{ST}, which is responsible for the canting of the Cu spins in the Néel phase. The rather subtle change of the Lorentzian amplitude A in the paramagnetic phase of La_2CuO_4 seems to be another manifestation of this anisotropy. From Figs. 4-16 and 4-17 it can be seen that at high temperatures A obtained with $E_i = 41meV$ and $90meV$ decreases. The

Lorentzian amplitude is more sensitive to the energy cut-off than ξ, since it depends on the square of ξ.

The correlation length data the two $S = 1/2$ Heisenberg antiferromagnets $Sr_2CuO_2Cl_2$ and La_2CuO_4 are shown together in Fig. 4-17. The data for La_2CuO_4 verify the results obtained for $Sr_2CuO_2Cl_2$, and are an experimental extention to higher temperatures (lower JS^2/T). Above $T_{ST} = 530K$, La_2CuO_4 has the same structure and spin Hamiltonian as $Sr_2CuO_2Cl_2$. For two reasons the experiment for $Sr_2CuO_2Cl_2$ could only be carried out up to $T/(2\pi\rho_s) = 0.36$ (down to $JS^2/T = 0.60$): First, the overall sample volume in the $Sr_2CuO_2Cl_2$ experiment was only $\sim 0.5\,cm^3$ (three crystals, each of volume $0.1 - 0.2cm^3$ were aligned), while the volume of the La_2CuO_4 crystal was $\sim 1.5cm^3$. A second limitation was the relatively large nuclear incoherent scattering from the Cl.

In summary, it has been established that for $S = 1/2$ the renormalized classical description for the spin-spin correlation length is in very good agreement with both experiment and Monte Carlo work for the NN Heisenberg Hamiltonian. Surprisingly, the temperature dependence of the static structure factor peak as predicted by the same RC theory could not be verified experimentally. Both tetragonal $Sr_2CuO_2Cl_2$ and La_2CuO_4 (above T_{ST}) give $S(0) \sim \xi^2$ rather than $S(0) \sim T^2\xi^2$. The behavior $S(0) \sim T\xi^2$ observed in La_2CuO_4 below T_{ST} is likely to be due to the appearance of the antisymmetric Dzyaloshinski-Moriya term in the spin Hamiltonian. While at low enough temperatures (not accessible experimentally) the theoretical scaling form for $S(0)$ might well be regained, it is clear that the analysis of NMR and NQR relaxation rates must not be based on this form.

A closely connected issue has been the claim [190], that the ratio $R \equiv TT_1/T_{2G}$ is a good indicator for a crossover from RC to QC scaling behavior. From Eqs. (4.25) and (4.28), one expects that $R \sim T^{1/2}$ in the RC regime. It has been claimed [190], that QC scaling could be verified if this ratio is independent of temperature. Since R was indeed found to be independent of temperature in the experiments by Imai et al. [192, 213] (over the entire range $450K \leq T \leq 1000K$), this was interpreted as additional evidence in favor of QC scaling. Again, the experiments presented in

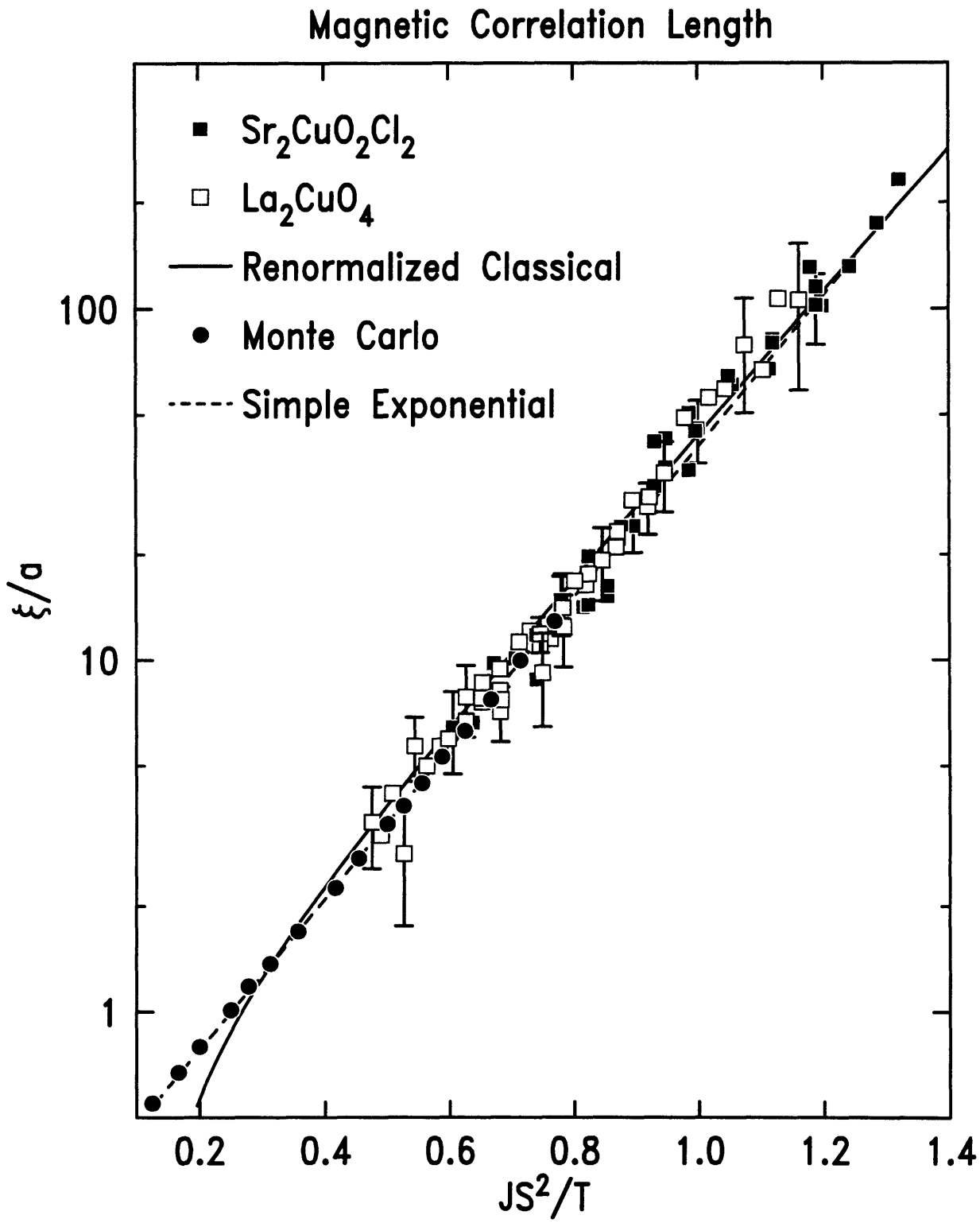

Figure 4-18: Semi-log plot of ξ/a versus J/S^2T: $Sr_2CuO_2Cl_2$ ($J = 125meV$), La_2CuO_4 ($J = 135meV$), Monte Carlo, and RC theory for the QNLσM.

this Chapter rule out this interpretation, and they furthermore point at the danger of using as an indicator a quantity from which the dominant exponential temperature dependence has been removed.

Chapter 5

Monte Carlo for $S = 1/2$

In the early 1990's, H.-Q. Ding and M.S. Makivić (DM) [168, 169] carried out a ground-breaking Monte Carlo study of the NN $S = 1/2$ 2DSLQHA. Their simulations, which were done on a parallel superconductor for lattices as large as $128 \times 128 \times 192$ spins, extended to rather low temperatures ($T \geq 0.27J$). On the one hand, DM's result for ξ is in excellent agreement with the experimental data presented in the previous Chapter. On the other hand, the static structure factor peak, $S(0)$, was found to be consistent with the theoretical form $S(0) \sim T^2\xi^2$ [56, 197], in disagreement with the neutron scattering results. However, the error bars for $S(0)$ were rather large so that in light of the observed discrepancy between experiment and theory for the QNLσM, a verification of DM's result became desirable. From the discussion in the previous Chapter it is clear that a resolution of this issue would, for the first time, put the interpretation of NMR and NQR relaxation rates for the $S = 1/2$ Heisenberg materials on solid ground. A successful reconciliation of neutron and NMR experiments for the undoped lamellar copper oxides would furthermore pave the way for a consistent quantitative understanding of the magnetism at finite doping.

In this Chapter, Monte Carlo results for the $S = 1/2$ NN SLQHA are presented. The work was carried out in collaboration with Uwe-Jens Wiese (MIT), and employed a rather novel and very efficient algorithm. Some general features of the quantum Monte Carlo technique will be reviewed first.

5.1 Quantum Monte Carlo simulations

Monte Carlo simulations for quantum spin systems generally rely on the *Suzuki-Trotter approach* [217], in which the partition function of a *d-dimensional quantum* spin system is expressed as a path integral equivalent to a *(d+1)-dimensional classical* spin system. As a relatively simple example, the $S = 1/2$ Heisenberg *chain*, i.e. the $S = 1/2$ NN 1DQHA, will be discussed. The Heisenberg Hamiltonian is decomposed

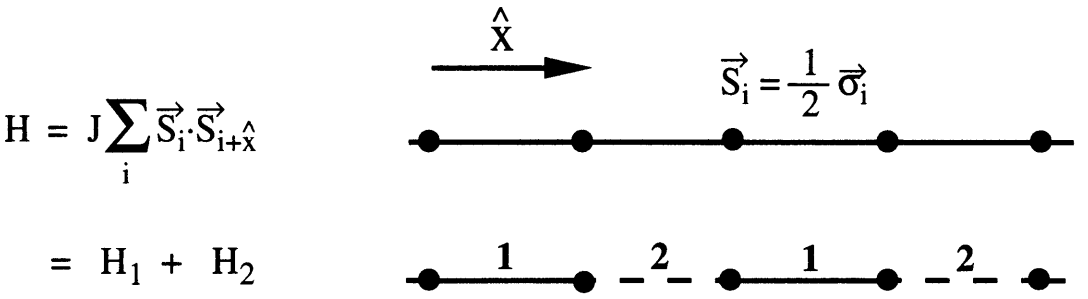

Figure 5-1: Decomposition of the Heisenberg Hamiltonian for a $S = 1/2$ chain ($\vec{\sigma}_i$ denotes the Pauli spin operator at site i.)

as shown in Fig. 5.1, so that the partition function can be written as

$$\begin{aligned} Z &= Tr\,[exp(-H/T)] \\ &= \lim_{m\to\infty} Tr\,[exp(-\epsilon H_1/T)exp(-\epsilon H_2/T)]^m\,, \end{aligned} \tag{5.1}$$

where m is the *Trotter number*, and $\epsilon = 1/m$. Complete sets of eigenstates $|"up"\rangle$ and $|"down"\rangle$ of σ_i^z are inserted between the factors $exp(-\epsilon H_i/T)$. This maps the d-dimensional quantum spin system of size L^d to a (d+1)-dimensional *induced* classical system with $2dmL^d$ Ising-like spin variables with four-spin couplings. Figure 5.2 gives an illustration of the result of this mapping for the case of the 1D spin chain. Note, that τ denotes *Euclidean (imaginary) time* and not real time. Since the action values $A[S]$ for most of the time-like plaquettes are infinite, the corresponding Bolzmann weights are zero. This fact leads to *frustration* in standard numerical simulations, because many spin configurations are not allowed so that the updating

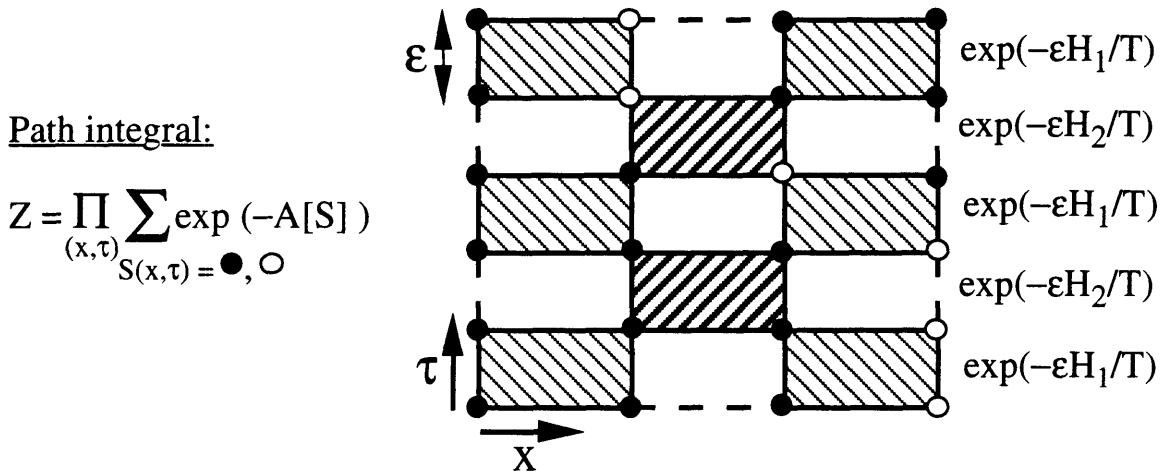

Figure 5-2: Four-spin plaquettes and Boltzmann weights in (1+1) dimensions. Filled and open circles denote "up" and "down" spins, respectively.

of an allowed configuration underlies various constraints. Evertz et al. [218] have developed a *loop cluster algorithm* for the vortex model, which is equivalent to the $S = 1/2$ chain. This algorithm was then applied to the $S = 1/2$ NN 2DSLQHA by Wiese and Ying [175], who determined the low-energy parameters of that model (Z_ρ, Z_c, M_s, and E_0; see also Table 4.1) by comparing size and temperature dependences of several thermodynamic quantities with the results from chiral perturbation theory by Hasenfratz and Niedermayer (HN) [219].

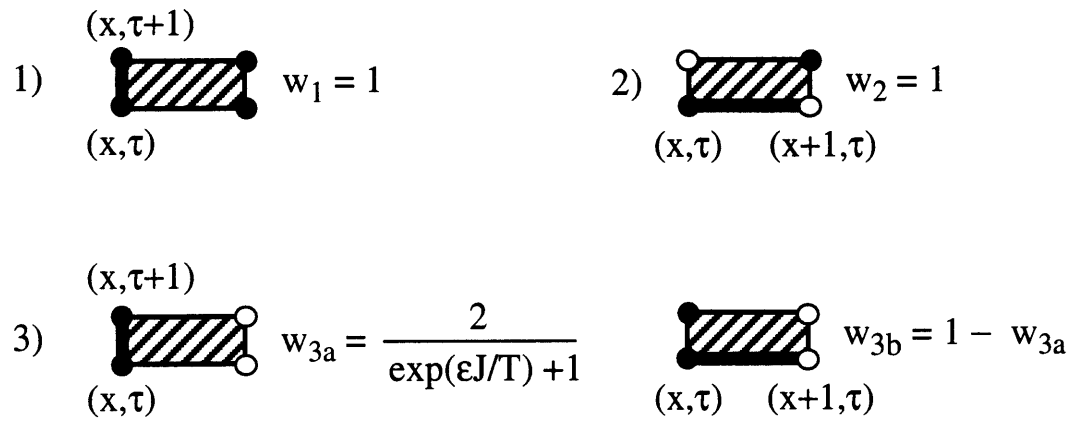

Figure 5-3: Growing a loop.

The loop cluster algorithm does not suffer from frustration since it creates only allowed spin configurations. A starting point (x, τ) is chosen randomly (from the $L \times L \times 2dm$ spins of the lattice). As can be seen from Fig. 5.2, each spin $S(x, \tau)$ participates in two plaquette interactions, and for $S(x, \tau) =$ "*up*" ($S(x, \tau) =$ "*down*") the interaction at a later (earlier) Euclidean time is considered. The three possible scenarious for an "up" spin, for example, are shown in Fig. 5.3. In the first (second) case, both time- and space-like neighbors are "up" ("down"), and the loop grows in the time (space) direction with probability $w_1 = 1$ ($w_2 = 1$). In the third case, a random number r ($0 < r < 1$) is generated. If $r \leq w_{3a}$, then the loop grows in the time direction, otherwise it grows in the space direction. This process is repeated until the loop closes. Once the loop is closed, all the spins on the loop are flipped, so that a new spin configuration is created. Loops will always close,

since the algorithm is *ergodic* (i.e. all possible spin configurations can in principle be created) and obeys *detailed balance* (e.g. $p_1 w_1 = p_3 w_{3a}$). Each new spin configuration represents an additional contribution to the partition function Eq. (5.1), and thus to the thermodynamic average of the physical quantities measured. The construction of the algorithm for the 2D Heisenberg antiferromagnet is such that a loop cannot branch out, and therefore *freezing* does not occur [175].

The absence of frustration and freezing renders loop cluster algorithms extremely efficient. Moreover, cluster algorithms allow for the implementation of *improved estimators* which significantly reduce the variance of observables. For the loop cluster algorithm used in this study, an improved estimator for a measured physical quantity essentially takes into account the fact that it is more likely that a large loop is created, rather than a small one. Wiese and Ying's algorithm, which was previously run on a Cray Research computer, was modified to run efficiently on a Digital Equipment Coorperation workstation. Furthermore, an improved estimator for the static staggered spin correlation function was implemented.

One finds empirically that finite-size effects are small for for $L \geq 5\xi$. The equivalence between quantum and classical system is exact only in the limit $m \rightarrow \infty$. In practice, however, m is finite and the systematic error is of order $O(mT/J)^{-2}$. The simulations in this study were carried out on clusters large enough so that $L > 6\xi$ and $(mT/J)^{-1} < 0.1$. The lowest temperature accessed in this study was $T = 0.325J$, for which a $80 \times 80 \times 192$ lattice was used. Typically, 10^4 updates were performed for equilibration, followed by 10^5 measurements employing improved estimators.

5.2 Measurement of the static staggered spin correlation function

The static staggered spin correlation function is given by

$$C(r) = (-1)^{r_x + r_y} \frac{1}{L^2} \sum_n \langle S_n^z S_{n+r}^z \rangle. \tag{5.2}$$

In an infinitely large system, the asymptotic behavior of $C(r)$ is given by

$$C_\infty(r) \sim \frac{e^{-r/\xi}}{r^\lambda} \quad (r \to \infty), \tag{5.3}$$

and $\lambda = (d-1)/2$ in Ornstein-Zernike theory. Periodic boundary conditions for a system of finite size L require fits to a symmetrized form:

$$C_L(r) = D\left[\frac{e^{-r/\xi}}{r^\lambda} + \frac{e^{-(L-r)/\xi}}{(L-r)^\lambda}\right]. \tag{5.4}$$

Ding and Makivić (DM) [168, 169] compared their Monte Carlo data to this form, with D, λ, and the correlation length ξ as fitting parameters. The disadvantage of fitting to Eq. (5.4) is that it is strictly valid only in the asymptotic $r \to \infty$ limit, a situation which can never be achieved in a simulation. Furthermore, in order to obtain reasonably good fits an artificial cutoff $r > 1$ has to be chosen.

Alternatively, one can fit the 1D Fourier transform

$$C_L(r_x, p_y) = \sum_y C(r_x, r_y) e^{i r_y p_y} \tag{5.5}$$

at $p_y = 0$ to

$$\begin{aligned} C_L(r_x, p_y = 0) &= \sum_y C(r_x, r_y) \\ &= D\,cosh\left(\frac{L/2 - r_x}{\xi}\right) + D_1\,cosh\left(\frac{L/2 - r_x}{\xi_1}\right) + \cdots \end{aligned} \tag{5.6}$$

The form Eq. (5.6) is accurate at all distances r_x as long as a large enough number of *cosh*-terms is used in the fits. The lengths $\xi_1, \xi_2, etc.$, are related to the correlation length ξ by a (unknown) constant of proportionality. In Fig. 5-4, the correlation function $C_L(r_x, p_y = 0)$ is shown for the lowest temperature ($T = 0.325J$) and largest lattice ($80 \times 80 \times 192$) accessed in this study. The two-parameter fit to the first term in Eq. (5.6) (dashed line) is already very good. Note, that for this fit r_x was artificially constrained to lie in the range $4 < r_x < 76$. An excellent description over the entire range of values r_x is obtained for a four-parameter fit (fitting parameters

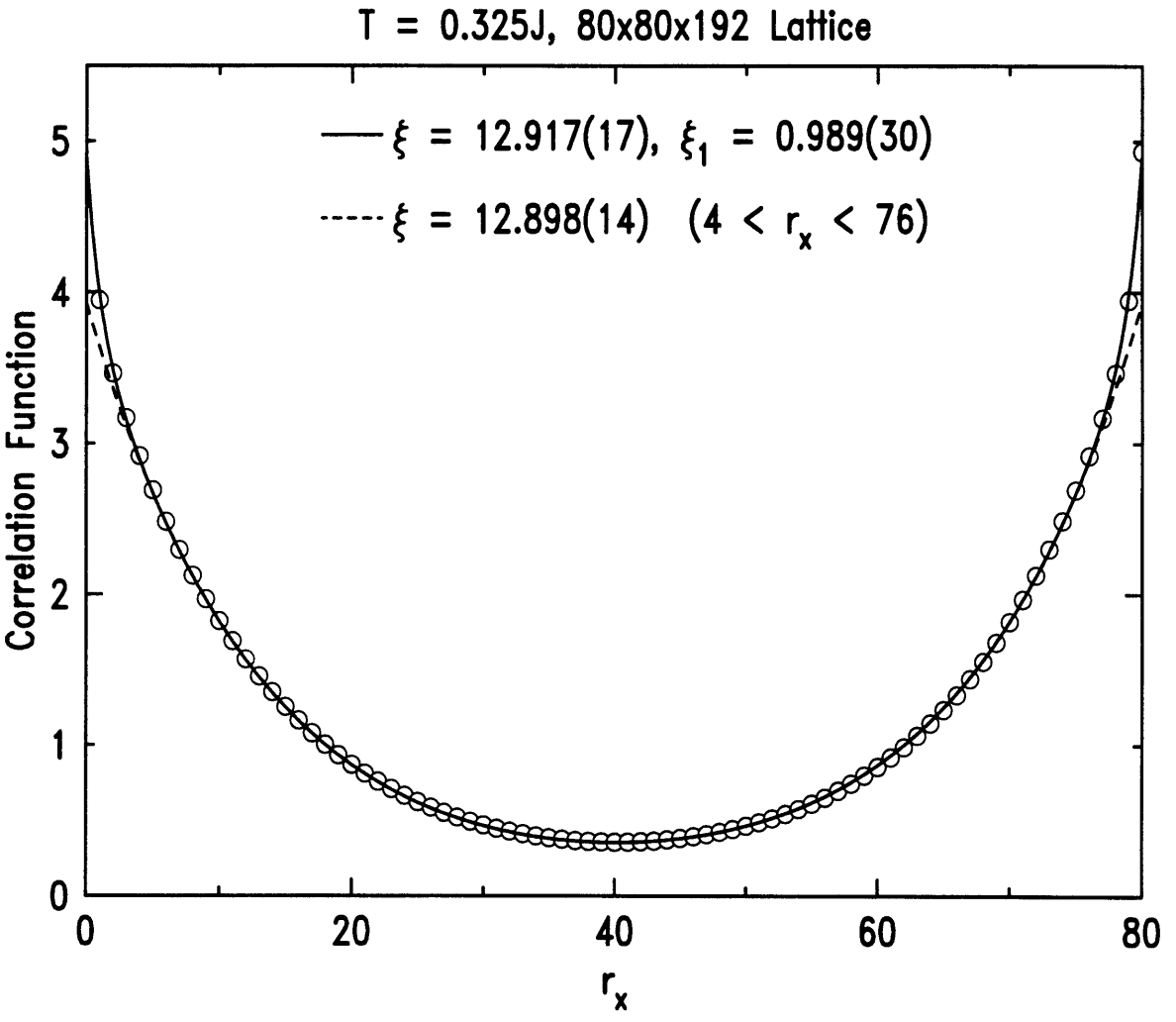

Figure 5-4: Correlation function at $T = 0.325J$ for a $80 \times 80 \times 192$ lattice. Note, that $a = 1$ here.

D, ξ, D_1, ξ_1). The value for ξ agrees with that for the two-parameter fit, while ξ_1 is about an order of magnitude smaller. Overall, it was found that the two-parameter fits to the first term in Eq. (5.6) were already better than three-parameter fits to Eq. (5.4).

In Fig. 5-5, the correlation length is shown (open circles) and compared to the earlier result by DM (solid squares) [168, 169]. While the agreement between the two

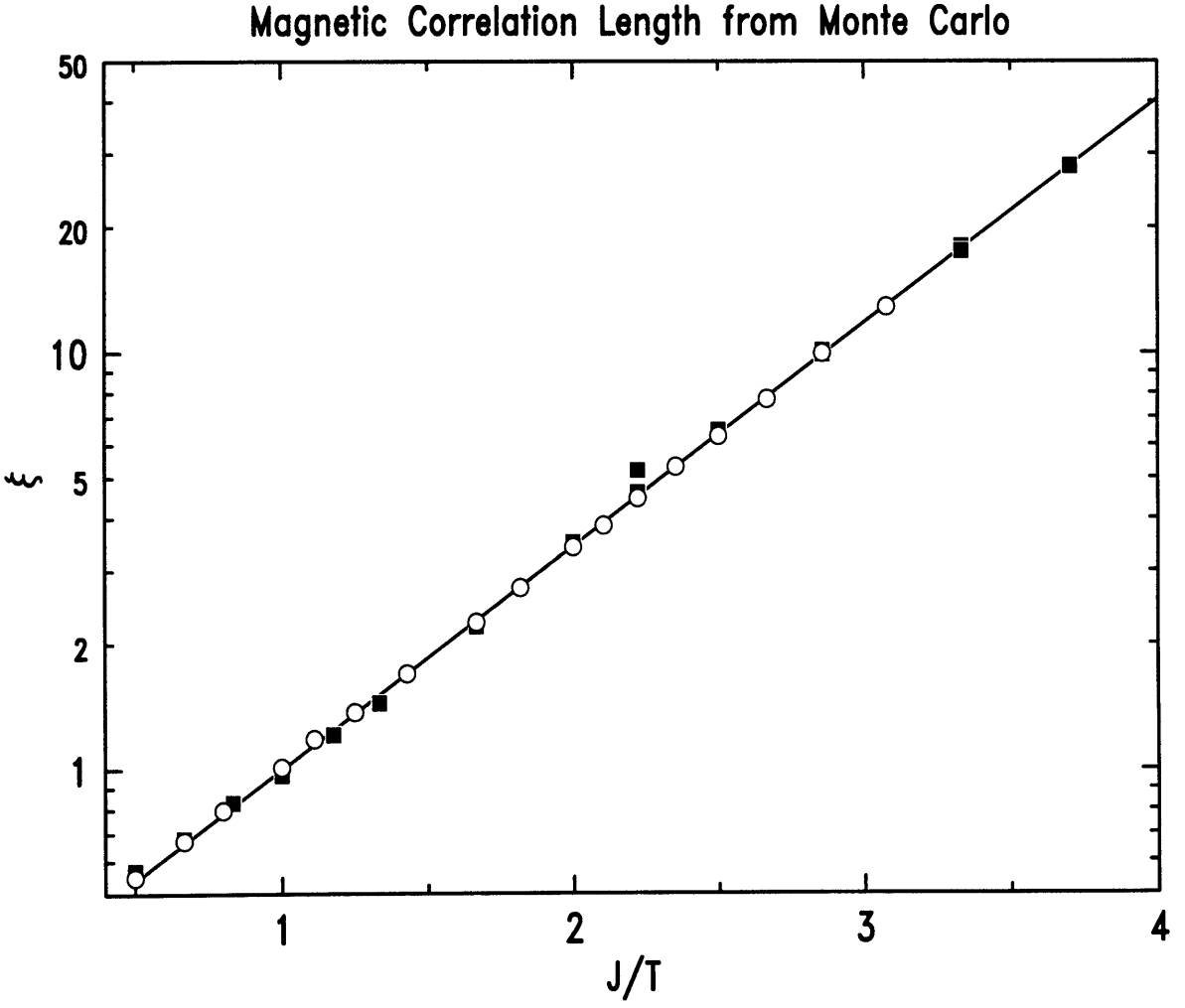

Figure 5-5: Semilog plot of the magnetic correlation length from Monte Carlo versus J/T. The open circles are the result obtained in this study, and the line is a fit to a simple exponential. The solid squares represent earlier Monte Carlo data by Ding and Makivić [168, 169]. Note, that $a = 1$ here.

is found to be very good, the error bars on the data obtained in the current study are

smaller (well within the symbol size in Fig. 5-5). The line is the result of a fit (in the range $0.325 \leq T/J \leq 1$) to a simple exponential: $\xi/a = 0.290(5)\, exp(1.235(6)J/T)$. This empirical exponential form is completely consistent with DM's earlier result $\xi/a = 0.276(6)\, exp(1.250(13)J/T)$.

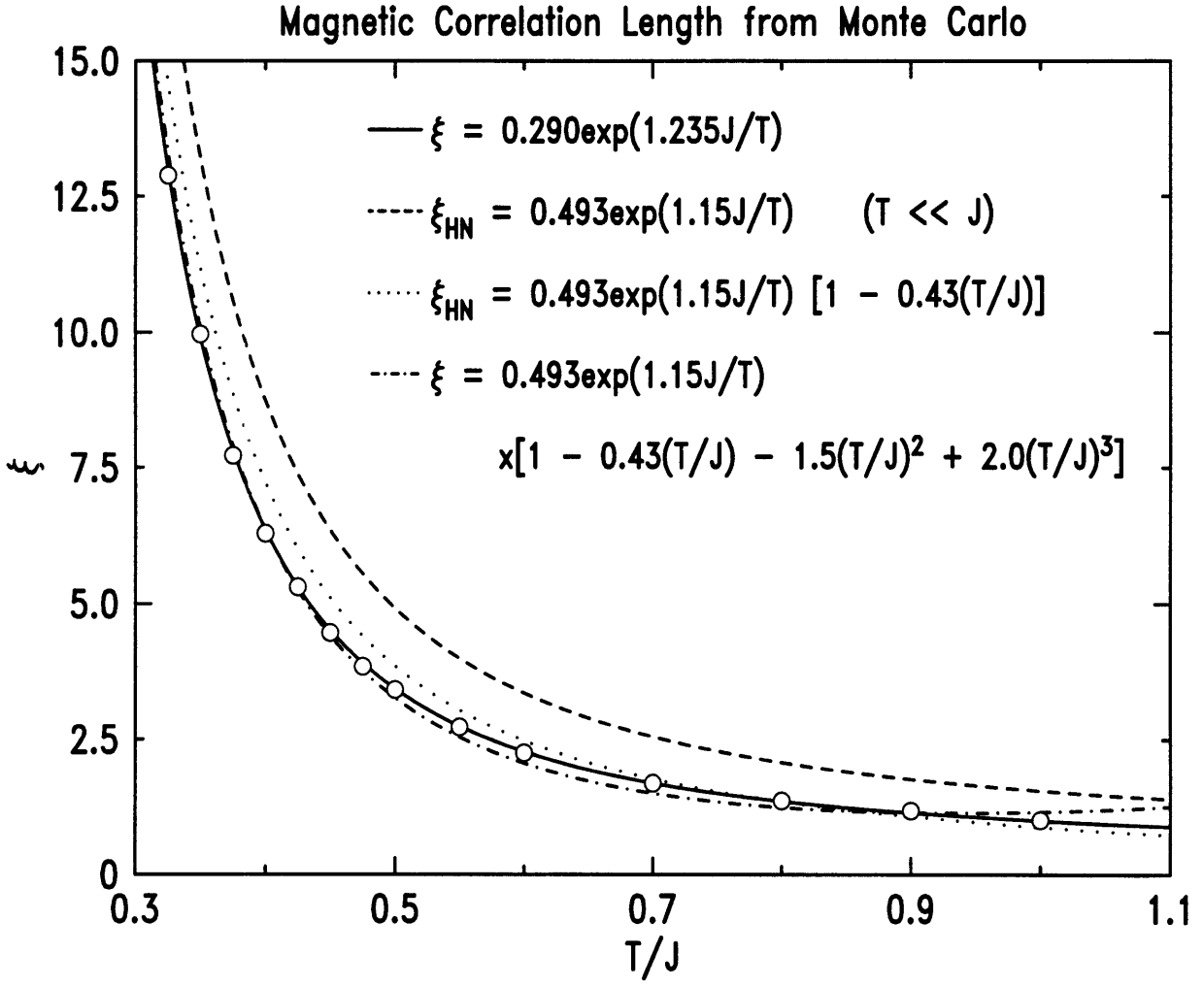

Figure 5-6: Magnetic correlation length from Monte Carlo: comparison with RC theory for the QNLσM. Note, that $a = 1$ here.

The correlation length obtained from Monte Carlo is plotted in Fig. 5-6 on a linear scale versus T/J. It is somewhat mysterious, why a simple exponential should describe the correlation length so well over the entire temperature range of Fig. 5-6. The analytical result obtained by HN (Eqs. (4.18) and (4.19)) is also an exponential at low temperatures, $\xi/a = 0.493\, exp(1.15J/T)$, shown as a dashed line in

Fig. 5.6. However, at intermediate and higher temperatures there will be corrections to this form. HN have also obtained the $O(T/J)$ correction, and their full result, including the term $0.43(T/J)$, is indicated by the dotted line. The next two terms, $-1.5(3)(T/J)^2+2.0(4)(T/J)^3$, were obtained empirically from a fit of the Monte Carlo data in the range $0.325 \leq T/J \leq 1$, shown as a dot-dashed line. While this fit yields very good agreement up to $T/J \sim 0.5$, it is not as good at higher temperatures as the simple exponential two-parameter fit. Note, that $2\pi\rho_s = 1.15J$, or equivalently $Z_\rho(1/2) = 0.73$, was chosen in Fig. 5-6 as well as in the analysis in the previous Chapter. It can be seen form Table 4.1, that $Z_\rho(1/2) = 0.73$ is the intermediate of the three theoretically predicted values for $S = 1/2$.

The static structure factor peak is given by the 2D Fourier transform of $C(r_x, r_y)$ at $p_x = p_y = 0$:

$$S(0) = \sum_{x,y} C(r_x, r_y). \tag{5.7}$$

In Fig. 5-7, the Lorentzian amplitude $A = S(0)\xi^{-2}$ is shown. The temperature ranges of the $Sr_2CuO_2Cl_2$ and La_2CuO_4 experiments are indicated as solid and dashed lines, respectively. Note, that it is not possible to obtain the absolute value of A from experiment. Clearly, the experimentally observed behavior $A = const$ is in disagreement with the Monte Carlo result for the $S = 1/2$ NN 2DSLQHA. However, the Monte Carlo data agree very well (below $T/J = 0.5$) with recent series expansion results [220] (which extend down to $\sim 0.35T/J$), and both follow the renormalized classical from $A \sim T^2$ rather well. It is found that $S(0) = aT^2\xi^2$, with $a = 1.48(4)$ for $0.325 \leq T/J \leq 0.40$. This is furthermore consistent with $A \simeq 1.65T^2$ obtained by DM, given the relatively large uncertainty in their result.

The discrepancy between the theoretically predicted and numerically observed behavior $A \sim T^2$ on the one hand, and the behavior $A \sim constant$ observed in neutron scattering experiments on the other hand, remains unexplained. Interestingly, the constant of proportionality as determined numerically for the $S = 1/2$ NN 2DSLQHA, $a = 1.48(4)$, disagrees with current estimates for the RC regime of the QNLσM by

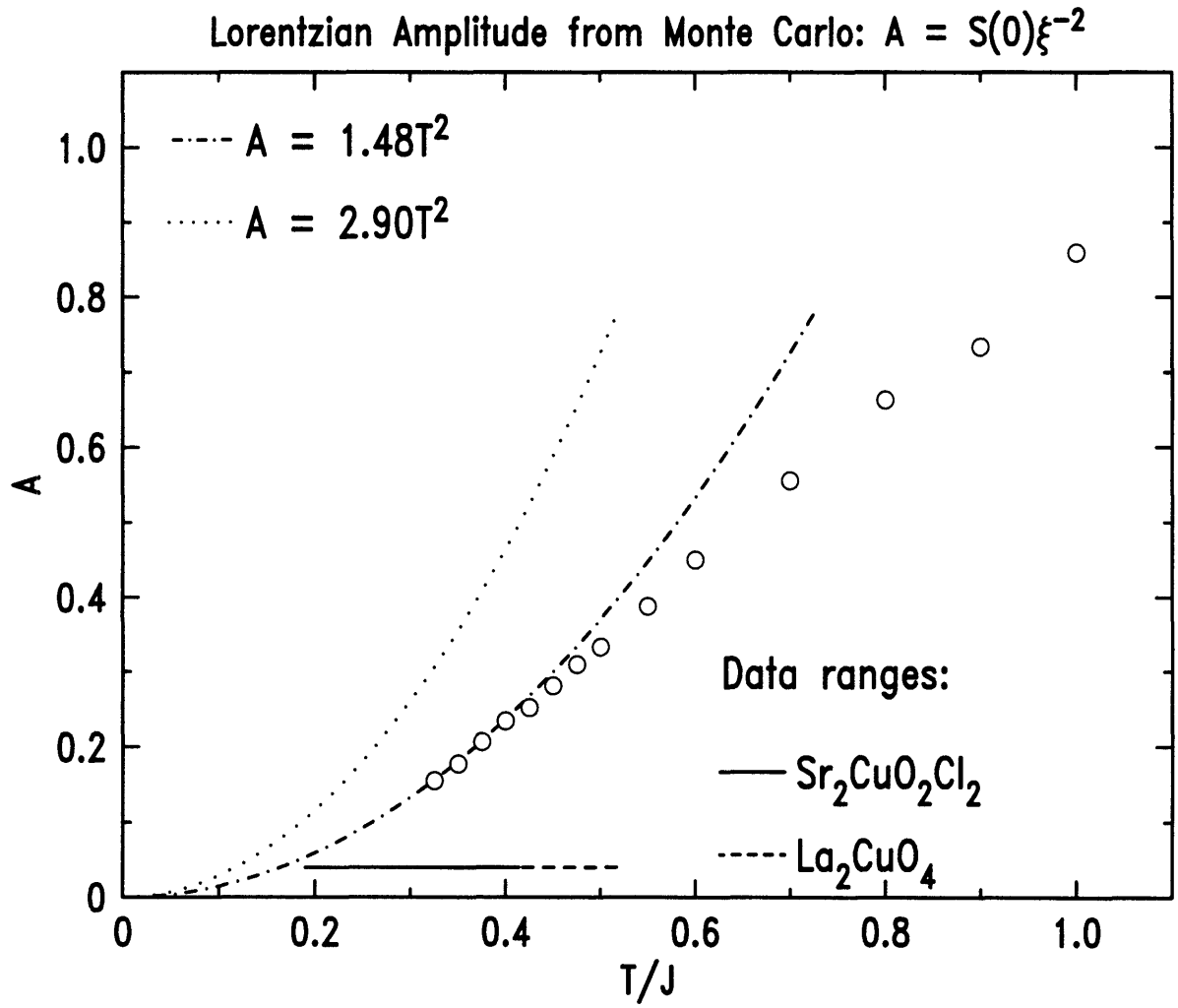

Figure 5-7: Lorentzian amplitude from Monte Carlo.

about a factor of two [221]. The RC scaling prediction for $S(0)$ is

$$S(0) = 2\pi Z_3 M_s^2 \left(\frac{T}{2\pi\rho_s}\right)^2 \xi^2, \tag{5.8}$$

where Z_3 is a universal number. M_s and ρ_s are the $T = 0$ sublattice magnetization and spin stiffness, respectively, and are known for $S = 1/2$ (as discussed in Chapter 4.2.1). The value $a = 1.48(4)$, as found by Monte Carlo at a temperature $T_{min}(S = 1/2) \simeq 0.325$, corresponds to $Z_3(S = 1/2) \simeq 3.4$. The value of Z_3 that enters the RC prediction is that of the *classical* ($S \to \infty$) model. From the lowest temperature $T_{min}(S \to \infty) \simeq 0.8JS^2$ in numerical studies of the classical model [163, 186, 222, 223], one obtains $Z_3(S \to \infty) \simeq 6.6$ (or $a \simeq 2.9$), about a factor of two larger than the estimate for $S = 1/2$ [221]. The dotted and dashed lines in Fig. 5-7 correspond to $a = 2.90$ and $a = 1.48$, respectively. Since $Z_3(S \to \infty)$ in the classical scaling limit is expected to agree with $Z_3(S = 1/2)$ in the RC scaling limit, it seems possible that at least one of the two models is not in its scaling limit at the respective T_{min}. Another possible cause of this discrepancy (as well as of the discrepancy with the experiments) might be that lattice corrections (i.e. the finite size of the Brillouin zone) to $A = S(0)\xi^{-2}$ play an important role at the temperatures studied.

The quantity Z_3 can also be calculated directly using $1/N$ expansion techniques for the $O(N)$ non-linear sigma model, without having to employ Eq. (5.8). Very recently, $Z_3 = 2.15$ was obtained in this fashion [224], a value that is even 40% smaller than the estimate for $S = 1/2$ based on Monte Carlo.

5.3 Measurement of $\chi(0)$ and χ_u

Two other physical quantities besides ξ and $S(0)$ were obtained in the Monte Carlo simulations: the static staggered susceptibility at $q = 0$, $\chi(0)$, and the *uniform susceptibility*, χ_u. Together with the correlation length, ξ, and the static structure factor peak, $S(0)$, it is then possible to form the two dimensionless ratios $W(T)$ and

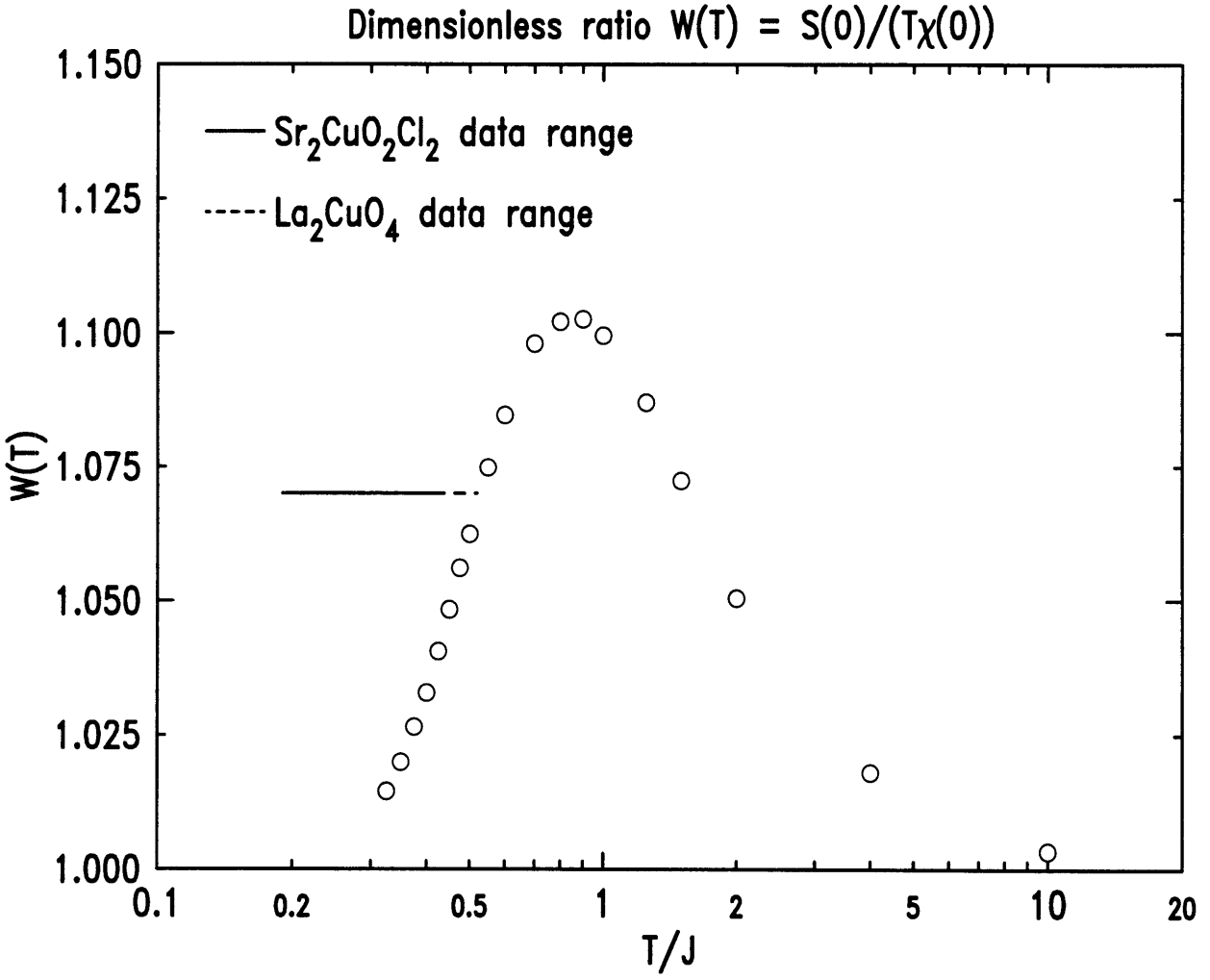

Figure 5-8: Dimensionless ratio $W(T) = S(0)/(T\chi(0))$ versus the logarithm of T/J.

$Q(T)$, defined as:

$$W(T) = \frac{S(0)}{T\chi(0)} \tag{5.9}$$

and

$$Q(T) = \frac{\xi^{-1}}{(T\chi_u)^{1/2}}. \tag{5.10}$$

It has been predicted from $1/N$-expansions of the $O(N)$ NLσM, that both $W(T)$ and $Q(T)$ take on T-independent values at the quantum critical point [189]. For

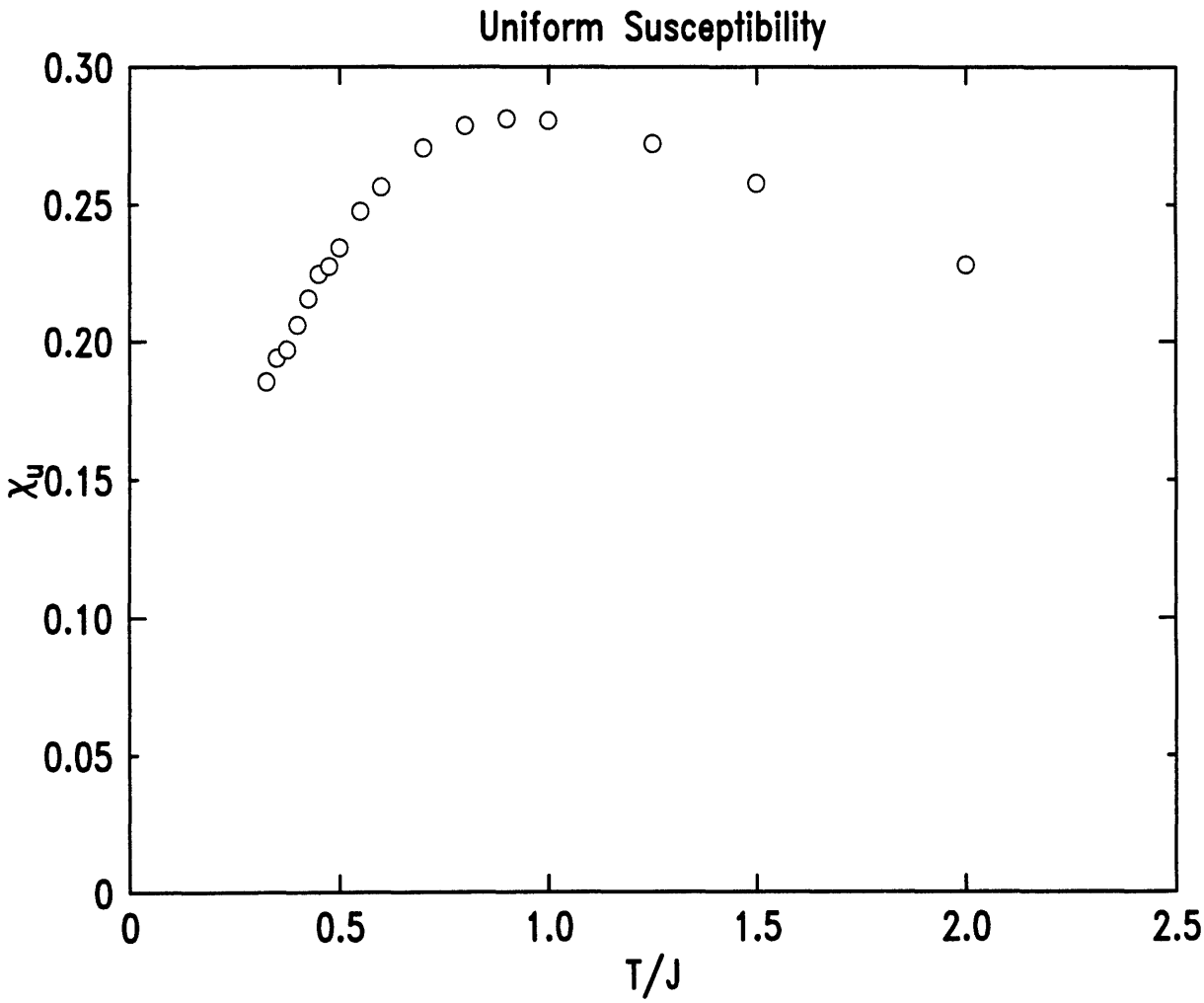

Figure 5-9: Uniform susceptibility.

$N = 3$, the two ratios are predicted to be $Q \simeq 2.0$ and $W \simeq 1.09$ [189, 224]. In a recent numerical study of the two-layer SLQHA, these universal values were indeed observed over a rather wide temperature range (for $J_\perp/J \simeq 2.50$, where $J_\perp$ and J are

the inter- and intralayer exchange integrals, respectively).

In earlier work on the $t - J$ model, it was found that at half-filling, which corresponds to the $S = 1/2$ NN 2DSLQHA, $W(T) = 1.10(2)$ over the range $0.6 \leq T/J \leq 1.0$. This result was interpreted in favor of a QC regime for $T \geq 0.6J$. In Fig. 5-8,

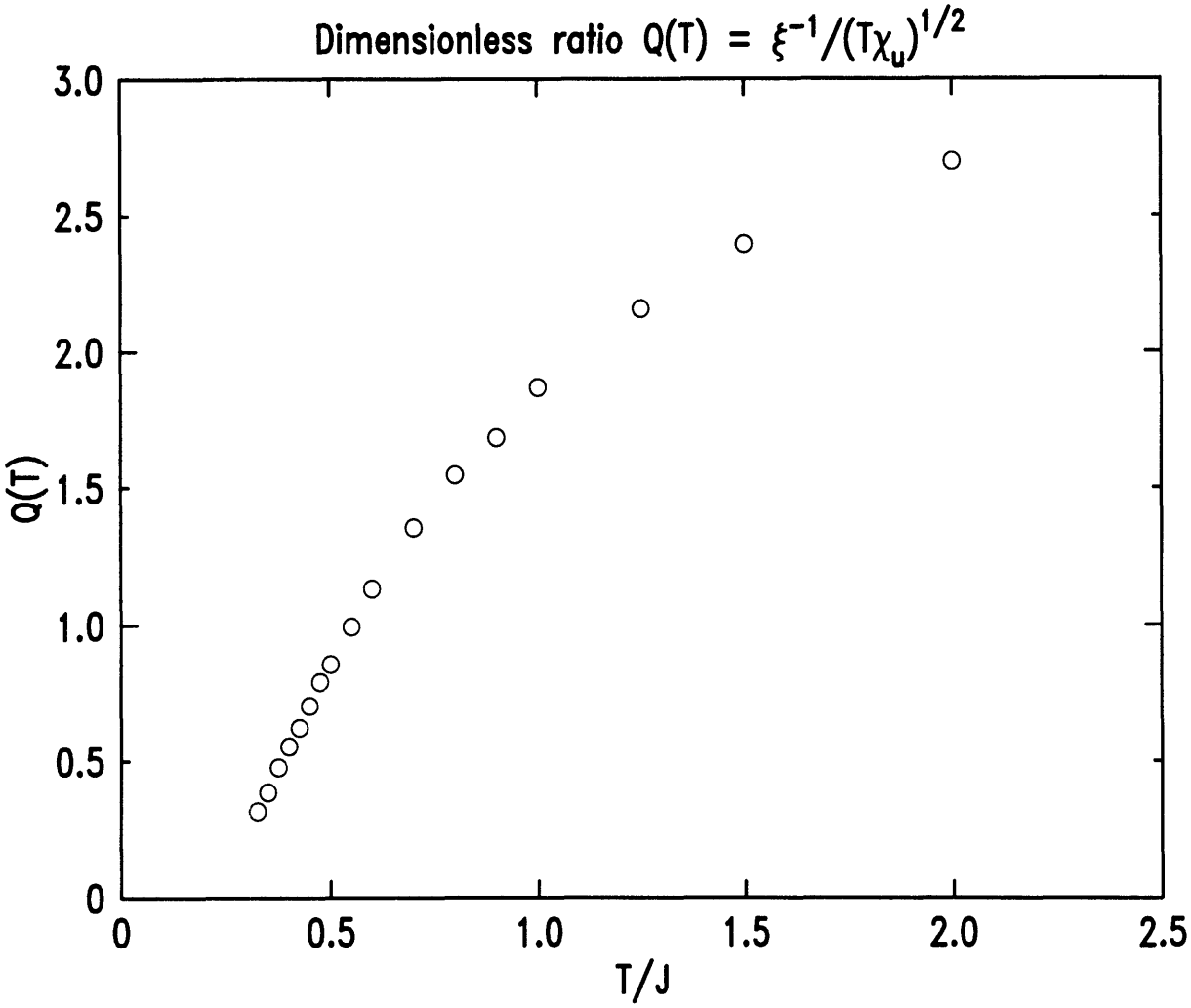

Figure 5-10: Dimensionless ratio $Q(T) = \xi^{-1}/(T\chi_u)^{1/2}$.

$W(T)$ is shown, as obtained form the Monte Carlo simulation. This quantity is an indicator of the frequency distribution of the spectral weight at $q = 0$. At low temperatures, the characteristic energy $\omega_0 \sim \xi^{-1}$ is very small, and $W(T) \rightarrow 1$, as expected. In the high-temperature limit, one also expects that $W(T) \rightarrow 1$, since the thermal energy is much larger than the superexchange coupling between neighboring spins.

The Monte Carlo data indicate that indeed $W(T) \simeq 1.10$ for $T \sim 0.8J$. However, $W(T)$ is not independent of temperature, but rather peaks at $T \simeq 0.8J$. There is thus no evidence from the temperature dependence of $W(T)$ in favor of an extended QC regime. This observation is not very surprizing in the light of the experimental and numerical findings of an exponential temperature dependence for the correlation length.

In Figs. 5-9 and 5-10, the uniform susceptibility and the dimensionless ratio $Q(T) = \xi^{-1}/(T\chi_u)^{1/2}$ are shown. The result for χ_u agrees very well with previous work by DM [168, 169] and Wiese and Ying [175]. From Fig. 5-10, it can be seen that $Q(T)$ increases monotonically and crosses the "universal" value $Q(T) = 2.0$ at $T \sim 1.1J$. This temperature does not coincide with the peak in $W(T)$ at $T = 0.8J$. Again, there is no evidence in favor of an extended QC regime.

Chapter 6

The 2D Square-Lattice Heisenberg Antiferromagnet: $S \geq 1/2$

6.1 Experiments for $S = 1$

6.1.1 K_2NiF_4

Before the advent of the field of high-temperature superconductivity, K_2NiF_4 was considered to be the model NN 2DSLQHA. Experimental data for the spin-spin correlation length, ξ/a, and the static structure factor peak, $S(0)$, in K_2NiF_4 are shown in Figs. 6.1 and 6.2 , respectively. As demonstrated by Birgeneau et al. [51, 52, 53], at $T \simeq 102K$ K_2NiF_4 exhibits a crossover from 2D Heisenberg to 2D Ising behavior, ultimately exhibiting a 2D Ising phase transition at $T_N = 97.23K$ with exponents in agreement with those for the ideal 2D Ising model. In 1990, Birgeneau [164] re-analyzed the original K_2NiF_4 data within the CHN-framework. The data for $T > 102K$ were shown to be well-described by CHN's results, Eqs. (4.9) and (4.17), with the spin stiffness ρ_s fixed at the spin-wave value. However, in order to obtain this agreement for ξ/a, the exponential prefactor had to be adjusted by more than 30% from the CHN-value, Eq. (4.9). Furthermore, no attempt was made to include the Ising anisotropy explicitly.

In light of the results for the $S = 1/2$ systems $Sr_2CuO_2Cl_2$ and La_2CuO_4 it is of

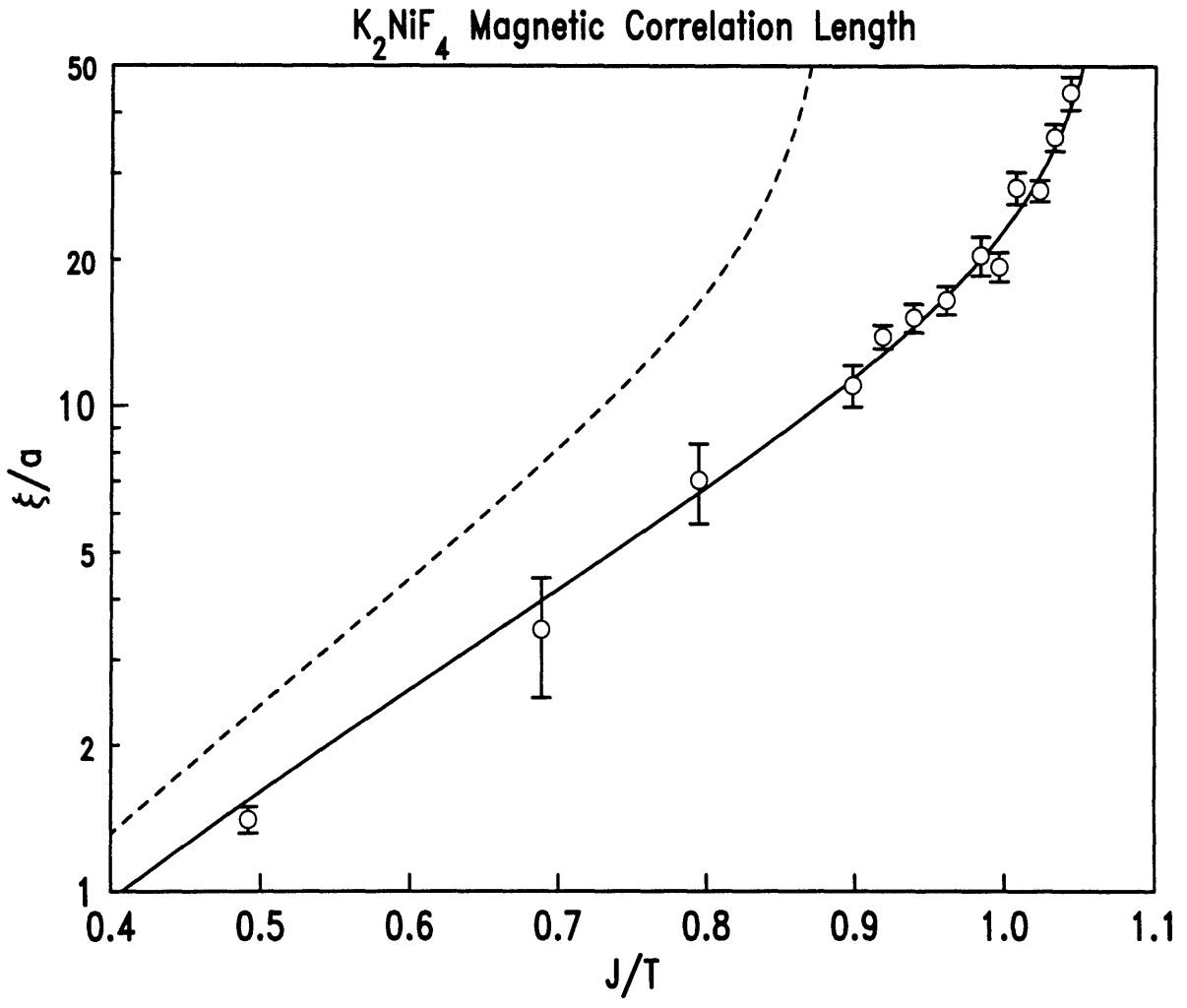

Figure 6-1: Magnetic correlation length in K_2NiF_4. Both lines were obtained from Eq. (6.1). The dashed line has no adjustable parameters, whereas the solid line is the result of a fit of the spin stiffness, which yielded a value $\sim 20\%$ smaller than that given by theory.

interest to re-analyze the K_2NiF_4 data using the more recent exact expression for the correlation length, ξ_{HN}, Eq. (4.18). Moreover, as discussed by Keimer at al. [60], the Ising anisotropy may be taken into account to leading order via the mean-field result

$$\xi(\alpha_I, T)/a = \frac{\xi_{HN}(T)/a}{\sqrt{1 - \alpha_I \, (\xi_{HN}(T)/a)^2}} \tag{6.1}$$

where α_I is the reduced Ising anisotropy. In K_2NiF_4, spin-wave measurements yield $\alpha_I = 2.1 \times 10^{-3}$ and $c = (109 \pm 2)\, meV\mathring{A}$ [53]. Thus, the spin stiffness ρ_s is the only remaining parameter needed for Eq. (6-1).

As discussed in Chapter 4.2.1, the quantum renormalization factors $Z_\rho(S) = \rho_s/(JS^2)$ and $Z_c(S) = c/(2^{3/2}aJS)$ are known rather precisely for $S = 1$: $Z_\rho(1) \simeq 0.87$ and $Z_c(1) \simeq 1.084$. Thus one has $J = 8.9(2)meV$ and $2\pi\rho_s = 2\pi Z_\rho JS^2 = 5.47J = 48.7(5)meV$. It is clear from Fig. 6.1, that the correlation length is not described by the theoretical value for the spin stiffness. On the other hand, ξ is described very well by the fitted value $2\pi\rho_s = 38.5meV$, represented by the solid line in the figure. In particular, the crossover from 2D Heisenberg to 2D Ising behavior is now captured, and the resulting value predicted for the Néel temperature is $T_N = 96.7K$, which is very close to the measured value of $T_N = 97.23K$. Surprisingly, the spin stiffness for the $S = 1$ system K_2NiF_4 is apparently $\sim 20\%$ smaller than that predicted by theory. In other words, quantum fluctuations seem to renormalize ρ_s more strongly than expected.

The static structure factor peak intensity is shown in Fig. 6-2. As for $Sr_2CuO_2Cl_2$ and La_2CuO_4 (for $T > T_{ST}$), it is found to be simply proportional to the square of the magnetic correlation length. However, while the form $A \sim T^2$ (or $S(0) \sim T^2\xi^2$) can be ruled out for K_2NiF_4, the data are also consistent with $A \sim T$ within the experimental error.

The good agreement shown in Fig. 6.1 between experiment and theory would appear to be a striking triumph for theory. However, the fact that theory seems to predict $2\pi\rho_s$ accurately in the $S = 1/2$ systems $Sr_2CuO_2Cl_2$ and La_2CuO_4 and less accurately in the $S = 1$ system K_2NiF_4 is a major conundrum. The good agreement

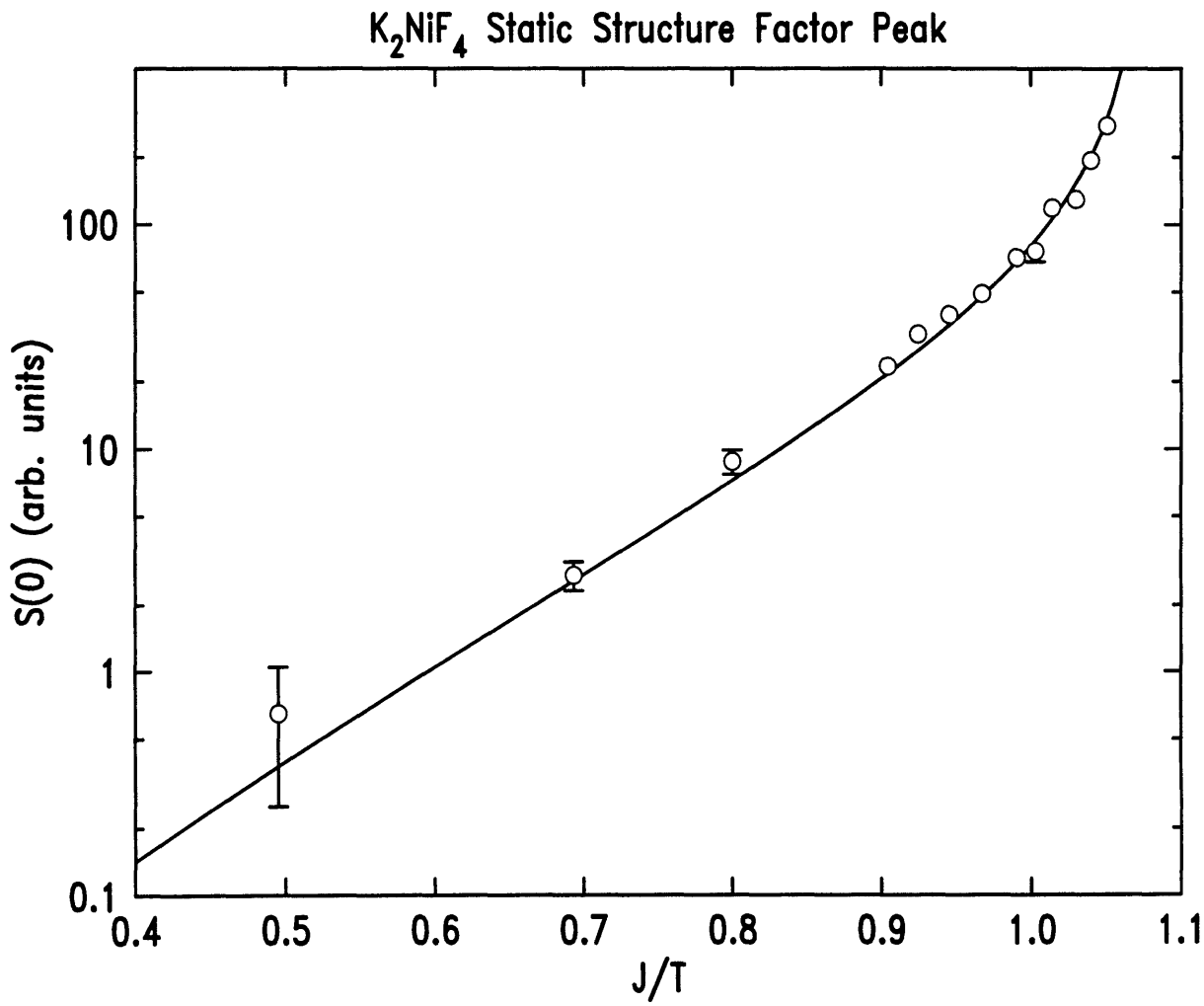

Figure 6-2: Static structure factor peak in K_2NiF_4. The solid line corresponds to $S(0) \sim \xi^2(\alpha_I, T)$ with $2\pi\rho_s = 38.5meV$.

for $Z_c(1)$ and $Z_\rho(1)$ between continuum (i.e. SWT [173, 174]) and lattice (i.e. series expansion techniques for the Heisenberg-Ising model [174]) approaches makes the observed behavior in K_2NiF_4 very difficult to understand. In particular, one would expect that SWT ought to become a better rather than a worse approximation with increasing S.

One possible caveat is that all of these calculations assume NN interactions alone. There are undoubtedly weak second neighbor exchange interactions in K_2NiF_4. In a study of the related $S = 5/2$ compound Rb_2MnF_4 [124], the ratio of second neighbor to NN exchange was determined to be $J_2/J_1 = 0.02$. However, only a much larger relative second neighbor exchange could possibly explain the significant discrepancy between the data for K_2NiF_4 and theory. Moreover, one would also have to understand why the NN theory works so well for the $S = 1/2$ systems $Sr_2CuO_2Cl_2$ and La_2CuO_4, and less well for the $S = 1$ system K_2NiF_4.

A rather exotic possibility is that, as in one dimension [225], there might by topological terms in the Lagrangian which lead to different physics for integer and half-integer spin values. To explore this further, experiments on other Heisenberg materials with $S \geq 1$ as well as numerical work (e.g. Monte Carlo and high-temperature series expansion) are clearly required. In the next Section, new results for the $S = 1$ system La_2NiO_4 are presented [54]. Section 6.2 contains a comparison of the experimental findings for the $S = 1/2$ and $S = 1$ materials with recent series expansion results [221].

6.1.2 La_2NiO_4

In the previous Section, the static structure factor data for K_2NiF_4 [52, 53] were re-analized [167] in the framework of HN's exact expression for the correlation length. The Ising anisotropy was taken into account via Eq. (6.1) and it was found, that $\xi(T)$ was described very well once the spin stiffness was reduced by $\sim 20\%$ from its theoretically predicted value. In this Section, recent results by Nakajima et al. [54] for the analogous $S = 1$ material La_2NiO_4 are presented. As we will see, the observations made for K_2NiF_4 are verified in detail.

Measurements of the spin-wave velocity in K_2NiF_4 give $c = 340(8) meV\mathring{A}$, which corresponds to $J = 28.5(7) meV$. This in turn corresponds to $2\pi\rho_s = 156 meV$ which, by coincidence, almost exactly equals the value for $2\pi\rho_s$ in La_2CuO_4. The measured in-plane spin-wave gap of La_2NiO_4 corresponds to an effective reduced Ising anisotropy field $\alpha_I = 0.002$. This value is very close to $\alpha_I = 0.0021$ found in K_2NiF_4.

In Figs. 6-3 and 6-4 the correlation length and Lorentzian amplitude for La_2NiO_4 are shown, respectively. Just as in K_2NiF_4, Eq. (6.1) with $\alpha_I = 0.002$ and $2\pi\rho_s$ fixed at the theoretical value does not describe the measured data satisfactorily. However, if the spin stiffness is reduced by $\sim 20\%$ to $2\pi\rho_s = 122 meV$, the data for La_2NiO_4 are again described very well. For both $S = 1$ systems it is found that fits of the exponential prefactor of Eq. (4.18) (with the spin stiffness held fixed at the theoretical value) describe the measured data reasonably well. However, the resultant prefactor is half of the *exact* value of $e/8 = 0.34$ obtained by HN. Given that the latter result is exact, there does not seem any justification for allowing the prefactor to be treated as an adjustable parameter.

Equation (6-1) with $\alpha_I = 0.002$ and $2\pi\rho_s = 122 meV$ predicts that $\xi/a \rightarrow \infty$ at $T = 305K$, which is about $23K$ below the 3D Néel temperature in the La_2NiO_4 crystal studied. The value $T = 305K$ is the predicted 2D Ising phase transition temperature. As noted in the previous Section, in K_2NiF_4 the identical theory predicts the observed phase transition temperature to within 1%. However, K_2NiF_4 is tetragonal while La_2NiO_4 is orthorhombic below $T_{ST} \sim 700K$. The resultant 3D interactions between the NN NiO_2 sheets in La_2NiO_4 apparently increase T_N from the 2D value of $\sim 305K$ to the 3D Néel temperature of $327.5K$.

In Fig. 6-4 the Lorentzian amplitude is shown. Over the temperature range $350K \leq T \leq 600K$, or equivalently, $0.19 \leq T/(2\pi\rho_s) \leq 0.33$ (with $2\pi\rho_s = 156 meV$), A is constant within the errors. Below $350K$, where there is a crossover from 2D Heisenberg to 3D Ising behavior, A decreases slightly. This implies a transfer of intensity from the 2D ridge to 3D critical scattering, which has been observed experimentally [54]. The behavior $A \sim$ *constant* above $350K$, as opposed to the theoretically predicted $A \sim T^2$ behavior, is fully consistent with the findings made for the

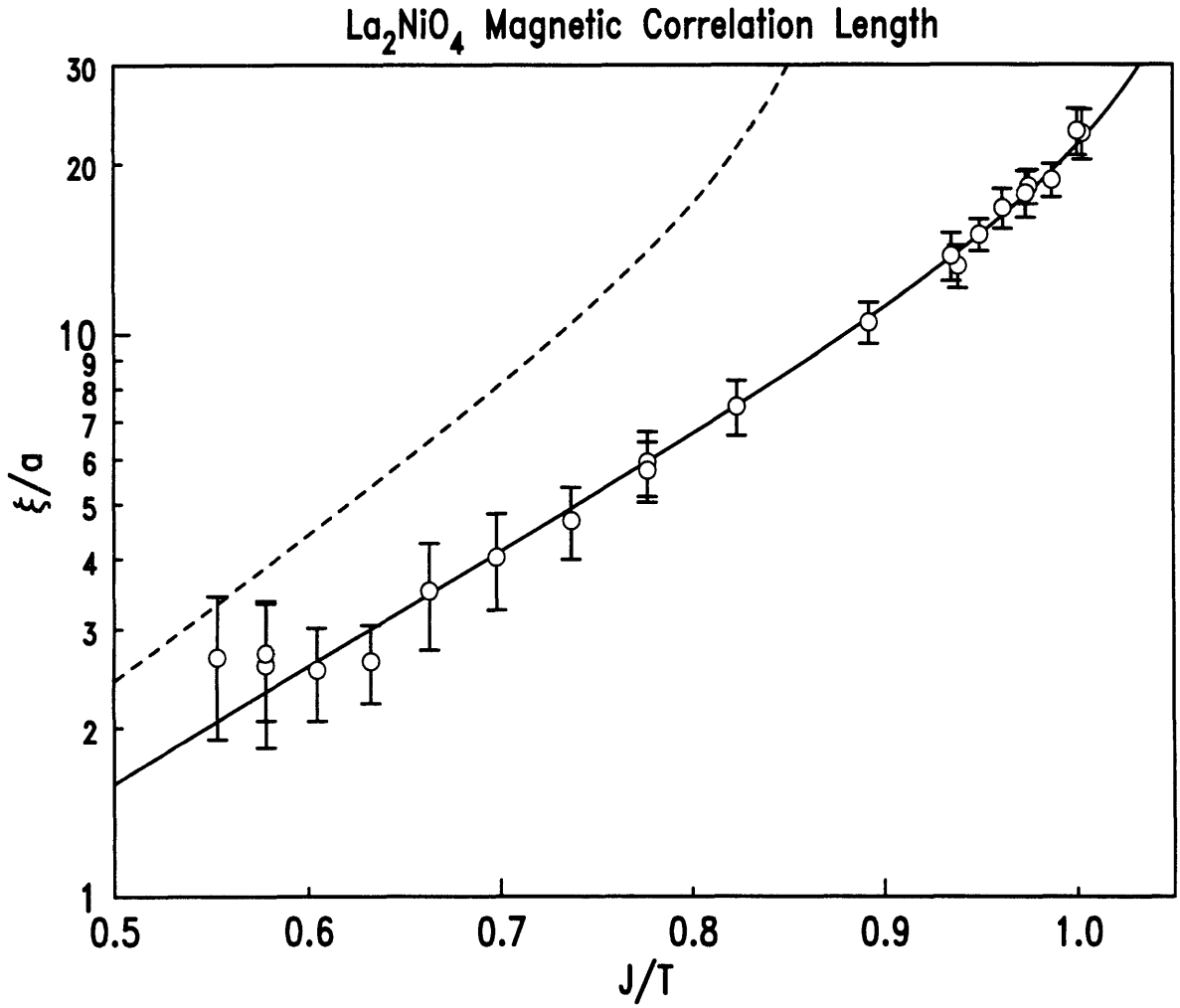

Figure 6-3: Magnetic correlation length in La_2NiO_4. Both lines were obtained from Eq. (6.1). The dashed line has no adjustable parameters, whereas the solid line is the result of a fit of the spin stiffness, which yielded a value $\sim 20\%$ smaller than that given by theory.

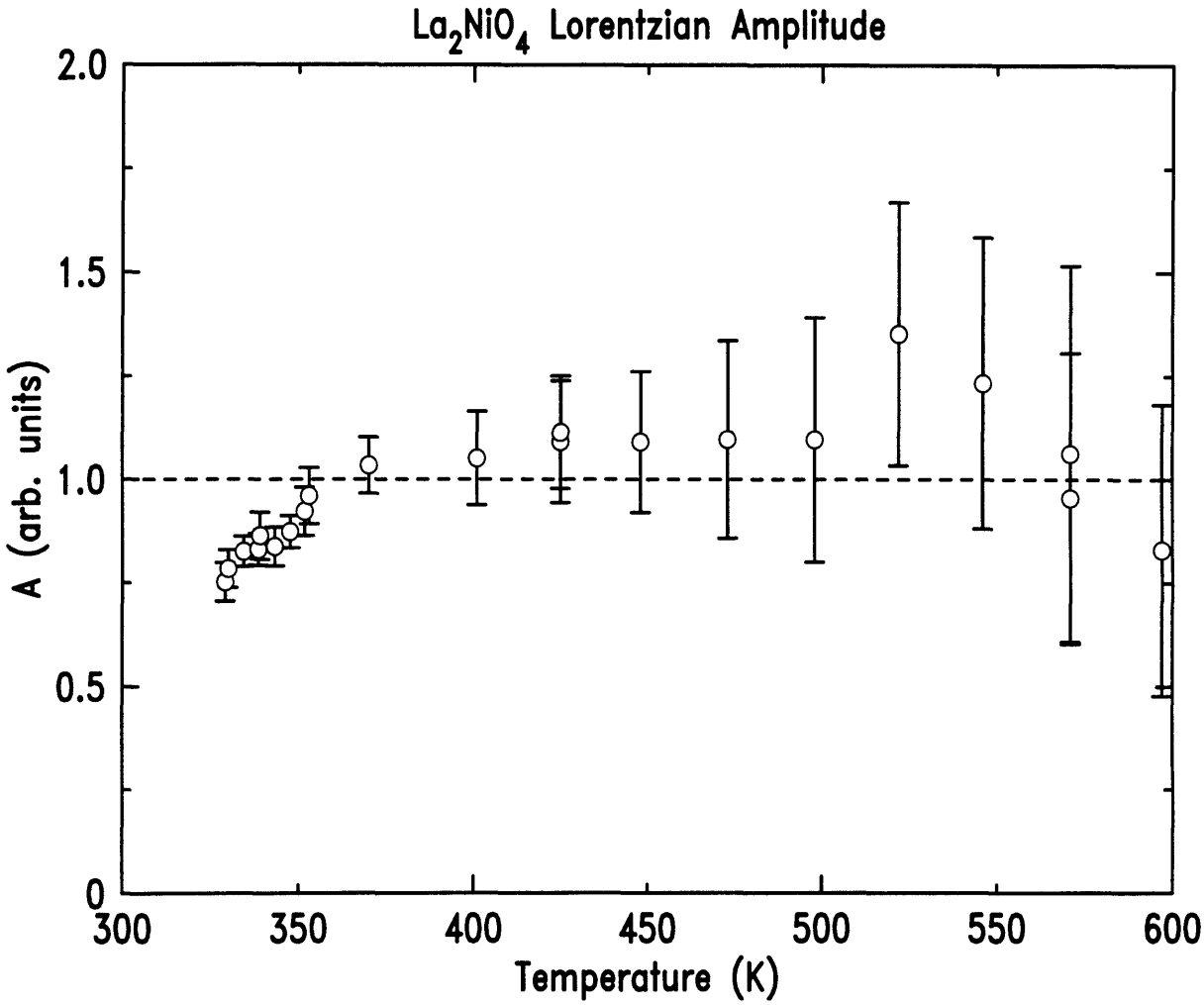

Figure 6-4: Lorentzian amplitude in La_2NiO_4.

other three Heisenberg systems studied in this thesis. While this might simply reflect the effects of higher order terms in $T/(2\pi\rho_s)$, it may indicate some deeper problem with the CHN-theory.

6.2 The 2D square-lattice Heisenberg antiferromagnet: Neutron scattering, Monte Carlo, series expansion, and theory for the QNLσM

The neutron scattering measurements of the correlation length in the $S = 1/2$ NN 2DSLQHA materials $Sr_2CuO_2Cl_2$ and La_2CuO_4 reveal a remarkable agreement with the analytic from Eq. (4.18) obtained by HN [57]. At first sight, one would expect the RC description to improve as the value of the spin increases. If S is formally regarded as a continuous variable, then the Néel order is expected to vanish for some $S < 1/2$. At the critical point of CHN's phase diagram, Fig. 4.1, where ρ_s vanishes, Eq. (4.18) fails, and the correlation length is inversly proportional to the temperature. Naively, increasing the value of spin moves the system away from this limit, so that the RC behavior would be more pronounced.

However, the analysis of the neutron scattering measurements of the correlation length in the $S = 1$ systems K_2NiF_4 and La_2NiO_4 shows that such an expectation does not hold. The correlation length data for both materials are shown in Fig. 6-5, and they agree very nicely. Note, that the superexchange differs by about a factor of three for the two materials. The dashed line is HN's analytical result Eq. (4.18), with the known values of ρ_s and c (Table 4.1). As discussed in the previous Sections, for both $S = 1$ systems the correlation length is described by Eq. (4.18) *only once the spin stiffness is reduced by* $\sim 20\%$. Interestingly, a reduction by $\sim 20\%$ of the quantum renormalization factor $Z_\rho(1) \simeq 0.87$ approximately equals $Z_\rho(1/2)$, the value for $S = 1/2$ (see Table 4.1). *It therefore seems as if quantum fluctuations renormalize the spin stiffness for* $S = 1$ *as strongly as for* $S = 1/2$. Note, that in the classical ($S \to \infty$) limit $Z_\rho, Z_c \to 1$.

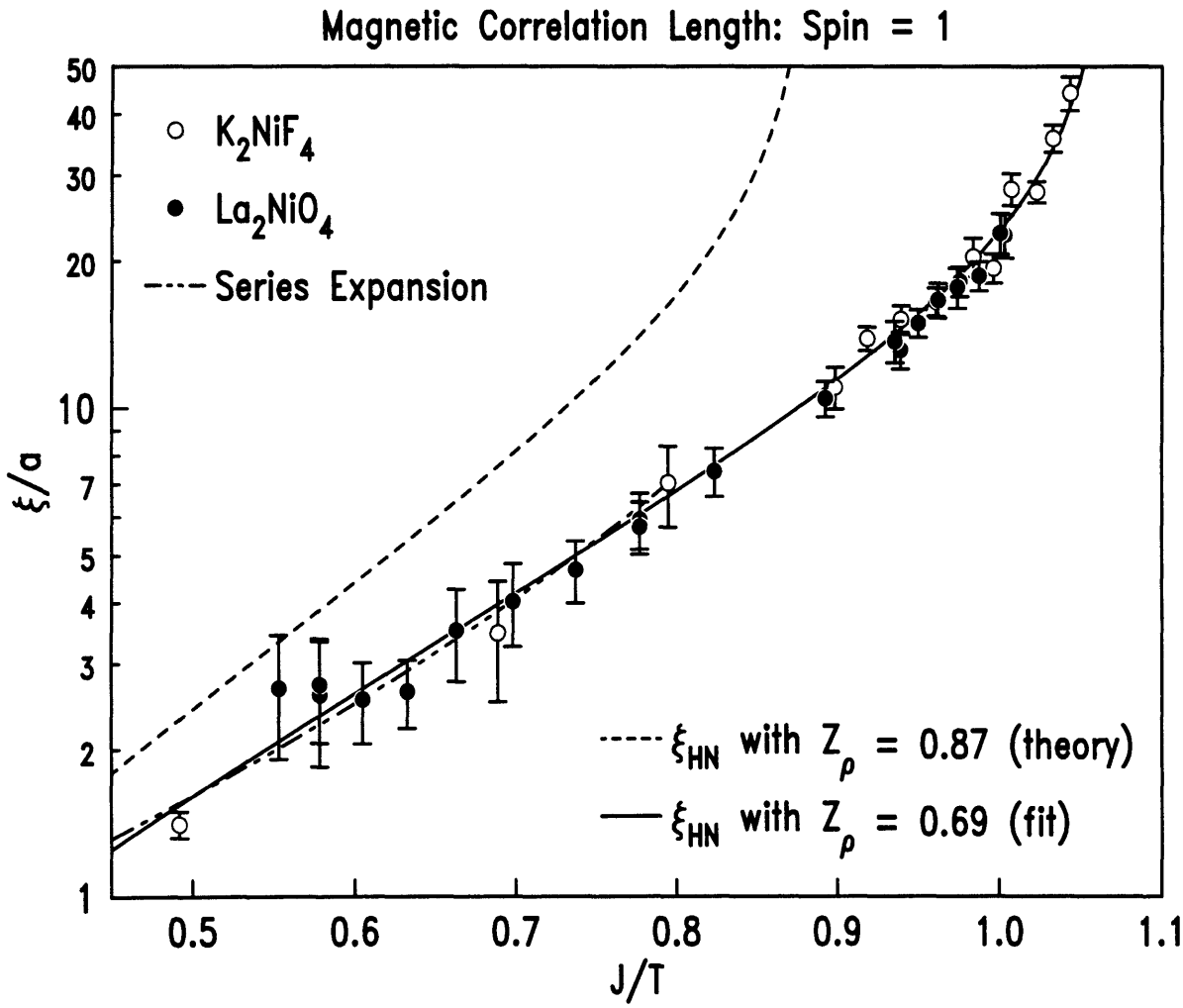

Figure 6-5: Magnetic correlation length for $S = 1$: K_2NiF_4, La_2NiO_4, series expansion, and RC theory for the QNLσM.

The long-short dashed line in Fig. 6-5 is the result of a very recent high-temperature series expansion study for the $S = 1$ NN 2DSLQHA [220]. It is found to be in excellent agreement with the neutron scattering results. Note, that this comparison contains no adjustable parameters. On the one hand, the series expansion result is a gratifying verification of the correctness of the neutron scattering work, while on the other hand it reinforces the discrepancy found with theory. *It is important to realize, that the comparison made is bewteen neutron scattering and series expansion work on the one side, and with the analytical result Eq. (4.18) for the QNLσM in the RC regime together with the quantum renormalization factors $Z_\rho(S)$ and $Z_c(S)$ on the other side.* The result by HN, Eq. (4.18), appears to be correct if only $Z_\rho(1)$ is replaced by $Z_c(1/2)$, as shown by the solid line in Fig. 6-5.. However, there is no theoretical justification (at least as of now) for such a reduction of $Z_\rho(1)$.

A systematic study of the 2D NN SLQHA as a function of spin S should give important insights into the source of the observed disagreement for $S = 1$ with theory. Preliminary experiments on the $S = 5/2$ system Rb_2MnF_4 reveal an even larger discrepancy with theory than that found for $S = 1$ [226]. Unfortunately, there are not many other good experimental realizations of the 2D NN SLQHA for $S > 1$. Moreover, Monte Carlo simulations for $S > 1/2$ have so far been hindered by the freezing effect discussed in the previous Chapter.

However, it is possible to carry out high-temperature series expansion to larger values of spin. In a collaboration with Norbert Elstner, Rajiv Singh, and Alexander Sokol, the spin dependence of correlations obtained from series expansion was analyzed [221]. The ratio between ξ, as obtained form series expansion, and the Hasenfratz and Niedermayer formula is plotted in Fig. 6-6 as a function of T/ρ_s for $1/2 \leq S \leq 5/2$. Since the values used for c and ρ_s are those from SWT, Table 4.1, the theoretical correlation length is labelled ξ_{HN}^{SWT}. Contrary to the naive expectation that the RC behavior becomes more pronounced as S increases, but consistent with the systematic trend seen experimentally, it is found that for the ranges of temperature probed ξ monotonically deviates from ξ_{HN}^{SWT} as S increases.

In an attempt to understand this result, three possible scaling scenarios are con-

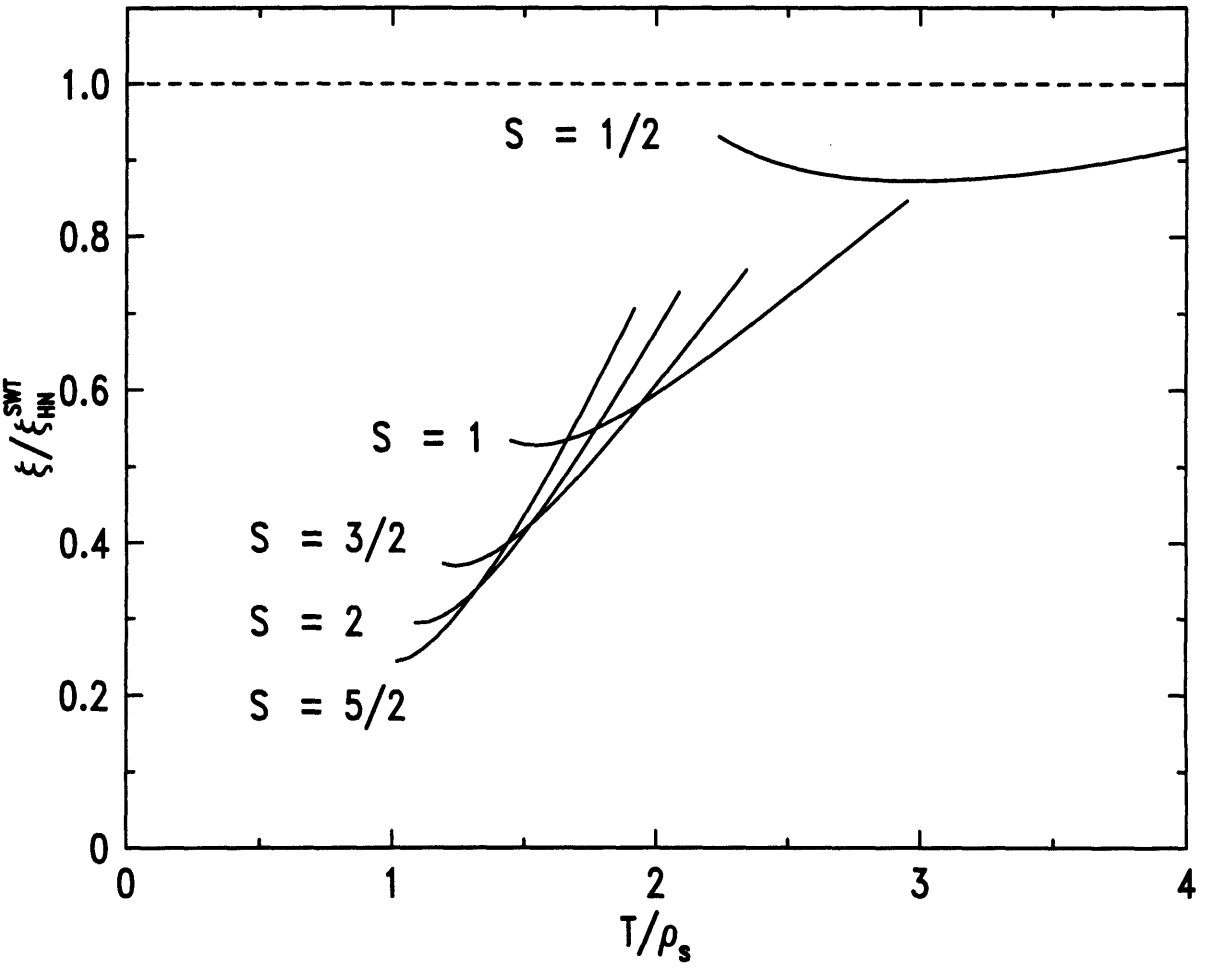

Figure 6-6: Series expansion results for the correlation length for $1/2 \leq S \leq 5/2$ plotted as ξ/ξ_{HN}^{SWT} versus T/ρ_s. ξ_{HN}^{SWT} is the exact RC prediction, Eq. (4.18), with c and ρ_s from SWT (see Table 4.1)

sidered. Note, that HN's analytic form for the correlation length, Eq. (4.18), may be written as

$$\frac{S\xi}{a} = \frac{eZ_c(S)}{2^{5/2}\pi Z_\rho(S)} exp\left(2\pi Z_\rho(S)\left(\frac{JS^2}{T}\right)\right)\left[1 - \frac{1}{4\pi Z_\rho(S)}\left(\frac{T}{JS^2}\right) + \cdots\right], \qquad (6.2)$$

which suggests plotting $S\xi/a$ versus $T/(JS^2)$ to elucidate the dependence on S. The result is shown in Fig. 6-7 for $Sr_2CuO_2Cl_2$ ($S = 1/2$), K_2NiF_4 ($S = 1$), Monte Carlo ($S = 1/2$), and series expansion ($1/2 \leq S \leq 5/2$). For K_2NiF_4, only the data above the 2D Heisenberg to 2D Ising crossover regime are shown. Surprisingly, over the range $S\xi/a$ from 1 to ~ 50, the data to a good approximation fall on the same curve. The experimental data for La_2CuO_4 ($S = 1/2$) and La_2NiO_4 ($S = 1$), which also fall onto the approximate "scaling" curve of Fig. 6-7, have been omitted for the sake of clarity.

It was demonstrated in Chapter 4 that Eq. (6.2) describes the correlation length data in the two $S = 1/2$ systems $Sr_2CuO_2Cl_2$ and $La_2Cu_2O_4$ extremely well *in absolute units*. This theoretical prediction is indicated by the solid line in Fig. 6-7. (Note, that while $Z_c(1/2)$ is consistently predicted to be $Z_c(1/2) \simeq 1.18$ by the three different theoretical approaches listed in Table 4.1, the values for $Z_\rho(S)$ vary slightly. In the analysis in this and the preceeding Chapters, the intermediate value $Z(1/2) = 0.73$, i.e. $2\pi\rho_s = 1.15J$, was chosen.) Interpreted naively, Fig. 6-7 would then suggest that RC behavior holds for all S, but with quantum renormalization factors $Z_\rho(S)$ and $Z_c(S)$ that are nearly S-independent for $1/2 \leq S \leq 5/2$ and close to their values at $S = 1/2$

An even better agreement is achieved if $Z_c(S)$ is allowed to vary as predicted by SWT. This second scaling scenario is shown in Fig. 6-8, which was derived form Fig. 6-7 by simply scaling the correlation length by the additional factor $1/Z_c^{SWT}(S)$. From Eq. (6.2) it can be seen that, upon dividing both sides by $Z_c^{SWT}(S)$, the right-hand side depends on S only through $Z_\rho(S)$ and $T/(JS^2)$. On the one hand, Fig. 6-8 appears to suggest that the implicit S-dependence through $Z_\rho(S)$ is nearly negligible, i.e. that $Z_\rho(S) \simeq Z_\rho(1/2)$. This observation was already made earlier for the $S = 1$

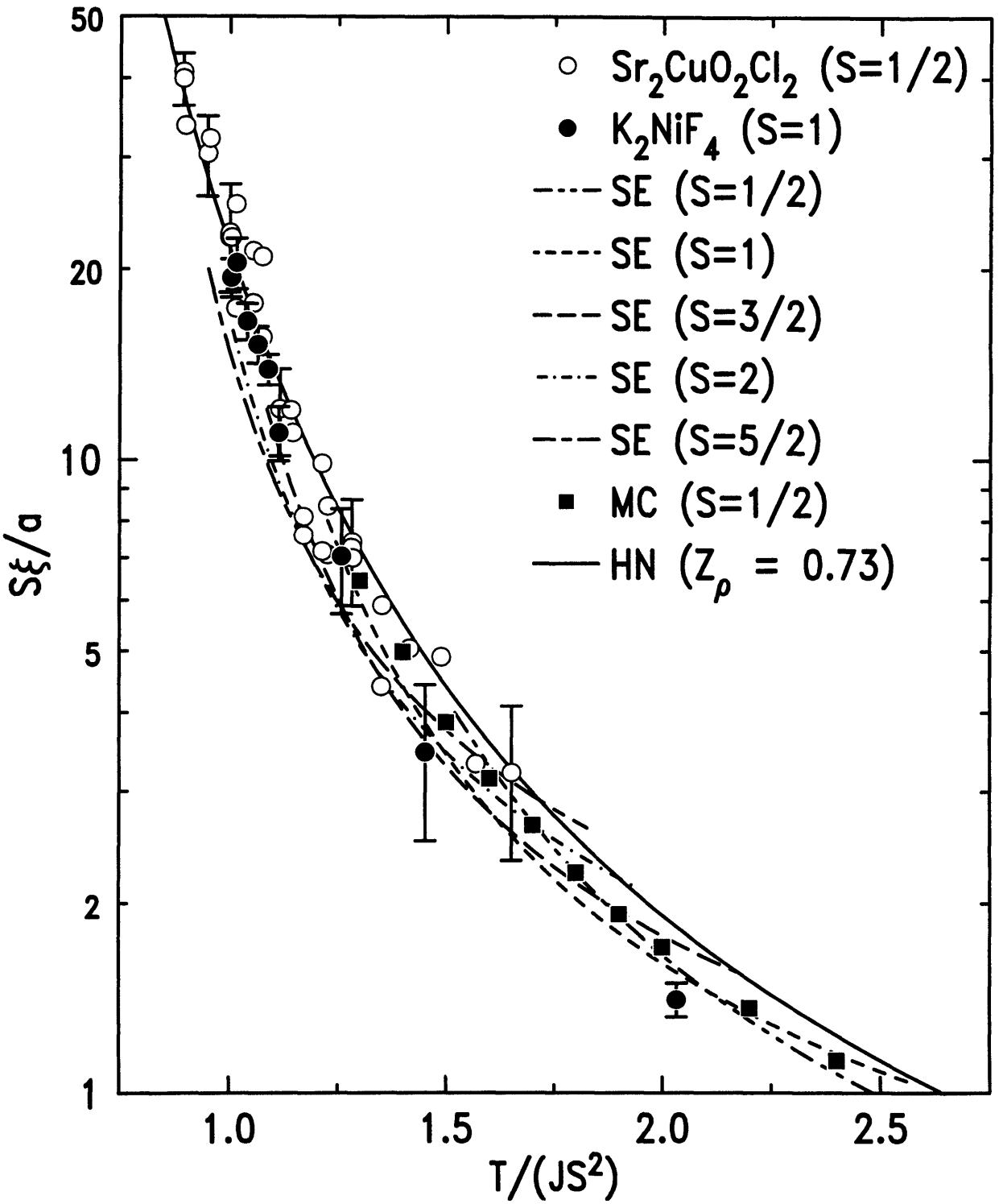

Figure 6-7: Semilog plot of $S\xi/a$ versus T/JS^2: $Sr_2CuO_2Cl_2$ ($S = 1/2$), K_2NiF_4 ($S = 1$), series expansion ($1/2 \leq S \leq 5/2$), Monte Carlo ($S = 1/2$), and RC theory for the QNLσM.

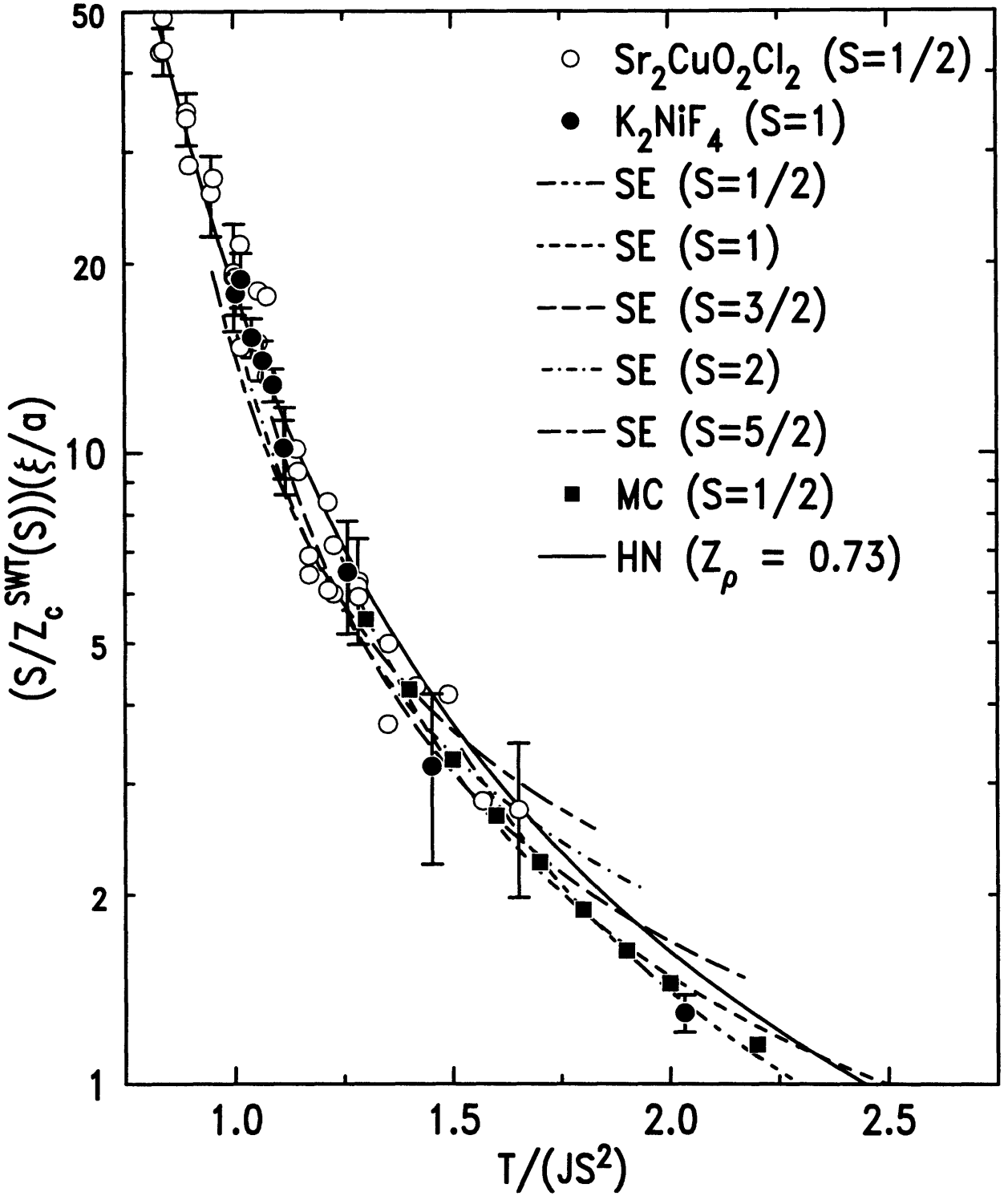

Figure 6-8: Semilog plot of $(S/Z_c^{SWT}(S))(\xi/a)$ versus T/JS^2: $Sr_2CuO_2Cl_2$ ($S = 1/2$), K_2NiF_4 ($S = 1$), series expansion ($1/2 \leq S \leq 5/2$), Monte Carlo ($S = 1/2$), and RC theory for the QNLσM.

systems. Since the series expansion data extend to temperatures at which $\xi = a$, the systematic deviation at high temperatures for $S > 1$ from the "scaling curve" might thus be due to lattice effects. On the other hand, SWT predicts a substantial S-dependence: $Z_\rho(5/2) \simeq 0.95$, which is already close to the classical limit ($S \to \infty$) in which $Z_\rho \to 1$. Serious errors in the SWT values for $Z_\rho(S)$ (and $Z_c(S)$) seem unlikely, given their good agreement for $S = 1/2$ and $S = 1$ with those obtained by other methods.

A third approach to understand these data comes from the observation that at any fixed $T/(JS^2)$ RC theory will inevitably fail for sufficiently large values of spin. Indeed, a straightforward application of Eq. (6.2) to the $S \to \infty$ limit taken at $T/(JS^2) \sim 1$ would predict that $\xi \to 0$. However, the above limit corresponds to the *classical* Heisenberg model, ξ/a is known to be non-zero and of order unity for $T \sim JS^2$.

One can understand where Eq. (6.2) may fail by following CHN in their derivation of the leading asymptotic behavior in the RC regime, but taking into account that S may be large. CHN have shown that for $T << \rho_s$ the magnetic correlations can be calculated using *classical dynamics*, except that all wavevector integrations should be limited to $|\vec{q}| \lesssim q_c = T/c$ rather than taken over the whole Brillouin zone. The words "classical dynamics" simply mean that for $|\vec{q}| \lesssim q_c$, all Bose factors for spin-waves can be approximated assuming $cq << T$. For $T << \rho_s$, the correlation length $\xi(T)$ of the *quantum* Heisenberg model can then be obtained from the expression for the correlation length $\xi_{CL}(T)$ of the *classical* Heisenberg model,

$$\xi_{CL} = a_{CL} \frac{T}{\rho_{CL}} exp\left(\frac{2\pi\rho_{CL}}{T}\right), \tag{6.3}$$

by substituting the lattice spacing of the classical model, a_{CL}, by $const \times (c/T)$. Note, that $\rho_{CL} = JS(S+1)$ is the *classical* spin stiffness, and that the above expression for ξ_{CL} is the asymptotic $T \to 0$ form.

The cutoff wavevector can be estimated as

$$q_c \sim \frac{T}{c} = \frac{\rho_s}{c}\frac{T}{\rho_s} \sim \frac{S}{a}\frac{T}{\rho_s} \sim \frac{S}{a}\frac{T}{JS^2}. \tag{6.4}$$

For $S >> 1$ and $T \sim \rho_s \sim JS^2$, $q_c \sim S/a >> \pi/a$ is *outside* the Brillouin zone. Hence, the requirement that $cq \lesssim T$, or equivalently $q \lesssim q_c$, places no further restrictions on the q-integrations which are already limited by the Brillouin zone. In this case, all of the integrals are the same as those of the classical Heisenberg magnet, and the classical ($S \to \infty$) limit is recovered.

The crossover temperature T_{cr} between RC and classical regime depends on S, and its order of magnitude can be estimated as the temperature where $q_c \sim 1/a$:

$$T_{cr} \sim \frac{c}{a} \sim JS. \tag{6.5}$$

By Substituting T_{cr} into Eq. (6.2), one concludes that the crossover from RC behavior at low temperatures to classical behavior at higher temperatures should occur for a crossover length $\xi_{cr} = \xi(T_{cr})$ that is larger for larger S.

In order to test this scenario, the correlation length is plotted in Fig. 6-9 as a function of $T/(JS(S+1))$, where $JS(S+1)$ is the *classical* (and not $T = 0$) spin stiffness. In replacing S^2 by $S(S+1)$, one follows a purely empirical observation that the correlation length, as determined by high-temperature series expansion, seems to depend on S primarily through the combination $S(S+1)$ for $S > 3/2$ and $T >> JS$. (For $T << JS$, ξ depends on S through ρ_s and c.) The series expansion results for $T >> JS$ indicate that

$$\xi(S,T) \simeq \xi_{CL}(T_{CL}), \tag{6.6}$$

where $T_{CL} = T/(JS(S+1))$. This result supports the hypothesis that the deviations from asymptotic RC behavior in Figs. 6-5 and 6-6 are primarily driven by RC to classical crossover effects. It furthermore suggests that the phase diagram for the QNLσM has to be modified as shown schematically in Fig. 6-10.

In summary, three possible scaling scenarios for the combined Monte Carlo ($S =$

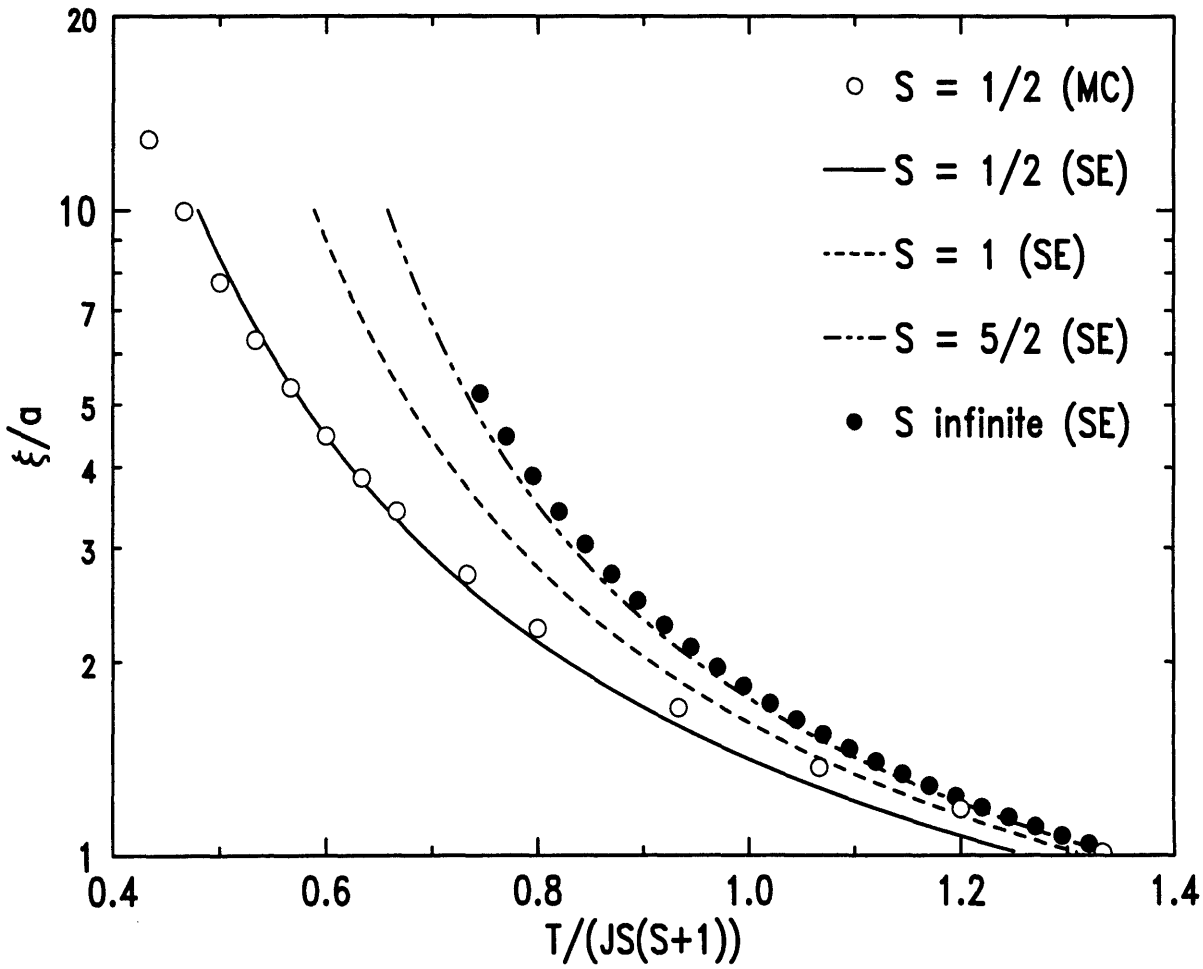

Figure 6-9: Semi-log plot of the correlation length versus $T/(JS(S+1))$: Monte Carlo (MC; $S = 1/2$) and series expansion (SE; $S = 1/2, 1, 5/2$, and infinite). For larger spins, ξ/a is close to the classical ($S \rightarrow \infty$) limit, which provides evidence that classical ($S \rightarrow \infty$) magnetic behavior holds for $JS << T << JS^2$. Note, that in most of the temperature range shown, the $S \rightarrow \infty$ model is not in the scaling limit, and its correlation length deviates from the expected $T \rightarrow 0$ behavior $\xi/a \simeq 0.01 \times T/(JS^2)exp(2\pi JS^2/T)$ [186].

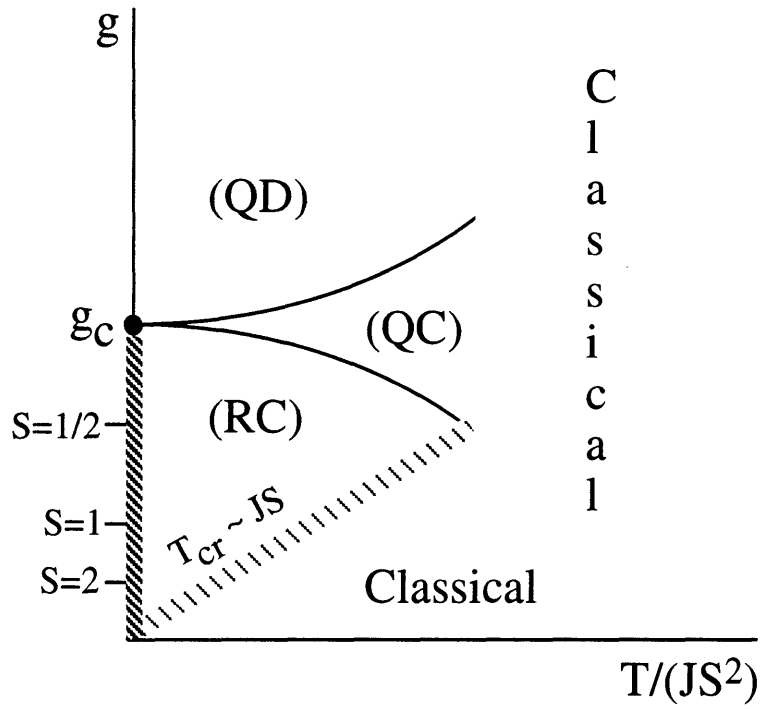

Figure 6-10: Modified phase diagram for the QNLσM as suggested by the third scaling scenario discussed in the text.

1/2), neutron scattering ($S = 1/2$ and 1), and high-temperature series expansion ($1/2 \leq S \leq 5/2$) data for the spin-S NN 2DSLQHA have been discussed. On the one hand, the first two scenarios (represented by Figs. 6-7 and 6-8) seem to suggest that quantum fluctuations for the spin stiffness are more prominent for $S \geq 1$ than previously thought. In particular, Fig. 6-8 appears to imply that $Z_\rho(5/2) = Z_\rho(2) = \cdots = Z_\rho(1/2)$. On the other hand, the third scaling scenario seems to suggests just the opposite: The quantum renormalization factors are predicted correctly by theory (Table 4.1), but the RC form for the correlation length, ξ_{HN}, must not be used for $S \geq 1$ for the temperatures accessed experimentally and numerically. According to the latter scenario, the relevant physics for $S > 1/2$ is that of the crossover regime from RC to classical, and the RC expression for the correlation length, ξ_{HN}, would only become valid at much lower temperatures (i.e. much larger ξ). The data collapse in Figs. 6-7 and 6-8 would then be a mere coincidence. Clearly, more theoretical work is required in order to resolve this issue.

Chapter 7

Photoemission Spectroscopy in $Sr_2CuO_2Cl_2$

For reasons not yet understood, as charge carriers are introduced into the CuO_2 sheets, the lamellar copper oxides evolve from insulating 2D antiferromagnets to high-temperature superconductors, and finally to non-superconducting metals. There exist two contrasting views of the metallic normal state of these materials. The first view is that a one-electron approach to the description of the metallic phase is appropriate. This scenario has been supported by the observation of seemingly large Fermi surfaces in photoemission spectroscopy studies [6, 227, 228, 229], consistent with local density approximation (LDA) band calculations. Since it is known that a one-electron description fails to describe the physics at low doping (e.g., La_2CuO_4 is a charge-transfer insulator and not a metal), this approach is based on the belief that the physics of the superconductors is fundamentally different from that of the insulators.

The second view of the phase diagram in Fig. 1-5 is that electron-electron correlations are still fundamentally important in the metallic state. There is strong evidence from transport, neutron scattering, and NMR, against the existence of a sharp phase transition, and in favor of a continuous evolution of the physical properties as a function of doping. In particular, while a one-electron picture would require the Fermi surface to become smaller upon doping, transport measurements indicate that the number of carriers grows linearly, and therefore suggest that the Fermi surface in-

creases as well. Direct evidence that strong correlation effects persist in the metallic samples comes from the observation by PES of satellite structures near the Cu core levels and below the valence band [230].

Most theories that attempt to describe the normal state of the lamellar copper oxides indeed follow the second approach, and are generally based on variants of the Hubbard or $t-J$ Hamiltonians discussed in Chapter 1. In the undoped limit, they correctly capture the *low-energy* behavior of the lamellar copper oxides, i.e. they reduce to the $S = 1/2$ Heisenberg model studied in the previous Chapters. However, away from this limit these models are not well defined. Yet despite these idealizations they still seem intractable, and it is not uncommon that completely different conclusions are deduced from the same Hamiltonian.

Very clean and well-defined sample surfaces are needed for a successful PES experiment. Consequently, measurements in the lamellar copper oxides have been limited to only a few selected compounds which could meet these requirements. In particular, previous experiments have almost exclusively focussed on metallic lamellar copper oxides. The study of $Sr_2CuO_2Cl_2$ by Wells et al. [135, 136] presented in this Chapter constitutes the first conclusive PES measurement of an insulating lamellar copper oxide. More precisely, the dispersion of a single hole in an antiferromagnetic background has been measured. It has thus become possible to test the $t-J$ and Hubbard models in a regime in which they are believed to best describe the physics of the lamellar copper oxides. Furthermore, a direct comparison with existing PES data for metallic (and at low enough temperatures superconducting) compounds provides new insights into the phenomenology of the doping process.

Figure 7-1 is a schematic diagram of the PES experiment, which was carried out at the undulator beam line 5 at the Stanford Synchrotron Radiation Laboratory. A clean sample surface was prepared by cleaving the $Sr_2CuO_2Cl_2$ crystals in ultra-high vacuum (UHV). $Sr_2CuO_2Cl_2$ is very micatious and cleaves naturally in the [0 0 1]-direction. Monochromatic light is shone onto the sample and absorbed by electrons in the material. Since the photons have negligible momentum compared to the electrons, the electron momentum $\vec{k}$ is essentially conserved in the excitation process (apart from

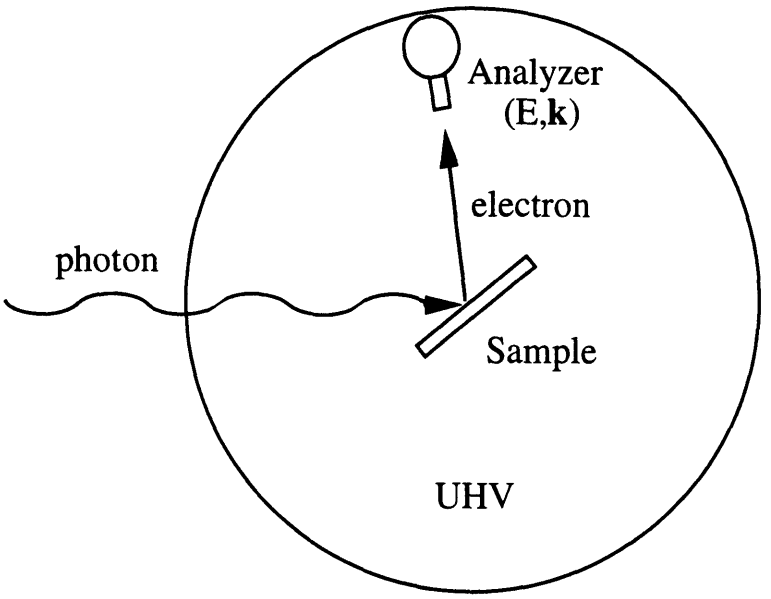

Figure 7-1: Schematic diagram of the photoemission experiment. A clean surface was prepared by cleaving the $Sr_2CuO_2O_2$ crystals in ultra-high vacuum (UHV). Monochromatic photons excite electrons into the vacuum. The electrons are collected, energy analyzed, and counted [5].

a reciprocal lattice vector). For electrons that are sufficiently energetic to overcome the work function and exit the sample, the momentum parallel to the sample surface will be conserved. It is therefore possible to map out the energy versus $\vec{k}$ relations in the two-dimensionally correlated lamellar copper oxides, with $\vec{k}$ confined to the CuO_2 sheets [5].

The study discussed here is an angle-resolved PES (ARPES) experiment in which the band structure of $Sr_2CuO_2Cl_2$ was mapped out as a function of the 2D electron momentum $\vec{k}$. The experiment had an energy resolution of $75meV$, and the angular resolution of the emitted electrons was $\pm 1°$, or $\pm(1/20)\pi$ in k_x and k_y. Note, that in this Chapter the notation for the 2D Brillouin zone for the square-planar CuO_2 sheet (with lattice constant $a = 1$) will be used. In this notation, the Brillouin zone has edges at $(\pm\pi, k_y)$ and $(k_x, \pm\pi)$, and corners at $(\pm\pi, \pm\pi)$. The corners correspond to the antiferromagnetic ordering wavevectors denoted (1 0 0) in the Bmab notation used in the previous Chapters.

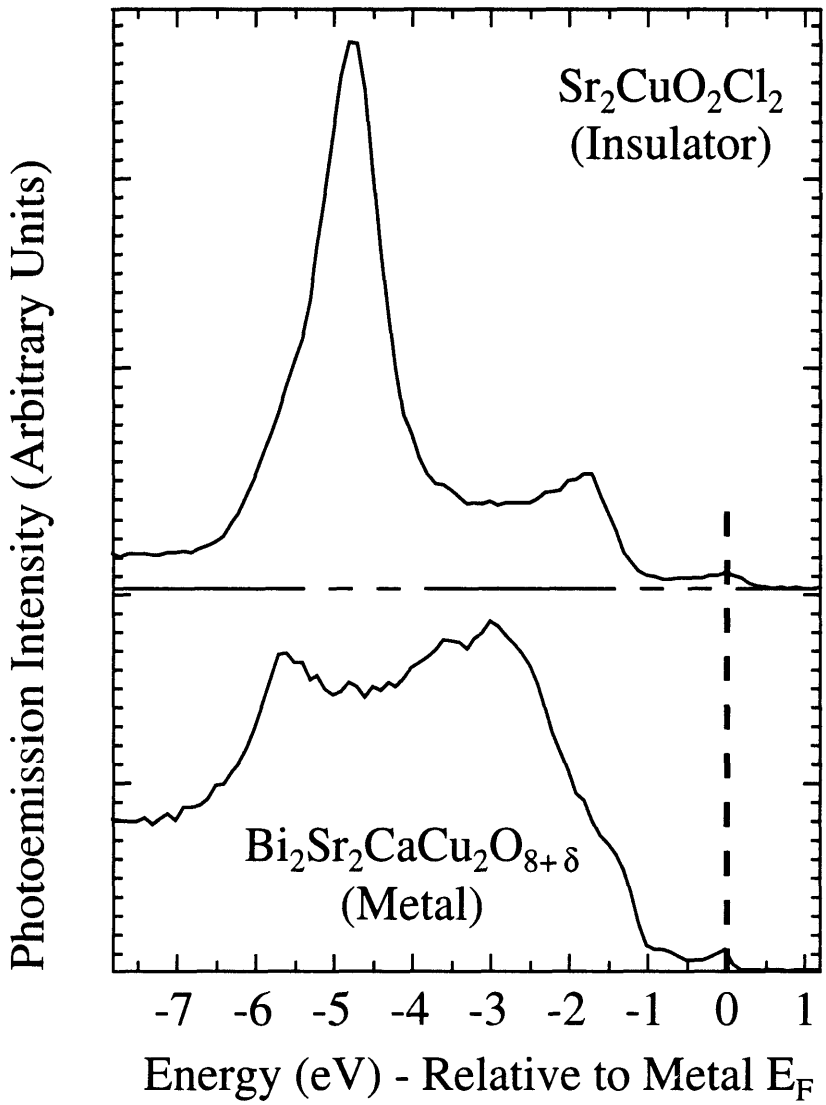

Figure 7-2: Comparison of the photoemission spectra near $(\pi/2, \pi/2)$ of the entire valence band in insulating $Sr_2CuO_2Cl_2$ and metallic $Bi_2Sr_2CaCu_2O_{8+\delta}$. The spectra are aligned so that the "feet" at the highest energy match, and the energy scale is that for $Bi_2Sr_2CaCu_2O_{8+\delta}$ (from Wells [5]).

The full valence band spectrum of $Sr_2CuO_2Cl_2$ is very similar to the spectra for the metallic lamellar copper oxides [227, 228, 6, 229]. This can be seen from Fig. 7-2, in which the spectrum obtained in $Sr_2CuO_2Cl_2$ is compared with that of metallic $Bi_2Sr_2CaCu_2O_{8+\delta}$ [5]. Both spectra are $\sim 7eV$ wide, and exhibit several intense peaks as well as a "foot" with relatively small intensity. The foot region at the top of the valence band spectrum contains the band of lowest energy (i.e. the band closest to the Fermi level) and will be the focus of the discussion below.

All data were taken at $T = 350K$ since the conductivity at this temperature was large enough to avoid charging of the sample. At $T = 350K$ the magnetic correlation length of $Sr_2CuO_2Cl_2$ is $\xi \sim 250\AA$ (see Fig. 4-5). Since PES is a very fast local probe, the effects of antiferromagnetic order are therefore still be visible. Figure 7-3(a) contains a set of scans taken at different $\vec{k}$ positions along the direction from the zone center $(0,0)$ to the antiferromagnetic superlattice position (π,π). As $\vec{k}$ is increased, a peak appears and disperses towards higher energies, reaches a maximum at $(\pi/2,\pi/2)$, then suddenly loses intensity, and shifts back to lower energies. The total dispersion is $280(60)meV$, and the point $(\pi/2,\pi/2)$ is the *valence band maximum*, with an energy $\sim -0.8eV$ relative to E_f. To obtain an accurate measure of the Fermi energy E_f, the Fermi-Dirac cutoff of a Au reference sample was used.

In Fig. 7-3(b), analogous data for the metallic copper oxide $Bi_2Sr_2CaCu_2O_{8+\delta}$ are shown [6]. The peaks in the metal are sharper and disappear after crossing the Fermi level near $(0.45\pi, 0.45\pi)$. From the similarity between the two spectra it is tempting to conclude that doping has moved the Fermi level into the valence band of the insulator. Within the experimental error, the insulator and the metal have the same dispersion over the $\vec{k}$ range from $(0.27\pi, 0.27\pi)$ to $(0.45\pi, 0.45\pi)$: $240(30)meV$ and $270(30)meV$, respectively.

For sets of scans parallel to the one shown in Fig. 7-3a, the peak intensity was always found to drop as the antiferromagnetic Brillouin zone boundary (the line connecting $(\pi,0)$ and $(0,\pi)$) was crossed. The weak part of the band results from a folding of the zone due to the presence of antiferromagnetic correlations. This drop in spectral weight is analogous to that expected for a weak coupling spin-density

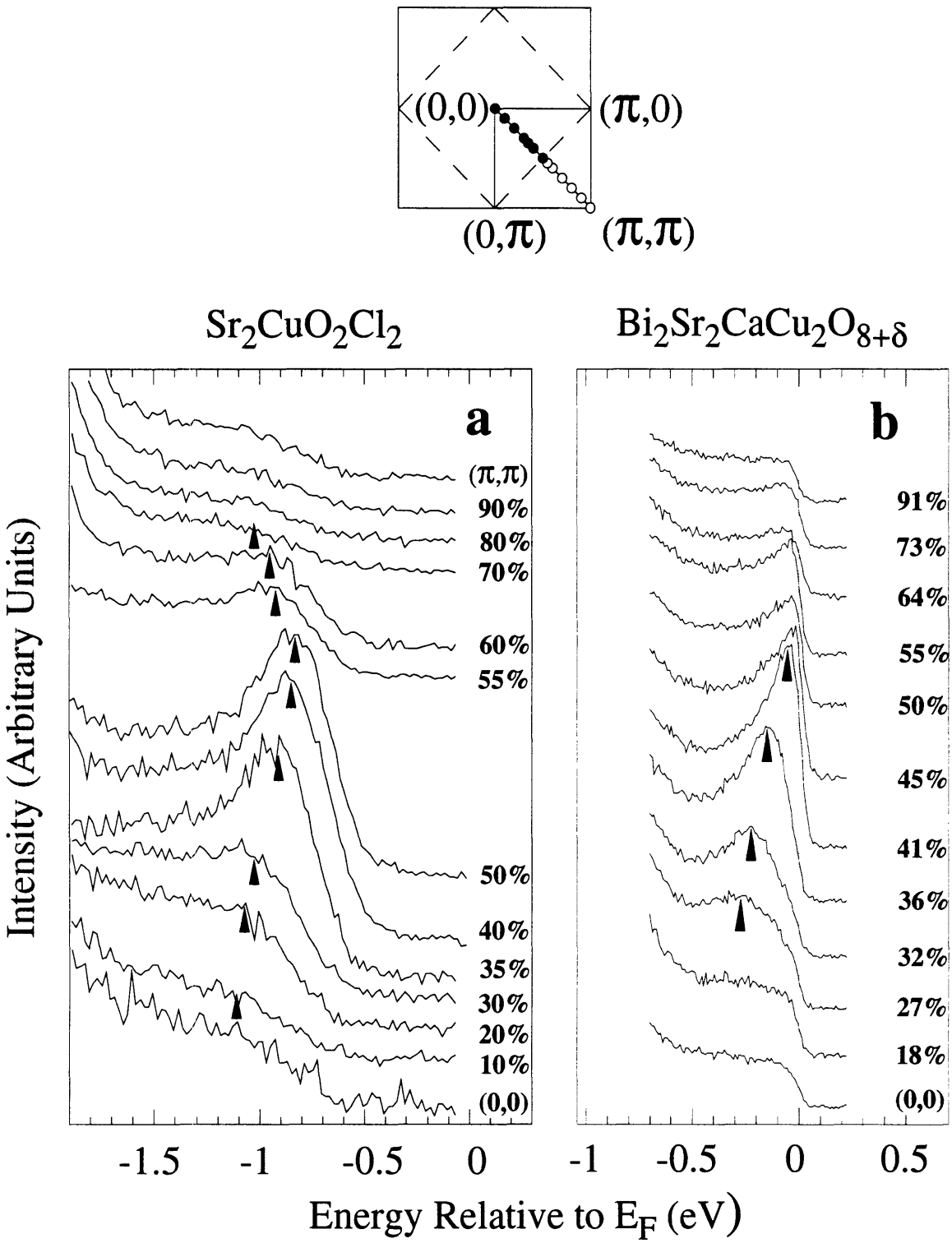

Figure 7-3: ARPES data of the peak dispersion from $(0,0)$ to (π,π) for (a) insulating $Sr_2CuO_2Cl_2$ and (b) metallic $Bi_2Sr_2CaCu_2O_{8+\delta}$ (from Dessau et al. [6]). The daggers beneath each spectrum are guides to the eye. The dark (open) circles in the legend are on the side of the zone where the peak is strong (weak) in the insulator. The size of the circles indicates the experimental $\vec{k}$ resolution.

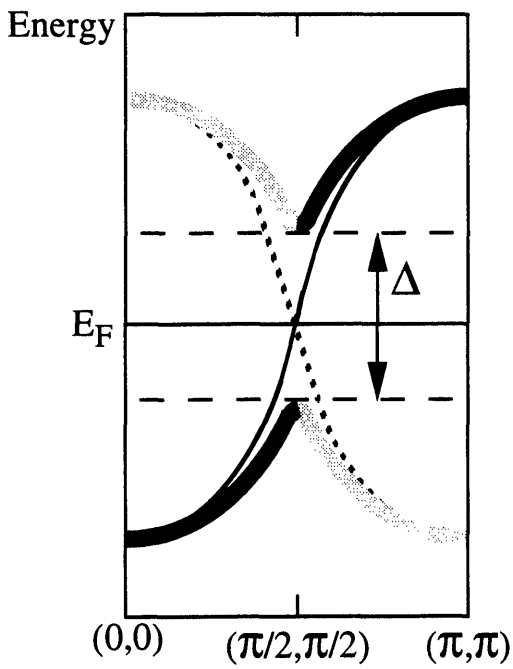

Figure 7-4: Spin-density wave analogy of the formation of an insulating gap. The original band is indicated by the continuous thin line. The folding of the zone due to the presence of antiferromagnetic correlations results in new bands with parts of weak (shaded thick line) and strong (solid thick line) oscillator strength.

wave model [231], as illustrated in Fig. 7-4, and is also evident in Monte Carlo calculations of the spectral weight function for the Hubbard model at intermediate coupling strengths [231]. For strong coupling one would expect that the original and folded sections of the band would have nearly equal weight. Thus the variation in spectral weight could indicate that $Sr_2CuO_2Cl_2$ is in the intermediate coupling regime.

The peak dispersion of $Sr_2CuO_2Cl_2$ along the antiferromagnetic Brillouin zone boundary is shown in Fig. 7-5(a). The dispersion in this direction of the Brillouin zone is very similar to that of Fig. 7-3(a), but there is no sudden drop in in intensity as observed in the (π,π)-direction. It is found that the overall band dispersion is isotropic around $(\pi/2,\pi/2)$ within the experimental error. In Figs. 7-5(b) and 7-5(c) data for $Sr_2CuO_2Cl_2$ and $Bi_2Sr_2CaCu_2O_{8+\delta}$ [6] taken from $(0,0)$ to $(\pi,0)$ are compared. While the insulator exhibits no peak dispersion and only shows some modulation in spectral weight, a peak disperses to near E_F in the metal, and remains in the vicinity of the Fermi level over a wide range of $\vec{k}$. This flat-band region is part

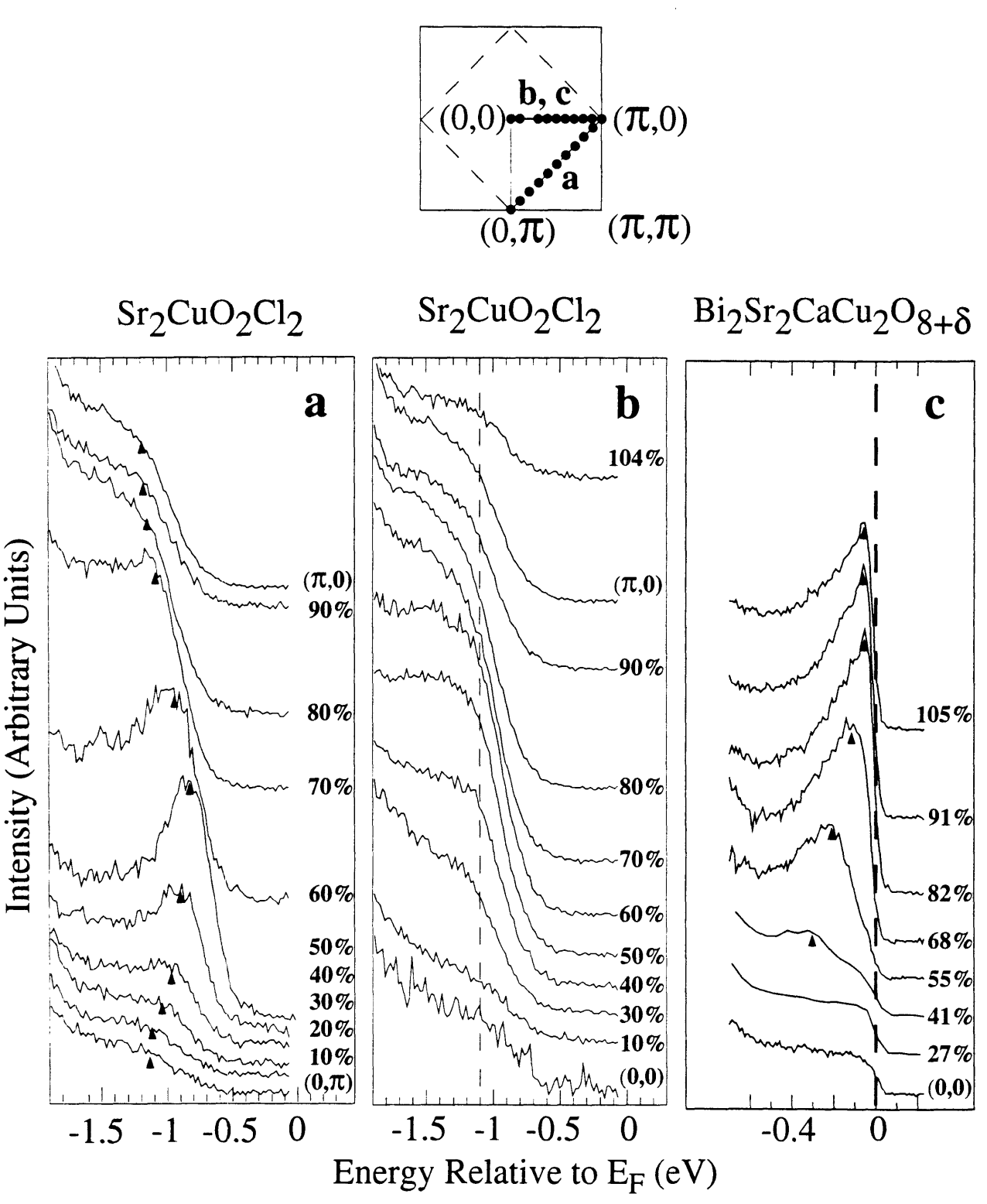

Figure 7-5: PES data along $(\pi, 0) - (\pi/2, \pi/2) - (0, \pi)$ for (a) $Sr_2CuO_2Cl_2$, and along $(0, 0) - (\pi, 0)$ for both (b) $Sr_2CuO_2Cl_2$ and (c) $Bi_2Sr_2CaCu_2O_{8+\delta}$ (from Dessau et al. [6]).

of an extended saddle point feature near $(\pi, 0)$, and has been observed in all hole-doped compounds studied to-date [230]. It contains most of the spectral weight in the density of states near E_F, and is furthermore the region in $\vec{k}$-space where the largest superconducting gaps have been observed in $Bi_2Sr_2CaCu_2O_{8+\delta}$ [230]. The states that form the extended saddle point are the key feature that distinguishes the metal from the insulator, and must move up in energy upon doping.

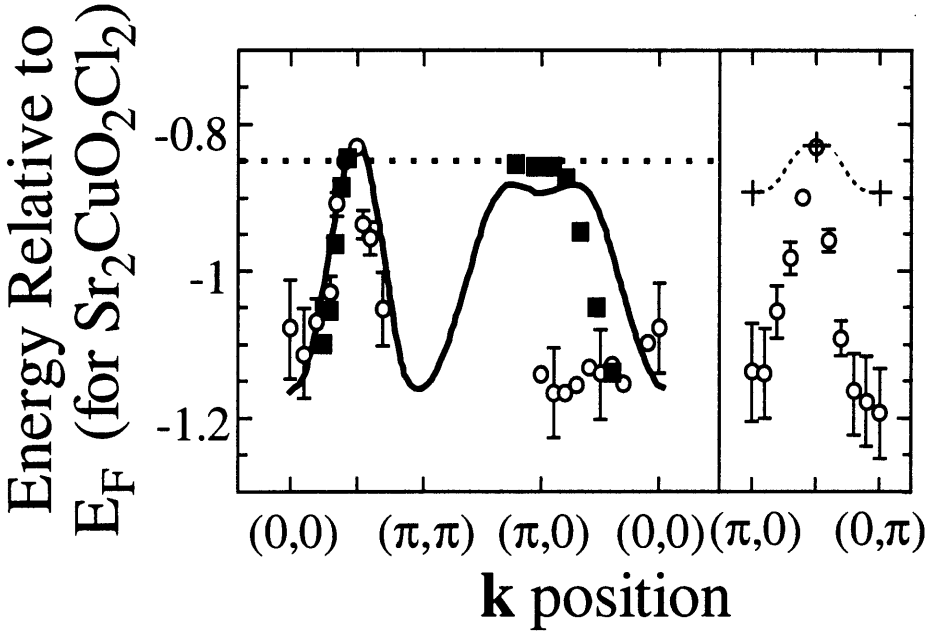

Figure 7-6: Comparison of the dispersion relations in $Sr_2CuO_2Cl_2$ and $Bi_2Sr_2CaCu_2O_{8+\delta}$ (from Dessau et al. [6]) with a calculation for the $t-J$ model (from Liu and Manousakis [7]).

In Fig. 7-6, the dispersion relation for $Sr_2CuO_2Cl_2$ is compared with the result of a numerical solution of one hole in the $t-J$ model [7]. The peak positions for the measured spectra were obtained from fits to a simple Lorentzian added to a background and convolved with the experimental resolution function. In the region from $(0,0)$ to (π,π) the $t-J$ model provides a good description of the results for the insulator. The experimental band width from $(0,0)$ to $(\pi/2,\pi/2)$ is $W = 280(60)meV = 2.2(5)J$ (with $J = 125(6)meV$ for $Sr_2CuO_2Cl_2$ [1]), in very good agreement with the $t-J$ model calculation which predicts that $W = 2.2J$ over a wide range of t/J [7]. One-electron calculations, on the other hand, yield a total occupied bandwidth of $\sim 1eV$

at half filling, and a total bandwidth of $\sim 3.25eV$ [232].

The good agreement between experiment and $t-J$ model calculation for the segment from $(0,0)$ to (π,π) as well as for the overall bandwidth is contrasted by the stark difference found near $(\pi,0)$. While the overall dispersion for $Sr_2CuO_2Cl_2$ is isotropic, the nature of the band as predicted by the $t-J$ model is very different. *Probably the most striking observation to be made from Fig. 7-6 is that the $t-J$ model calculation appears to agree better with the data for the metal than with those for the insulator.* Note, that the data for $Bi_2Sr_2CaCu_2O_{8+\delta}$ have been shifted in energy in order to facilitate the comparison. If it were not for the fact that theory disagrees with the experiment for the insulator in an important way, the good agreement with the data for the metal would imply that the process of doping has simply filled a rigid band of undoped states. In analogy to the observation made for the insulator, the apparent lack of dispersing peaks in the second magnetic Brillouin zone can be ascribed to a drop in spectral weight due to the folding of the zone. However, the $t-J$ model calculation is only truly defined for a single hole dispersing in an antiferromagnetic background. Since it does not even fully agree with the measurements for $Sr_2CuO_2Cl_2$, a comparison with the data for the metal seems rather inappropriate. More recent $t-J$ model calculations [89, 233] as well as calculations on small clusters of the Hubbard model with intermediate U [231] also disagree with the experiment near $(\pi/2,0)$. It therefore seems that the physics of the doped lamellar copper oxides contains important aspects not fully captured by these simplified models. However, very recent work on the three-band Hubbard model appears to correctly capture the full dispersion observed in the $Sr_2CuO_2Cl_2$ [234].

From the discussion above it is clear that a rigid band doping model could only account for the evolution upon doping seen from $(0,0)$ to (π,π). The states that make up the extended saddle point in the metal must move up in energy as a result of doping. At low doping one would expect a small ellipsoidal hole pocket Fermi surface centered at $(\pi/2,\pi/2)$, as shown in Fig. 7-7(e). If the spectral weight variation observed in $Sr_2CuO_2Cl_2$ is still present in the metallic copper oxides, then this would affect the measured Fermi surfaces. Photoemission would not easily detect the band

dispersing back down below E_F from $(\pi/2, \pi/2)$ to (π, π). This is indicated by the thin lines in Fig. 7-7(e). At higher doping, the hole pockets may merge together to form large Fermi surfaces as indicated in Fig. 7-7(f). The Fermi surfaces that correspond to the bands with low spectral weight may furthermore be too faint to be detected. The parts of the Fermi surface that are easily visible might then resemble a large one-electron Fermi surface derived from rigid band doping, as shown in Fig. 7-7(c).

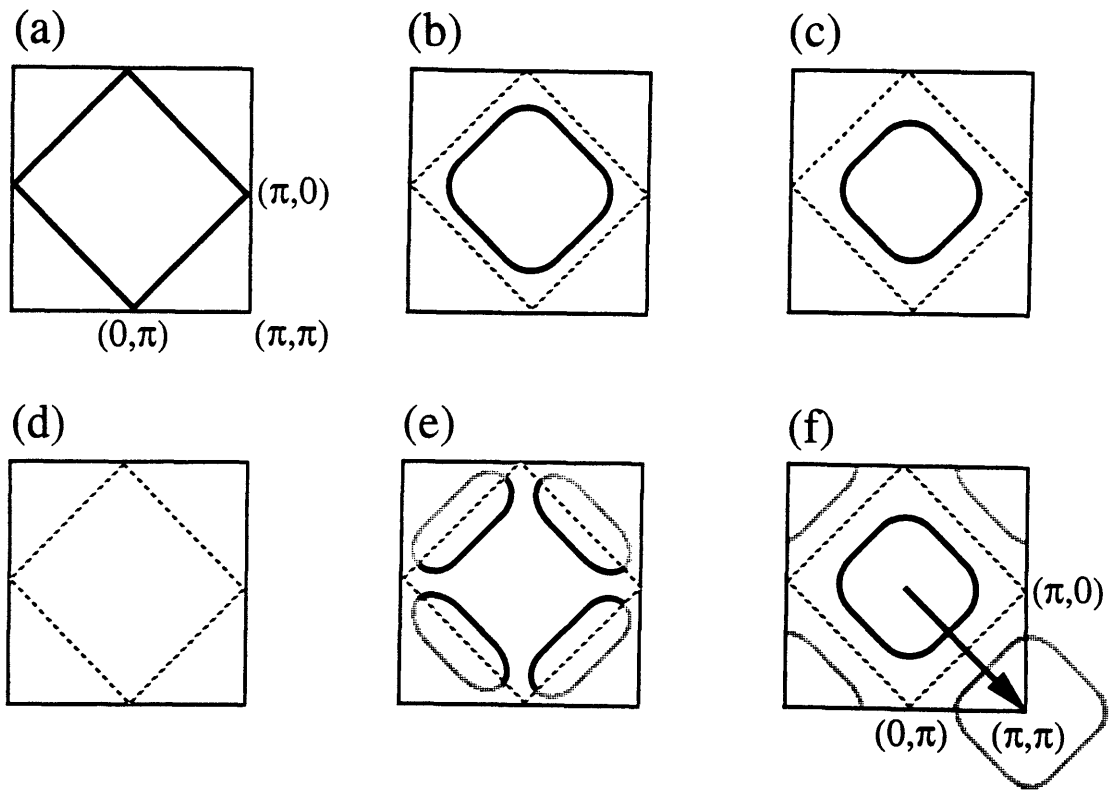

Figure 7-7: (a)-(c) Evolution of the Fermi surface upon doping as expected from band theory, and (d)-(f) as suggested by the comparison of the data in the insulator $Sr_2CuO_2Cl_2$ with those of the metal $Bi_2Sr_2CaCu_2O_{8+\delta}$. The portion of the Fermi surface that derives from the original band has stronger oscillator strength (thick lines).

Aebi et al. [235] have recently reported a ARPES study of the Fermi surface in metallic $Bi_2Sr_2CaCu_2O_{8+\delta}$. They found a strong Fermi surface close to that expected from LDA calculations, as well as a weak Fermi surface of similar shape, but shifted by a translation of (π, π). These features were interpreted in terms of antiferromagnetic correlations resulting in a $c(2 \times 2)$ superstructure. In light of the

results for $Sr_2CuO_2Cl_2$ discussed in this Chapter is appears that this interpretation may be correct. At least it seems very likely that the weak Fermi surface sections in $Bi_2Sr_2CaCu_2O_{8+\delta}$ correspond to the regions where the weak band was observed in $Sr_2CuO_2Cl_2$.

In summary, the $\vec{k}$-dependent single particle excitation spectrum of the highest energy band in the model insulating copper oxide $Sr_2CuO_2Cl_2$ has been measured by ARPES. The analysis of the band dispersion indicates that a Hubbard-type model may be a proper starting point to describe the doped lamellar copper oxides. Calculations based on the $t-J$ and one-band Hubbard models correctly predict the band width and the location of the valence band maximum, but do not correctly describe the overall band shape. The evolution of states near $(\pi, 0)$ as well as the stong variation in spectral weight are new and important aspects of the physics of the lamellar copper oxides. Clearly, more experimental and theoretical work is necessary to further explore these issues.

Chapter 8

Magnetism in superconducting $La_{1.85}Sr_{0.15}CuO_4$ ($T_C = 37.3K$) and non-superconducting $La_{1.83}Tb_{0.05}Sr_{0.12}CuO_4$

8.1 Symmetry of the superconducting order parameter

Below the superconducting transition temperature T_c, the electron-pair wavefunction $\phi(\vec{r})$, which is proportional to the order parameter of the macroscopic condensate, has non-zero amplitude. Its symmetry properties are constrained by the Pauli exclusion principle, and the BCS-mechanism of phonon-mediated pairing results in a spin-singlet ($S = 0$) s-wave ($L = 0$) pairing state. The energy gap, $\Delta(\vec{k})$, in the quasiparticle excitation spectrum is the absolute value of the Fourier transform of $\phi(\vec{r})$. Since for conventional superconductors the pairing state is s-wave, the corresponding gap is isotropic, as illustrated in Fig. 8-1(a). Furthermore, the BCS-model for weak electron-phonon coupling predicts $2\Delta = 3.54T_c$. Consequently, the density of states for one-quasiparticle excitations is zero below the gap, which manifests

itself in exponentially activated temperature dependences of many thermodynamic properties.

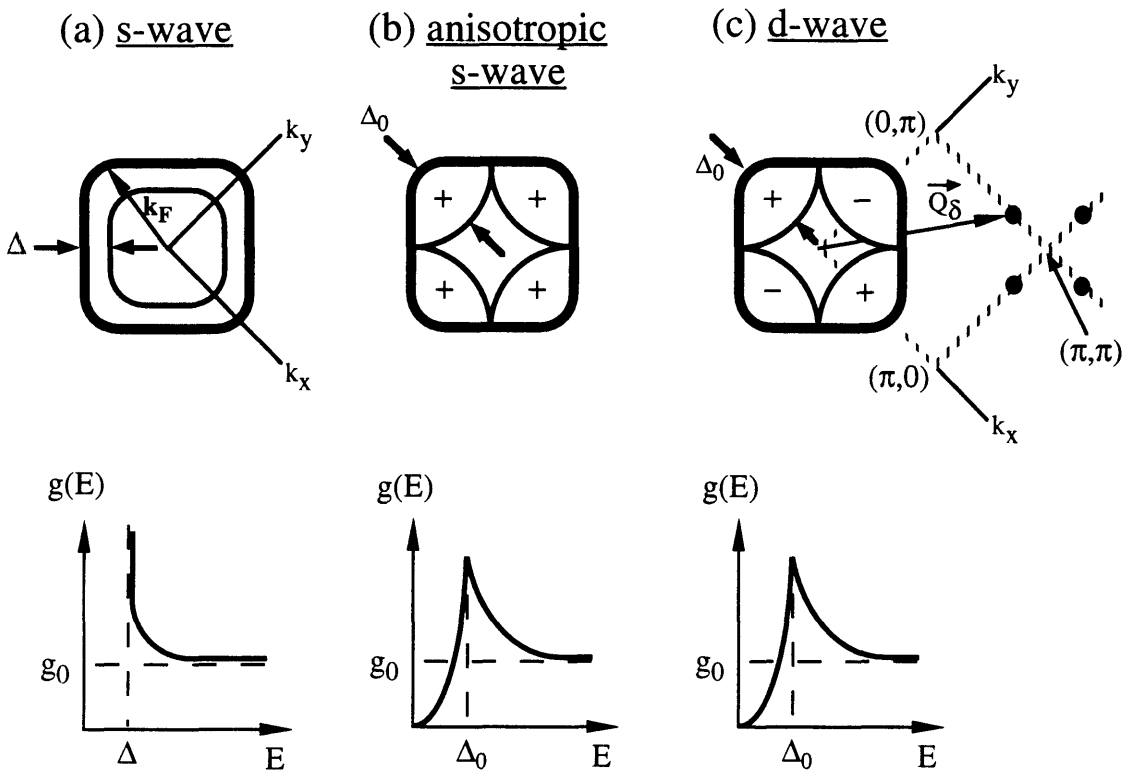

Figure 8-1: Superconducting gap function and density of states $g(E)$ for various pairing symmetries of a superconductor with tetragonal symmetry. The Fermi surface is indicated by the thick lines. The amplitude of the order parameter is given by the distance of the thin lines from the Fermi surface, while its relative phase can be either "+" or "-". (a) s-wave symmetry has constant amplitude and phase. (b) Anisotropic s-wave has the four-fold symmetry of the lattice. (c) d-wave symmetry has two-fold symmetry. A phase-sensitive probe is required to distinguish between (b) and (c). Note, that the order parameter in (b) and (c) has zeros (nodes) in the directions $(\pm\pi, \pi)$ and $(\pi, \pm\pi)$, and maxima in the directions $(\pm\pi, 0)$ and $(0, \pm\pi)$. It is furthermore finite in the directions $\vec{Q}_\delta$ of the incommensurate inelastic magnetic scattering observed in $La_{2-x}Sr_xCuO_4$.

For the high-temperature superconductors, knowledge of the symmetry of the pairing state would serve as an important constraint for the development of a successful theory. Because of the presence of strong electronic correlations and the concurrent weak electron-phonon coupling, the pairing attraction is thought to predominantly

(if not exclusively) result from the electronic degrees of freedom. Theories based on strong correlations [236, 237, 90] or exchange of spin fluctuations [238, 239] all necessitate that the pairing symmetry is $d_{x^2-y^2}$-wave (i.e., $L = 2$), since for this symmetry the competing effects of on-site Coulomb repulsion and pairing attraction are optimized. As a result, the quasiparticle gap is expected to have nodes, as shown in Fig. 8-1(c), and to be of lower symmetry than the CuO_2 sheets. Since the gap vanishes at nodes on the Fermi surface, the density of states is finite at low energies, giving rise to power-law (rather than exponentially activated) behavior in thermodynamic quantities. For example, one would expect $\lambda_0(T) \sim T$ for the temperature dependence of the London penetration depth [240]. Such a temperature dependence has indeed been observed by Hardy et al. [241] in high-quality crystals of $YBa_2Cu_3O_{6.95}$. In conventional s-wave superconductors, the square-root singularity of the density of states at $E = \Delta$ (see Fig. 8-1(a)) gives rise to a coherence peak (or Hebel-Schlichter peak) in the NMR relaxation rate $1/T_1$ just below T_c. This peak is absent in the high-temperature superconductors. Moreover, it was found in studies of $YBa_2Cu_3O_7$ that $1/T_1 \sim T^3$ at low temperatures [242, 243], rather than exponentially activated behavior.

The penetration depth and NMR experiments point to the existence of nodes in the gap. However, the evidence from these probes is only indirect, as they measure averages over the Fermi surface. The first direct evidence for the existence of an anisotropic gap came from the angle-resolved photoemission (ARPES) experiments in $Bi_2Sr_2CaCu_2O_{8+\delta}$ by Wells et al. [244], which were later on verified in greater detail [245]. These measurements were found to be consistent with $d_{x^2-y^2}$-wave pairing, and therefore provided an important constraint for theoretical models. However, the superconducting gap as revealed be ARPES only reflects the magnitude of the order parameter. In order to distinguish between $d_{x^2-y^2}$-wave and anisotropic s-wave, illustrated in Fig. 8(b), information about the phase of the pairing wavefunction is required. The first experiment sensitive to the phase of the order parameter was carried out by Wollman et al. [246], who measured the phase coherence in bimetallic dc SQUIDs made up out of $YBa_2Cu_3O_{6.8}$ and Pb. They found evidence for a phase

shift of π between the $\hat{a}$- and $\hat{b}$-directions of their single crystals, as expected for a $d_{x^2-y^2}$-wave pairing state. There have been many other experimental attempts to determine the symmetry of the order parameter, and the vast majority of them are most naturally interpreted as evidence for either $d_{x^2-y^2}$-wave or "dirty" $d_{x^2-y^2}$-wave pairing. Dirty $d_{x^2-y^2}$-wave [247, 248] means that the additional effects of impurity and disorder scattering have been taken into account. Quite generally, this results in averages of the order parameter over the Fermi surface.

By far most of the experiments pertaining to the gap symmetry have been carried out in the bilayer materials $Bi_2Sr_2CaCu_2O_{8+\delta}$ and $YBa_2Cu_3O_{6+\delta}$. The only measurement to date that provides evidence of an anisotropic gap in a single-layer material has been the Raman study by Chen et al. [249] in $La_{1.83}Sr_{0.17}CuO_4$. Neutron scattering measurements in $La_{1.85}Sr_{0.15}CuO_4$ by Thurston et al. [75] and Matsuda et al. [8] were found to be inconsistent with simple s-wave superconductivity, since low-energy excitations ($< 3.54T_c$) were observed well below T_c. Mason et al. [9] pursued a neutron scattering and specific heat study of $La_{1.86}Sr_{0.14}CuO_4$ and suggested that their result was consistent with gapless superconductivity induced by localized magnetic impurities. Matsuda et al. [8] demonstrated that their data are in complete agreement with those by Mason et al. [9]. This comparison is reproduced in Fig. 8-2. In $La_{2-x}Sr_xCuO_4$, for $x \gtrsim 0.05$, the magnetic scattering is incommensurate and centered at the four equivalent positions $((1 \pm \delta)\pi, \pi))$ and $((\pi, (1 \pm \delta)\pi)$, also referred to as $\vec{Q}_\delta$ ($\delta = 0.22 - 0.24$ for $x = 0.14 - 0.15$). This is illustrated in Fig. 8-3. The comparison made in Fig. 8-2 is thus for the dynamic susceptibility $Im\chi(\vec{Q}_\delta, \omega)$. It is evident that the temperature dependences exhibited by the two sets of data agree within the experimental error. In particular, the susceptibility at low temperatures and energies is non-zero, and thus there is no sign of a gap in the magnetic excitation spectrum due to the superconductivity. Nevertheless, the measured spectra could be consistent with dirty $d_{x^2-y^2}$-wave or dirty anisotropic s-wave pairing.

Because of limitations in crystal volume and homogeneity, the only other lamellar copper oxide studied by neutron scattering has been the bi-layer compound $YBa_2Cu_3O_{6+\delta}$ [250, 251, 252, 253]. Curiously, the spin fluctuations in this mate-

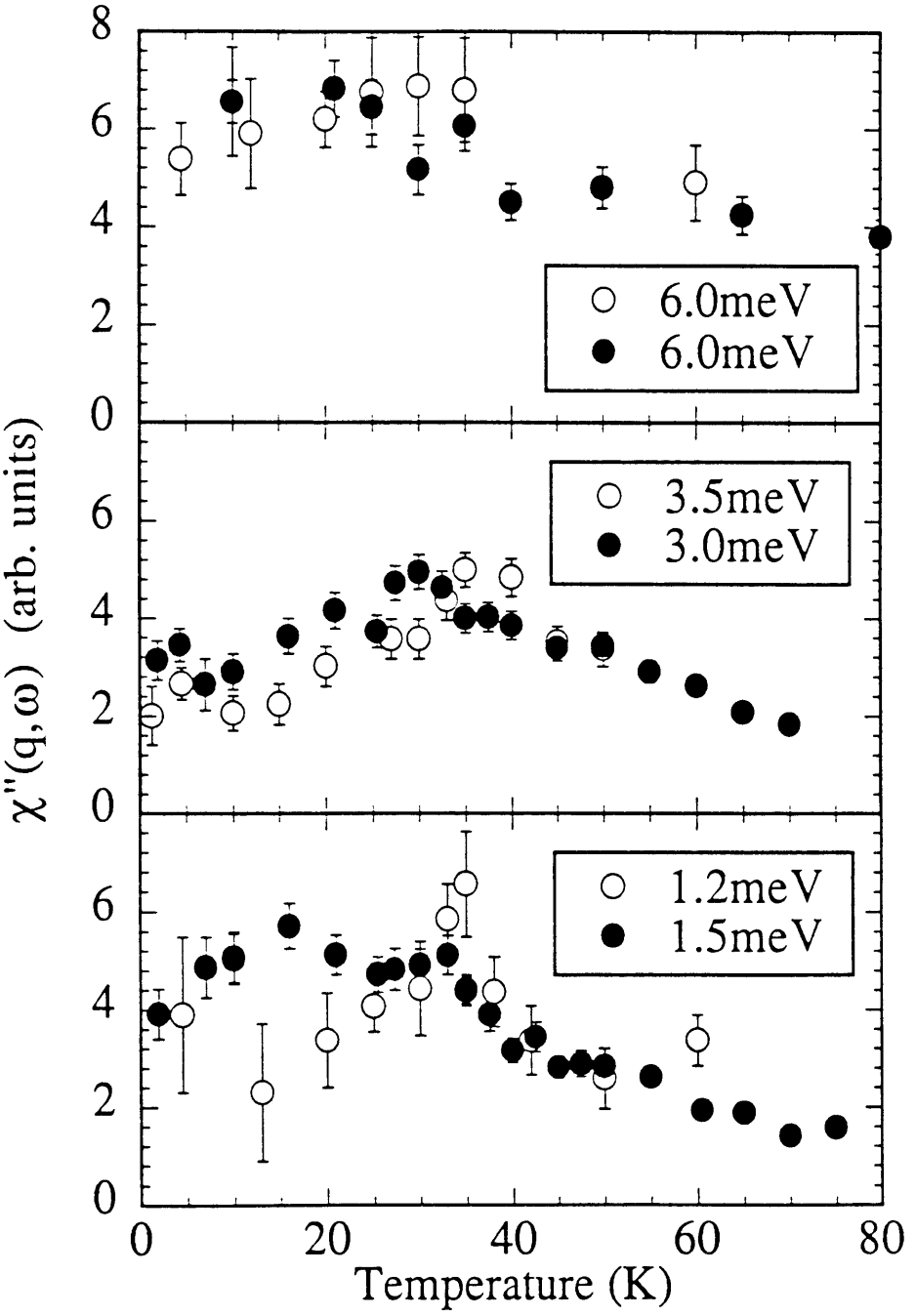

Figure 8-2: Temperature dependence of $Im\chi(\vec{Q}_\delta, \omega)$ as measured by Matsuda et al. [8] in $La_{1.85}Sr_{0.15}CuO_4$ ($T_c = 33K$, closed circles) and by Mason et al. [9] in $La_{1.86}Sr_{0.14}CuO_4$ ($T_c = 35K$, open circles).

rial have been found to differ from those in the single-layer material $La_{2-x}Sr_xCuO_4$ in two fundamental ways: They are essentially commensurate and furthermore exhibit a clear and very large gap in the superconducting state. The difference in the structure of the scattering (i.e., commensurate versus incommensurate) may be due to the different shapes of the Fermi surfaces in the two materials [254, 255, 256]. However, the absence of a magnetic superconducting gap in $La_{2-x}Sr_xCuO_4$ presents a major conundrum for any model of the superconductivity in the single-layer materials. For the development of a consistent picture of the lamellar copper oxides, it is necessary to determine if the observed absence of such a gap in the single-layer material $La_{2-x}Sr_xCuO_4$ is intrinsic, or arises from magnetic impurities or disorder. A successful experiment to that end would require the preparation of voluminous single crystals of unprecedented quality, and the consequent study of low-energy fluctuations in the superconducting state. In the next Section, recent neutron scattering data on new $La_{1.85}Sr_{0.15}CuO_4$ crystals of extremely high quality will be presented [257]. For the first time, a magnetic superconducting gap has been directly observed for a single-layer material.

8.2 Direct observation of a magnetic superconducting gap in $La_{1.85}Sr_{0.15}CuO_4$ ($T_c = 37.3K$)

Three single crystals of $La_{1.85}Sr_{0.15}CuO_4$ of unusually high quality were used in this experiment, all grown under identical conditions by the travelling solvent floating-zone method at Tohoku University, Sendai, Japan [258]. The characteristics of these "Sendai" crystals were discussed in Chapter 3.2, and compared to those of the "Koshu" crystals previously studied by Thurston et al. [75] and Matsuda et al. [8]. The Sendai crystals exhibit a sharp superconducting transition at $T_c = 37.3K$ (onset), the highest T_c among all the $La_{2-x}Sr_xCuO_4$ crystals used in neutron scattering measurements to date.

The horizontal collimations of the triple axis spectrometer were $40-80-S-80-80$, and the incident neutron energy was held fixed at $14.7meV$. Two configurations were

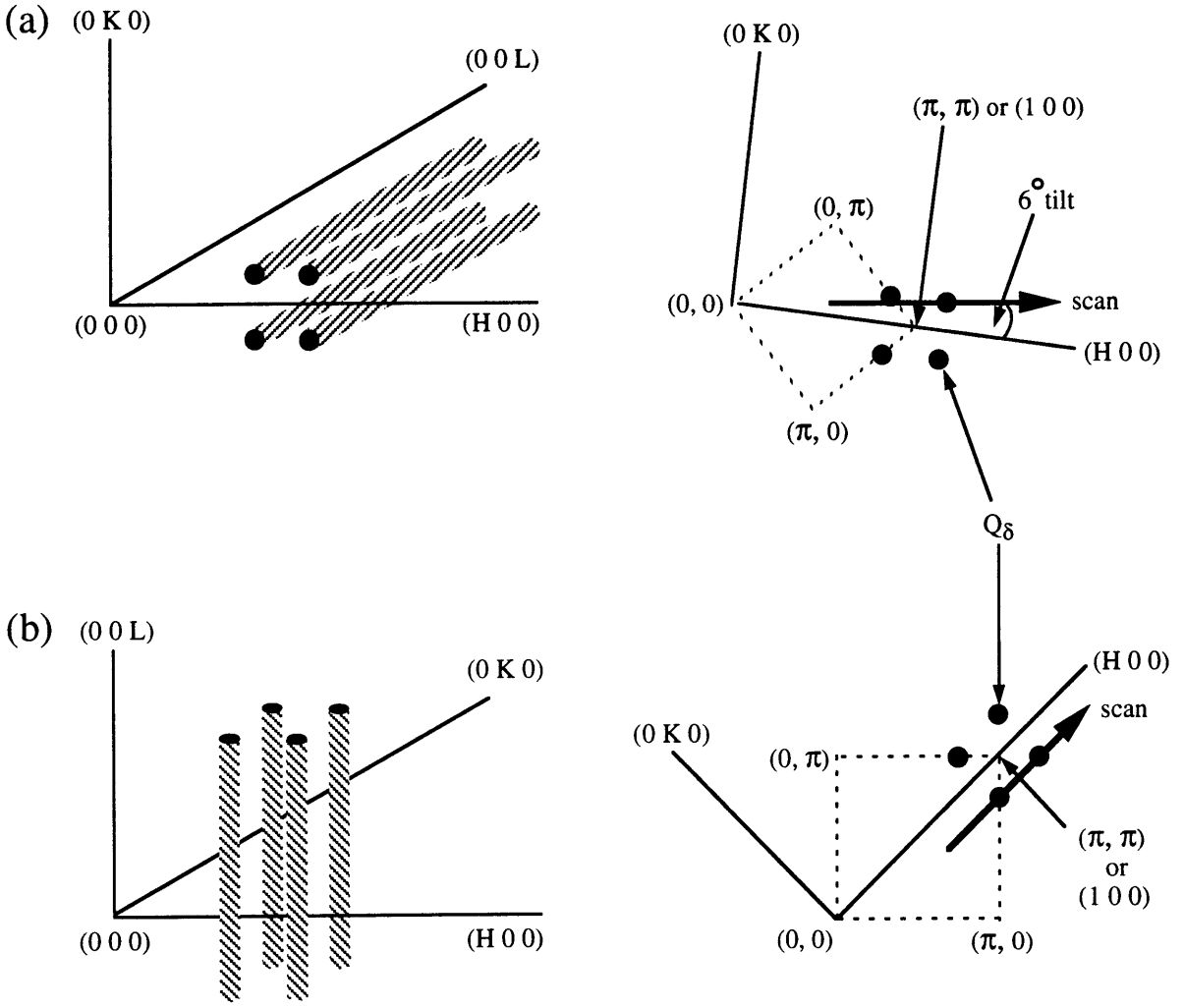

Figure 8-3: Scattering configurations: (a) (H 0 L) geometry and (b) (H K 0) geometry. The four incommensurate magnetic rods are located at $((1 \pm \delta)\pi, \pi)$ and $(\pi, (1 \pm \delta)\pi)$, with $\delta \simeq 0.24$ in $La_{1.85}Sr_{0.15}CuO_4$. In the right-hand figures, the rods of incommensurate magnetic scattering are represented by solid circles.

used in this experiment. In the first configuration, illustrated in Fig. 8-3(a), one of the crystals (labeled Sendai 1) was mounted in the (H 0 L) zone and tilted about the (0 0 1) axis by an angle Φ, so that scans with $Q_x = Hcos\Phi, Q_y = Hsin\Phi$, and $Q_z = L$ arbitrary were possible. With Φ set at 6°, the scattering near the incommensurate peak positions $(0.88, 0.12, L)$ and $(1.12, 0.12, L)$ or, equivalently, $(0.76\pi, \pi)$ and $(\pi, 1.24\pi)$ could then be probed. In the second configuration, illustrated in Fig. 8-3(b), the other two crystals (labeled Sendai 2+3) were carefully aligned and mounted together in the (H K 0) zone.

In Fig. 8-4, representative tilt scans for Sendai 1 at $\omega = 3meV$ are shown for $T = 40K$, which is just above T_c, and $T = 4K$. Evidently, the sharp incommensurate scattering observed at $T = 40K$ has completely disappeared at $4K$. This is in stark contrast with previous results [75, 9, 8], shown in Fig. 8-2, where significant intensity was observed at low temperatures for $\omega \sim 3meV$. Even at $T = 40K$, the integrated magnetic intensity for $\omega = 3meV$, when normalized by phonon scattering, is about a factor of two weaker in Sendai 1 than in the previously studied Koshu crystals. Another important result is that scans with zero tilt, i.e. along (H 0 0), show no scattering at $T = 40K$ above the background level. This agrees with previous results for the Koshu crystals [75, 8], but not with the work by Mason et al. [9], who reported a measurable peak intensity for such zone-diagonal scans. The latter result is likely to be an experimental artifact due to coarser spectrometer resolution.

Figure 8-5 shows the temperature dependence of the dynamic susceptibility for energies $\omega = 2, 3$, and $4.5meV$. The data at $\omega = 2meV$ correspond to the integral of $Im\chi(\vec{q}, \omega)$ with respect to $\vec{q}$ along the scan direction indicated in Fig. 8-3(a). The results at $\omega = 3$ and $4.5meV$ are simply $Im\chi(\vec{Q}_\delta, \omega)$, that is, the measured peak intensity with the Bose factor removed. For $\omega = 2meV$ and $3meV$, the susceptibility peaks near $T = T_c$, and then falls off very quickly at lower temperatures. Within the experimental error, $Im\chi(\vec{Q}_\delta, 2meV)$ is zero below $T \sim 20K$, while $Im\chi(\vec{Q}_\delta, 3meV)$ becomes zero below $T \sim 10K$. For $\omega = 4.5meV$, on the other hand, the susceptibility exhibits a weak peak near T_c and is still large at $T = 4K$. Evidently, a gap for magnetic fluctuations of magnitude between $\omega = 3meV$ and $4.5meV$ has opened up

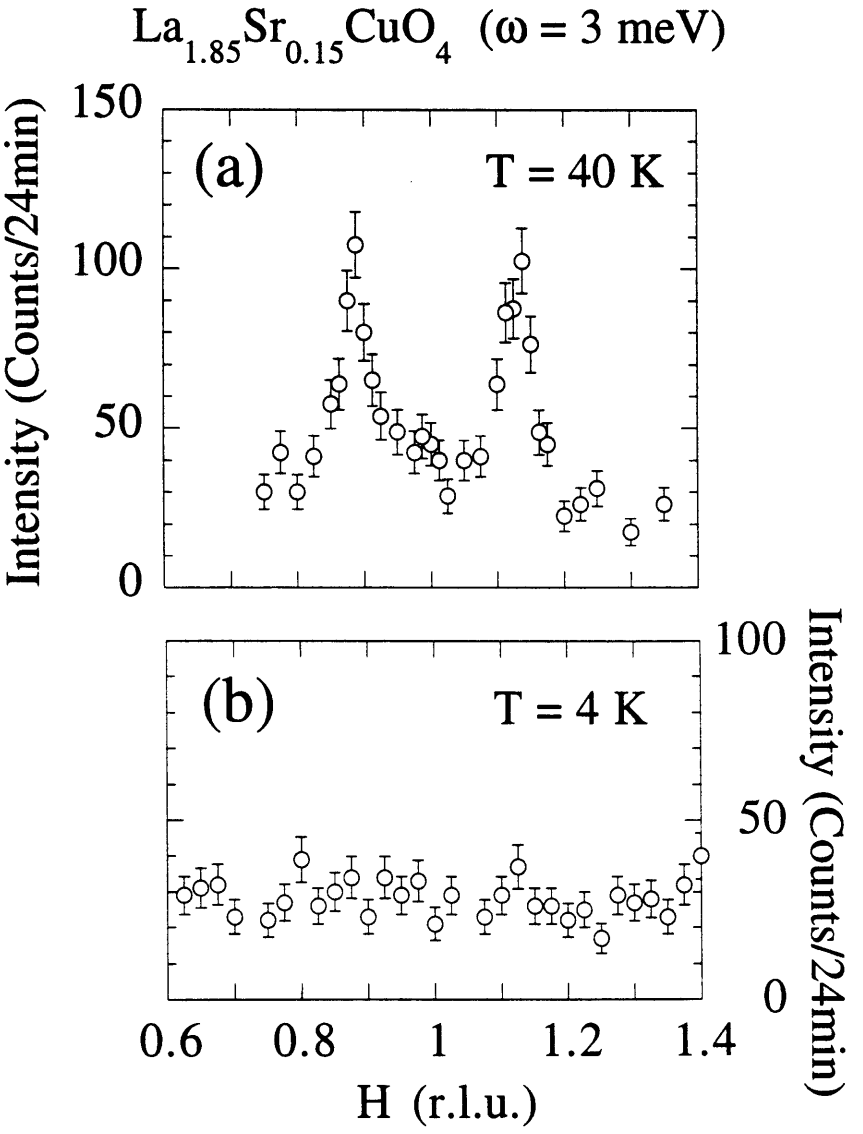

Figure 8-4: Inelastic neutron scattering spectra in $La_{1.85}Sr_{0.15}CuO_4$ at $\omega = 3meV$ in the (H 0 L) geometry: (a) $T = 40K$ and (b) $T = 4K$.

at $T = 4K$.

The observations made for Sendai 1 were verified in detail with Sendai 2+3 in the (H K 0) geometry, illustrated in Fig. 8-3(b). In Fig. 8-6, the energy dependence of $Im\chi(\vec{Q}_\delta, \omega)$ for Sendai 2+3 is shown at $T = 40K$ and $T = 4K$. For $T = 40K$ (i.e., just above T_c), $Im\chi(\vec{Q}_\delta, \omega)$ decreases gradually with decreasing energy, and appears to extrapolate to zero for $\omega \rightarrow 0$. At $T = 4K$, $Im\chi(\vec{Q}_\delta, \omega)$ becomes zero below $\sim 3.5meV$. In other words, there is a magnetic gap of magnitude $\omega_g = 3.5(5)meV$ for spin fluctuations at $\vec{Q} = \vec{Q}_\delta$ due to the superconductivity in $La_{1.85}Sr_{0.15}CuO_4$ ($T_c = 37.3K$). For the first time, a clean gap in the magnetic scattering has been observed in a single CuO_2-layer material. The absence of such a gap in previous studies [75, 9, 8] is presumably due to the lesser quality (more defects and/or impurities) of the crystals used.

The measured magnetic gap energy is much smaller than the BCS s-wave gap energy $2\Delta = 3.54T_c = 11.4meV$, but it may be consistent with an anisotropic s-wave or d-wave order parameter. In a Fermi-liquid picture, $Im\chi(\vec{Q}, \omega)$ originates from particle-hole excitations. In such a picture, the incommensurability of the magnetic scattering in $La_{2-x}Sr_xCuO_4$ at positions $\vec{Q}_\delta$ is explained to be due to the geometry of the Fermi surface. An explicit electronic structure calculation is required in order to relate the momentum-dependent magnetic gap energy to any presumed momentum-dependent superconducting electronic gap energy. No such calculations appear to be available for anisotropic s-wave pairing, but several such estimates exist for a presumed d-wave order parameter [255, 259, 260] of the form

$$\Delta(\vec{k}) = \frac{\Delta_0}{2} |cosk_x - cosk_y|. \tag{8.1}$$

Tanamato et al. [255] predict a momentum-dependent magnetic gap $\omega_g(\delta) = 2^{3/2}\Delta_0/3\, sin(\delta\pi/2)$ from their $t - J-$model calculations. For $\delta = 0.24$ this implies that $\omega_g(0.24) = 0.35\Delta_0$, or $2\Delta_0 = 20.2meV = 6.3T_c$. Scalapino and co-workers [256, 259] obtain $\omega_g(0.24) = 0.36\Delta_0$ based on Hubbard model calculations, which gives $2\Delta_0 = 6.1T_c$. Finally, Zha et al. [254, 260] have also calculated $Im\chi(\vec{Q}, \omega)$

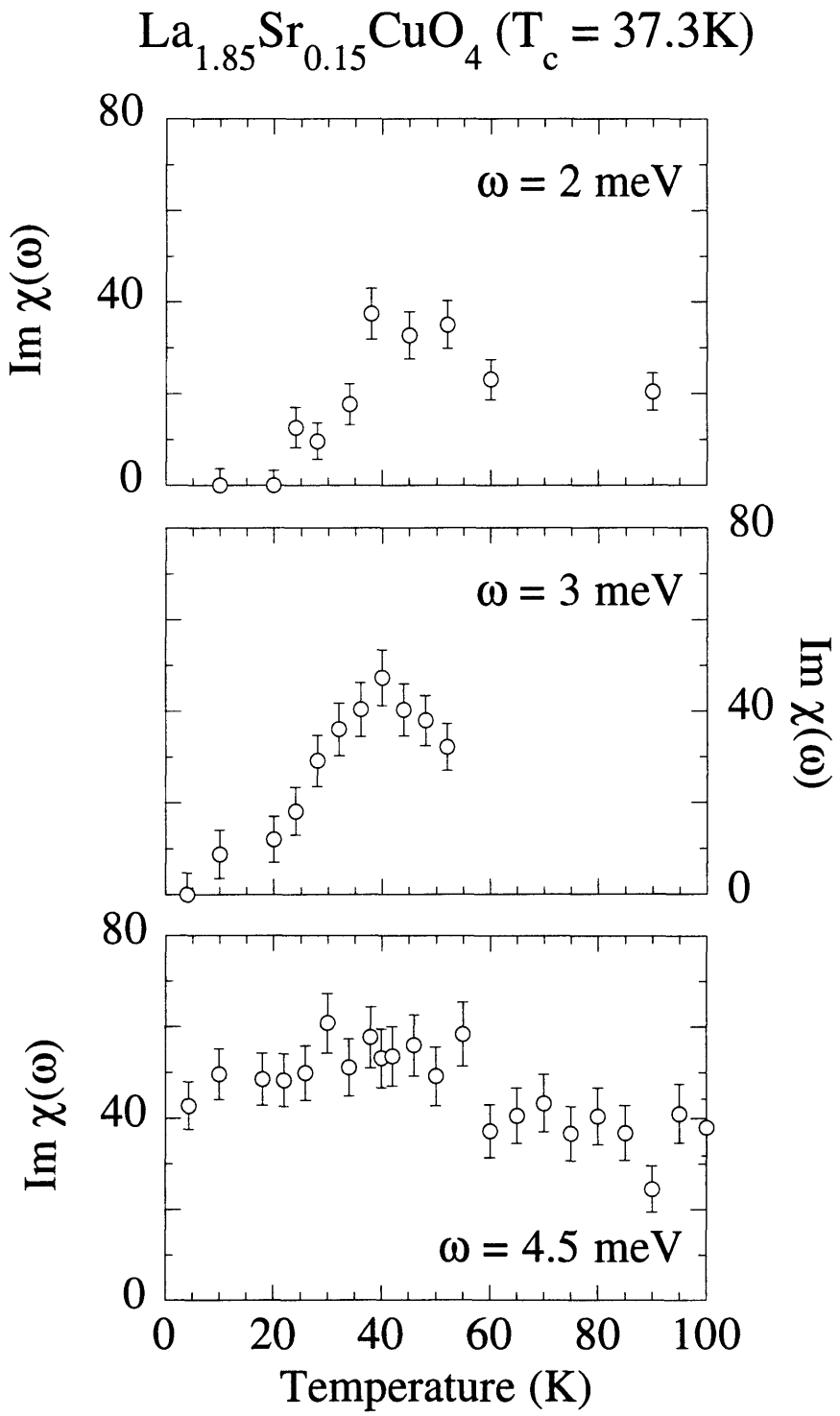

Figure 8-5: Temperature dependence of the dynamic susceptibility in $La_{1.85}Sr_{0.15}CuO_4$ at $\omega = 2, 3$, and $4.5meV$.

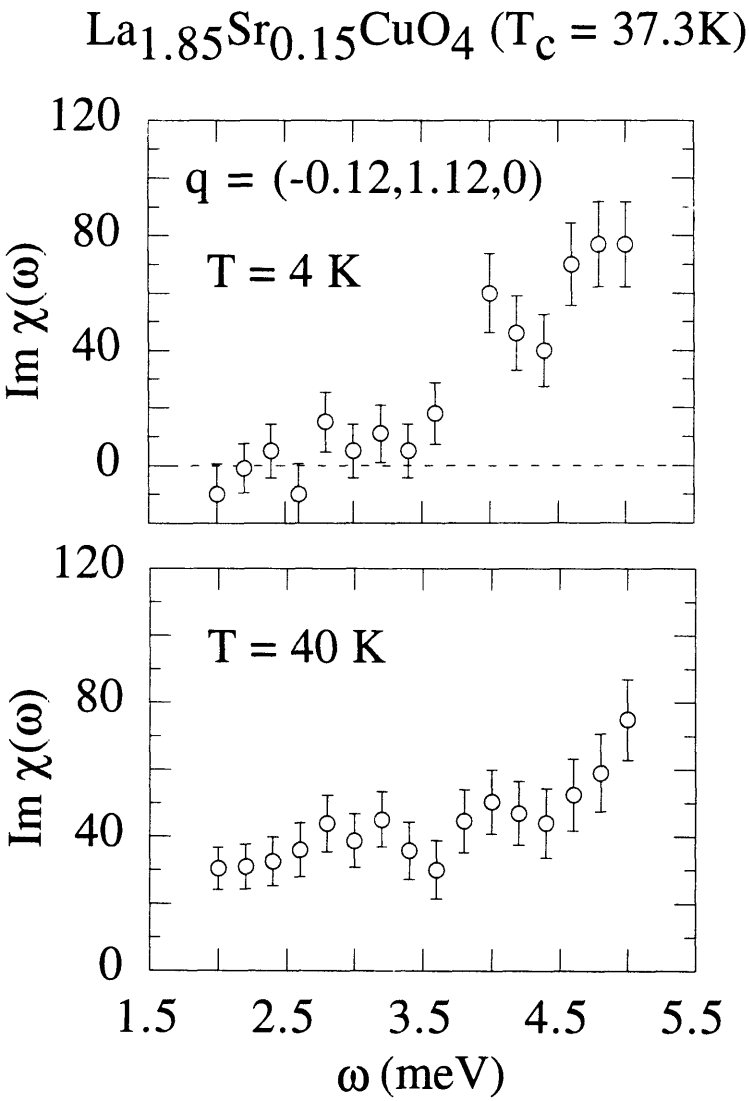

Figure 8-6: $Im\chi(\vec{Q}_\delta, \omega)$ in $La_{1.85}Sr_{0.15}CuO_4$ at $T = 40K$ and $T = 4K$.

for $La_{1.85}Sr_{0.15}CuO_4$, and for a d-wave state with $2\Delta_0 = 7T_c$ they obtain a similar gap. If one naively assumes that the magnetic gap at the positions $\vec{Q}_\delta$ derives directly from an electronic superconducting gap at the positions $\pm 1/2\vec{Q}_\delta$ on the Fermi surface, as shown in Fig. 8-7, one obtains $\omega_g(0.24) = 2(\Delta_0/2)\,|cos(0.24\pi/2) - cos(\pi/2)| = \Delta_0 sin(\delta\pi/2) = 0.37\Delta_0$, or $2\Delta_0 = 5.9T_c$. Curiously, this agrees with the more sophisticated calculations, which represent weighted averages over the Fermi surface. It should also be noted, that the neutron scattering result is consistent within the

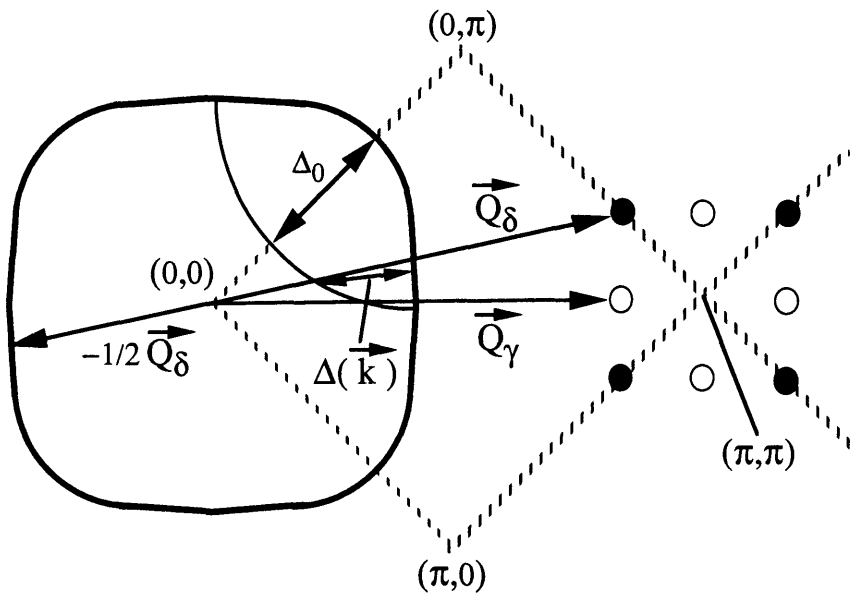

Figure 8-7: Simple schematic of a nested Fermi surface in $La_{1.85}Sr_{0.15}CuO_4$. The Fermi surface contains parallel pieces connected by an effective nesting vector $\vec{Q}_\delta$.

combined experimental errors with the Raman scattering study of $La_{1.83}Sr_{0.17}CuO_4$ by Chen et al. [249], who interpreted their data on the basis of $d_{x^2-y^2}$ symmetry with a full gap of $7.7T_c$.

Based on the invariance of the geometry of the low-energy excitations in the normal and superconducting state, Mason et al. [9] have argued against a clean or weak-impurity $d_{x^2-y^2}$-wave superconducting state. In agreement with the previous experiments by Thurston et al. [75] and Matsuda et al. [8], but in disagreement with the experiment by Mason et al. [9], no evidence for scattering along the (π, π)-direction in

either the normal or superconducting states was observed in the current experiment. Various theoretical calculations have predicted scattering in $La_{2-x}Sr_xCuO_4$ from the four equivalent positions $\vec{Q}_\gamma$ (see Fig. 8-6) [254, 256]. However, recent calculations that include exchange enhancement predict that at low energies $Im\chi(\vec{Q},\omega)$ in the (π,π)-direction should decrease in amplitude as the temperature is lowered below T_c [259]. Since no such scattering has been observed in the normal state, the absence of measurable zone-diagonal magnetic scattering in the superconducting phase has no implications for the symmetry of the order parameter.

8.3 Magnetism in $La_{1.83}Tb_{0.05}Sr_{0.12}CuO_4$

In this Section, inelastic magnetic neutron scattering measurements in non-superconducting $La_{1.83}Tb_{0.05}Sr_{0.12}CuO_4$ will be presented. The growth of the sample, which has a volume of $2cm^3$, was discussed in Chapter 3. From neutron depolarisation measurements it is known that this crystal is not a bulk superconductor (see Fig. 2-11). This ought to be contrasted with a T_c of $\sim 25K$ found for $La_{1.88}Sr_{0.12}CuO_4$. It is known that co-doping superconducting $La_{2-x}Sr_xCuO_4$ with rare earths suppresses T_c, and that a large enough rare earth content completely destroys the superconductivity [261, 262, 263, 264]. The Tb-doped crystal studied here was grown from a Pt crucible and quite naturally contains some small amount of Pt contamination. As discussed in Chapter 3, Pt is also known to suppress T_c. The lack of bulk superconductivity in the $La_{1.83}Tb_{0.05}Sr_{0.12}CuO_4$ crystal is likely to be crucial for the interesting magnetic response exhibited by this sample. It is found that while the inelastic magnetic scattering for this system is still incommensurate as in superconducting $La_{2-x}Sr_xCuO_4$, the overall magnetic response is strikingly similar to that of non-superconducting lightly doped La_2CuO_4.

In Fig. 8-8, some representative scans at $\omega = 3$ and $4meV$, taken in the (H 0 L) configuration at $T = 35K$, are shown. The horizontal collimations of the three-axis spectrometer were $40 - 40 - S - 80 - 80$, and the incident neutron energy was held fixed at $14.7meV$. A tilt angle of $\Phi = 5°$ was chosen so that the scatter-

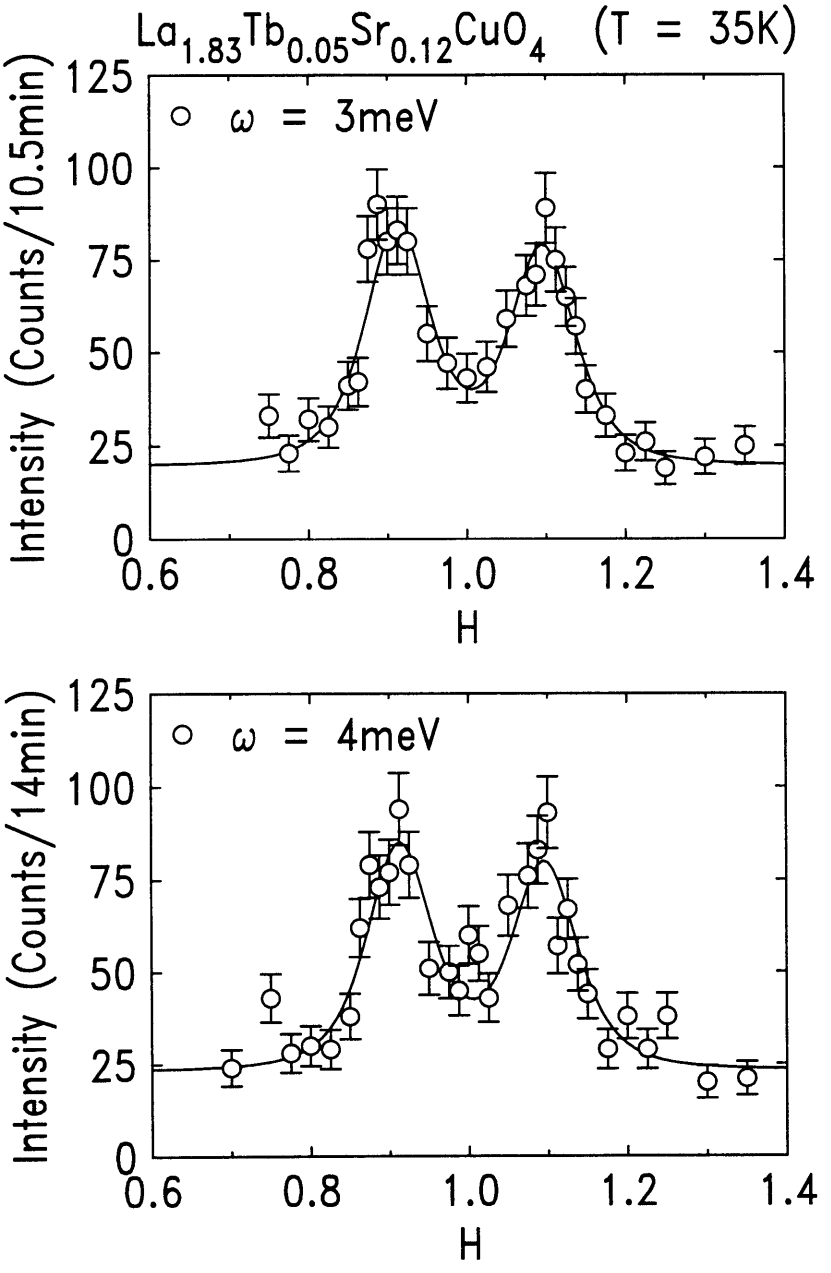

Figure 8-8: Inelastic neutron scattering scans taken in the (H 0 L) geometry in non-superconducting $La_{1.83}Tb_{0.05}Sr_{0.12}CuO_4$ at $T = 35K$ for $\omega = 3$ and $4meV$.

ing near the positions $(0.91, 0.09, L)$ and $(1.09, 0.09, L)$ or, equivalently, $(0.82\pi, \pi)$ and $(\pi, 1.18\pi)$ could be probed, as illustrated in Fig. 8-3(a). It is indeed found that the inelastic magnetic scattering in this sample is incommensurate with $\delta \simeq 0.18$, the same incommensurability as expected for superconducting $La_{1.88}Sr_{0.12}CuO_4$ [74]. The solid lines are the result of fits to 2D Lorentzians convoluted with the spectrometer resolution function. The Lorentzian width at $T = 35K$ is found to be $\kappa = 0.045(10)\mathring{A}^{-1}$ for $\omega \leq 12meV$. This behavior is different from that found for superconducting samples. For example, the measurements in $La_{1.85}Sr_{0.15}CuO_4$ by Matsuda et al. [8] reveal a strong energy dependence of the Lorentzian width. At $T = 35K$, which is just above $T_c = 33K$ in this sample, κ was found to increase from $\sim 0.020\mathring{A}^{-1}$ at $\omega = 2meV$ to $\sim 0.10\mathring{A}^{-1}$ at $\omega = 12meV$. On the other hand, for lightly Sr-doped La_2CuO_4 the inelastic magnetic scattering is commensurate, with a peak width that is independent of energy for $\omega \leq 12meV$ [2, 8]. In $La_{1.96}Sr_{0.04}CuO_4$, for example, Keimer et al. [2] found $\kappa \simeq 0.024\mathring{A}^{-1}$.

Figure 8-9 contains a comparison of the 2D momentum-integrated susceptibility $Im\chi(\omega) = \int dq_{2D} Im\chi(\vec{q}, \omega)$ at $\omega = 2meV$ for $La_{1.83}Tb_{0.05}Sr_{0.12}CuO_4$ and the Sendai 1 sample. The data were normalized to give the best agreement for $50K \leq T \leq 100K$. As discussed in the previous Section, a magnetic superconducting gap opens up at low temperatures in the Sendai samples, and there is no observable intensity below $T = 20K$ for $\omega = 2meV$. The data for the non-superconducting Tb-doped crystal, on the other hand, show no sign of such a gap. Instead, the susceptibility is found to increase continuously with decreasing temperature.

The energy-dependence of the 2D momentum integrated intensity at $T = 35K$ is shown in Fig. 8-10 for $La_{1.83}Tb_{0.05}Sr_{0.12}CuO_4$ and for $La_{1.98}Sr_{0.02}CuO_4$, as obtained by Matsuda et al. [8]. The data were normalized to give the best overall agreement. In both systems the spectral weight increases at lower energies, and the overall increase is found to be the same to within the combined experimental error. The same qualitative trend, that is, an increasing spectral weight with decreasing ω, persists down to low temperatures, in contrast to the gap-behavior observed for the Sendai crystals (see Fig. 8-6).

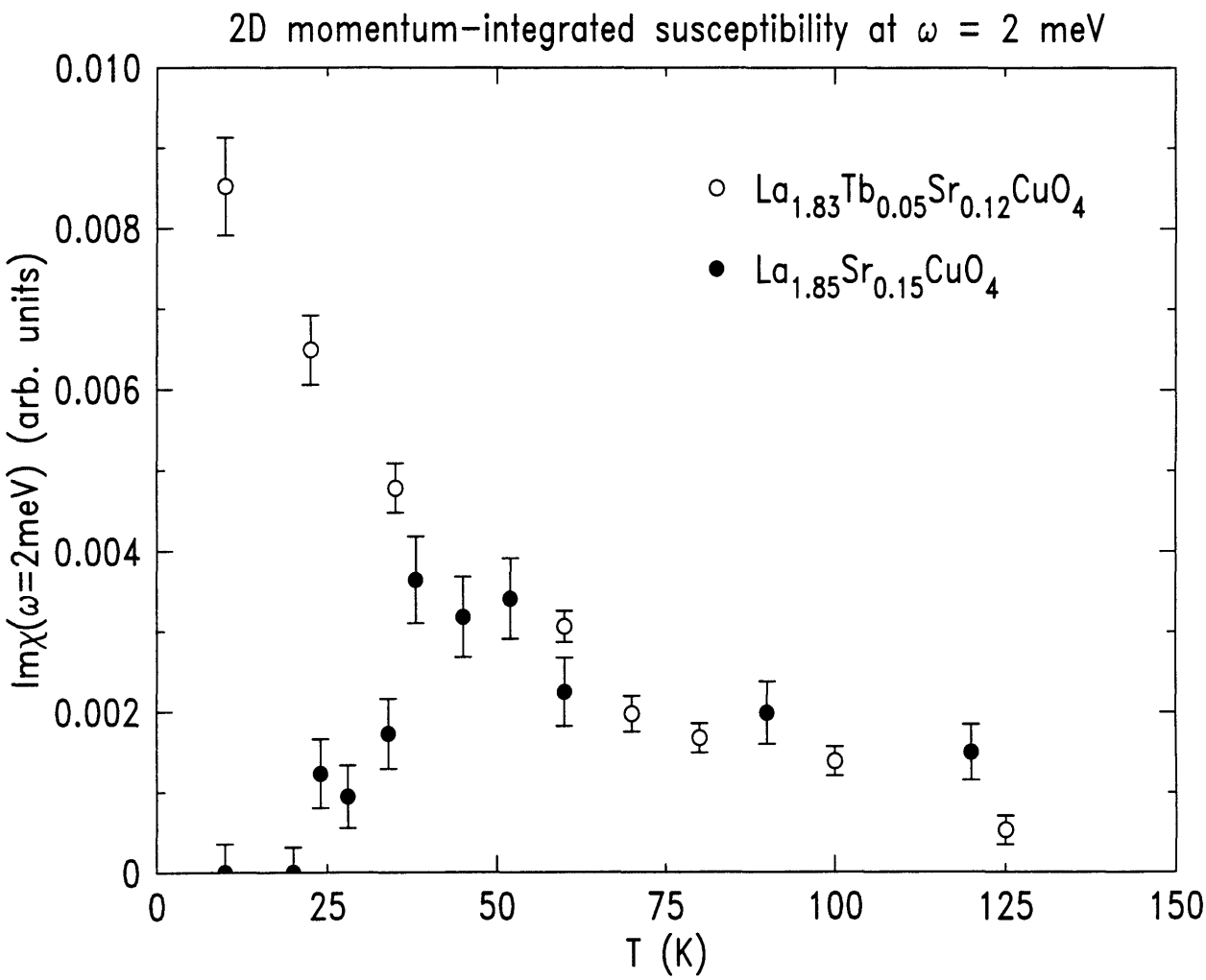

Figure 8-9: 2D $\vec{q}$-integrated susceptibility at $\omega = 2meV$ for non-superconducting $La_{1.83}Tb_{0.05}Sr_{0.12}CuO_4$ and superconducting $La_{1.85}Sr_{0.15}CuO_4$. The data were normalized for $50K \leq T \leq 100K$.

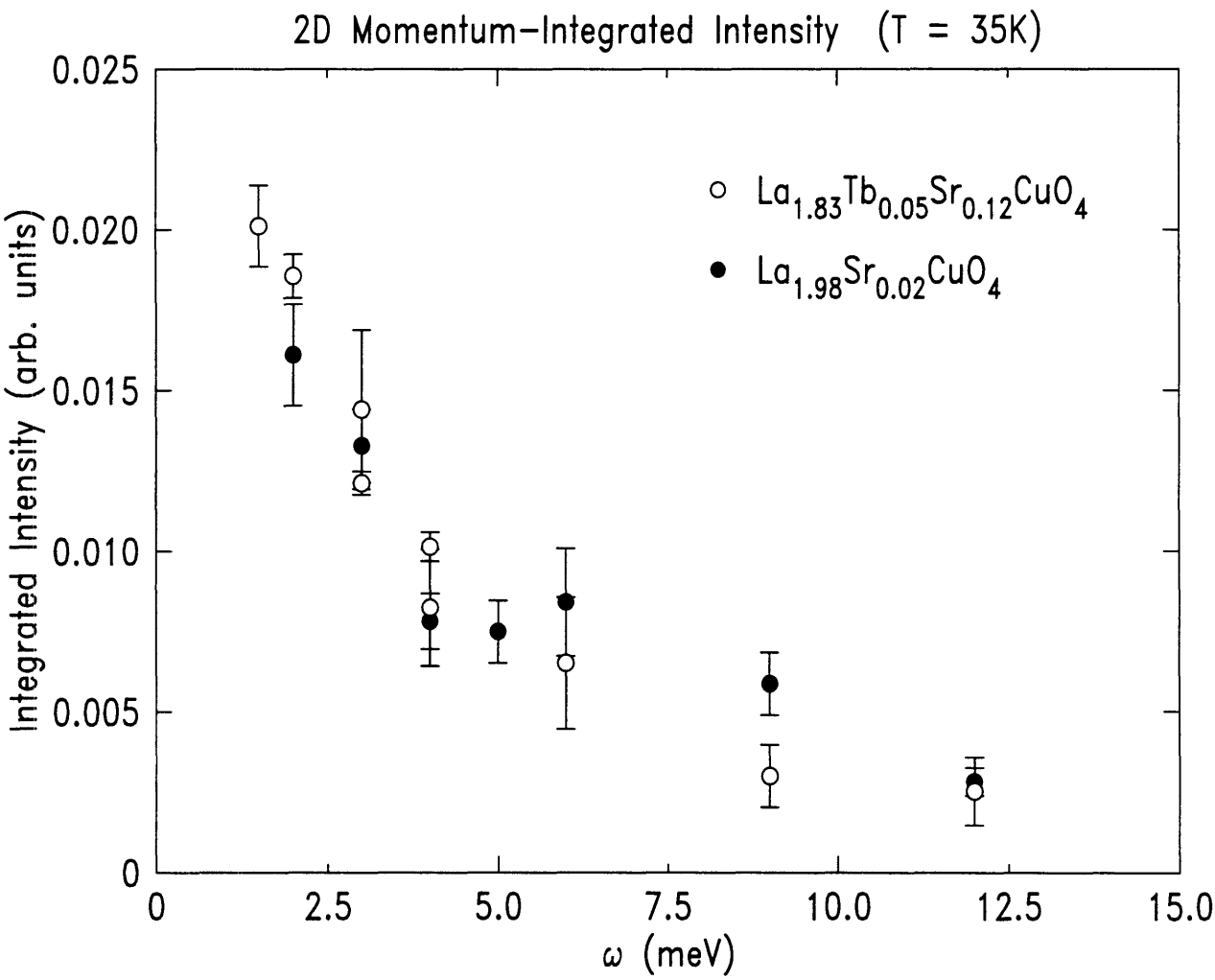

Figure 8-10: 2D $\vec{q}$-integrated intensity at $T = 35K$ for $La_{1.83}Tb_{0.05}Sr_{0.12}CuO_4$ and $La_{1.98}Sr_{0.02}CuO_4$ (from Matsuda et al. [8]). The data were normalized to give the best overall agreement.

The main difference between the magnetic scattering in $La_{1.83}Tb_{0.05}Sr_{0.12}CuO_4$ and lightly doped La_2CuO_4 is that the response in the former system is incommensurate, while it is commensurate in the latter. For $La_{1.96}Sr_{0.04}CuO_4$, Keimer et al. [265, 2] have discovered that the spin fluctuations exhibit a simple scaling behavior in ω/T for $2meV \leq \omega \leq 45meV$ and $10K \leq T \leq 500K$. This ω/T-scaling is a rather universal property of the lamellar copper oxides, since it has also been found in non-superconducting $La_{1.98}Sr_{0.02}CuO_4$ [266] and $YBa_2Cu_{2.9}Zn_{0.1}O_{6.6}$ [267], as well as in superconducting $YBa_2Cu_3O_{6+\delta}$ [251, 268] above T_c. However, so far it has not been established if this scaling also descibes the magnetic fluctuations in the single-layer materials in the doping regime in which the magnetic fluctuations are incommensurate. In this Section, it was demonstrated that the magnetic response of (non-superconducting) $La_{1.83}Tb_{0.05}Sr_{0.12}CuO_4$ strongly resembles that of lightly-doped La_2CuO_4. A broad mapping of the energy- and temperature-dependence of the magnetic fluctuations in the Tb-doped crystal is required to establish if this system exhibits ω/T-scaling as well.

Appendix A

Nuclear spin and isotope incoherence

Consider a system made up out of one isotope. If the nuclear spin of that isotope is zero, the scattering length is fully coherent since it is the only length that enters the problem. If, however, the isotope has a non-zero nuclear spin I, then the total spin of the neutron-nucleon system can take on one of the two values $J = I \pm 1/2$, with the corresponding scattering lengths $b^{\pm}$ and with $n_{\pm} = [2(I \pm 1/2) + 1]$ possible spin states. Unless the neutron beam is polarized *and* the nuclear spins are not randomly distributed, the scattering length is given by

$$\bar{b} = \frac{n_+}{n_+ + n_-} b^+ + \frac{n_-}{n_+ + n_-} b^- = \frac{1}{2I+1}[(I+1)b^+ + Ib^-]. \tag{A.1}$$

For a system that contains several isotopes i, one has

$$\bar{b} = \sum_i \frac{c_i}{2I_i + 1}[(I_i + 1)b_i^+ + I_i b_i^-] \tag{A.2}$$

and

$$\bar{b^2} = \sum_i \frac{c_i}{2I_i + 1}[(I_i + 1)(b_i^+)^2 + I_i(b_i^-)^2], \tag{A.3}$$

where c_i denotes the relative abundance of the i^{th} isotope. In the tables below [269], the coherent bound scattering length, the scattering cross-section

$$\sigma_s = \sigma_c + \sigma_{inc} = 4\pi(\bar{b})^2 + 4\pi(\bar{b^2} - (\bar{b})^2) = 4\pi\bar{b^2}, \tag{A.4}$$

as well as the absorption cross-section σ_a, are given for various elements pertinent to this thesis. The cross-sections are given in units of *barns* ($1barn = 10^{-28}m^2 = 100fm^2$), and the absorption cross-sections are given for neutrons with velocity $v = 2200m/s$ ($T = 297K$). The total cross-section is $\sigma = \sigma_s + \sigma_a$. Note, that for condensed matter applications the bound-atom scattering length and not the free-atom scattering length is relevant. In the Tables A.1 and A.2, the bound-atom scattering lengths are therefore listed. It is a fortunate fact that σ_{inc} and σ_a are relatively small for all the elements of interest. In Table A.1, both Al and He are listed, since the sample cans are made out of Al, and the neutron detectors out of ^{3}He.

E	Z	A	I(P)	NA (%)	b_c (fm)	σ_c (barns)	σ_s (barns)	σ_a (barns)
He	2				3.26(3)	1.34(2)	1.34(2)	0.00747(1)
		3	1/2(+)	0.00014	5.74(7)	4.42(10)	5.6(3)	5333(7)
		4	0(+)	99.99986	3.26(3)	1.34(2)	1.34(2)	0
O	8				5.805(4)	4.235(6)	4.235(7)	0.00019(2)
		16	0(+)	99.762	5.805(5)	4.235(7)	4.235(7)	0.00010(2)
		17	5/2(+)	0.038	5.78(12)	4.2(2)	4.2(0)	0.236(10)
		18	0(+)	0.200	5.84(7)	4.29(10)	4.29(10)	0.00016(1)
F	9	19	1/2(+)	100.0	5.654(12)	4.017(17)	4.018(17)	0.0096(5)
Al	13	27	5/2(+)	100.0	3.449(5)	1.495(4)	1.504(4)	0.231(3)
Cl	17				9.5792(8)	11.531(2)	16.7(2)	33.5(3)
		35	3/2(+)	75.77	11.66(2)	17.08(6)	21.6(3)	44.1(4)
		37	3/2(+)	24.23	3.08(6)	1.19(5)	1.19(5)	0.433(6)
K	19				3.71(1)	1.73(2)	1.98(10)	2.1(1)
		39	3/2(+)	93.258	3.79(2)	1.81(2)	2.06(11)	2.1(2)
		40	4(-)	0.012	3(1)	1.1(8)	1.2(9)	35(8)
		41	3/2(+)	6.730	2.58(6)	0.84(4)	0.84(4)	1.46(3)
Ni	28				10.3(1)	13.3(3)	18.5(3)	4.49(16)
		58	0(+)	68.27	14.4(1)	26.1(4)	26.1(4))	4.6(3)
		60	0(+)	26.10	2.8(1)	0.99(7)	0.99(7)	2.9(2)
		61	3/2(-)	1.13	7.60(6)	7.26(11)	9.3(3)	2.5(8)
		62	0(+)	3.59	-8.7(2)	9.5(4)	9.5(4)	14.5(3)
		64	0(+)	0.91	-0.38(7)	0.018(7)	0.018(7)	1.52(3)
Cu	29				7.718(4)	7.486(8)	8.01(4)	3.78(2)
		63	3/2(-)	69.17	6.43(15)	5.2(2)	5.2(2)	4.50(2)
		65	3/2(-)	30.83	10.61(19)	14.1(5)	14.5(5)	2.17(3)
Sr	38				7.02(2)	6.19(4)	6.23(9)	1.28(6)
		84	0(+)	0.56	5(2)	3(2)	3(2)	0.87(7)
		86	0(+)	9.86	5.68(5)	4.05(7)	4.05(7)	1.04(7)
		87	9/2(+)	7.00	7.41(7)	6.90(13)	7.03(28)	16(3)
		88	0(+)	82.58	7.16(6)	6.44(11)	6.44(11)	0.058(4)

Table A.1: Bound-atom cross-sections of various elements pertinent to this thesis. The meaning of the various symbols is: Element (E), atomic number (Z), mass number (A), nuclear spin (S) and parity (P) of the nuclear ground state, and natural abundance (NA).

E	Z	A	I(P)	NA (%)	b_c (fm)	σ_c (barns)	σ_s (barns)	σ_a (barns)
La	57				8.24(4)	8.53(8)	9.66(17)	8.97(5)
Ce	58				4.84(2)	2.94(2)	2.94(10)	0.63(4)
Pr	59	141	5/2(+)	100	4.45(5)	2.49(6)	2.51(6)	11.5(3)
Nd	60				7.69(5)	7.43(10)	18(2)	50.2(2)
Sm	62				4.2(3)	2.5(3)	52(6)	5670(100)
Eu	63				6.68(12)	5.8(2))	2.2(4)	4600(100)
Gd	64				9.5(2)	34.5(5)	158(4)	48890(104)
Tb	65	159	3/2(+)	100	7.38(3)	6.84(6)	6.84(6))	23.4(4)
DY	66				16.9(2)	35.9(8)	90.4(1.7)	940(15)
Ho	67	165	7/2(-)	100	8.08(5)	8.20(10)	8.53(13)	64.7(1.2)
Er	68				8.03(3)	8.10(6)	9.3(7)	159.2(3.6)
Tm	69	169	1/2(+)	100	7.05(5)	6.25(9)	6.66(17)	105(2)
Yb	70				12.40(10)	19.3(3)	22.3(4)	35.1(2.2)
Lu	71				7.3(2)	6.7(4)	6.8(4)	76.4(2.1)

Table A.2: Bound-atom cross-sections of La and the rare-earth elements (with the exception of the radioactive element Pm ($Z = 61$)). Note, that for those elements with more than one naturally abundant isotope, only the average values are listed.

Bibliography

[1] Y. Tokura, S. Koshihara, T. Arima, H. Takagi, S. Ishibashi, T. Ido, and S. Uchida, Phys. Rev. B **41**, 11657 (1990).

[2] B. Keimer, N. Belk, R.J. Birgeneau, A. Cassanho, C.Y. Chen, M. Greven, M.A. Kastner, A. Aharony, Y. Endoh, R.W. Erwin, and G. Shirane, Phys. Rev. B **46**, 14034 (1992).

[3] H. Takagi, B. Batlogg, H.L. Kao, J. Kwo, R.J. Cava, J.J. Krajewski, and W.F. Peck, Jr., Phys. Rev. Lett. **69**, 2975 (1992).

[4] H.Y. Hwang, B. Batlogg, H. Takagi, H.L. Kao, J. Kwo, R.J. Cava, J.J. Krajewski, and W.F Peck, Jr., Phys. Rev. Lett. **72**, 2636 (1994).

[5] For more details about the PES technique, see for example B.O. Wells, Ph.D. thesis, Stanford University, (1992).

[6] D.S. Dessau, Z.-X. Shen, D.M. King, D.S. Marshall, L.W. Lombardo, P.H. Dickinson, A.G. Loeser, J. DiCarlo, C.-H. Park, A. Kapitulnik, and W.E. Spicer, Phys. Rev. Lett. **71**, 2781 (1993).

[7] Z. Liu and E. Manousakis, Phys. Rev. B **45**, 2425 (1992).

[8] M. Matsuda, K. Yamada, Y. Endoh, T.R. Thurston, G. Shirane, R.J. Birgeneau, M.A. Kastner, I. Tanaka, and H. Kojima, Phys. Rev. B **49**, 6958 (1994).

[9] T.E. Mason, G. Aeppli, S.M. Hayden, A.P. Ramirez, and H.A. Mook, Phys. Rev. Lett. **71**, 919 (1993).

[10] H. Kamerlingh Onnes, Comm. Phys. Lab. Univ. Leiden, Nos. 119, 120, 122 (1911).

[11] W. Meissner and R. Ochsenfeld, Naturwiss. **21**, 787 (1933).

[12] J. Bardeen, L.N. Cooper, and J.R. Schrieffer, Phys. Rev. **108**, 1175 (1957).

[13] C. Gorter and H. Casimir, Phys. Z. **35**, 963 (1934).

[14] C. Gorter and H. Casimir, Z. Tech. Phys. **15**, 539 (1934).

[15] F. London and H. London, Proc. Roy. Soc. (London) **A149**, 71 (1935).

[16] F. London and H. London, Physica **2**, 341 (1935).

[17] F. London, Phys. Rev. **74**, 562 (1948).

[18] J. Gavaler, Appl. Phys. Lett **23**, 480 (1973).

[19] J.G. Bednorz and K.A. Müller, Z. Phys. B **64**, 189 (1986).

[20] M.K. Wu, J.R. Ashburn, C.J. Torny, P.H. Hor, R.L. Meng, L. Gao, Z.J. Huang, Y.Q. Wang, and C.W. Chu, Phys. Rev. Lett. **58**, 908 (1987).

[21] S.S.P. Parkin, V.Y. Lee, E.M. Engler, A.I. Nazzel, T.C. Huang, G. Gorman, R. Savoy, and R. Beyers, Phys. Rev. Lett. **60**, 2539 (1988).

[22] Z. Sheng and A. Hermann, Nature **332**, 55 (1988).

[23] S. Putilin, E. Antipov, O. Chmaissem, and M. Marezio, Nature **362**, 226 (1993).

[24] A. Schilling, M. Cantoni, J. Guo, and H. Ott, Nature **363**, 56 (1993).

[25] G. Blatter, M.V. Feigel'man, V.B. Geshkenbein, A.I. Larkin, and V.M. Vinokur, Rev. Mod. Phys. **66**, 1125 (1994).

[26] D. Vaknin, S.K. Sinha, C. Stassis, L.L. Miller, and D.C. Johnston, Phys. Rev. B **41**, 1926 (1990).

[27] L. Mattheiss, Phys. Rev. Lett. **58**, 1028 (1987).

[28] J. Yu, A. J. Freeman, and J.-H. Xu, Phys. Rev. Lett. **58**, 1035 (1987).

[29] J.M. Tranquada et al., Phys. Rev. B **36**, 5263 (1987).

[30] Z.X. Shen et al., Phys. Rev. B **36**, 8414 (1987).

[31] N. Nücker, J. Fink, B. Renker, D. Ewert, C. Politis, P.J.W. Weijs, and J.C. Fuggle, Z. Phys. B **67**, 9 (1987).

[32] J. Feinlieb and D. Adler, Phys. Rev. Lett. **21**, 1010 (1968).

[33] V. Emery, Phys. Rev. Lett. **58**, 2794 (1987).

[34] P. Anderson, Science **256**, 1526 (1992).

[35] G. Aeppli, S. M. Hayden, H. A. Mook, Z. Fisk, S. W. Cheong, D. Rytz, J. P. Remeika, G. P. Espinosa, and A. S. Cooper, Phys. Rev. Lett. **62**, 2052 (1989).

[36] R. Singh, P. Fleury, K. Lyons, and P. Sulewski, Phys. Rev. Lett. **62**, 2736 (1989).

[37] K.B. Lyons, P.A. Fleury, J.P. Remeika, A.S. Cooper, and T.J. Negran, Phys. Rev. B **37**, 2353 (1988).

[38] T. Yildirim, A. Harris, O. Entin-Wohlman, and A. Aharony, Phys. Rev. Lett. **72**, 3710 (1994).

[39] T. Yildirim, A. Harris, O. Entin-Wohlman, and A. Aharony, Phys. Rev. Lett. **73**, 2919 (1994).

[40] I. Dzyaloshinskii, J. Phys. Chem. Solids **4**, 241 (1958).

[41] T. Moriya, Phys. Rev. **120**, 91 (1960).

[42] D. Coffey, T. Rice, and F. Zhang, Phys. Rev. B **46**, 5884 (1992).

[43] L. Shekhtman, O. Entin-Wohlman, and A. Aharony, Phys. Rev. Lett. **69**, 5 (1992).

[44] L. Shekhtman, A. Aharony, and O. Entin-Wohlman, Phys. Rev. B **47**, 174 (1993).

[45] N. Bonesteel, Phys. Rev. B **47**, 11302 (1993).

[46] W. Koshibae, Y. Ohta, and S. Maekawa, Phys. Rev. B **47**, 3391 (1993).

[47] T. Thio, T.R. Thurston, N.W. Preyer, P.J. Picone, M.A. Kastner, H.P. Jenssen, D.R. Gabbe, C.Y. Chen, R.J. Birgeneau, and A. Aharony, Phys. Rev. B **38**, 905 (1988).

[48] T. Thio, C.Y. Chen, B.S. Freer, D.R. Gabbe, H.P. Jenssen, M.A. Kastner, P.J. Picone, N.W. Preyer, and R.J. Birgeneau, Phys. Rev. B **41**, 231 (1990).

[49] B. Keimer, R.J. Birgeneau, A. Cassanho, Y. Endoh, M. Greven, M.A. Kastner, and G. Shirane, Z. Phys. B **91**, 373 (1993).

[50] E. F. Shender, Sov. Phys. JETP **56**, 178 (1982).

[51] J. Skalyo, Jr., G. Shirane, R. Birgeneau, and H. Guggenheim, Phys. Rev. Lett. **23**, 1394 (1969).

[52] R. Birgeneau, J. Skalyo, Jr., and G. Shirane, Phys. Rev. B **3**, 1736 (1971).

[53] R. Birgeneau, J. Als-Nielsen, and G. Shirane, Phys. Rev. B **16**, 280 (1977).

[54] K. Nakajima, K. Yamada, S. Hosoya, Y. Endoh, M. Greven, and R.J. Birgeneau, Z. Phys. B **96**, 479 (1995).

[55] S. Chakravarty, B. Halperin, and D. Nelson, Phys. Rev. Lett. **60**, 1057 (1988).

[56] S. Chakravarty, B. Halperin, and D. Nelson, Phys. Rev. B **39**, 2344 (1989).

[57] P. Hasenfratz and F. Niedermayer, Phys. Lett. B **268**, 231 (1991).

[58] K. Yamada, K. Kakurai, Y. Endoh, T.R. Thurston, M.A. Kastner, R.J. Birgeneau, G. Shirane, Y. Hidaka, and T. Murakami, Phys. Rev. B **40**, 4557 (1989).

[59] N.W. Preyer, R.J. Birgeneau, C.Y. Chen, D.R. Gabbe, J.P. Jenssen, M.A. Kastner, P.J. Picone, and T. Thio, Phys. Rev. B **42**, 11563 (1989).

[60] B. Keimer, A. Aharony, A. Auerbach, R.J. Birgeneau, A. Cassanho, Y. Endoh, R.W. Erwin, M.A. Kastner, and G. Shirane, Phys. Rev. B **45**, 7430 (1992).

[61] J. Cho, F. Chou, and D. Johnston, Phys. Rev. Lett. **70**, 222 (1993).

[62] C.Y. Chen, R.J. Birgeneau, M.A. Kastner, N.W. Preyer, and T. Thio, Phys. Rev. B **43**, 392 (1991).

[63] F.C. Chou, F. Borsa, J.H. Cho, D.C. Johnston, A. Lascialfari, D.R. Torgeson, and J. Ziolo, Phys. Rev. Lett. **71**, 2323 (1993).

[64] R. Gooding, Phys. Rev. Lett. **66**, 2266 (1991).

[65] R. Gooding and A. Mailhot, Phys. Rev. B **44**, 11852 (1991).

[66] M. Ivanov, V. Loktev, and Y. Pogorelov, Zh. Eksp. Teor. Fiz. **101**, 596 (1992).

[67] D.R. Harshman, G. Aeppli, G.P. Espinosa, A.S. Cooper, J.P. Remeika, E.J. Ansaldo, T.M. Riseman, D.L. Williams, D.R. Noakes, B. Ellman, and T.F. Rosenbaum, Phys. Rev. B **38**, 852 (1988).

[68] B.J. Sternlieb, G.M. Luke, Y.J Uemura, T.M. Rieseman, J.H. Brewer, P.M. Gehring, K. Yamada, Y. Hidaka, T. Murakami, T.R. Thurston, and R.J. Birgeneau, Phys. Rev. B **41**, 8866 (1990).

[69] F.C. Chou, N. Belk, M.A. Kastner, and R.J. Birgeneau (preprint).

[70] A. Aharony, R.J. Birgeneau, A. Coniglio, M.A. Kastner, and H.E. Stanley, Phys. Rev. Lett. **60**, 1330 (1988).

[71] M. Filipowski, J. Budnick, and Z. Tan, Physica **167C**, 35 (1990).

[72] H. Yoshizawa, S. Mitsuda, H. Kitazawa, and K. Katsumata, J. Phys. Soc. Jpn. **57**, 3686 (1988).

[73] R.J. Birgeneau, Y. Endoh, Y. Hidaka, K. Kakurai, M.A. Kastner, T. Murakami, G. Shirane, T.R. Thurston, and K. Yamada, Phys. Rev. B **39**, 2868 (1989).

[74] S.-W. Cheong, G. Aeppli, T.E. Mason, H. Mook, S.M. Hayden, P.C. Canfield, Z. Fisk, K.N. Clausen, and J.L. Martinez, Phys. Rev. Lett. **67**, 1791 (1991).

[75] T.R. Thurston, P.M. Gehring, G. Shirane, R.J. Birgeneau, M.A. Kastner, Y. Endoh, M. Matsuda, K. Yamada, H. Kojima, and I. Tanaka, Phys. Rev. B **46**, 9128 (1992).

[76] A.R. Moudenbaugh, Y. Xu, M. Suenaga, T.J. Follcerts, and R.N. Shelton, Phys. Rev. B **38**, 4596 (1988).

[77] J.D. Axe, D.E. Cox, K. Mohanty, H. Moudden, A.R. Moudenbough, Y. Xu, and T.R. Thurston, IBM J. Res. Rev. **33**, 382 (1989).

[78] M.K. Crawford, W.E. Farneth, E.M. McCarron, R.L. Harlow, A.H. Moudden, Science **250**, 1390 (1990).

[79] H. Takagi, R.J. Cava, M. Marezio, B. Batlogg, J.J. Krajewski, W.F. Peck, Jr., P. Bordet, and D.E. Cox, Phys. Rev. Lett. **68**, 3777 (1992).

[80] W. Schäfer, M. Breuer, G. Bauer, A. Freimuth, N. Knauf, B. Roden, W. Schlabitz, and B. Büchner, Phys. Rev. B **49**, 9248 (1994).

[81] G. Xiao, A. Bakhshai, M.Z. Cieplak, Z. Tesaonovic, and C.L. Chien, Phys. Rev. B **39**, 315 (1989).

[82] W. Kang, H.J. Schulz, D. Jérome, S.S.P. Parkin, J.M. Bassat, and P. Odier, Phys. Rev. B **37**, 5132 (1988).

[83] B. Battlog, H. Takagi, H.L. Kao, and J. Kwo, Springer Series in Sol. State Sci., **13**, 5 (1993).

[84] Y. Nakamura and S. Uchida, Phys. Rev. B **47**, 8369 (1993).

[85] Y. Hidaka and M. Suzuki, Nature **338**, 635 (1989).

[86] C. Tsuei, A. Gupta, and G. Koren, Physica C **161**, 415 (1989).

[87] T.R. Thurston, M. Matsuda, K. Kakurai, K. Yamada, Y. Endoh, R.J. Birgeneau, P.M. Gehring, Y. Hidaka, M.A. Kastner, T. Murakami, and G. Shirane, Phys. Rev. Lett. **65**, 263 (1990).

[88] V.Z. Kresin, H. Morawitz, S.A. Wolf, *Mechanisms of Conventional and High T_c Superconductivity* , International Series of Monographs in Physics (1993).

[89] E. Dagotto, Rev. Mod. Phys. **66**, 763 (1994).

[90] P. Lee and N. Nagaosa, Phys. Rev. B **46**, 5621 (1992).

[91] V. Emery and S. Kivelson, Physica C **209**, 597 (1993).

[92] R. Laughlin, Science **242**, 525 (1988).

[93] P. Littlewood, C. Varma, and E. Abrahams, Phys. Rev. Lett. **60**, 379 (1987).

[94] C. Varma, S. Schmitt-Rink, and E. Abrahams, Solid State Commun. **62**, 681 (1987).

[95] V. Emery and G. Reiter, Phys. Rev. B **38**, 4547 (1988).

[96] P. Fulde, *Electron Correlations in Molecules and Solids*, Springer Series in Solid-State Sciences Vol.100, (1991).

[97] S.M. Hybertsen, E.B. Stechel, M. Schlüter, and N.E. Christensen, Phys. Rev. B **39**, 11068 (1990).

[98] P. Anderson, Science **235**, 1196 (1987).

[99] F. Zhang and T. Rice, Phys. Rev. B **37**, 3759 (1988).

[100] J. Hubbard, Proc. R. Soc. London, Ser. A **276**, 238 (1963).

[101] J. Chadwick, Nature **129**, 312 (1932).

[102] J. Chadwick, Proc. Roy. Soc. (London) **136**, 692 (1932).

[103] J. Axe, Science **252**, 795 (1991).

[104] C. Shull, K. Billman, and F. Wedgewood, Phys. Rev. **153**, 1415 (1967).

[105] J. Halpern, I. Estermann, O. Simpson, and O. Stern, Phys. Rev. **52**, 142 (1937).

[106] J. Schwinger, Phys. Rev. **52**, 1250 (1937).

[107] J. Hoffman, M. Livingston, and H. Bethe, Phys. Rev. **51**, 214 (1937).

[108] L. Alvarez and F. Bloch, Phys. Rev. **57**, 111 (1940).

[109] A. Snell and L. Miller, Phys. Rev. **74**, 1217 (1948).

[110] S.W. Lovsey, *Theory of Neutron Scattering from Condensed Matter*, vol. 1, (Oxford University Press, Oxford, 1984).

[111] L. Van Hove, Phys. Rev. **95**, 249 (1954).

[112] L. Van Hove, Phys. Rev. **95**, 1374 (1954).

[113] R. Cowley, Adv. Phys. **29**, 1 (1980).

[114] P.W. Anderson, *Fizika Dielectrikov*, edited by G.I. Skanavi (Moskow: Acad. Nauk. SSR, 1960).

[115] W. Cochan, Adv. Phys. **9**, 387 (1960).

[116] R.J. Birgeneau, C.Y. Chen, D.R. Gabbe, H.P. Jenssen, M.A. Kastner, P.J. Picone, T. Thio, T.R. Thurston, and H.L. Tuller, Phys. Rev. Lett. **59**, 1329 (1987).

[117] P. Boni, J.D. Axe, G. Shirane, R.J. Birgeneau, D.R. Gabbe, H.P. Jenssen, M.A. Kastner, C.J. Peters, P.J. Picone, and T.R. Thurston, Phys. Rev. B **38**, 185 (1993).

[118] S.W. Lovsey, *Theory of Neutron Scattering from Condensed Matter*, vol. 2, (Oxford University Press, Oxford, 1984).

[119] W. Marshall and R. Lowde, Rep. Prog. Phys. **31**, 705 (1968).

[120] A. Boothroyd, S. Doyle, D. Paul, and R. Osborn, Phys. Rev. B **45**, 10075 (1992).

[121] T. Riste and K. Otnes, Nucl. Instr. and Meth. **75**, 197 (1969).

[122] S. Shapiro and N. Chesser, Nucl. Instr. and Meth. **101**, 183 (1972).

[123] see e.g. P.K. Iyengar, in "*Thermal Neutron Scattering*", (P.A. Egelstaff, ed.) Academic Press, London, (1965).

[124] R.A. Cowley, G. Shirane, R.J. Birgeneau, and H.J. Guggenheim, Phys. Rev. B **15**, 4292 (1977).

[125] J. Als-Nielsen, Phys. Rev. Lett. **25**, 730 (1970).

[126] M. Schulhof, P. Heller, R. Nathans, and A. Linz, Phys. Rev. B **1**, 2304 (1970).

[127] A. Tucciarone, H.Y. Lau, L.M. Corliss, A. Delapalme, and J.M. Hastings, Phys. Rev. B **4**, 3206 (1971).

[128] T. Freltoft, G. Shirane, S. Mitsuda, J.P Remeika, and A.S. Cooper, Phys. Rev. B **37**, 137 (1988).

[129] M. Matsuda (private communication).

[130] M. Cooper and R. Nathans, Acta Cryst. **23**, 357 (1967).

[131] N. Chesser and J. Axe, Acta Cryst. **29**, 160 (1973).

[132] M. Cooper and R. Nathans, Acta Cryst. **24**, 481 (1968).

[133] P. Picone, D. Gabbe, and H. Jenssen, J. Crystal Growth **85**, 576 (1987).

[134] Y. Hidaka, Y. Enomoto, M. Suzuki, M. Oda, and T. Murakami, J. Crystal Growth **85**, 581 (1987).

[135] B.O. Wells, Z.-X. Shen, A. Matsuura, D.M. King, M.A. Kastner, M. Greven, and R.J. Birgeneau, Phys. Rev. Lett. **74**, 964 (1995).

[136] B.O. Wells, Z.-X. Shen, A. Matsuura, D.M. King, M.A. Kastner, M. Greven, and R.J. Birgeneau, *Spectroscopies in Novel Superconductors*, conference proceedings (1995).

[137] J.D. Perkins, J.M. Graybeal, M.A. Kastner, R.J. Birgeneau, J.P. Falck, and M. Greven, Phys. Rev. Lett. **71**, 1621 (1993).

[138] J.D. Perkins, Ph.D. thesis, MIT, (1993).

[139] A. Cassanho, B. Keimer, and M. Greven, J. Crystal Growth **128**, 813 (1993).

[140] Y. Hidaka, 9^{th} Intern. Conf. on Crystal Growth (ICCG-9), Sendai, Japan (1989).

[141] L.L. Miller, X.L. Wang, S.X. Wang, C. Stassis, D.C. Johnston, J. Faber, and C.-K. Loong, Phys. Rev. B **41**, 1921 (1990).

[142] H. Bethe, Z. Phys. **71**, 205 (1931).

[143] L. Hulthén, Ark. Mat. Astron. Fys. **26A**, no. 11 (1938).

[144] J. des Cloizeaux and J. Pearson, Phys. Rev. **128**, 2131 (1962).

[145] Y. Endoh, G. Shirane, R.J. Birgeneau, P.M. Richards, and S.L. Holt, Phys. Rev. Lett. **32**, 718 (1974).

[146] H. Mikesaka, Phys. Rev. B **12**, 2794 (1975).

[147] R. Orbach, Phys. Rev. **112**, 309 (1958).

[148] F. Haldane, Phys. Lett. A **93**, 464 (1983).

[149] F. Haldane, Phys. Rev. Lett. **50**, 1153 (1983).

[150] T. Holstein and H. Primakoff, Phys. Rev. **58**, 1098 (1940).

[151] P. Anderson, Phys. Rev. **86**, 694 (1952).

[152] R. Kubo, Phys. Rev. **87**, 568 (1952).

[153] P. Hohenberg, Phys. Rev. **158**, 383 (1967).

[154] N. Mermin and H. Wagner, Phys. Rev. Lett. **22**, 1133 (1966).

[155] P. Anderson, Mater. Res. Bull. **8**, 153 (1973).

[156] S. de Jongh and A. Meidema, Adv. Phys. **23**, 1 (1974).

[157] E. Neves and J. Peres, Phys. Lett. A **114A**, 331 (1986).

[158] I. Affleck, T. Kennedy, E. Lieb, and H. Tasaki, Commun. Math. Phys. **115**, 477 (1988).

[159] I. Affleck, Z. Zou, T. Hsu, and P. Anderson, Phys. Rev. B **38**, 745 (1988).

[160] F. Manousakis, Rev. Mod. Phys **63**, 1 (1991).

[161] D. Vaknin, S.K. Sinha, D.E. Moncton, D.C. Johnston, J.M. Newsam, C.R. Safinya, and H.E. King, Phys. Rev. Lett. **58**, 2802 (1987).

[162] Y. Endoh, K. Yamada, R.J. Birgeneau, D.R. Gabbe, H.P. Jennsen, M.A. Kastner, C.J. Peters, P.J. Picone, T.R. Thurston, J.M. Tranquada, G. Shirane, Y. Hidaka, M. Oda, Y. Enomoto, M. Suzuki, and T. Murakami, Phys. Rev. B **37**, 7443 (1988).

[163] S. Tyč, B. Halperin, and S. Chakravarty, Phys. Rev. Lett. **62**, 835 (1989).

[164] R. Birgeneau, Phys. Rev. B **41**, 2514 (1990).

[165] M. Greven, R.J. Birgeneau, Y. Endoh, M.A. Kastner, B. Keimer, M. Matsuda, G. Shirane, and T.R. Thurston, Phys. Rev. Lett **72**, 1096 (1994).

[166] M. Greven, R.J. Birgeneau, Y. Endoh, M.A. Kastner, B. Keimer, M. Matsuda, G. Shirane, and T.R. Thurston, Physica B **199-200**, 642 (1994).

[167] M. Greven, R.J. Birgeneau, Y. Endoh, M.A. Kastner, M. Matsuda, and G. Shirane, Z. Phys. B **96**, 465 (1995).

[168] H.-D. Ding and M. Makivić, Phys. Rev. Lett. **64**, 1449 (1990).

[169] M. Makivić and H.-Q. Ding, Phys. Rev. B **43**, 3562 (1991).

[170] A. Sokol, R. Glenister, and R. Singh, Phys. Rev. Lett. **72**, 1549 (1994).

[171] T. Oguchi, Phys. Rev. **117**, 117 (1960).

[172] K. Yamada, E. Endoh, Y. Endoh, Y. Hidaka, M. Oda, M. Suzuki, and T. Murakami, Solid State Commun. **64**, 753 (1987).

[173] J. Igarashi, Phys. Rev. B **46**, 10763 (1992).

[174] C. Hamer, Z. Weihong, and J. Oitmaa, Phys. Rev. B **50**, 6877 (1994).

[175] U.-J. Wiese and H.-P. Ying, Z. Phys. B **93**, 147 (1994).

[176] W. Zheng, J. Oitmaa, and C.J. Hamer, Phys. Rev. B **43**, 8321 (1991).

[177] D. Arovas and A. Auerbach, Phys. Rev. B **38**, 316 (1988).

[178] A. Auerbach and D. Arovas, Phys. Rev. Lett. **61**, 617 (1988).

[179] M. Takahashi, Phys. Rev. B **40**, 2494 (1989).

[180] J. Hirsch and S. Tang, Phys. Rev. B **40**, 4769 (1989).

[181] E. Manousakis and R. Salvador, Phys. Rev. Lett. **61**, 1210 (1989).

[182] E. Manousakis and R. Salvador, Phys. Rev. B **40**, 2205 (1989).

[183] S. Chakravarty (private communication).

[184] A. Chubukov and S. Sachdev, Phys. Rev. Lett. **71**, 169 (1993).

[185] S. Sachdev and J. Ye, Phys. Rev. Lett. **69**, 2411 (1992).

[186] S. Shenker and J. Tobochnik, Phys. Rev. B **22**, 4462 (1980).

[187] B. Halperin and P. Hohenberg, Phys. Rev. **177**, 952 (1969).

[188] M. Makivić and M. Jarrell, Phys. Rev. Lett. **68**, 1770 (1992).

[189] A. Chubukov, S. Sachdev, and J. Ye, Phys. Rev. B **49**, 11919 (1994).

[190] A. Sokol and D. Pines, Phys. Rev. Lett. **71**, 2813 (1993).

[191] V. Barzykin, D. Pines, A. Sokol, and D. Thelen (unpublished).

[192] T. Imai, C.P. Schlichter, K. Yoshimura, M. Katoh, and K. Kosuge, Phys. Rev. Lett. **71**, 1254 (1993).

[193] H.-D. Ding and M. Makivić, Phys. Rev. B **42**, 6827 (1990).

[194] J. Kosterlitz and D. Thouless, J. Phys. C **6**, 1181 (1973).

[195] M. Matsuda, K. Yamada, H. Kadowaki, T.R. Thurston, Y. Endoh, Y. Hidaka, R.J. Birgeneau, M.A. Kastner, P.M. Gehring, A.H. Moudden, and G. Shirane, Phys. Rev. B **42**, 10098 (1990).

[196] F. Borsa, M. Corti, T. Goto, A. Rigamonti, D.C. Johnston, and F.C. Chou, Phys. Rev. B **45**, 5756 (1992).

[197] P. Kopietz, Phys. Rev. Lett. **64**, 2587 (1990).

[198] J.H. Kim (preprint).

[199] S. Chakravarty and R. Orbach, Phys. Rev. Lett. **64**, 224 (1990).

[200] T. Imai, C. Schlichter, K. Yoshimura, and K. Kosuge, Phys. Rev. Lett. **70**, 1002 (1993).

[201] A. Chubukov, S. Sachdev, and A. Sokol, Phys. Rev. B **49**, 9052 (1994).

[202] L.P. Le, G.M. Luke, B.J. Sternlieb, Y.J. Uemura, J.H. Brewer, T.M. Riseman, D.C. Johnston, and L.L. Miller, Phys. Rev. B **42**, 2182 (1990).

[203] S. Bramwell and P. Holdsworth, J. Phys.: Condens. Matter **5**, L53 (1993).

[204] S. Bramwell and P. Holdsworth, J. Appl. Phys. **73**, 6096 (1993).

[205] S. Bramwell and P. Holdsworth, Phys. Rev. B **49**, 8811 (1994).

[206] T. Thio and A. Aharony, Phys. Rev. Lett. **73**, 894 (1994).

[207] R. Birgeneau, H. Guggenheim, and G. Shirane, Phys. Rev. Lett. **22**, 720 (1969).

[208] R. Birgeneau, F. De Rosa, and H. Guggenheim, Solid State Commun. **8**, 13 (1970).

[209] J.M. Tranquada, G. Shirane, B. Keimer, S. Shamoto, and M. Sato, Phys. Rev. B **40**, 4503 (1989).

[210] H.-Q. Ding, Phys. Rev. Lett. **68**, 1927 (1992).

[211] T. Moriya, J. Phys. Soc. Jpn. **18**, 516 (1963).

[212] C. Pennington and C. Schlichter, Phys. Rev. Lett. **66**, 381 (1991).

[213] T. Imai (private communication).

[214] M. Takahashi, Phys. Rev. Lett. **58**, 168 (1987).

[215] M. Takahashi, Prog. Theor. Phys. Suppl. **101**, 487 (1990).

[216] G. Wysin and A. Bishop, Phys. Rev. B **42**, 810 (1990).

[217] M. Suzuki, Prog. Theor. Phys **56**, 1457 (1976); J. Stat. Phys. **43**,883 (1986).

[218] H. Evertz, G. Lana, and M. Marcu, Phys. Rev. Lett. **70**, 875 (1993).

[219] P. Hasenfratz and F. Niedermayer, Z. Phys. B **92**, 91 (1993).

[220] N. Elstner, R.L. Glenister, R.R.P. Singh, and A. Sokol (preprint).

[221] N. Elstner, A. Sokol, R.R.P. Singh, M. Greven, and R. J. Birgeneau (preprint).

[222] M. Lüscher and P. Weisz, Nucl. Phys. B **300**, 325 (1988).

[223] D. Lambeth and H. Stanley, Phys. Rev. B **12**, 5302 (1975).

[224] A.W. Sandvik and A.V. Chubukov and S. Sachdev (preprint).

[225] F. Haldane, J. Appl. Phys. **57**, 3359 (1985).

[226] Y.S. Lee, M. Greven, B.O. Wells, and R.J. Birgeneau (unpublished).

[227] C.G. Olson, R. Liu, D.W. Lynch, R.S. List, A.J. Arko, B.W. Veal, Y.C. Chang, P.Z. Jiang, and A.P. Paulikas, Phys. Rev. B **42**, 381 (1990).

[228] J.C. Campuzano, G. Jennings, M. Faiz, L. Beaulaigue, B.W. Veal, J.Z. Liu, A.P. Paulikas, K. Vandervoort, H. Claus, R.S. List, A.J. Arko, and R.J. Bartlett, Phys. Rev. Lett. **64**, 2308 (1990).

[229] K. Gofron, J.C. Campuzano, H. Ding, C. Gu, R. Liu, B. Dabrowski, B.W. Veal, W. Cramer, and G. Jennings, J. Phys. Chem. Solids **54**, 1193 (1993).

[230] Z.-X. Shen, W.E. Spicer, D.M. King, D.S. Dessau, and B.O. Wells, Science **267**, 343 (1995).

[231] N. Bulut, D.J. Scalapino, and S.R. White (preprint).

[232] O. Jepsen (unpublished).

[233] E. Dagotto, F. Ortolani, and D. Scalapino, Phys. Rev. B **46**, 3183 (1992).

[234] A. Nazarenko, K.J.E. Vos, S. Haas, E. Dagotto, and R.J. Gooding (preprint).

[235] P. Aebi, J. Osterwalder, P. Schwaller, L. Schlapbach, M. Shimoda, T. Mochiku, and K. Kadowaki, Phys. Rev. Lett. **72**, 2757 (1994).

[236] G. Kotliar and J. Liu, Phys. Rev. B **38**, 5142 (1988).

[237] S.R. White, D.J. Scalapino, R. Sugar, N.E. Bickers, and R. Scalettar, Phys. Rev. B **39**, 839 (1989).

[238] D. Monthoux and D. Pines, Phys. Rev. Lett. **69**, 961 (1992).

[239] T. Moriya, Y. Takahashi, and K. Ueda, Physica **185-189C**, 114 (1991).

[240] J. Annett, N. Goldenfeld, and S. Renn, Phys. Rev. B **43**, 2778 (1991).

[241] W.N. Hardy, D.A. Bonn, D.C. Morgan, R. Liang, and K. Zhang, Phys. Rev. Lett. **70**, 3999 (1993).

[242] T. Imai, H. Yasuoka, T. Shimizu, Y. Ueda, K. Yoshimura, and K. Kosuge, Physica C **162-164**, 169 (1989).

[243] J.A. Martindale, S.E. Barrett, K.E. O'Hara, C.P. Schlichter, W.C. Lee, and D.M. Ginsberg, Phys. Rev. B **47**, 9155 (1993).

[244] B.O. Wells, Z.-X. Shen, D.S. Dessau, W.E. Spicer, D.B. Mitzi, L. Lombardo, A. Kapitulnik, A.J. Arko, Phys. Rev. B **46**, 11830 (1992).

[245] Z.-X. Shen, D.S. Dessau, B.O. Wells, D.M. King, W.E. Spicer, A.J. Arko, D. Marshall, L.W. Lombardo, A. Kapitulnik, P. Dickinson, S. Doniach, J. DiCarlo, A.G. Loeser, and C.H. Park, Phys. Rev. Lett. **70**, 1553 (1993).

[246] D.A. Wollman, D.J. Van Harlingen, W.C. Lee, D.M. Ginsberg, and A.J. Leggett, Phys. Rev. Lett. **71**, 2134 (1993).

[247] P. Lee, Phys. Rev. Lett. **71**, 1887 (1993).

[248] A.V. Balatsky, A. Rosengren, and B.L. Altshuler, Phys. Rev. Lett. **73**, 720 (1994).

[249] X.K. Chen, J.C. Irwin, H.J. Trodahl, T. Kimura, and K. Kishio, Phys. Rev. Lett. **73**, 3290 (1994).

[250] J. Rossat-Mignot et al., in Frontiers in Solid State Science: "Selected Topics in Superconductivity", World Scientific, Singapore, p.265 (1993).

[251] B.J. Sternlieb, G. Shirane, J.M. Tranquada, M. Sato, and S. Shamoto, Phys. Rev. B **47**, 5320 (1993).

[252] M.Sato, S. Shamoto, T. Kiyokura, K. Kakurai, G. Shirane, B.J. Sternlieb, and J.M. Tranquada, J. Phys. Soc. Jpn **62**, 263 (1993).

[253] H.F. Fong, B. Keimer, P.W. Anderson, D. Reznik, F. Dogan, and I.A. Aksay (preprint).

[254] Y. Zha, K. Levin, and Q. Si, Phys. Rev. B **47**, 9124 (1993).

[255] T. Tanamato, H. Kohno, and H. Fukuyama, J. Phys. Soc. Jpn. **63**, 2739 (1994).

[256] S.M. Quinlan and D.J. Scalapino, Phys. Rev B **51**, 497 (1995).

[257] K. Yamada, S. Wakimoto, G. Shirane, C.H. Lee, M.A. Kastner, S. Hosoya, M. Greven, Y. Endoh, and R. J. Birgeneau (preprint).

[258] S. Hosoya, C.H. Lee, S. Wakimoto, K. Yamada, and Y. Endoh, Physica C **235-240**, 547 (1994).

[259] D.J. Scalapino (unpublished).

[260] Y. Zha and K. Levin (unpublished).

[261] M.K. Crawford, R.L. Harlow, E.M. McCarron, W.E. Farneth, J.D. Axe, H. Chou, and Q. Huang, Phys. Rev. B **44**, 7749 (1991).

[262] Y. Nakamura and S. Uchida, Phys. Rev. B **46**, 5841 (1992).

[263] B. Büchner, M. Cramm, M. Braden, W. Braunisch, O. Hoffels, W. Schnelle, R. Müller, A. Freimuth, W. Schlabitz, G. Heger, D.I. Khomskii, and D. Wohlleben, Europhys. Lett. **21**, 953 (1993).

[264] T. Suzuki, M. Sera, T. Hanaguri, and T. Fukase, Phys. Rev. B **49**, 12392 (1994).

[265] B. Keimer, R.J. Birgeneau, A. Cassanho, Y. Endoh, R.W. Erwin, M.A. Kastner, and G. Shirane, Phys. Rev. Lett. **67**, 1930 (1991).

[266] M. Matsuda, R.J. Birgeneau, Y. Endoh, Y. Hidaka, M.A. Kastner, K. Nakajima, G. Shirane, T.R. Thurston, and K. Yamada, J. Phys. Soc. Jpn. **62**, 1702 (1993).

[267] K. Kakurai, S. Shamoto, T. Kiyokura, M. Sato, J.M. Tranquada, and G. Shirane, Phys. Rev. B **48**, 3485 (1993).

[268] R.J. Birgeneau, R.W. Erwin, P.M. Gehring, M.A. Kastner, B. Keimer, M. Sato, S. Shamoto, G. Shirane, and J.M. Tranquada, Z. Phys. B **87**, 15 (1992).

[269] V.F. Sears, "Thermal Neutron Scattering Length and Cross-Sections for Condensed Matter Research", Chalk River, Ontario, Canada (1984).

5895-25